



Time-Resolved X-ray Spectroscopy of 2-Thiouracil

Dennis Mayer

Publikationsbasierte Universitätsdissertation
zur Erlangung des akademischen Grades

doctor rerum naturalium
(*Dr. rer. nat.*)

in der Wissenschaftsdisziplin
Experimentalphysik

eingereicht an der
Mathematisch-Naturwissenschaftlichen Fakultät
der Universität Potsdam

Datum der Disputation: 29.11.2022

Betreuer

Prof. Dr. Markus Gühr
Universität Potsdam

Gutachter

Prof. Dr. Ingo Fischer
Universität Würzburg

Prof. Dr. Daniel Rolles
Kansas State University

Published online on the
Publication Server of the University of Potsdam:
<https://doi.org/10.25932/publishup-57163>
<https://nbn-resolving.org/urn:nbn:de:kobv:517-opus4-571636>

Abstract

In this thesis, I present my contributions to the field of ultrafast molecular spectroscopy. Using the molecule 2-thiouracil as an example, I use ultrashort x-ray pulses from free-electron lasers to study the relaxation dynamics of gas-phase molecular samples. Taking advantage of the x-ray typical element- and site-selectivity, I investigate the charge flow and geometrical changes in the excited states of 2-thiouracil.

In order to understand the photoinduced dynamics of molecules, knowledge about the ground-state structure and the relaxation after photoexcitation is crucial. Therefore, a part of this thesis covers the electronic ground-state spectroscopy of mainly 2-thiouracil to provide the basis for the time-resolved experiments. Many of the previously published studies that focused on the gas-phase time-resolved dynamics of thionated uracils after UV excitation relied on information from solution phase spectroscopy to determine the excitation energies. This is not an optimal strategy as solvents alter the absorption spectrum and, hence, there is no guarantee that liquid-phase spectra resemble the gas-phase spectra. Therefore, I measured the UV-absorption spectra of all three thionated uracils to provide a gas-phase reference and, in combination with calculations, we determined the excited states involved in the transitions.

In contrast to the UV absorption, the literature on the x-ray spectroscopy of thionated uracil is sparse. Thus, we measured static photoelectron, Auger-Meitner and x-ray absorption spectra on the sulfur L edge before or parallel to the time-resolved experiments we performed at FLASH (DESY, Hamburg). In addition, (so far unpublished) measurements were performed at the synchrotron SOLEIL (France) which have been included in this thesis and show the spin-orbit splitting of the S 2p photoline and its satellite which was not observed at the free-electron laser.

The relaxation of 2-thiouracil has been studied extensively in recent years with ultrafast visible and ultraviolet methods showing the ultrafast nature of the molecular process after photoexcitation. Ultrafast spectroscopy probing the core-level electrons provides a complementary approach to common optical ultrafast techniques. The method inherits its local sensitivity from the strongly localised core electrons. The core energies and core-valence transitions are strongly affected by local valence charge and geometry changes, and past studies have utilised this sensitivity to investigate the molecular process reflected by the ultrafast dynamics. We have built an apparatus that provides the requirements to perform time-resolved x-ray spectroscopy on molecules in the gas phase. With the apparatus, we performed UV-pump x-ray-probe electron spectroscopy on the S 2p edge

of 2-thiouracil using the free-electron laser FLASH2. While the UV triggers the relaxation dynamics, the x-ray probes the single sulfur atom inside the molecule. I implemented photoline self-referencing for the photoelectron spectral analysis. This minimises the spectral jitter of the FEL, which is due to the underlying self-amplified spontaneous emission (SASE) process. With this approach, we were not only able to study dynamical changes in the binding energy of the electrons but also to detect an oscillatory behaviour in the shift of the observed photoline, which we associate with non-adiabatic dynamics involving several electronic states. Moreover, we were able to link the UV-induced shift in binding energy to the local charge flow at the sulfur which is directly connected to the electronic state. Furthermore, the analysis of the Auger-Meitner electrons shows that energy shifts observed at early stages of the photoinduced relaxation are related to the geometry change in the molecule. More specifically, the observed increase in kinetic energy of the Auger-Meitner electrons correlates with a previously predicted C=S bond stretch.

Zusammenfassung

In dieser Arbeit präsentiere ich meine Beiträge zum Gebiet der ultraschnellen Molekülspektroskopie. Am Beispiel des Moleküls 2-Thiouracil verwende ich ultrakurze Röntgenpulse von Freie-Elektronen-Lasern, um die Relaxationsdynamik von Molekülproben in der Gasphase zu untersuchen. Unter Ausnutzung der für Röntgenstrahlung typischen Element- und Ortsselektivität untersuche ich den Ladungsfluss und die geometrischen Veränderungen in den angeregten Zuständen von 2-Thiouracil.

Um die photoinduzierte Dynamik von Molekülen zu verstehen, ist das Wissen über die Grundzustandsstruktur und die Relaxation nach Photoanregung entscheidend. Daher befasst sich ein Teil dieser Arbeit mit der elektronischen Grundzustandsspektroskopie von 2-Thiouracil, um die Grundlage für die zeitaufgelösten Experimente zu schaffen. Viele der bisher veröffentlichten Studien, die sich mit der zeitaufgelösten Dynamik von Thiouracilen in der Gasphase nach UV-Anregung befassten, stützten sich zur Bestimmung der Anregungsenergien auf Informationen aus der Spektroskopie in Lösung. Dies ist nicht optimal, da Lösungsmittel das Absorptionsspektrum verändern und es daher keine Garantie dafür gibt, dass die Spektren in Lösung den Spektren der Gasphase ähneln. Daher habe ich die UV-Absorptionsspektren aller drei Thiouracile gemessen, um eine Referenz für die Gasphase zu erhalten, und in Kombination mit Berechnungen die an den Übergängen beteiligten angeregten Zustände bestimmt.

Im Gegensatz zur UV-Absorption ist die Literatur zur Röntgenspektroskopie von thioniertem Uracil spärlich. Daher haben wir statische Photoelektronen-, Auger-Meitner- und Röntgenabsorptionsspektren an der Schwefel-L-Kante vor oder parallel zu den zeitaufgelösten Experimenten an FLASH (DESY, Hamburg) gemessen. Darüber hinaus wurden (bisher unveröffentlichte) Messungen am Synchrotron SOLEIL (Frankreich) durchgeführt, die in diese Arbeit eingeflossen sind und die Spin-Orbit-Aufspaltung der S 2p-Photolinie und ihres Satelliten zeigen, die am Freie-Elektronen-Laser nicht beobachtet wurde.

Die Relaxation von 2-Thiouracil wurde in den letzten Jahren ausgiebig mit ultraschnellen Methoden im sichtbaren und ultravioletten Spektralbereich untersucht, die die ultraschnelle Natur des molekularen Prozesses nach der Photoanregung zeigen. Die ultraschnelle Spektroskopie, bei der die Elektronen des Kernniveaus untersucht werden, bietet einen ergänzenden Ansatz zu den üblichen optischen Techniken. Die Methode erhält ihre lokale Empfindlichkeit durch die stark lokalisierten Kernelektronen. Die Kernenergien und Kern-Valenz-Übergänge werden stark von lokalen Valenzladungs- und Geometrieänderungen beeinflusst, und frühere Studien haben diese Empfindlichkeit

genutzt, um den molekularen Prozess zu untersuchen, der sich in der ultraschnellen Dynamik widerspiegelt. Wir haben eine Apparatur gebaut, die die Voraussetzungen für die Durchführung zeitaufgelöster Röntgenspektroskopie an Molekülen in der Gasphase bietet. Mit dieser Apparatur haben wir Anregungs-Abfrage-Elektronenspektroskopie an der S 2p-Kante von 2-Thiouracil an dem Freie-Elektronen-Laser FLASH2 durchgeführt. Zuerst triggert ein UV-Puls die Relaxationsdynamik und anschließend tastet ein Röntgenpuls das einzelne Schwefelatom im Inneren des Moleküls ab. Für die Analyse der Photoelektronenspektren habe ich eine Selbstreferenzierung der Photolinie implementiert, mit deren Hilfe der spektrale Jitter des FEL minimiert werden konnte. Dieser ist auf den zugrunde liegenden Prozess der selbstverstärkten spontanen Emission (SASE) zurückzuführen. Mit diesem Ansatz konnten wir nicht nur dynamische Veränderungen in der Bindungsenergie der Elektronen untersuchen, sondern auch ein oszillierendes Verhalten in der Verschiebung der beobachteten Photolinie feststellen, das wir mit einer nicht-adiabatischen Dynamik in Verbindung bringen, an der mehrere elektronische Zustände beteiligt sind. Außerdem konnten wir die UV-induzierte Verschiebung der Bindungsenergie mit dem lokalen Ladungsfluss am Schwefel in Verbindung bringen, der direkt mit dem elektronischen Zustand verbunden ist. Darüber hinaus zeigt die Analyse der Auger-Meitner-Elektronen, dass die in frühen Stadien der photoinduzierten Relaxation beobachteten Energieverschiebungen mit der Geometrieänderung des Moleküls zusammenhängen. Genauer gesagt korreliert der beobachtete Anstieg der kinetischen Energie der Auger-Meitner-Elektronen mit einer zuvor vorhergesagten Dehnung der C=S-Bindung.

Contents

Abstract	iii
Zusammenfassung	v
Contents	vii
List of Figures	ix
List of Tables	xi
List of Abbreviations	xiii
1 Introduction	1
2 List of Publications and Contributions	5
3 Molecular Dynamics	9
3.1 Adiabatic and Born-Oppenheimer-Approximation	9
3.2 Potential Energy Surfaces and Wavepackets	11
3.3 Binding Energies and Molecular Orbitals	14
3.4 Molecular Dynamics of 2-Thiouracil	19
3.5 X-Ray Spectroscopy	23
3.5.1 Photoelectron Emission	24
3.5.2 Excited-State Chemical Shift	28
3.5.3 X-Ray Absorption	29
3.5.4 Auger-Meitner Effect	31
4 Gas-Phase Spectroscopy of Molecular Samples	35
4.1 Gas-Phase UV-Vis Absorption Spectroscopy	35
4.2 Time-of-Flight Measurements	38
4.3 X-ray Free-Electron Lasers	41
4.3.1 Basic Principle of SASE Free-Electron Lasers	41
4.3.2 FLASH	45

4.3.3	Spectral Resolution in Experiments	46
4.4	UV Pump - X-ray Probe Electron Spectroscopy	48
5	Articles	51
	Article 1	52
	Article 2	62
	Article 3	76
	Article 4	88
	Article 5	98
	Article 6	108
6	Conclusions & Outlook	121
	Bibliography	125
	Appendix	133
	A Supplementary Information to Article 1	133
	B Supplementary Information to Article 5	144
	Acknowledgements	167
	Declaration of Authorship	169

List of Figures

3.1	Scheme of potential curves for a diatomic molecule	12
3.2	Isosurface plots for HOMO and LUMO in 2-thiouracil	17
3.3	Absorption spectra and potential energy surfaces for uracil and 2-thiouracil	19
3.4	Excited state population and relaxation pathway of 2-thiouracil	21
3.5	Schemes of some x-ray spectroscopy methods.	23
3.6	S 2p photoelectron spectrum of 2-thiouracil	25
3.7	C 1s photoelectron spectra of uracil and 2-thiouracil	26
3.8	Excited-state chemical shift	29
3.9	NEXAFS spectra of 2-tUra at the S 2p and the C 1s edge	30
3.10	S2p Auger-Meitner spectrum of 2-thiouracil	33
4.1	Sketch of the home-built sample cell for the Cary UV-Vis spectrometer. .	36
4.2	Temperature-dependent absorption spectra of the gas cell	37
4.3	Sketch of a magnetic bottle time-of-flight spectrometer	39
4.4	Overview of components of a free electron laser.	42
4.5	Sketch of the electron motion and micro-bunching in an undulator. . . .	43
4.6	Single-shot and averaged S 2p spectra taken at FLASH	47
4.7	Scheme for the UV pump x-ray probe electron spectroscopy.	48

List of Tables

3.1	Hartree-Fock on 2-thiouracil compared to experiment	18
-----	---	----

List of Abbreviations

ADC	algebraic diagrammatic construction
AMS	Auger-Meitner spectroscopy
BAM	beam arrival time monitor
BOA	Born-Oppenheimer approximation
CoIn	conical intersection
C	carbon
ca.	circa
DS	difference spectrum
e.g.	exempli gratia
ES	excited-state spectrum
ESCS	excited-state chemical shift
et al.	et alii
FEL	free-electron laser
FLASH	free-electron laser in Hamburg
FWHM	full width at half maximum
GMD	gas monitor detector
GS	ground-state spectrum
HF	Hartree-Fock
HHG	high-order harmonic generation
HOMO	highest occupied molecular orbital
ICS	intersection coordinate space
i.e.	id est
IP	ionisation potential
IRF	instrument response function
ISC	intersystem crossing
LUMO	lowest unoccupied molecular orbital
MBES	magnetic bottle (time-of-flight) electron spectrometer
MCP	microchannel plates
MO	molecular orbital
MS-CASPT2	multi-state complete active space perturbation theory
N	nitrogen
NEXAFS	near edge x-ray absorption fine structure

O	oxygen
OPIS	online photoionization spectrometer
PDT	photodynamic therapy
PES	potential energy surface
PS	pumped spectrum
RF	radiofrequency
S	sulfur
S_x	singlet state x
SASE	self-amplified spontaneous emission
SCF	self-consistent field
SE	Schrödinger equation
SOLEIL	Source optimisée de lumière d'énergie intermédiaire du LURE
T_x	triplet state x
TAS	transient absorption spectroscopy
TOF	time of flight
TR	time-resolved
(d)tUra	(di-)thiouracil
URSA-PQ	Ultraschnelle Röntgenspektroskopie zur Abfrage der Photoenergiekonversion an Quantensystemen
XPS	x-ray photoelectron spectroscopy

1 | Introduction

Nucleobases are core molecules of DNA. Base pairs inside the DNA double helix encode the genetic information of life. This genetic code holds all information for the generation of a functioning organism, from its structure to its metabolism. Nucleobases have a large UV-absorption cross section and, therefore, due to its abundance in sunlight, all organisms will absorb UV light to a certain extent. Unfortunately, the absorption of UV light is dangerous as it is able to alter the bonding inside the DNA strand. In the case of nucleobases, this alternation can cause the formation of intrastrand dimers i.e., bases from neighbouring pairs start to form a bond. [1]. These lesions between base pairs can lead to mutation or cell death and are, thus, highly dangerous. However, the formation of dimers occurs often in long lived photoexcited states. One reason why those mutations do not happen frequently is that nucleobases show an ultrafast relaxation into their ground state after the excitation with UV light [2].

The UV-induced mutations in DNA may mostly lead to skin cancer as the skin is the only directly exposed part of the human body. General mutations, however, can lead to cell deformation and tumours and affect the metabolism. Finding treatments against cancer and other diseases is a crucial but challenging field of research. Surgery, chemo- and radiation therapy have become common methods for cancer treatment but they are usually very invasive and have strong side effects on the human body. In contrast, photodynamic therapy (PDT) provides a less invasive and more local treatment [3–6]. Here, a photosensitive but non-toxic molecule is brought into the body and primarily enriches the tumour. The sensitiser is activated by a proper light source i.e., it is excited using a distinct wavelength. During the relaxation, the molecules tend to create singlet excited molecular oxygen - a highly reactive compound that can attack the tumor cells. The formation of singlet molecular oxygen often happens due to type II photosensitisation i.e., a triplet-excited photosensitiser is deactivated into the singlet ground state *via* energy transfer to the ground-state molecular oxygen (which is also a triplet state) [7, 8]. This reaction requires sensitisers that tend to relax into long-lived triplet states after photoexcitation.

Examples for molecules, that undergo an ultrafast relaxation into triplet states, are thionated organic compounds [9] and, in particular, thionated nucleobases [10–13]. Here, oxygen is substituted by sulfur inside the molecule [14]. The advantage of thionucleobases is their structural similarity to their canonical counterparts due to which they are able to substitute canonical nucleobases in the DNA. Further, the introduction of the sulfur

atom shifts to excitation wavelength from the UVC range (ca. 200 - 280 nm) more towards the UVB (ca. 280 - 315 nm) and UVA range (ca. 315 - 400 nm) and, thus, separates the excitation from that of the canonical nucleobases [10, 11]. These properties make thionucleobases interesting candidates for PDT. However, they also have a long history in immunosuppression [15–18]. Unfortunately, the relaxation into triplet states after photoexcitation and the subsequent generation of singlet oxygen comes also as a disadvantage because the UVA range is less absorbed in the earth's atmosphere. Patients that are treated with this class of molecules and that are exposed to sunlight, therefore, develop an increased risk for skin cancer as the singlet oxygen can also attack healthy cells. Additionally, thionated nucleobases can also produce photolesions (intrastrand dimers) [9, 19] and interstrand cross-linking [20]. Understanding the photoinduced relaxation of these molecules and also the possible reactions, that come with it, are two cornerstones for evaluating the usefulness of thionated nucleobases in therapy and medical research.

With regards to the ultrafast relaxation mechanisms in thionated nucleobases, various ultrafast experiments have been performed and combined with static and dynamic calculations in order to understand the physics behind it (see references [10, 11] and the references therein). Amongst the broad variety of these molecules, thionated uracil has been studied most extensively, especially in the form of 2-thiouracil (2-tUra) [21–31] but also its isomer 4-thiouracil (4-tUra) [32–34] and the double thionated analogue 2,4-dithiouracil (2,4-dtUra) [30, 35]. The time-resolved experiments performed so far were focused primarily on probing the valence electrons of the systems, deriving relaxation times from transient features in different observables and comparing them to values from calculations [21–23, 30–35]. For 2-tUra, transients have been measured using photoelectron [22, 24] or photoion [21] spectroscopy with a UV probe or using transient absorption spectroscopy with broadband optical pulses [25, 30]. After comparing the results to different types of theory, most of the studies come to the conclusion that an intermediate, “spectroscopically elusive” dark state might act as a doorway to populate the triplet states [22, 24, 25, 34]. The same is proposed for the isomer 4-tUra [33, 34]. However, Chakraborty *et al.* state in a recent publication that comparing time constants derived in experiments with those derived from calculating the population of electronic states is an inadequate measure for determining the correct pathway as the excited states may not have a unique and separable response on the experimentally measured observable [36]. According to them, a full simulation of the actual observable in experiment should be performed; however, this is more computationally cumbersome than the derivation of time constants from a population analysis. One might add that even a complete simulation may not lead to a definite answer. Theories are based on approximations and experiments are subject to uncertainties. Thus, it may happen that different processes have very similar observables so that the interpretation is not unambiguous.

Furthermore, the calculations performed so far suggested that 2-thiouracil also undergoes geometrical changes during relaxation [26–29]. In particular, the C=S bond should stretch and bend against the molecular plane. Though valence spectroscopy may be technically sensitive to these changes, it cannot give a direct and unambiguous answer

to whether they occur or not.

X-rays, in contrast, are known to provide an element and site-selectivity as they can address highly localised core-level electrons. The binding energy of these electrons is different for each element and depends on the chemical surrounding [37]. In excited states, the molecule can undergo geometrical changes but also the valence charge distribution will change dynamically during the relaxation. These changes strongly affect the binding energies of core-level electrons. Probing on these deep-lying electrons in a time-resolved experiment can give more direct insight into the electronic states involved in the relaxation [38–41]. Especially, the population of different excited states can give rise to new, distinct resonant excitation channels [42–44]. With the advance of free-electron lasers (FELs) and high-order harmonic generation (HHG) over the past two decades, ultrashort x-ray pulses can now be used in time-resolved studies and open the opportunity to access electronic state information more directly than the spectroscopy is able to achieve.

During this doctoral thesis, we tested the concepts of time-resolved x-ray photoelectron (TR-XPS) and Auger-Meitner spectroscopy (TR-AMS) on the molecule 2-thiouracil [39, 40]. The extensive studies mentioned above provided a benchmark on the timescales of transient features expected in the experiments. However, the uncertainty of the existence of a doorway state to the triplet manifold as well as the effect of predicted geometry changes of the molecules during the relaxation provided an opportunity to give a benchmark on x-ray spectroscopy possible at FELs. The experiments were conducted at the FLASH free-electron laser in Hamburg using the URSA-PQ apparatus [45]. By combining the results with quantum chemical calculations, we were able to give more insight into the relaxation of 2-thiouracil upon UV excitation. With TR-XPS on the sulfur 2p edge, we developed the concept of the excited-state chemical shift (ESCS) that connects the binding energy of core-level electrons with the dynamical valence charge flow during the relaxation [39]. Further, TR-AMS provides insight on the geometrical changes within the first stages of the relaxation process as we could show based on a Coulomb model that the C=S bond elongation affects the non-resonant Auger-Meitner channels [40].

This thesis will include the following: Chapter 2 lists my (co-) authored manuscripts that have been published or accepted during my doctoral studies. Six of these manuscripts contribute to this publication-based thesis and are, thus, accompanied by a statement on my contributions to these papers. Chapter 3 gives a brief overview of concepts of molecular dynamics. In particular, the excited states and possible relaxation pathways of the molecule 2-tUra are discussed in section 3.4. The static x-ray spectroscopy of the molecule is discussed in sec. 3.5. Chapter 4 covers methodological aspects of the experiments performed during the doctoral work. Section 4.1 discusses experimental details on the UV absorption spectroscopy performed on thiouracils. Sec. 4.2 describes the concept of time-of-flight measurement and magnetic bottle spectrometers. A brief overview on the working principle of an FEL is given in section 4.3 together with a short description of the FLASH2 FEL in Hamburg. Finally, section 4.4 describes the time-resolved experiment performed at FLASH. In Chapter 5, one can find the articles that contribute to this thesis. These are a comprehensive experimental and theoretical study

on the UV absorption of thionated uracils in the gas-phase (Article 1), a technical paper on the instrument used at FLASH (Article 2), a paper on the static NEXAFS spectroscopy of 2-tUra at the sulfur L edge (Article 3), a technical study on the analysis of FEL data on TR-XPS (article 4) and based on this analysis a scientific discussion of TR-XPS of 2-tUra at the sulfur 2p edge (Article 5). Finally, Article 6 includes the TR-AMS of 2-tUra we performed at FLASH. Chapter 6 gives a short summary and conclusion on the work performed during the thesis.

2 | List of Publications and Contributions

During my doctoral works in the group of Experimental Quantum Physics headed by Prof. Dr. Markus Gühr at the Institute of Physics and Astronomy in Potsdam I (co-)authored 11 published articles. Six of these articles are included in this thesis as the main core of my studies. The other five articles are collaborative works, which are less strongly tied with my thesis. They will, however, be listed at the end for completeness.

1. **Experimental and theoretical gas-phase absorption spectra of thionated uracils**

Dennis Mayer, David Picconi, Matthew S. Robinson, Markus Gühr; *Chem. Phys.* **558**, 111500 (2022)

Contribution: I set up the experiment and performed the measurements and data analysis. Also, I contributed to writing the manuscript.

2. **URSA-PQ: A Mobile and Flexible Pump-Probe Instrument for Gas Phase Samples at the FLASH Free Electron Laser**

Jan Metje, Fabiano Lever, **Dennis Mayer**, Richard J. Squibb, Matthew S. Robinson, Mario Niebuhr, Raimund Feifel, Stefan Düsterer, Markus Gühr; *Appl. Sci.* **10** (21), 7882 (2020)

Contribution: I supported J. Metje in building the apparatus and setting up the experiment at FLASH. Further, I participated in the beamtime and did parts of the data analysis used for the paper. I commented on the manuscript.

3. **Core-Level Spectroscopy of 2-Thiouracil at the Sulfur L₁- and L_{2,3}-Edges Utilizing a SASE Free-Electron Laser**

Fabiano Lever, **Dennis Mayer**, Jan Metje, Skirmantas Alisauskas, Francesca Calegari, Stefan Düsterer, Raimund Feifel, Mario Niebuhr, Bastian Manschwetus, Marion Kuhlmann, Tomaso Mazza, Matthew S. Robinson, Richard J. Squibb, Andrea Trabattoni, Mans Wallner, Thomas J.A. Wolf, Markus Gühr; *Molecules* **26** (21), 6469 (2021)

Contribution: I prepared the instrument, participated in the beamtime and commented on the manuscript.

4. **Data analysis procedures for time-resolved photoelectron spectroscopy at a SASE free electron laser**

Dennis Mayer, Fabiano Lever, Markus Gühr; *J. Phys. B: At. Mol. Opt. Phys.* **55**, 054002 (2022)

Contribution: I implemented the self-referencing approach into the analysis of the FLASH data and performed the analysis of the spectra. I wrote the manuscript.

5. **Following UV-induced electronic dynamics of thiouracil by ultrafast x-ray photoelectron spectroscopy**

Dennis Mayer, Fabiano Lever, David Picconi, Jan Metje, Skirmantas Alisauskas, Francesca Calegari, Stefan Düsterer, Christopher Ehlert, Raimund Feifel, Mario Niebuhr, Bastian Manschwetus, Marion Kuhlmann, Tomaso Mazza, Matthew S. Robinson, Richard J. Squibb, Andrea Trabattoni, Mans Wallner, Peter Saalfrank, Thomas J.A. Wolf, Markus Gühr; *Nat. Commun.* **13**, 198 (2022)

Contribution: I prepared the instrument, participated in the beamtime at FLASH and worked on the data analysis and interpretation together with F. Lever. I contributed to writing the paper.

6. **Ultrafast dynamics of 2-thiouracil investigated by time-resolved Auger spectroscopy**

Fabiano Lever, **Dennis Mayer**, David Picconi, Jan Metje, Skirmantas Alisauskas, Francesca Calegari, Stefan Düsterer, Christopher Ehlert, Raimund Feifel, Mario Niebuhr, Bastian Manschwetus, Marion Kuhlmann, Tomaso Mazza, Matthew S. Robinson, Richard J. Squibb, Andrea Trabattoni, Mans Wallner, Peter Saalfrank, Thomas J.A. Wolf, Markus Gühr; *J. Phys. B: At. Mol. Opt. Phys.* **54**, 014002 (2020)

Contribution: I prepared the instrument, participated in the beamtime at FLASH and worked on the data analysis together with F. Lever. I commented on the paper.

For completeness, the following (co-)authored articles were also published during my doctoral studies but are less strongly related to this work:

- **Dennis Mayer**, Christian Matthaei, Axel Heuer, Markus Gühr, *Kagome-fiber prism compressor combination for Yb:KGW laser pulse compression to sub-40fs*, *J. Opt.* **21**, 025503 (2019)
- Marius Gerlach, Felipe Fantuzzi, Lilith Wohlfahrt, Karina Kopp, Bernd Engels, John Bozek, Christophe Nicolas, **Dennis Mayer**, Markus Gühr, Fabian Holzmeier, Ingo Fischer, *Fragmentation of isocyanic acid, HNCO, following core excitation and ionization*, *J. Chem. Phys.* **154**, 114302 (2021)
- Matthew S. Robinson, Mario Niebuhr, Fabiano Lever, **Dennis Mayer**, Jan Metje, Markus Gühr, *Ultrafast Photo-ion Probing of the Ring-Opening Process in Trans-Stilbene Oxide*, *Chem. Eur. J.* **27**, 11418-11427 (2021)
- Wen Li, Oksana Kavatsyuk, Wessel Douma, Xin Wang, Ronnie Hoekstra, **Dennis Mayer**, Matthew S. Robinson, Markus Gühr, Mathieu Lalande, Marwa Abdelmouleh, Michal Ryszka, Jean Christophe Pouilly, Thomas Schlathölter, *Multiple valence*

electron detachment following Auger decay of inner-shell vacancies in gas-phase DNA, Chem. Sci. **12**, 13177 (2021)

- Marius Gerlach, Tobias Preitschopf, Emil Karaev, Heidy Quitian-Lara, **Dennis Mayer**, John Bozek, Ingo Fischer, Reinhold Fink, *Auger electron spectroscopy of fulminic acid, HCNO: An experimental and theoretical study, Phys. Chem. Chem. Phys.* **24**, 15217-15229 (2022)

3 | Molecular Dynamics

3.1 Adiabatic and Born-Oppenheimer-Approximation

The static Schrödinger equation (SE) describes the energy of a quantum system [46–50]. The energy usually divides into kinetic energy T and potential energy V for each quantum particle in the system. For atoms and molecules, the terms are often separated between electron and nucleus-only terms as well as interaction terms. The SE for those systems reads:

$$[\hat{T}_e + \hat{T}_n + V(\mathbf{r}, \mathbf{R})] \Psi(\mathbf{r}, \mathbf{R}) = E\Psi(\mathbf{r}, \mathbf{R}), \quad (3.1)$$

where \hat{T}_e describes the kinetic terms for electrons, \hat{T}_n for the nuclei and V the interaction potential energy terms between electrons and electrons, nuclei and nuclei and electrons and nuclei due to their electrostatic fields. The coordinate \mathbf{r} describes the electron position and \mathbf{R} the nuclear coordinate. Both are multidimensional variables *i.e.*, three space dimensions times the number of nuclei N or electrons n . The term $V(\mathbf{r}, \mathbf{R})$ can be written as (using atomic units *i.e.*, $e = m_e = \hbar = 1$):

$$V(\mathbf{r}, \mathbf{R}) = V_{ee}(\mathbf{r}) + V_{nn}(\mathbf{R}) + V_{en}(\mathbf{r}, \mathbf{R}) \quad (3.2)$$

$$= \sum_{i \neq j}^n \frac{1}{|r_j - r_i|} + \sum_{k \neq l}^N \frac{Z_k Z_l}{|R_l - R_k|} - \sum_{i=1}^n \sum_{k=1}^N \frac{Z_k}{|r_i - R_k|}. \quad (3.3)$$

The more particles are involved, the more complicated the calculation will become. In general, the equation is only analytically solvable for the H_2 molecule. So, assumptions must be made in order to simplify quantum calculations for atomic and especially molecular systems. From classical perspectives, the mass of electrons and nuclei seems to be a good starting point for that. The mass ratio between a proton and an electron is $m_p/m_e \approx 2000$. Electrons are significantly lighter than protons or even a nucleus consisting of several protons and neutrons. As Coulomb force is the only force that accelerates the particles here, it is obvious that electrons experience a stronger change in their velocity than the nuclei as the acceleration is $a = F/m$. This means that electrons will react much faster to any force applied to them and especially will immediately react to any change in the nuclear geometry. The nuclei, however, will only slowly adapt to changes in the electronic system. Thus, we can assume that the kinetic terms for the electrons are significantly stronger than the nuclear terms and the latter can be treated

as a perturbation for the electronic system. We call this adiabatic approximation. The approximation suggests writing the Hamiltonian as

$$\hat{H} = \hat{H}_0 + \hat{H}' \text{ with } \hat{H}_0 = \hat{T}_e + V(\mathbf{r}, \mathbf{R}) \text{ and } \hat{H}' = \hat{T}_n, \quad (3.4)$$

where \hat{H}' is a perturbation to the unperturbed (electronic) SE

$$\hat{H}_0 \Psi^{el}(\mathbf{r}; \mathbf{R}) = E^0(\mathbf{R}) \Psi^{el}(\mathbf{r}; \mathbf{R}). \quad (3.5)$$

Here, the molecule is restricted to a predefined nuclear geometry. The nuclear coordinate \mathbf{R} is considered as a parameter in the unperturbed case. The solutions $\Psi_k^{el}(\mathbf{r}; \mathbf{R})$ can be written as an orthonormal system and any solution to the general equation (including the perturbation) can be approximated by a series of so-called wavefunctions:

$$\Psi(r, R) = \sum_k \phi_k(\mathbf{R}) \cdot \Psi_k^{el}(\mathbf{r}; \mathbf{R}). \quad (3.6)$$

The nuclear wave function $\phi_k(\mathbf{R})$ appears here as an expansion coefficient. With some mathematical treatment the SE can be rewritten as a set of two coupled equations [51, pp. 18-20]

$$\hat{H}_0 \Psi^{el}(\mathbf{r}; \mathbf{R}) = E^0(\mathbf{R}) \Psi^{el}(\mathbf{r}; \mathbf{R}), \quad (3.7)$$

$$\hat{H}' \phi_k(\mathbf{R}) + \sum_m (a_{km} \phi_m(\mathbf{R})) = (E - E_k^0(\mathbf{R})) \phi_k(\mathbf{R}). \quad (3.8)$$

Equation 3.7 is again the unperturbed electronic SE for a given molecular geometry \mathbf{R} . Equation 3.8 describes the nuclear wavefunction $\phi_m(\mathbf{R})$ and is coupled to the electronic system *via* the coefficient a_{km} which depends on the electronic wavefunction. More precisely, it includes derivatives of the electronic wavefunction with respect to the internuclear coordinates $\nabla_R \Psi(\mathbf{r}; \mathbf{R})$ and $\nabla_R^2 \Psi(\mathbf{r}; \mathbf{R})$. If we assume the molecule to be in its equilibrium position R_0 , the electronic wavefunction may not vary much in the vicinity of the equilibrium and the contributions of its derivatives to the coefficients are very small. In addition, the a_{km} scale with $1/M$ where M is the mass of the nuclei. Both arguments justify to set the coefficients a_{km} to zero. This is called the Born-Oppenheimer approximation (BOA) and results into two decoupled equations:

$$\hat{H}_0 \Psi^{el}(\mathbf{r}; \mathbf{R}) = E^0(\mathbf{R}) \Psi^{el}(\mathbf{r}; \mathbf{R}), \quad (3.9)$$

$$(\hat{T}_n + E_k^0(\mathbf{R})) \phi_k(\mathbf{R}) = E_{k,i} \phi_{k,i}(\mathbf{R}). \quad (3.10)$$

Here, the electronic system is solved for a given molecular configuration \mathbf{R} and thus for a static/non changing potential. The equation for the nuclear motion still inherits the solution of the electron system as a static potential.

3.2 Potential Energy Surfaces and Wavepackets

In the BOA, the motion of electrons and nuclei are separated. In the case of the electrons, the molecular geometry is a given parameter for which the Schrödinger equation has to be solved. This, however, means that there is a set of eigenstates with eigenvalue E_n and eigenvectors ϕ_n for each multidimensional coordinate R that describes the electronic behaviour for this geometry. The function $E_n(R)$ forms a multidimensional energy landscape which is called the potential energy surface (PES). This electronic potential affects the nuclear wavefunction and gives rise to energy contribution that are due to changes in the geometry. The full energy of a molecular quantum state, $E_{n,v,J}$, is defined by the electronic $E_n^{el}(R)$, vibronic $E_v(R)$ and rotational energy $E_J(R)$:

$$E_{n,v,J} = E_n^{el}(R) + E_v(R) + E_J(R) . \quad (3.11)$$

The contributions to the overall energy are different. Whilst for electronic states the energy goes from tens of eV in valence states to hundreds or thousands of eV in core-level states, vibronic states usually contribute energies in the range of meV and rotational states only in the μeV range. When studying electronic states, the rotational component, thus, has a negligible contribution and we may ignore it here.

In the case of a diatomic molecule, the multidimensional potential energy landscape reduces to a curve as a function of one coordinate only, which is the distance between the two atoms. A typical potential for those molecules can be seen in 3.1. The distance where the potential shows a minimum is called equilibrium distance R_0 (e.g., X_0 and X_1 in 3.1). Each bound state has its equilibrium distance. The depth of the potential defines the dissociation energy E_d . A state with a potential that does not show a minimum in energy but instead continues to decrease in energy towards $R \rightarrow \infty$ is called a dissociative state as it pushes apart the interacting atoms. Vibronic states are determined by the electronic potential and describe stretching modes of different frequencies for this diatomic molecule. In case of a harmonic potential, the vibronic states would be equally spaced in energy. If the potential is anharmonic, the energies are slightly corrected. The equal spacing is lost and with increasing quantum number the distance between the states reduces.

The more atoms involved in forming a molecule, the more difficult it becomes to draw reasonable representations of the potential energy landscape. In the case of a triatomic molecule, the number of coordinates necessary to describe the geometry (degrees of freedom) is three (or four in case of a linear molecule) which is still easy to cope with. In general, the degrees of freedom are $3N - 6$ (or $3N - 5$ for linear molecules). Thus, the larger the number of atoms N gets, the more often one uses generalised coordinates or focuses on the variation of only a few parameters such as a particular bond distance.

Potential energy surfaces determine the molecular dynamics in the excited state. Excitation of molecules happens, for example, by the absorption of a photon. However, the absorption of a photon of a certain frequency may not lead to the excitation of a single state but usually to a manifold of vibronic excited states. The Franck-Condon principle

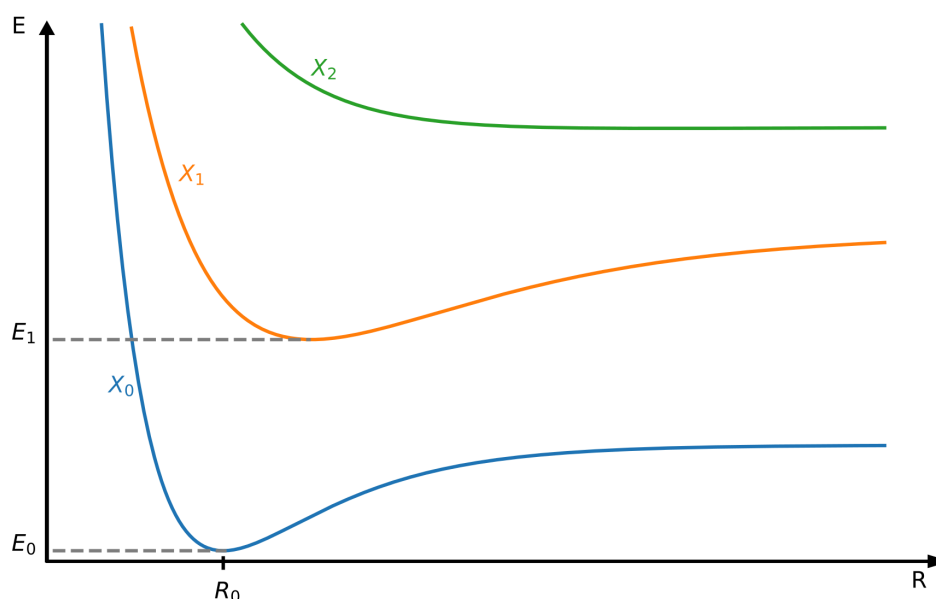


Figure 3.1: Scheme of potential curves for a diatomic molecule. Bound states show a minimum for a certain geometry (X_0 , X_1) whilst dissociative states don't (X_2).

states that during an excitation the molecular geometry does not change [52–54], which is classical momentum conservation and only those vibrational states are populated that have a significant overlap with the ground state wavefunction. That leads in general to the preparation of a so-called vibrational wavepacket *i.e.*, a coherent superposition of different vibronic states within an electronic state. These wavepackets evolve on a PES *i.e.*, it will follow the gradient along the molecular coordinates. This, in consequence, means that during the evolution the molecule undergoes geometrical changes. These can be changes in bond distance, twists or even the breaking of bonds.

While structural changes can occur during the evolution on the PES of a single electronic state, it becomes complex when the PES of two different states get very close. Above we discussed the Born-Oppenheimer approximation which arises from the combination of how the coupling coefficients scale with, first, the inverse nuclear mass and, second, the gradients $\nabla_R \Psi(\mathbf{r}, \mathbf{R})$ which vanish in the vicinity of the equilibrium. After an excitation, however, the molecule is forced to leave the equilibrium geometry and follows the gradient. Expressing the matrix element $\langle \Psi_j | \nabla_R | \Psi_i \rangle$ for two different electronic states with energies E_i and E_j yields $1/(M \cdot (E_i - E_j))$ where M is again the mass of the nuclei. Therefore, if two potential energy surfaces come very close in energy, the influence of the nuclear gradient on the electron wavefunction cannot be neglected anymore and the BOA breaks down. The vicinity of the region where $E_j = E_i$ *i.e.*, where the potential energy surfaces intersect, are of particular interest as these allow a vibronic wavepacket to change the electronic state without emitting a photon. Moreover, they allow the molecule to

convert electronic energy into vibrational energy which is important for photoprotection as molecules in excited states are in danger two forming new bonds. These regions of intersecting PES are called conical intersections (CoIns). It is now commonly accepted that CoIns play a crucial role in the relaxation dynamics of molecules [55].

In order for a CoIn to exist, the approaching PES E_i and E_j have to satisfy two conditions [56]:

$$H_{ii}(\mathbf{r}; \mathbf{R}) = H_{jj}(\mathbf{r}; \mathbf{R}), \quad (3.12)$$

$$H_{ij}(\mathbf{r}; \mathbf{R}) = 0. \quad (3.13)$$

Here, $H_{ij}(\mathbf{r}; \mathbf{R})$ is defined by

$$H_{ij}(\mathbf{r}; \mathbf{R}) = \langle \Psi_i(\mathbf{r}; \mathbf{R}) | \hat{H}_e(\mathbf{r}; \mathbf{R}) | \Psi_j(\mathbf{r}; \mathbf{R}) \rangle, \quad (3.14)$$

where $\Psi_{i/j}$ are the wavefunctions of the approaching PES. The reason is that both surfaces are solutions to the same eigenvalue problem and hence depend on each other. A single condition that forces only the equality of energies *i.e.*, eq. 3.12, is not sufficient in general. The subspace where the conditions are satisfied is called the intersection coordinate space (ICS) or seam space. The two conditions force it to be of dimension $s - 2$, where s are the degrees of freedom of that molecule [55, 56]. The remaining branching space is given by two vectors p_1 and p_2 (also often called g and h). They are determined by the electronic structure of the PES and describe the energy difference gradient (p_1) and the nonadiabatic coupling (p_2) [55]:

$$p_1 = \frac{1}{2} \left(\langle \Psi_i(\mathbf{r}; \mathbf{R}) | \nabla \hat{H}_e(\mathbf{r}; \mathbf{R}) | \Psi_i(\mathbf{r}; \mathbf{R}) \rangle - \langle \Psi_j(\mathbf{r}; \mathbf{R}) | \nabla \hat{H}_e(\mathbf{r}; \mathbf{R}) | \Psi_j(\mathbf{r}; \mathbf{R}) \rangle \right) \quad (3.15)$$

$$p_2 = \langle \Psi_i(\mathbf{r}; \mathbf{R}) | \nabla \hat{H}_e(\mathbf{r}; \mathbf{R}) | \Psi_j(\mathbf{r}; \mathbf{R}) \rangle \quad (3.16)$$

The other orthogonal coordinates p_3, \dots, p_s that define the ICS are equal to 0 in the branching space (and vice versa, $p_1 = p_2 = 0$ in the ICS). Along the two coordinates, the degeneracy of the two PES is lifted [56]:

$$E_{1,2} = \langle \hat{H}_e(p_1, p_2) \rangle \pm \sqrt{p_1^2 + p_2^2} \quad (3.17)$$

The lifted PES form a cone shape surface; hence the name "conical intersection". There are slightly different shapes of intersections. For all of them, however, the PES form a continuous slope from one to the other state [56]. In consequence, this means that a wavepacket that is propagating on the gradient of the PES and passing the CoIn changes its electronic character abruptly.

Conical intersections do not appear in all molecules. In diatomic molecules, there is only one degree of freedom *i.e.*, the bond distance R . It is obvious that one parameter cannot satisfy the two conditions at the same time. There must be at least two independent parameters. Thus, two approaching PES in a diatomic molecule will avoid the crossing

and repel each other. This “non-crossing rule” was brought up by F. Hund and was later proven by E. Wigner and J. von Neumann [57, 58]. More strictly, it states that potential energy curves cannot cross if they correspond to electronic states of the same symmetry. This rule, however, is limited to diatomic molecules [59, 60].

3.3 Binding Energies and Molecular Orbitals

So far, nothing has been said on how wavefunctions and energies can be derived from the (stationary) Schrödinger equation. There are different theoretical approaches on how to evaluate the electronic SE for molecular systems. The Hartree-Fock (HF) Self-consistent field (SCF) method gives in many cases reasonable estimations for binding energies and the wavefunctions. Within HF-SCF framework different assumptions are made. Further, relativistic effects and spin-orbit coupling are neglected. Neglecting correlation effects, however, forces the estimated energy of the molecular system to be an upper bound which can be optimised towards the “real” value by introducing correlation coefficients during the calculation [61, pp. 15-19].

The starting point of HF is to assume that the energy eigenvalues can be described using a Slater determinant *i.e.*, the electronic wavefunction is approximated by N orthonormal one-electron spin-orbitals in the following way:

$$\Psi_e \approx \frac{1}{\sqrt{N!}} \begin{vmatrix} \psi_1(x_1) & \dots & \psi_N(x_1) \\ \vdots & \ddots & \vdots \\ \psi_1(x_N) & \dots & \psi_N(x_N) \end{vmatrix} \quad (3.18)$$

where $\psi(x) = \phi(x) \cdot s$ with ϕ a spatial wavefunction and $s = \uparrow, \downarrow$ the spin. The Slater determinant, in the way it is constructed, automatically satisfies the Pauli exclusion principle (*i.e.*, the total wavefunction is antisymmetric).

The energy of the system is defined by

$$\langle E_0 \rangle = \langle \Psi_e | \hat{H} | \Psi_e \rangle \quad (3.19)$$

with \hat{H} being the Hamilton operator of the molecular system *i.e.*, it includes interaction terms between electron-electron, electron-nucleus and (sometimes) nucleus-nucleus (see eq. 3.3). To evaluate this equation, the quantum-mechanical variational principle is applied which assumes a small variation $\delta\Psi$ to the electronic wavefunction. Utilising the method of Lagrangian multipliers, the calculation yields a set of N so-called Hartree-Fock equations [61, pp. 15-19]

$$\hat{F}_i \psi_i(x_i) = \sum_{k=1}^N \lambda_{ik} \psi_k(x_1) . \quad (3.20)$$

Here, $\hat{F}_i = \hat{H}_{ii} + \sum_{k=1}^N (\hat{J}_k - \hat{K}_k)$ is called the Fock operator with \hat{H}_{ii} the one-electron

Hamiltonian. The Coulomb operator

$$\hat{J}_k |\psi_i(i)\rangle = \langle \psi_k(k) | r_{ik}^{-1} | \psi_k(k) \rangle |\psi_i(i)\rangle \quad (3.21)$$

accounts for the repulsive electron-electron interaction. The exchange operator

$$\hat{K}_k |\psi_i(i)\rangle = \langle \psi_k(k) | r_{ik}^{-1} | \psi_i(k) \rangle |\psi_k(k)\rangle \quad (3.22)$$

is responsible for the spin correlation according to Pauli's principle.

In the canonical form, the right-hand side of the above equation is brought into a diagonal form via a unitary transformation under which the Fock operator and the total wavefunction are invariant. Then, the energy eigenvalues (called canonical energies or orbital energies) are defined by three integrals [61]:

$$E_i = H_{ii} + \sum_{k=1}^N (J_{ik} - K_{ik}) \quad (3.23)$$

with

$$H_{ii} = \langle \psi_i(i) | \hat{H}_{ii} | \psi_i(i) \rangle, \quad (3.24)$$

$$J_{ik} = \langle \psi_i(i) | \langle \psi_k(k) | r_{ik}^{-1} | \psi_k(k) \rangle | \psi_i(i) \rangle \quad (3.25)$$

and

$$K_{ik} = \langle \psi_k(k) | \langle \psi_k(k) | r_{ik}^{-1} | \psi_i(k) \rangle | \psi_k(k) \rangle. \quad (3.26)$$

Similar to the names of the operators above, J_{ik} is called the *Coulomb integral* and K_{ik} the *exchange integral*. Since both correlate different spin-orbitals, they are usually harder to evaluate than H_{ii} . The variation principle requires to go through several iterations of calculating the integrals and wavefunctions (called canonical (molecular) orbitals), starting with an initial guess. The calculation comes to an end when the difference of the total energy of the system $\langle E_0 \rangle$ between two iterations is below an initially defined threshold.

The integrals in the HF calculation already require an initial guess for the wavefunction. For this guess, one usually assumes a reasonably large basis set of atomic orbitals which form by linear combination the initial molecular orbitals. Throughout the iterations, the atomic orbitals remain fixed but the expansion coefficients, with which they are combined, are adjusted. This gives self-consistency. The usage of atomic orbitals is justified by two reasons. First, if the molecule breaks apart the molecular orbitals must converge smoothly towards atomic orbitals. Second, the form of molecular orbitals that are near a particular atom must look similar to atomic orbitals of that atom.

At the beginning of the section, it was mentioned that correlation effects are ignored in the HF approach. Strictly speaking, this is not correct. The HF approach neglects dynamical correlations. On a very crude level, electron correlations are included *via* the mean field approach. The HF method uses averages in the calculation so that each

solution to the above stated integrals behaves as if an electron would be exposed to the mean field of all other particles but does not change the field itself. This, indeed, introduces some electron correlations by means of the exchange integral but ignores all dynamical effects.

In the framework of HF theory, the derived orbital energies E_i are equivalent to the binding energy (or ionisation potential) of the electronic state. This is called Koopmans' theorem. This allows one to directly compare photoelectron data with orbital energies. The assumption made here is that the removal of an electron from an orbital does not affect the other orbitals. This is strictly correct within the HF, or in other words, dynamical correlation is neglected as described above. In case of valence orbitals, this gives a rather accurate estimation. However, it is inadequate for strongly bound orbitals such as the K-shell (1s) and can lead to larger deviations from the experimentally found results up to tens of eV. Post-HF methods have HF as its fundamental theory but overcome some of its shortcomings. Thus, they are more accurate but also more computationally expensive. Further, these methods can be adapted to excited state calculations. Two examples are coupled cluster [62] and configuration interaction [63]. However, HF-SCF already gives important physical insight in the experiment in most of the cases.

Apart from the binding energies, the shape of molecular orbitals (MOs) can also be insightful. Depending on the electron density, geometry changes in (excited) electronic states can be anticipated. When looking at molecular orbitals, one often differentiates three different "classes" of MOs. Bonding orbitals show a significant electron density between atoms. The presence of an electron between two nuclei reduces the Coulomb repulsion between the nuclei. Hence, it lowers the system energy and the nuclei can move closer together. In anti-bonding orbitals, electrons are less likely between the two nuclei. The wavefunction often shows a node there. This, however, reduces the screening of the Coulomb repulsion and thus the nuclei would move further apart to reduce the force and energy. In other words, occupying an anti-bonding orbital increases the energy of the system. A last "category" of molecular orbitals are lone pairs *i.e.*, valence electrons that are not shared between atoms inside the molecule. These orbitals have a strong atomic character.

Let's finish this chapter with a short example, based on the molecule of interest of this thesis, 2-thiouracil (2-tUra). A HF-SCF calculation has been performed with the ORCA program [64–66] to evaluate binding energies and orbitals. The basis set def2-SVP [67] was used for an initial guess of the orbitals.

Table 3.2 summarises some orbital energies of the highest-occupied molecular orbitals (HOMO) and the strongly localised S 2p and S 2s orbitals. According to the HF calculation the first ionisation energy found in the molecule is at about 9 eV. Experiments performed at SOLEIL suggest a value of about 8.7 eV. That is a fairly good agreement. The expected HOMO-1 which lies at 9.34 eV is not observed in the experiment. However, the calculation does not consider aspects such as vibrational broadening. This will lead to strongly overlapping features and experimentally only one broad band might be observed. Calculations performed by Ruckebauer *et al.* back that the first observable band constitutes of two

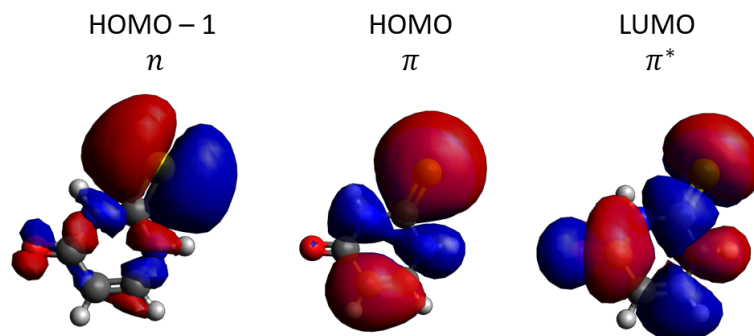
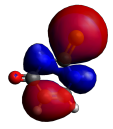
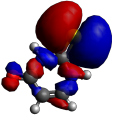
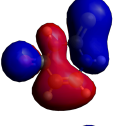
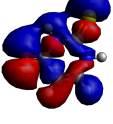


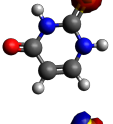
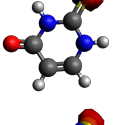
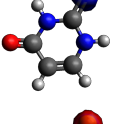
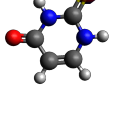


Figure 3.2: Isosurface plots for the highest occupied molecular orbital(s) (HOMO) and lowest unoccupied molecular orbital (LUMO) in 2-thiouracil. The orbitals were calculated using HF-SCF method and the ORCA program.

ionisation channels [68]. The following valence ionisation channels are much better separated. For the HOMO-2 an energy of 10.8 eV is expected. The experiment, however, shows the second band already at about 9.9 eV. Interestingly, Ruckebauer *et al.* predict that two orbitals contribute to the second observable band which is not found with the HF calculation. The following three orbital energies deviate from the experiment less than 1 eV. For core-level orbitals such as S 2s and S 2p the deviation is much stronger. The S 2p orbital energy is predicted to be at about 179 eV for all three orbitals $p_{x,y,z}$. In the experiment, however, only two peaks are found well separated at 168.3 eV and 169.5 eV. This is due to the spin-orbit coupling which is not accounted for in the HF calculations. In case of the S 2s energy, the prediction is again 10 eV higher than the experiment. Considering the relative error HF-SCF seems to give offsets in the range of 5-10 %.

In Figure 3.2 the HF results for the wavefunctions of the HOMO, HOMO-1 and the lowest-unoccupied molecular orbital (LUMO) are shown for the same isosurface value. The colours blue and red encode the sign of the wavefunction (negative/positive). The HOMO-1 has a strong electron localisation at the sulfur and has mostly $3p_x$ character (from the sulfur). As the orbital is dominated by the in-plane atomic p-orbital, it is of non-bonding character. Hence, it is called n_S (the index “S” indicates the strong domination of the sulfur 3p orbital). The HOMO and LUMO mostly combine out-of-plane p orbitals. Thus, they are called $\pi^{(*)}$ orbitals. The asterisk for the LUMO indicates that it is an anti-bonding orbital. Similar to the HOMO-1, the wavefunction in the HOMO shows a significant value around the sulfur. However, HOMO and LUMO are much stronger delocalised than the HOMO-1. Interesting details may be observed when looking closer at the C=S bond. In case of the HOMO, the orbital covers the space between the two atoms. In the LUMO, in contrast, the orbital shows a node. Based on the above stated argument on reduction of Coulomb repulsion, it is to be expected that the bond will stretch when an electron is promoted from the HOMO to the LUMO. More sophisticated theoretical approaches indeed predict a bond stretch [26, 27] and time-resolved Auger spectroscopy may back this prediction for the C=S bond [40] (see Article 6 in chapter 5).

Table 3.1: Comparison of Hartree-Fock calculations on 2-thiouracil with (unpublished) experimental ionisation energies measured at the synchrotron SOLEIL. In addition, the HF orbitals are shown for a fixed isovalue.

State	HF-SCF (eV)	Exp. (eV)	HF orbitals
HOMO	-9.04	8.7	
HOMO-1	-9.34	-	
HOMO-2	-10.83	9.93	
HOMO-3	-12.52	11.8	
HOMO-4	-13.53	13.2	
HOMO-5	-14.65	14.3	
	-179.33	168.35	
S 2p	-179.35	169.53	
	-179.45		
S 2s	-242.34	232.6	

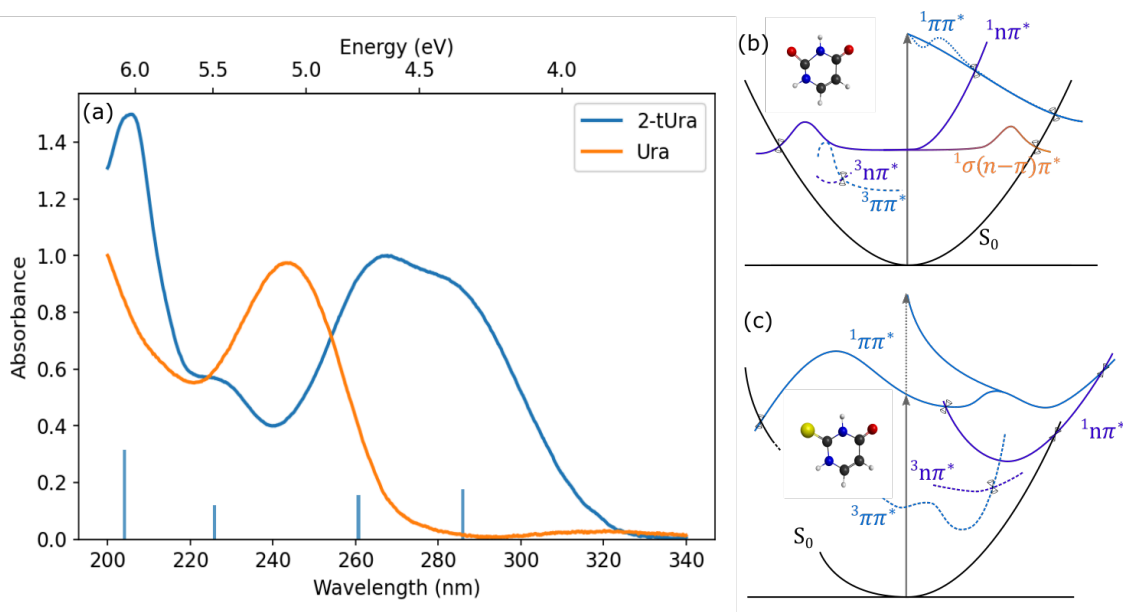


Figure 3.3: (a) Gas-phase UV absorption spectra of uracil (Ura) and 2-tUra. The sticks mark the excitation energies for 2-tUra as derived by a Gaussian decomposition (see Supplementary Information of [69]). (b) and (c) are schemes of the potential energy surfaces of Ura and 2-tUra, respectively, based on different calculations that are summarised in Refs. [70] and [10]. The dotted blue line in the scheme for uracil shows the local minimum in the S_2 state found in some theoretical studies. The dashed arrow in the right scheme indicates an excitation into the S_4 state.

3.4 Molecular Dynamics of 2-Thiouracil

In the final paragraph of the previous section, a prediction has been made on a C=S bond length alternation occurring in the excited state of 2-tUra. To study those effects more thoroughly, more accurate calculations than HF need to be performed in order to understand which states are involved in the transition and relaxation and how the geometry of the molecule changes.

In Ref. [69] (see Article 1 in chapter 5), we have measured the gas-phase UV absorption spectra of all three thionated uracils. The absorption spectrum of 2-tUra is shown in Figure 3.3 (a) together with that of uracil. In case of 2-tUra, we observe a strong first absorption in the range 250 - 300 nm which corresponds to an excitation energy of 4.2 - 5 eV. This is backed by other experiments performed in gas-phase that show similar absorption bands [71, 72]. A Gaussian-fit analysis of the spectrum reveals that the broad feature can be described by two excitations at 287 nm (4.7 eV) and 261 nm (4.3 eV). Quantum chemical calculations show that the occupied excited states that belong to the two lowest excitations are of $^1\pi\pi^*$ character [26, 27, 69]. This means that the π and π^* states are occupied by one electron each. As we consider a direct transition, this means also that an electron was promoted from the π to the π^* orbital. In comparison with the canonical nucleobase uracil, this first absorption band (which is also of $\pi\pi^*$ character) is

shifted towards lower excitation energies (higher wavelength). This trend is observed in all three thiouracil to a different extent [69] and, in general, in all thionated nucleobases compared to their canonical counterparts [10].

These $^1\pi\pi^*$ states are, however, not the lowest excited states inside the molecule. Theoretical calculations show that there are a variety of excited states with lower binding energy which cannot be excited due to the violation of transition rules and are, thus, “optically dark”. Below the lowest $^1\pi\pi^*$ states calculations suggest an $^1n\pi^*$ state at about 3.8 eV that involves the lone-pair orbital n which has a very strong sulfur 3p character. A number of triplet states are proposed at even lower energies [26, 27] but these require a change of the spin of the excited electron and are, thus, not allowed in optical excitation.

In Figure 3.3 (b), a sketch of the potential energy landscapes of uracil (Ura) and 2-tUra are shown. The sketches are summaries of various calculations that have been performed on these molecules, with refs. [10] and [70] providing a suitable overview. In short, the $^1\pi\pi^*$ that can be excited in Ura (called S_2) shows conical intersections with a singlet $^1n\pi^*$ state (S_1) and the ground state (S_0). The $^1n\pi^*$ state shows also CoIns with the S_0 , either *via* a barrier or an intermediate state. Triplet states do not cross any of the states. Hence, it can be deduced that an excitation in uracil will lead to an efficient relaxation into the ground state. This is indeed observed in experiments for nucleobases [73].

For 2-tUra, a more complicated relaxation process to the ground state is expected as seen in Figure 3.3 (c). The two excitations observed in the absorption spectra lead to two slightly different initial states, S_2 and S_4 , which, however, are both of $\pi\pi^*$ character. Calculations that include the S_4 state suggest that those two states merge very quickly [26]. Therefore, it may be assumed that an S_4 excitation will undergo the same relaxation as an S_2 relaxation [26]. The S_2 state shows a CoIn with both S_0 and S_1 ($^1\pi\pi^*$). However, the S_0 is only reachable *via* an energy barrier what reduces the likelihood of a ground state relaxation channel. Hence, it will be more feasible for an electronic wavepacket to relax into the S_1 state. There, the ground state is again only accessible *via* an energy barrier. A triplet state of $^3\pi\pi^*$ character, however, is close to the S_1 minimum. Together with the high barrier, it facilitates an inter-system crossing from the singlet $^1n\pi^*$ to the triplet $^3\pi\pi^*$ where the wavepacket may relax into other triplet states. As these states are spin-excited states, a direct radiative transition towards the ground state is very unlikely. If there is no other nonradiative decay channel (as currently predicted by theory), then these triplet states last rather long (*i.e.*, up to a few 100 ps [21–24]). The existence of a long-lasting excited state has been observed not only in 2-thiouracil; it is a well-known behaviour of thionated nucleobases in general [10, 11].

The calculations that led to the discussed potential energy surfaces mostly focus on static approaches *i.e.*, they focus on certain geometries of the molecule and calculate the potential energy point by point for the excited states. They do not address the question how a prepared wavepacket would evolve under the gradients of each PES. Dynamical calculations that consider the evolution of a wavepacket have been performed by Mai *et al.* [27, 28]. They calculated the evolution of a wavepacket with both multi-state complete active space perturbation theory (MS-CASPT2) [27] and algebraic diagrammatic

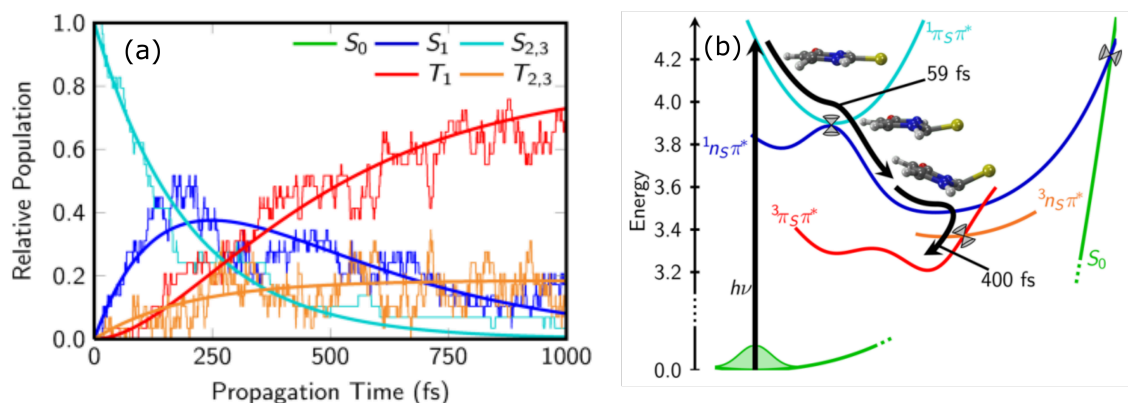


Figure 3.4: (a) Excited-state population from the ADC(2) calculations in Ref. [28]. Reprinted from Mai *et al.*, J. Chem. Phys. 47, 184109 (2017), with the permission of AIP Publishing. (b) Potential energy scheme with a possible relaxation pathway for 2-tUra including some geometry changes from Ref. [27]. Reprinted from Mai *et al.*, J. Phys. Chem. Lett. 7, 1978–1983 (2016) used under the Creative Common Attribution (CC-BY) Licence.

construction (ADC) [28], deriving possible relaxation pathways for the wavepacket. This includes estimates for the time-dependent population of each state, their lifetimes and geometry changes during the relaxation. First, we discuss the relaxation path found in the two calculations and after that briefly look into geometry changes.

The excited state populations of 2-tUra are shown in Figure 3.4 (a). The populations were calculated via a trajectory propagation on the excited states, using ADC(2) for calculating the electronic structure [28]. In these calculations, the S_2 state was initially populated and the evolution of the prepared wavepacket along gradients of the PES was followed. It can be seen that the S_2 population decays exponentially to the S_1 state, leading to a relative population of about 50 % in the S_1 state 200 fs after excitation. Decay to the triplet states, however, is slower. The T_1 state overcomes the S_1 state after about 350 fs and becomes the most populated state with an occupation of up to 70 %. The intermediate T_2 and T_3 states gain only some population up to a value of 20 % and stay relatively stable according to the fits applied in the graph. These findings do not change much when looking at the MS-CASPT2 calculations performed by Mai *et al.* [27]. The first state populated after the excitation seems to be the S_1 followed by a gradual occupation of the triplet states. This pathway is also depicted in PES scheme in Figure 3.4 (b).

There are, however, some differences in the results produced by the two different electronic structure methods; the major of which are the proposed time constants for the relaxation. The MS-CASPT2 approach estimates much faster time constants for the relaxation into the S_1 (60 fs vs. 250 fs) as well as for the triplet states $T_{2/3}$ (250 fs vs. 1060 fs) as compared to the ADC(2) approach. There are also two interesting details. First, the MS-CASPT2 calculations predict a very weak ground-state relaxation channel from the S_1 state with picosecond decay time. However, the long decay time will make the

relaxation into the triplet states the dominant channel. In fact, only one trajectory out of 44 calculations ended up in this ground state relaxation channel making it an even more unlikely event [27]. This channel is also not observed in the ADC(2) calculations.

The second detail concerns the curve shape of the excited state populations in the ADC calculation. A closer look reveals that the S_1 and the $T_{2/3}$ curves show an oscillating behaviour that appears to be in antiphase. To a much lesser extent slight oscillating features can also be observed in the other two curves. These oscillations may suggest that there is an oscillating population exchange between the S_1 ($^1n\pi^*$) and the triplet states of $^3\pi\pi^*$ character. In the MS-CASPT2 calculations, there also seems to be some alternating exchanges of population between states but an oscillating behaviour is not as distinct.

Figure 3.4 (b) shows the most striking predicted geometry change the molecule undergoes during the relaxation. In the ground state S_0 , the molecule is planar. It is predicted in all calculations of Mai *et al.* that the C=S bond will stretch and the sulfur will move out of the molecular plane (pyramidalization) at some point during the relaxation process [26–28]. The static calculation by Mai *et al.* found that there is already a non-planar S_2 state where the sulfur moves out of the molecular plane [26]. The dynamical calculations suggest, however, that the non-planar S_2 minimum is a minority channel [27, 28]. It is further predicted that the molecule will undergo pyramidalization when it enters the S_1 state (unless it did enter the non-planar S_2 minimum) [27, 28]. Alongside the out-of-plane motion, the C=S double bond elongates by up to 15 % [26]. Another change in bond distance is predicted for the C=C double bond that is supposed to narrow by up to 10 % [27, 28].

To conclude this section, a very brief overview shall be given on some ultrafast experiments utilising mostly visible and UV light. Different experimental studies have been performed to test the proposed relaxation pathways. Pollum *et al.* showed with femtosecond transient absorption spectroscopy (fs-TAS) that the S_1 ($^1n\pi^*$) state acts as a doorway for populating the T_1 ($^3\pi\pi^*$) [25]. The major pathway was found to be S_2 ($^1\pi\pi^*$) \rightarrow S_1 ($^1n\pi^*$) \rightarrow T_1 ($^3\pi\pi^*$). This contrasts the predictions of Mai *et al.* who claim that an intermediate T_2 ($^3n\pi^*$) state is populated before relaxing into the T_1 [26, 28]. However, Mai *et al.* note that due to the similar electronic character of the intermediate triplet state(s) (especially T_2) with the S_1 the experimental observation (or differentiation) of these states might be difficult due to a low transient T_2 population. Teles-Ferreira *et al.* argued by investigating 2-tUra also by means of fs-TAS that there is either a direct ISC from the S_2 to the $T_{2/3}$ or an intermediate, “spectroscopically elusive” S_1 state which connects to the triplet manifold [30]. This agrees with the prediction of Mai *et al.* who also found a certain amount of trajectories going directly from the S_2 to $T_{2,3}$. Interestingly, studies on 4-tUra also suggest an optically dark intermediate state (the S_1 ($^1n\pi^*$)) [30, 33, 34]. By studying fs-TAS and photoelectron spectra and systematically varying the excitation energy, Sanchez-Rodriguez *et al.* found that the excitation of out-of-plane vibrational modes which lead, for example, to pyramidalization are necessary to access the ISC relaxation pathways [23].

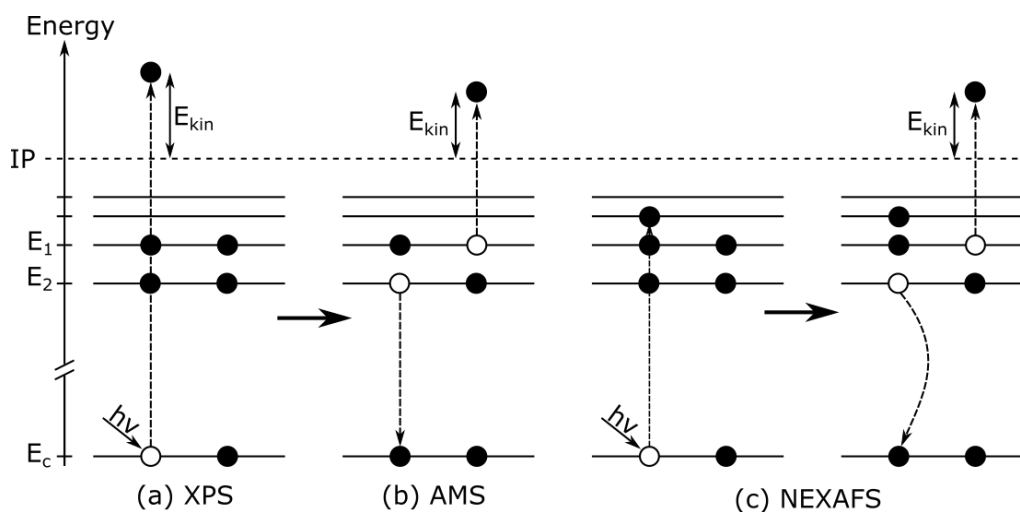


Figure 3.5: Schemes of some x-ray spectroscopy methods. (a) X-ray photoelectron spectroscopy (XPS). (b) Auger-Meitner electron spectroscopy (AMS) as a follow up process of the photoelectron emission. (c) Resonant x-ray absorption and the following AM process leading to the near edge x-ray absorption fine structure (NEXAFS).

3.5 X-Ray Spectroscopy

From the HF calculation in section 3.3, one can see that strongly bound electrons are located in orbitals that represent mostly the deep-lying atomic orbitals of the respective atom (see table 3.1 on page 18). For example, those orbitals in the HF calculation that have energies around 179 eV and 242 eV are strongly located at the sulfur atom of 2-tUra and resemble the 2p and 2s atomic orbitals. For lower binding energy, the orbitals happen to be primarily the C, N, O and S 1s atomic orbitals. Due to the high binding energies of these orbitals, only x-ray light (ca. 0.1 – 10 keV) is able to address these electrons. X-ray spectroscopy, therefore, has two advantages over spectroscopy with UV or visible light. First, core levels of different elements have different binding energies *e.g.*, S 1s 1400 eV, O 1s 540 eV, N 1s 400 eV *etc.* Thus, by choosing different wavelength for the resonant excitation or ionisation one can address specific elements inside a molecule. X-rays are element-specific. Further, they are site-selective within molecules. That means they can address specific regions inside the molecule. This is due to the fact that the core-levels are tightly localised at the specific atom (see orbital figures of S 2p and S 2s in table 3.1). For example, as 2-tUra has only one sulfur atom, a photon with an energy of 250 eV will only address that particular sulfur atom (as $E_b(S\ 2p) < E_b(S\ 2s) < 250\ \text{eV}$) and one is sensitive to whatever happens in its vicinity. Site-selectivity, however, goes further. Even atoms of the same species inside the molecule can be distinguishable due to so-called chemical shift which will be discussed later. X-rays can hence be an interesting probe not only for studying the static structure of molecules but also track excitation induced changes that happen at particular elements/sites of a molecule. Thus, the following section gives a brief overview of static x-ray spectroscopy with a main focus on 2-tUra.

In Figure 3.5, schemes of different x-ray-induced processes are shown. The non-resonant absorption of a photon with an energy above the ionisation potential (IP) of a core-level leads to photoelectrons that can be measured (fig. 3.5 (a)). The existence of a core-hole triggers an Auger-Meitner (AM) process where a valence electron fills the core vacancy and another electron is emitted due to energy conservation (fig. 3.5 (b)). Apart from ionisation, resonant excitation into the unoccupied valence states can take place as well and can also trigger an AM process. Thus, one can observe fine structure in the x-ray absorption spectra resulting from the resonant excitation channels from a core-level to the valence states. These spectra can either be measured in transmission or by electron/ion yield and are called near edge x-ray absorption fine structure (NEXAFS) spectra.

In the following, the emission of photoelectrons is discussed first followed by resonant absorption. At the end, the Auger-Meitner process will be discussed.

3.5.1 Photoelectron Emission

The orbital energies derived from a HF calculation are assumed to be the binding energies of the respective electronic states (Koopmans' theorem). This is the minimum amount of energy needed to excite an electron from a bound to a continuum state. A bound electron that absorbs a photon with higher energy will end up with a kinetic energy $E_{kin} = h\nu - E_b$. The strength of this transition is given by the dipole matrix element. In its general form it looks [61, pp. 26-30]

$$D_{if} = \langle \Psi_f(N) | \sum_{k=1}^N \hat{p}_k | \Psi_i(N) \rangle . \quad (3.27)$$

Here, $\Psi_{i/f}(N)$ are the Slater determinants of the initial and final states and the \hat{p}_k the momentum operators for each electron. The final state Slater determinant is a mix of one electron in a continuum state and $N - 1$ electrons in bound states. For simplicity, it is often assumed that the process of excitation or ionisation is sudden and other electrons are not affected (the sudden approximation). This allows to approximate eq. 3.27 with an "active" one-electron and a "passive" multi-electron part [61, pp. 26-30]:

$$D_{if} = \langle \phi_f | \hat{p}_i | \psi_i \rangle \langle \Psi_f(N - 1) | \Psi_i(N - 1) \rangle . \quad (3.28)$$

While the initial state ψ_i is a bound state, ϕ_f is an unbound continuum state. A simple, but not accurate, approximation for these continuum states can be a plane wave. This is especially true in the asymptotic limit $r \rightarrow \infty$ but not necessarily in the vicinity of the (now ionised) molecule. Thus, more sophisticated models may be used which, however, are not discussed here.

The created core hole has a lifetime τ as it is not an energetically favourable state and will quickly be filled by another electron. As the electron can either emit a photon (x-ray fluorescence) or give the surplus energy to another electron (Auger-Meitner decay), the time-scales of these two processes determine the lifetime of the core hole ($\tau^{-1} = \tau_{AM}^{-1} + \tau_{fl}^{-1}$).

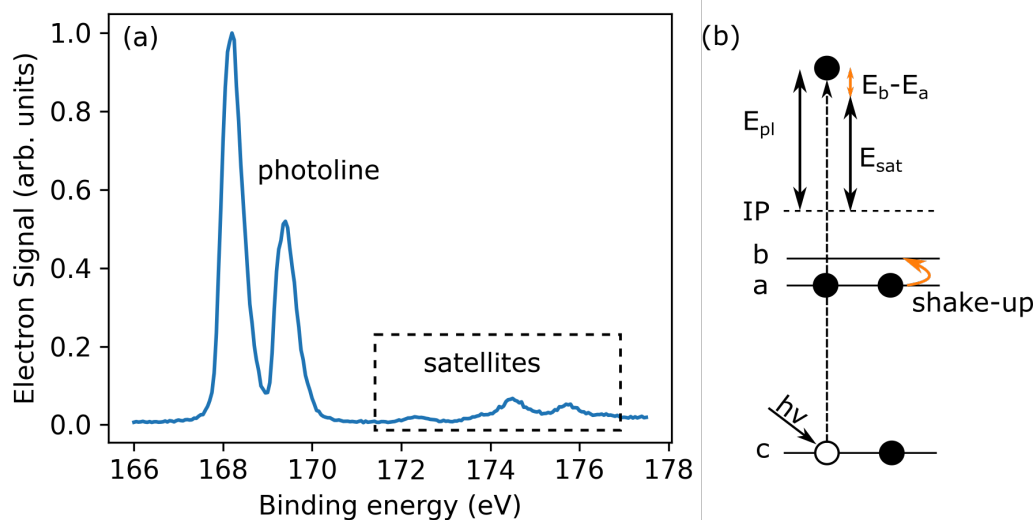


Figure 3.6: (a) Photoelectron spectrum of 2-tUra at S 2p edge taken at Pleiades beamline of the synchrotron SOLEIL [unpublished]. The spectra shows a spin-orbit split main line and satellite features. Inset shows structure of 2-tUra with common numbering of atoms. (b) Energy scheme of direct ionisation and shake-up involving ionisation.

However, the existence of the lifetime means that each process that is associated with the creation or extinction of the vacancy will be spectrally broadened according to the Heisenberg uncertainty principle ($\Delta E \cdot \tau \geq \hbar/2$). The broadening is called lifetime broadening. The lifetime for electronic states is usually in the order of femtoseconds ($10^{-15} - 10^{-13}$ s) resulting in a spectral broadening on the order of 100 meV. Vibrational states could, in principle, also be visible in the spectra but are often buried under the lifetime broadening of the electronic states.

In Figure 3.6 (a) the x-ray photoelectron spectrum of 2-tUra at the sulfur 2p edge is shown. The spectra taken by our group at a synchrotron (SOLEIL) are still unpublished, but for illustration of the theoretical background used in this thesis. Different features can be observed in the spectrum. First, there is the spin-orbit split photoline showing two strong peaks at 168.3 eV and 169.5 eV similar to what has been observed previously [74]. At higher binding energies, small side peaks are observed. These are called satellites and result from correlation effects [75–81]. When looking at excitation of electrons, it is often assumed in calculations that the process of excitation is a strict “one-electron” event as already mentioned above. It means that if the electron is excited into a bound or continuum state, none of the other electrons react immediately. The excitation process is just much faster and appears to be sudden. However, the removal of an electron from an orbital does affect the full configuration of electrons and, hence, it is a multi-electron effect. This gives rise to additional sidebands that result from possible excitation (and relaxation) of some of the “passive electrons”. Thus, the satellites are also called shake-up/off satellites. This is depicted in figure 3.6 (b). Consider the core level *c*, an occupied valence state *a* and an unoccupied valence state *b*. The kinetic energy of the main

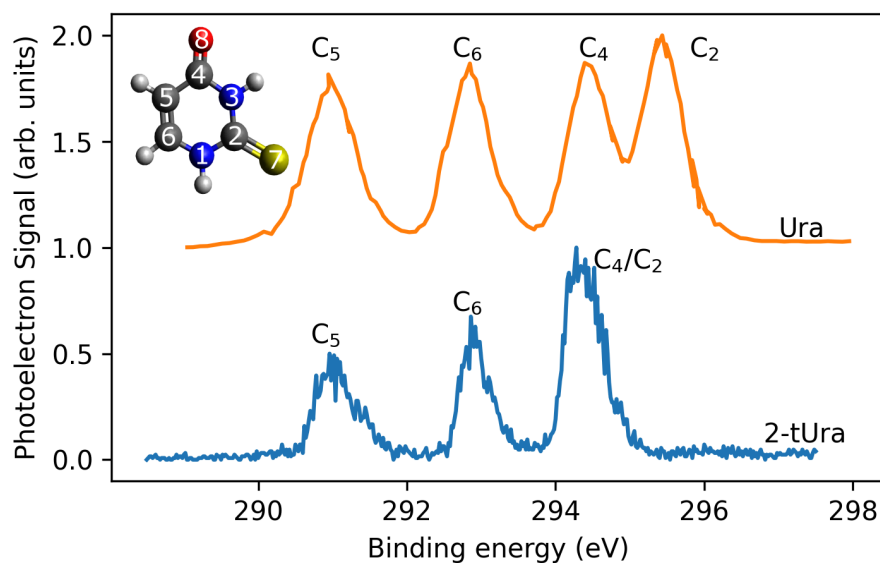


Figure 3.7: X-ray photoelectron spectra of uracil (Ura) and 2-thiouracil (2-tUra) taken at the C 1s edge. The 2-tUra spectrum is unpublished data taken at the Pleiades beamline at the synchrotron SOLEIL, France. The Ura spectrum was taken from Ref. [82]. The inset shows 2-tUra with used numbering of atoms which also applies for Ura.

photoline can easily be understood in the single-electron picture as it is the difference between the photon energy used and the binding energy of the core level. To understand the satellite, however, one has to include the possibility that some of the excess energy can be transferred to other electrons resulting in an excitation e.g., from a to b . In the sketch, more arrows need to be drawn to indicate that $a \rightarrow b$ excitation and the "lost" kinetic energy.

In Figure 3.7, the C 1s photoelectron spectra of uracil and 2-thiouracil are shown. Both molecules have four carbon atoms. Uracil shows four peaks and it is possible to attribute each of the peaks to one of the carbon atoms. The concept behind this is the chemical shift and was studied extensively by the group of K. Siegbahn in the 1960s [37]. One needs to consider the location of atoms within the molecule and the electronegativity of the neighbouring atoms. The C₅ atom - the numbering can be found in fig. 3.7 - is located between two C and an H atom. The C₆ is similar but sees one N atom instead of a C. For C₄, the hydrogen is replaced by an O atom and again there are a C and an N. C₂, however, sees two N and an O atom¹. The electronegativity ϵ is different between C, N and O *i.e.*, oxygen has the highest and carbon the lowest among these atoms. The higher ϵ the more likely (valence) electrons are pulled towards that atom. That, however, means that some negative charge is missing at the parent atom and the screening of the Coulomb potential of the nucleus for the remaining electrons is reduced. The higher Coulomb force leads to a higher binding energy. In the example of Ura, it leads to the following: The C₅, which

¹The sketch in fig. 3.7 shows 2-tUra. For Ura, replace the sulfur (7, yellow) with oxygen (red).

only has other carbon atoms in its neighbourhood, is not going to be affected. The C₆ will have a slightly reduced screening of the nuclear charge as it sees a nitrogen atom. The C₄ has, in addition, an oxygen atom in its surrounding. Hence, the screening is even more reduced and the binding energy for 1s electrons should increase even more. The highest binding energy must have the C₂ as it is surrounded by atoms that all have a higher electronegativity than itself. Thus, the binding energy order from lowest to highest is C₅, C₆, C₄ and C₂. That simple heuristic explanation is backed by HF and more sophisticated calculations [82].

As a comparison, 2-tUra was added to Figure 3.7. In 2-tUra, the oxygen is substituted with sulfur which has an electronegativity slightly above that of carbon. Thus, it can be expected that the C₂ reduces in binding energy a bit compared to Ura and the peak should move closer to that of C₄. The other three peaks, however, should be similar as to what is observed in Ura. In fact, the experimental spectrum only exhibits three peaks and that with the highest binding energy has about double the intensity than the other two. Therefore, it is to be assumed that this big feature consists of two very close features. The HF calculations performed in sec. 3.3 back this (heuristic) prediction.

The explanation based on the electronegativity of surrounding atoms gives already a qualitative order of observed shifts. It suggests that the observed binding energy difference can be directly connected to (partial or effective) charges at particular atoms inside a molecule. Siegbahn *et al.* developed a model that connects the binding energy with the atomic charges inside the molecule – first based purely on electrostatic considerations and later from the Schrödinger equation utilizing the HF approach [37, 83, 84]. The binding energy of the electrons in molecules is determined by the effective molecular potential *i.e.*, by all charges inside the molecule. However, since core-level electrons remain closely located to single atoms, it is reasonable to assume that the effective charge q_A at the atom A of interest has the strongest effect. The effective charge is determined by atomic charge Z reduce by the number of core electrons N_c remaining at the atom and an effective valence charge P_A located around the atom and considered as a point charge [83, 84]:

$$q_A = Z_A - N_c - P_A \quad (3.29)$$

The influence of the other atoms depends on the distance to the atom A as the Coulomb potential scales with relative distance between atom A and B $|r_A - r_B|^{-1} = R_{AB}^{-1}$. From the discussion of the HF approach in section 3.3, we know that the energy eigenvalues are determined by Coulomb and exchange integrals. It can be shown that the only relevant terms for the discussion of the chemical shift are the Coulomb repulsion integral between the core-level electron of interest and the valence electrons as well as the effective charge on the other atoms (see ref. [84] and references therein). The binding energy change can, then, be approximated by the following potential model [83, 84]:

$$\Delta E_i = k_i q_A + \sum_{B \neq A} \frac{q_B}{R_{AB}} + l \quad (3.30)$$

The constant k_i is equal to the Coulomb repulsion integral between the core-level electron and the valence electrons [84]. The constant l is an offset and accounts for the fact that chemical shifts are often given relative to a reference compound [83]. In case of Ura (fig. 3.7), for example, the reference would be the C₅ atom which is not affected by its surroundings and the energies for the other carbons would be given relative to it. The constants can be either calculated or determined experimentally. Comparisons to experiments show very good agreement between the calculated and observed shifts [37, 83, 84]. Thus, XPS can deliver a direct measure for the atomic charge and bonding character inside a (free) molecule. The model can be extended by, for example, considering the influence of bonds with strong polarity *i.e.*, ionic bonds, to give more accurate results [84].

3.5.2 Excited-State Chemical Shift

To summarise the above, the electronegativity of the atoms inside a molecule leads to a valence charge rearrangement so that different atoms have different effective charges. The combined effect of the effective charges in the vicinity of the core-level electron of interest change its binding energy with respect to the value found in (neutral) atoms. However, this idea that the atomic charge determines the binding energy of core-level electrons becomes even more interesting when we consider that a charge flow can also be achieved by the excitation of an electron into an unoccupied valence state. In 2-tUra, the two highest occupied molecular orbitals are the n and the π orbital; the first optical excitation is a $\pi \rightarrow \pi^*$ transition as discussed earlier. Figure 3.8 (a) depicts a sketch of the energy levels together with the respective orbitals. The π and the n orbital have a significant S 3p character. That means the valence electrons have a significant localisation at the sulfur atom. The π^* orbital, in contrast, shows a stronger delocalisation for the electron. Upon a $\pi \rightarrow \pi^*$ transition, an electron is removed from an orbital with strong localisation at the sulfur atom reducing the screening of the nuclear charge (as P_A reduces). If the potential model still holds in this case, it has to be assumed that the binding energies of the core-level electrons at the sulfur increase after the excitation. This is depicted in Figure 3.8 (a) by a lowered S 2p energy in the excited state. The effect should increase if the molecule relaxes into an $n\pi^*$ state because the lone-pair orbital n has a very strong S 3p character and, hence, a stronger charge flow is expected. We call this effect excited-state chemical shift (ESCS).

As can be expected by the nature of excited states, this is a dynamical effect and will change during the relaxation of the molecule. A dynamical shift in the binding energy of core electrons can thus be attributed to a charge movement over the molecule. Moreover, this charge movement is directly connected to the electronic states involved in the relaxation mechanism. In Ref. [39] (see Article 5 in chapter 5), we showed that quantum chemical calculations verify this concept in the case of 2-tUra. The binding energy change for the S 2p core electrons in excited states is primarily determined by the local charge at the sulfur atom. This charge, in turn, is mainly determined by the

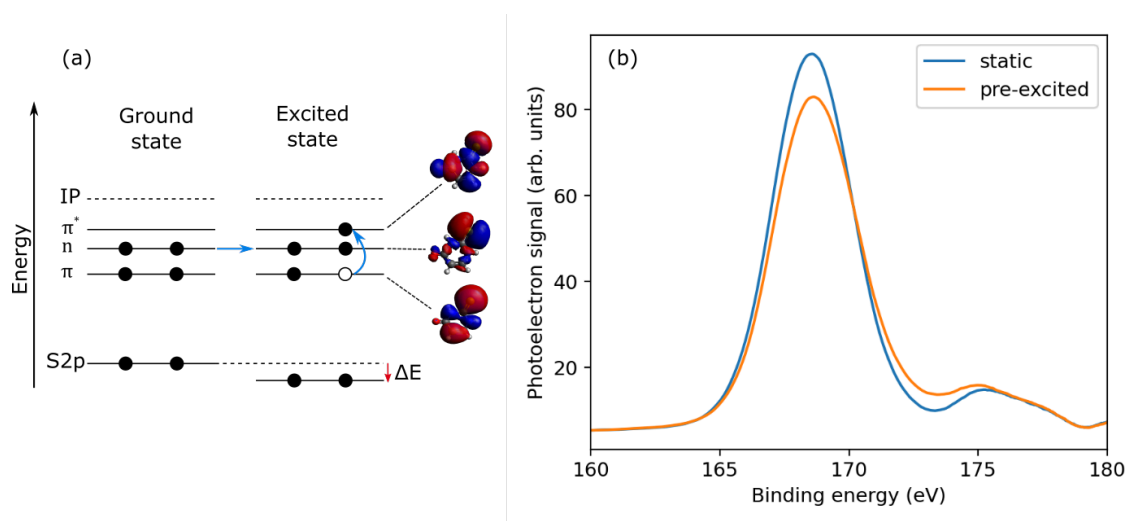


Figure 3.8: (a) Scheme for the Excited-state Chemical Shift (ESCS) in 2-tUra. UV excitation moves valence charge away from the sulfur. Hence, the binding energy of core-level S 2p electrons increases. (b) Experimental S 2p photoelectron spectra of 2-tUra with and without (static) UV pre-excitation. A shift of the binding energy towards higher values can be observed after excitation confirming the ESCS model. A more detailed analysis of these spectra can be found in Ref. [39].

electronic character of the state. The influence of the geometry, however, is small. We also tested a potential model based on the calculated atomic charges and found very good agreement with the binding energies derived by ab initio calculations (see Supplementary Information of Ref. [39]).

Figure 3.8 (b) shows the experimental S 2p photoelectron spectra of 2-tUra taken at the free-electron laser FLASH. The blue curve is the static spectrum that shows the photoline at about 169 eV binding energy and the satellites at about 176 eV. The spin-orbit splitting shown in Figure 3.6 (a) cannot be observed here due to the large bandwidth of the FEL. The orange curve shows the S 2p photoline 1 ps after UV excitation. This pre-excited spectrum has two contributions as only a fraction of the molecules is excited. Hence, it is a combination of the ground state (blue) and the excited state spectrum. The main photoline has a reduced intensity but some signal is gained around 173 eV. So, we can expect that excited state spectrum has shifted to higher binding energies with respect to the ground state. This is exactly what we predicted above with the model of the ESCS. A more detailed analysis of these spectra can be found in Ref. [39].

3.5.3 X-Ray Absorption

The excitation of an electron upon photon absorption can happen into continuum as well as bound states. In the case of resonant absorption, the photon energy, however, satisfies the condition $h\nu = E_f - E_i$ where E_f and E_i are the binding energies of the initial and final state, respectively. Here, the initial state is a core level e.g., S 2p or C 1s, and the

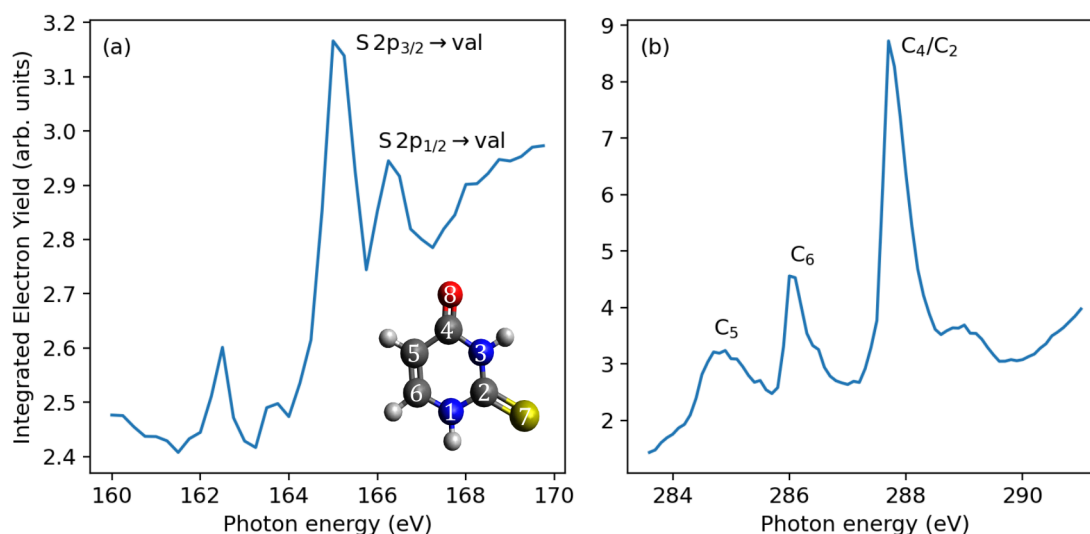


Figure 3.9: Unpublished NEXAFS spectra of 2-tUra at the S 2p (a) and the C 1s (b) edge. The spectra were taken at the Pleiades beamline of the Synchrotron SOLEIL. The observed peaks are core-level to valence excitations.

final state an unoccupied valence orbital. The dipole matrix element D_{if} is the same as in the case for the ionisation (eq. 3.28) except that the final state is a bound excited state. These excited states are, however, not exactly the virtual orbitals derived from a ground state calculation but are described by an electron removed from an inner valence orbital and placed in an outer orbital [61, pp. 30-33]. Simpler models neglect the influence of the outer valence orbital and, for example, calculate the excited states for the singly ionized molecule. As an alternative for core-excited states, the core equivalent model can be used which assumes that upon removal of a core electron the outer electrons behave as if they see a nucleus of charge $Z + 1$ [61, pp. 30-33].

Promoting a core-level electron into a bound valence state by absorption of a photon is a way to study the structure and dynamical behaviour of molecules. The unoccupied valence states in a molecule give rise to various resonances just before the ionisation threshold. The binding energy of the excited valence states is only a fraction of the binding energy of the core-level state. Hence, the resonances appear close to the IP.

In Figure 3.9, two NEXAFS spectra are shown. The spectra have been taken at Pleiades beamline of the SOLEIL synchrotron. The absorption was measured *via* integrating over the whole kinetic energy range of the AM decay. Figure 3.9 (a) shows the S 2p and (b) the C 1s spectrum of 2-tUra. The S 2p spectrum shows two double features at around 165 eV, with the peaks at 166 eV being stronger than these around 163 eV. The difference between two peaks in a double feature matches the S 2p spin-orbit splitting known from the photoelectron spectra above and from Giuliano *et al* [74]. This indicates that the spin-orbit split states have the similar final states. At about 168 eV photon energy, the spectrum goes towards a plateau region indicating the S 2p ionisation. The C 1s NEXAFS shows

three peaks that match the observed number of peaks in the photoelectron spectrum. Further analysis reveals that the splitting of the peaks matches the splitting of the XPS. It may therefore be a valid assumption that all C 1s electrons also end up in very similar final states.

NEXAFS is a tool to be used for time-resolved probing [42–44] *i.e.*, an initial valence excitation was performed before resonantly exciting a core-level electron. Though no time-resolved x-ray absorption measurements are included among the publications in this thesis, I anyhow include a short abstract on this topic to give a concise overview on the possible methods for probing molecular dynamics with x-rays. Consider again an initial $\pi \rightarrow \pi^*$ transition. The excitation creates a hole in the π orbital and the previously unoccupied π^* orbital is partially filled with an electron. This hole creates a new excitation channel for the core-level electron. Provided that the core-level to π transition is allowed, it would create a new resonance in the NEXAFS spectrum that emerges at lower photon energies as the resonances known from the static spectroscopy. Furthermore, the molecule might undergo electronic relaxation through different electronic states. In the case of 2-tUra for example, $n\pi^*$ states can be populated. Here, the hole is in the n orbital and situated at even higher binding energies. Thus, a new feature may rise during the relaxation that shows up only for a certain time. In the case of thymine, this behaviour has been observed in a time-resolved study [42]. The molecule has been pre-excited into a $\pi\pi^*$ state with UV light and pulsed x-ray light around the O 1s edge from an FEL was used to probe the sample. It could be found that 60 fs after the excitation the NEXAFS spectrum shows an additional peak that is located about 4 eV below the main oxygen resonance. This peak was attributed to a $1s \rightarrow n$ transition. In thymine, the n orbital has a strong O 2p character according to calculations. There is a similar effect as we observe with the n orbital in 2-tUra which shows strong S 3p character. The localisation of the lone-pair orbital leads to a strong absorption from the 1s. Hence, it can be observed as an additional feature in the time-resolved study. This experiment is another good example on why time-resolved measurements involving x-ray probes are sensitive to the electronic character of the excited state.

3.5.4 Auger-Meitner Effect

Regardless of how and to where a core-level electron is excited, the molecule remains with a core-hole. The lifetime of such an inner-shell vacancy is rather short *i.e.*, in the range of $10^{-15} - 10^{-14}$ s. The decay of the core hole includes an electron from a higher shell that occupies the vacancy. Due to energy conservation, the electron can emit a photon of energy $h\nu = |E_{val} - E_c|$ where E_{val} and E_c are the binding energies of a higher lying (valence) orbital and the core orbital, respectively. The process is called x-ray emission or fluorescence. However, the energy can also be directly transferred to another valence electron *via* Coulomb interaction. The electron is then emitted with a kinetic energy of $E_{kin} = E_c - E_1 - E_2$ where E_c , E_1 and E_2 are the binding energies of the core-level and the two valence electrons, respectively. The process is called Auger

(-Meitner) effect². The probability of each process depends on the element involved. From the Einstein coefficients, one can deduce that the fluorescence yield increases with the increasing fluorescence photon energies for high-Z atom. Thus, the x-ray fluorescence is the dominant decay channel for high-Z elements. For low-Z atoms, the Auger lifetime happens to be much smaller than the fluorescence lifetime; hence, the Auger-Meitner process is the preferred decay channel [61, pp. 13-14]. Technically, all higher lying electrons are possible candidates for such a decay. However, if the hole can be filled by an electron from the same shell *e.g.*, a 2s hole is closed by a 2p electron from the same atom, the process is called Coster-Kronig decay [85]. Due to the high overlap of the wavefunction, this process has a large rate.

The matrix element describing the AM effect may be written in a very general form as [86, pp. 11-16]

$$D \propto \langle \Psi_c^{N-1} | \hat{V} | \Psi_{ij}^{N-1} \rangle . \quad (3.31)$$

Ψ_c^{N-1} is the core-ionised initial state and Ψ_{ij}^{N-1} represents the final state where two electrons have been removed from the valence shells *i* and *j* but an electron in a continuum state has been added in order to account for the ionisation. Thus, both states are multi-electron wavefunction which are again written as determinants. The coupling operator is described by a Coulomb potential $V \propto 1/r$ [71]. Equation 3.31 may be reduced to a problem that only considers two electrons, that one which fills the core vacancy and the emitted electron. The transition element can then be written [86, p. 11-16]

$$D \propto \langle \Psi_f(r_1, r_2) | \frac{1}{|r_1 - r_2|} | \Psi_i(r_1, r_2) \rangle , \quad (3.32)$$

where

$$\Psi_{i,f}(r_1, r_2) = \psi_{i,f}(r_1)\phi_{i,f}(r_2) - \psi_{i,f}(r_2)\phi_{i,f}(r_1)$$

are two-electron wavefunctions. The difference preserves the Pauli principle as we cannot distinguish which electron fills the vacancy and which is ejected.

Depending on the triggering process, the atom or molecule, that undergoes an Auger-Meitner decay, ends up either in a cationic, dicationic or even tricationic state [87] (see also Figure 3.5 (b) and (c)). Consider the process of photoelectron emission. A core electron is removed by the absorption of a photon and leaves behind a core hole. Therefore, the atom or molecule is positively charged afterwards (*i.e.*, it is a cation). Then, it undergoes an Auger-Meitner process *i.e.* leading to the emission of an Auger electron (also from a valence shell), and the creation of a doubly-charged species. If, however, a Coster-Kronig decay happens *e.g.* 2p \rightarrow 2s, then another AM decay can take place as there is a vacancy in another core-hole. The molecule or atom ends up in a tricationic state.

After a resonant excitation with x-ray light, the molecule will end up in a singly-charged state. An electron that is resonantly excited from a 1s to a π^* orbital (see Figure 3.5 (c)) will trigger an AM decay due to the core vacancy and another valence electron is removed

²Named after Pierre Auger who dedicated his PhD thesis to this decay in 1926 and Lise Meitner who originally discovered the effect in 1922 during her research on β -decays.

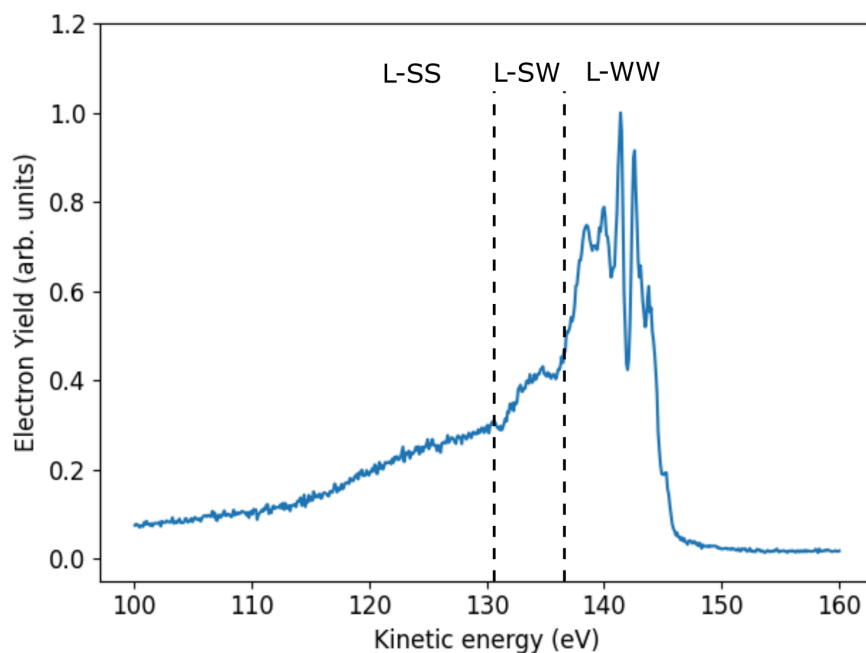


Figure 3.10: S2p Auger-Meitner spectrum of 2-tUra taken at the PLEIADES beamline of the synchrotron SOLEIL [unpublished]. The three regions separated by dashed lines indicate possible Auger transitions.

from the configuration. As there has not been an initial ionisation process, the molecule is only in a cationic state. Moreover, one can distinguish between two sets of decays. In a participator decay, the previously excited electron participates in the decay process. That means that it will be emitted during the process or occupies the core vacancy³. Here, the final state is indistinguishable from a direct (valence) photoelectron emission. In a spectator decay, the excited electron will remain in its excited state valence orbital and a different valence electron is emitted during the process (“the electron watches the AM decay”).

In Figure 3.10, the non-resonant Auger-Meitner spectrum of 2-tUra is shown using an S 2p ionisation. A photon energy of 250 eV was used to ionise an S 2p electron and the following Auger electrons emitted within an energy range of 100-150 eV were collected. A broad feature can be observed that can be analysed in a bit more detail. A strong band at energies around 135 eV to 145 eV shows some structure. A shoulder-like feature is observed between 130 - 135 eV, and a wider tail-like feature covers the area between 110 and 130 eV. According to Moddeman *et al.*, the identification of Auger transition can be done by separating the possible valence states in weakly bound (w) (outer-lying) and strongly bound (s) (inner-lying) valence states [87]. At high kinetic energies, only weakly

³Under the assumption that the binding energies are not affected strongly during the AM process, it does not make a difference whether the excited electron fills the hole or is emitted.

bound states contribute to the decay (L-WW; L because L shell vacancy). In the S 2p example, this is likely the structured region above 135 eV, and the states involved are S 3p-like valence states (n or π orbitals). The HOMO and HOMO-1 have still a strong localisation at sulfur atom and, hence, are candidates for that structured region (see table 3.1 on page 18). The WW feature should be followed by a feature that is characterized by one strongly and one weakly bound electron that participate in the AM process (L-SW). This could be the shoulder-like feature at around 130 eV. Finally, a third feature should show up at even lower kinetic energies according to Moddemman *et al.* that involves only strongly bound inner valence states (L-SS). In our case, this could be the tail-like feature at around 120 eV. In an atomic setup, these inner valence states would be the 3s orbitals of sulfur. However, the inner valence orbitals of 2-tUra are not sulfur but rather strongly delocalised orbitals. This delocalisation broadens features and makes it more difficult to distinguish them.

4 | Gas-Phase Spectroscopy of Molecular Samples

This chapter covers concepts of experimental methods used during my doctoral studies and some further information on the experiments. First, the gas-phase UV-Vis absorption spectroscopy is briefly discussed and some details on the gas cell used in article 1 in chapter 5 and the analysis of the spectra are given. Then the concept of time-of-flight measurements is explained and how magnetic-bottle spectrometer can improve the collection efficiency. After this, the URSA-PQ apparatus is introduced. This is followed by a brief overview on the working principle of a general SASE FEL and the parameters of FLASH2 are given, including its spectral characteristics. At the end, the pump-probe experiment performed in the articles 5 and 6 is explained.

4.1 Gas-Phase UV-Vis Absorption Spectroscopy

Absorption spectroscopy from the near-infrared (NIR) up to the UV is an established experimental method and there are a variety of commercial spectrometers available. For example, in ref. [69] (article 1) we used a Cary 5E UV-Vis-NIR Spectrometer that was slightly modified for our samples. The principle of most of this apparatus is fairly simple. A light source with a broad spectrum illuminates the (mostly transparent) sample. The transmitted light is directed on a grating which spatially resolves the spectrum. Finally, a detector *e.g.*, a photodiode or CCD array, measures the spectral intensity for different wavelength.

The main focus in our research is to study molecules in their isolated form without the molecular interactions that occur in the solid and liquid phase. However, the samples we use (like thiouracil) are often solid at room temperature and not transparent. Thus, we must evaporate the samples to bring them into the gas-phase. Heating, however, can induce pyrolysis but other experiments have shown that this does not occur in our case [22, 24, 71, 72].

Evaporating solid samples requires a closed, transparent cell that contains the sample and a possibility to heat the whole arrangement. In the past, sealed quartz cells were used when taking spectra in the UV range [71, 72]. For the gas-phase UV-Vis absorption experiments performed in [69], we designed a small gas-cell that fits into the probe arm

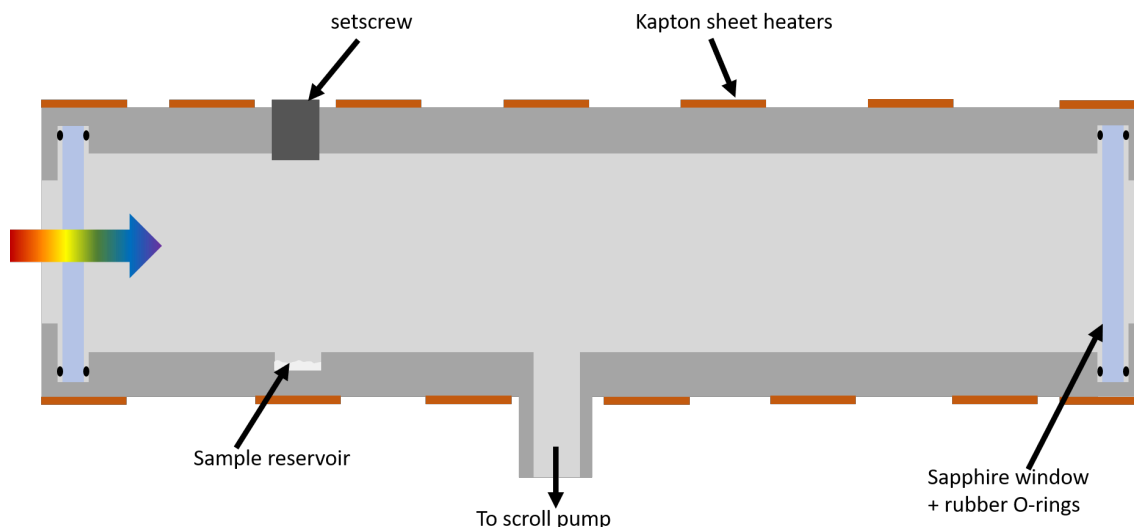


Figure 4.1: Sketch of the home-built sample cell for the Cary UV-Vis spectrometer.

of the aforementioned UV-Vis absorption spectrometer. A sketch of the cell is shown in fig. 4.1. The cell consists of a cylindrical, hollow aluminium body. On either end of the cell wedged sapphire windows allow the light to go through. Viton O-rings between the windows and the cell body achieve vacuum tight sealing (down to about 1×10^{-5} mbar). A trough on the inner wall of the cylinder serves as a sample reservoir and filling can be achieved through a screwable hole on the opposite side. Another threaded hole aligned with the reservoir is connected via Swagelok components with a vacuum pump. This allows one to evacuate the cell and thus avoids contributions of heated air in the spectrum. Kapton sheet heaters wrapped around the cell are used for heating. Here, the thermal conductivity of the Al body guarantees a faster heating of the molecule compared to a quartz cell. The temperature of the Al body is continuously measured with three thermocouples (one at each end and one in the middle).

Similar to experiments performed in solution, gas-phase experiments require a careful study of the background signal. While background contributions in solution-phase studies originate from the solvent as well as from the glass cuvette, in our gas-phase experiments mostly the heated sapphire windows introduce an additional signal. The measured signal at temperature ϑ can be written as:

$$A_{meas}(\lambda, \vartheta) = A_{sample}(\lambda, \vartheta) + A_{cell}(\lambda, \vartheta) \quad (4.1)$$

Here, $A(\lambda, \vartheta)$ is the absorbance. It is defined as $A = \log(I/I_0)$ where I is the transmitted signal and I_0 the incident light. Absorption spectra taken with the cell are shown in fig. 4.2 (a). First, one can see that all the spectra look similar as they show a strong absorption at about 200 nm that gradually decreases towards 400 nm. Only the red spectrum that contains 2-tUra at 150°C shows a stronger deviation especially in the region between 250

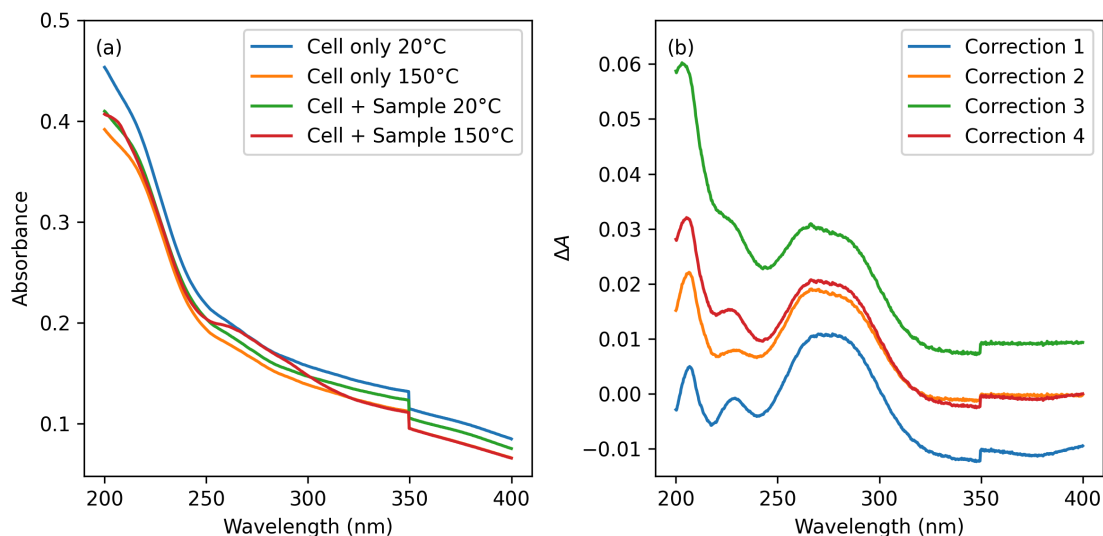


Figure 4.2: (a) Measured absorption spectra with and without sample (2-tUra) at temperatures of 20°C and 150°C. Opening and closing the cell to insert sample causes shifts in the spectrum. (b) Sample spectra derived for different corrections (see main text).

to 300 nm. That is the main sample contribution to spectrum.

Looking at the cell-only spectra (blue and orange curve), the spectrum at higher temperatures is shifted to lower absorbance. This, however, is not a single value that applies to all wavelengths but changes throughout the spectrum. This shift is stronger at around 200 nm than it is at 400 nm. There is a temperature behaviour of the cell that needs to be known to better estimate the actual sample spectrum. Hence, the spectra shown in [69] consisted of a set of measurements that included a prior temperature dependent background measurement (cell-only).

Comparing the cell-only spectra (blue & orange) with those that have been done with sample inside the cell (green & red), it is apparent that consecutive measurement series¹ show slightly different behaviour. The spectra at 20°C show a different offset and looking at the region between 350 to 400 nm, temperature-dependent drop between the two series is also different. A reason for the difference is likely that the sample was filled into the cell in between the measurements. For that, the screw above the reservoir needs to be untightened and tightened again. This comes with some displacements of the cell itself and hence the light path may slightly change. These differences make it more difficult to correct for the cell spectrum.

In figure 4.2 (b), some estimates for the 2-tUra spectrum using different corrections. Correction 1 simply subtracts the 20°C spectrum (green line in (a)) from the high temperature spectrum (red line in (a)). Correction number 2 subtracts only the high-temperature

¹Here, a “measurement series” are consecutive measurements where the cell temperature is gradually increased from room temperature up to about 180°C but the cell remains untouched.

cell-only spectrum (orange line in (a)). A combination of all four spectra is used in Correction 3. Here, ΔA is calculated by

$$\Delta A = A_{C+S}(150^\circ\text{C}) - A_{C+S}(20^\circ\text{C}) - [A_C(150^\circ\text{C}) - A_C(20^\circ\text{C})] \quad (4.2)$$

where the index C means cell only and C+S the spectra where sample was inside the cell. In addition to Correction 1, the temperature dependent behaviour of the cell is subtracted as measured in the cell-only scans. However, the temperature behaviour between the series is different. Thus, Correction 4 introduces an additional scaling:

$$\Delta A = A_{C+S}(150^\circ\text{C}) - A_{C+S}(20^\circ\text{C}) - (A_C(150^\circ\text{C}) - A_C(20^\circ\text{C})) \cdot \left. \frac{A_{C+S}(150^\circ\text{C}) - A_{C+S}(20^\circ\text{C})}{A_C(150^\circ\text{C}) - A_C(20^\circ\text{C})} \right|_{\lambda=400\text{ nm}} \quad (4.3)$$

The scaling factor is the ratio of the temperature-dependent absorbance differences at 400 nm between the measurement series. 400 nm was chosen because there is no signal from 2-tUra expected.

As can be seen in Figure 4.2 (b), the corrections lead to different results, but all show the main features of the thiouracil spectrum *i.e.*, a main absorption between 250 and 300 nm and peaks at about 240 nm and 205 nm. However, correction 1 obviously overcorrects the spectrum as a significant part of it is below 0 (what would mean emission instead of absorption). Correction 3 has an offset that is higher than what has been measured before. Therefore, it is not an optimal correction either. Correction 2 and 4 happen to be just right when it comes to the offset and show very similar behaviour. Only at lower wavelength is there a significant difference where the correction shows higher values than correction 2. The matching spectra are more a coincidence as the two 150°C spectra shown in (a) start with the same offset at 400 nm. However, it does not account for the stronger temperature dependent drop in absorbance found in the cell-only measurements. Hence, the spectrum is somewhat lower in the range between 200 and 300 nm. Correction 4 seems the most reasonable approach to estimate the sample spectrum and was, thus, used in ref. [69].

4.2 Time-of-Flight Measurements

A major part of the experiments performed utilize the concept of time-of-flight (TOF). As discussed in section 3.5, electrons emitted from the molecules have a certain kinetic energy which is a measure for their binding energy inside the molecule. To measure this kinetic energy, one usually measures the flight time t the electron needs to travel from the point of emission straight towards the detector. If this distance s is known, the kinetic energy is simply given by

$$E_{kin} = \frac{m_e}{2} \cdot \frac{s^2}{t^2} \quad (4.4)$$

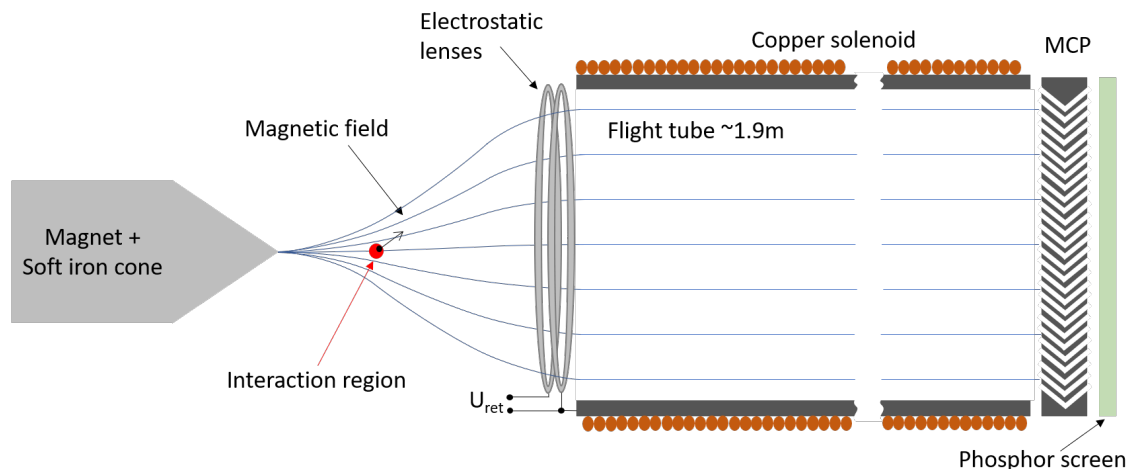


Figure 4.3: Sketch of a magnetic bottle time-of-flight spectrometer. A strong magnetic field expands adiabatically around the interaction region forcing emitted electrons to propagate towards the flight tube due to Lorentz force.

A time-of-flight measurement requires a distinct starting event *i.e.*, a well-defined time when electrons will be emitted from the molecule. This is usually the case when pulsed light is used. Then a bunch of electrons will be emitted every time a pulse hits the sample. The time window during which electrons will be emitted (femto- to picoseconds) is rather short compared to the time they need to travel towards the detector. For example, 1 eV of kinetic energy results in a velocity of about 1/1000 of the speed of light for an electron. Considering a distance of 1 m between interaction region and detector this gives a flight time of about 3 μs . Even an energy of 100 eV will only result in a flight time of about 0.3 μs . This is still considerably larger than femto- or picosecond pulses so that this trigger event can be considered as “instantaneous”. To define this starting point in the measured spectra, often a “photon prompt” can be observed which originates from scattered light that reaches the detector. This signal comes long before the first electrons hit the detector.

Electron signals are usually rather weak and, thus, amplification mechanisms are often implemented. In electron (or ion) spectroscopy, microchannel plates (MCP) are often used in the detector setup to enhance the incoming electron signal. These plates consist of a two-dimensional array of channels and each of these channels can serve as a secondary electron multiplier. By applying a voltage between the back and front of an MCP incoming electrons will be multiplied every time they hit the wall of a channel and eventually creating an electron pulse that can be easily detected. To optimize the enhancement effect, the channels of the MCP are not perpendicular to the surface of the plates but are angled. This forces every incoming electron to hit a channel wall and get multiplied. Depending on the application, usually multiple adjacent MCPs are used. For TOF measurements a so-called Chevron or V-stack is often used, in which two MCPs are combined.

Apart from a possibly weak signal from the sample, a standard TOF spectrometer restricts the collection solid angle because of the detector size and its distance from the interaction region ($\Omega = A/r^2$). The smaller the detector and the further away (*i.e.*, the longer the flight tube), the smaller the solid angle. Thus, the detector covers only a few percent of the total 4π emission angle for electrons. Further improvement of the signal can be achieved by directing more of the emitted electrons towards the detector. In the 1980s, Kruit and Read developed a technique to improve the collection angle for TOF experiments by introducing strong magnetic fields in the interaction region [88]. These so-called magnetic bottle spectrometers are able to increase the collection solid angle up to (nearly) full 4π [89]. A sketch of the variant we are using is shown in fig. 4.3. The field of a strong magnet is concentrated by attaching a soft iron cone to it. Its tip is placed close to the interaction region. The flight tube sits inside a solenoid made from copper wire and a current applied on it leads to a homogeneous magnetic field inside. From the tip of the iron cone towards the flight tube the magnetic field expands adiabatically. An electron that is now emitted inside this magnetic field will be deflected due to Lorentz force. The forced spiral motion of the electrons encloses a constant amount of field lines which “bend” their direction to the detector. A detailed description of the electron trajectory is given in Ref. [88].

The detection of the electron pulses is done (in our case) by using a conductive anode on a phosphor screen just behind the MCP configuration and measuring the time-dependent current. To improve the resolution of the signal, a long flight tube is used so that the fast electron can be measured on different time bins during the sampling process. As can be seen in the equation above, the TOF is in first approximation linear proportional to the distance travelled. However, the (physical) space for experiments is usually limited so that those spectrometers cannot be built to any length. The longest flight tube used so far was built by J. Eland, the pioneer in the field, and it was 5.5 m long [89]. If one is only interested in certain energy regions of the electron kinetic energy spectrum, implementing a retardation step before the electrons reach the tube is much more reasonable and the spectrometer can be kept shorter. Applying a negative potential U_{ret} between electrostatic lenses just in front of the tube will repel electrons with energies smaller than U_{ret} but those with higher energies will still reach the flight tube and can be detected. The resolution for those electrons improves.

I performed experiments at the FLASH free electron laser using the URSA-PQ apparatus [45]. The heart of this machine is a magnetic-bottle electron TOF spectrometer as described above. A strong inhomogeneous magnetic field of about 1 T forces emitted electrons towards the 1.9 m flight tube. A system of three electrical lenses can be used to accelerate or retard and focus incoming particles. A V-stack MCP pair amplifies the incoming signal, which is finally detected with an analog-digital converter that reads the current on an anode placed behind the MCPs on a phosphor screen. The details of the spectrometer and further information of this apparatus are described in [45] (article 2).

A final note in this subchapter concerns nonadiabatic behaviour, which is an important issue in those setups. In their 1983 paper, Kruit and Read already discuss the influence

of nonadiabatic field changes on the performance of a magnetic bottle spectrometer. They define an adiabatic variation of the magnetic field by the conservation of angular momentum which is the given if the “field experienced by an electron changes negligibly in the course of one revolution of the helical motion” [88]. Nonadiabaticity can be introduced by different means: electrons that are emitted far away from the symmetry axis experience a different magnetic field due to the inhomogeneity as if they were emitted close to it. A high kinetic energy electron may experience a stronger change in the magnetic field because, with a higher z-component, a faster change can be expected [88]. Also, a non-optimized field in the flight tube can cause stronger variations in the transition from an inhomogeneous to a homogeneous field [90]. The consequences of nonadiabaticity can be different. Kruit and Read studied the influence of displaced emission and found that the spatial resolution may be unchanged but the image of the electron beam is distorted [88]. Mucke *et al.* found that with an insufficiently high magnetic field in the flight tube the transmission of the spectrometer oscillates as a function of kinetic energy [90]. They attribute this effect to the development of nodes in the trajectories due to the cyclotron motion.

During one of the experiments at FLASH, we have tested the influence of different parameters of the magnetic bottle spectrometer on the S 2p difference spectra (“pre-excited spectrum” – “static spectrum”; see supplementary information in [39]). There, we observed that the signal intensity at different kinetic energies oscillates against magnetic field strength in the flight tube. Further the difference spectra shift slightly and broaden in shape especially for higher magnetic fields. We also attribute these signal changes to the alternation of the cyclotron motion.

4.3 X-ray Free-Electron Lasers

4.3.1 Basic Principle of SASE Free-Electron Lasers

Amongst high-order harmonic generation (HHG) and synchrotrons, free-electron lasers are one way to produce coherent and pulsed x-ray light. Though, FELs are not restricted to generate VUV and X-ray light and can technically be optimised for a variety of spectral region such as infrared [91, 92], VUV and x-ray FELs have emerged more frequently over the past decades [93–99]. An advantage of FELs compared to synchrotrons and HHG is the much higher brilliance of the generated light; up to 10 orders of magnitude larger than synchrotrons and more than 20 compared to HHG sources [100, 101].² X-ray pulses generated by FELs usually show pulse durations in the order of 10 to a few 100 fs [103, p. 170], but attosecond pulse trains have now been demonstrated as well [104, 105]. In addition to the short pulses and high brilliance, FELs offer also high spatial coherence.

²The HHG sources suffer especially from the fact that the intensity of the generated harmonics scales with $\lambda^{-6.5}$ where λ is the driving wavelength. In order to generate x-ray light, however, this wavelength must be pushed far into the infrared region as the cut-off energy of the harmonic plateau scales with λ^2 [102].

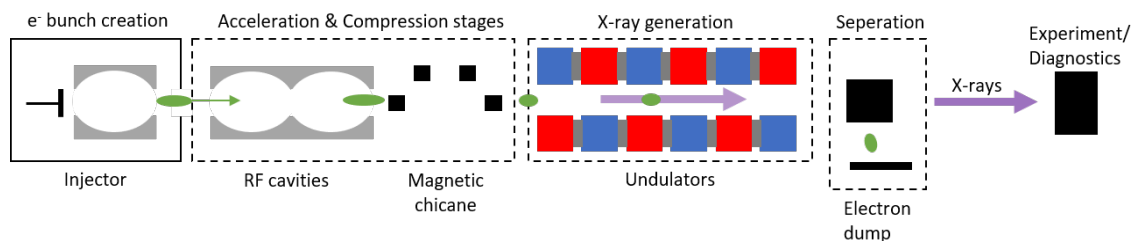


Figure 4.4: Overview of components of a free electron laser. An electron bunch is created in the injector. Then it is accelerated in RF cavities to relativistic energies and compressed using a magnetic chicane. In the undulator the electrons generate coherent x-ray pulses.

The longitudinal coherence of SASE FELs, however, is poor and, hence, they show strong shot-to-shot fluctuations.

In Figure 4.4, an overview of the important components of a SASE FEL is shown. Here, only a short description of each part will be given. A more detailed view on accelerator science and free-electron lasers can be found, for example, in refs. [101, 103, 106, 107]. First, a short electron bunch is created in the “injector”. In principle, a laser pulse hits a cathode and creates photoelectrons. These are then collimated and directed towards a first acceleration stage. In the linear accelerator, various compression and acceleration stages alternate. The acceleration is done within radiofrequency (RF) cavities. Here, an RF field is aligned parallel to the electron motion and synchronised in a way, that for each cavity the electrons experience only a positive acceleration. After an acceleration stage, bunch compression follows. Because the electron bunch has a certain length, the electrons will not experience the exact same electrical field which leads to slightly different energies. Another problem is the repulsive Coulomb interaction between electrons which can tear the bunch apart. The compression is often done with a so-called “magnetic chicane”. Here, the electron bunch is dispersed perpendicular to its motion by a magnetic field. This forces electrons with different kinetic energies on different paths. By adjusting the path length before an inverse magnetic field recombines the electrons to a compact bunch, the electron bunch can be spatially reduced in length and, hence, it is compressed temporally.

The electron bunch undergoes a couple of acceleration and compression stages until the final kinetic energy is reached. For x-ray FELs, this is usually in the order of MeV to GeV. The velocities reached with these energies are in the relativistic regime. For example, if the electron bunch reaches an energy of 2 GeV, the velocity would be almost (99.999’997 %) the speed of light. However, this energy does not only allow the generation of x-rays in the undulator, but also keeps the electron bunch compact in the laboratory frame due to Lorentz contraction. In the electron bunch rest frame, the distance between individual electrons is much bigger than in the laboratory frame. Hence, the electrons experience a lower Coulomb force and can be brought further together as it would be possible when they were in rest.

After the acceleration and compression, the bunch arrives at the undulator (see fig.

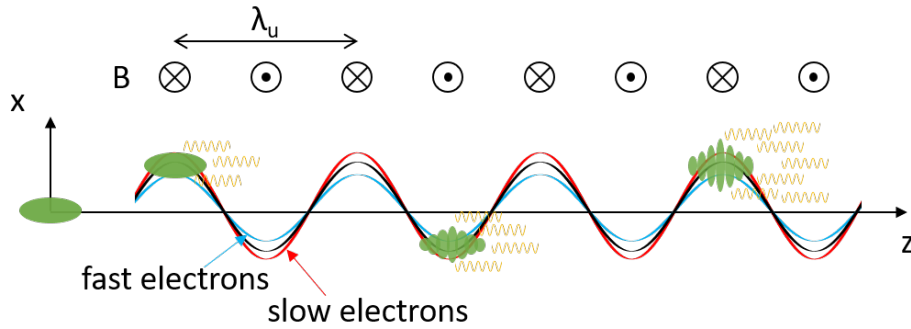


Figure 4.5: Sketch of the electron motion and micro-bunching in an undulator. Due to Lorentz force, the electrons will start a transverse motion that leads to undulator radiation. The interaction between the emitted light and the propagating electrons enforces a micro-bunching of the electrons. Since these micro-bunches are separated by a wavelength, the emitted light will interfere constructively between the bunches. This leads to an exponential increase in intensity and the transversal coherence improves..

4.4). This is a chain of periodically poled magnets and is the crucial part of any FEL. An electron (bunch) that enters the magnetic field will be deviated from its straight motion due to Lorentz force. As the magnetic field changes periodically its direction, the electron motion will follow a sinusoidal path through the undulator. This is depicted in figure 4.5 with the black sinusoidal curve. The strength of the modulation of the trajectory for a fixed electron energy is given by the undulator parameter [103, p. 13]:

$$K = \frac{eB\lambda_u}{2\pi m_e c} \quad (4.5)$$

where B is the magnetic field strength of the undulator, which depends on the gap between the two rows of magnets, and λ_u is the undulator period which is the distance between two consecutive magnets with the same magnetic field orientation. e , m_e and c are the charge and mass of the electron and the speed of light, respectively.

The acceleration, that an electron encounters, leads to the emission of synchrotron radiation. In a moving reference frame *i.e.*, a reference frame that travels longitudinal with the speed of the electrons, the motion can be approximated as a dipole and, hence, the emitted light propagates in longitudinal direction. In the laboratory frame, this radiation characteristics is transformed into a conical emission pointing forwards [103, pp. 14-19]. The light, that the electrons emit in the undulator, will primarily point into the positive z direction in figure 4.5. This is called undulator radiation. The wavelength of the emitted light can be approximated by [103]

$$\lambda_r = \frac{\lambda_u}{2\gamma^2} \cdot \left(1 + \frac{K^2}{2} + \gamma^2 \theta^2 \right) \quad (4.6)$$

close to the emission angle θ where $\gamma = (1 - (v/c)^2)^{-1/2}$ is the Lorentz factor. Due to the dipole-like characteristics, the electrical field of the emitted light is polarised parallel to the oscillatory motion of the electrons.

The electrons will start to interact with the generated light. Its electrical field will modulate the energy of the electrons. Since the bunch is much larger than the wavelength λ_r , electrons will be affected differently depending on the phase of the light field. Electrons that experience an electrical field counterphase to their transverse velocity component will be slightly slowed down, whilst others will slightly increase their velocity. The transverse velocity component affects the overall velocity and, thus, this leads to an energy modulation inside the bunch with the same wavelength as the emitted light. Slow and fast electrons start to approach each other because the deviation from the Lorentz force for faster electrons is smaller than for the slower electrons (see blue and red curve in fig. 4.5) [107]. Eventually, the electrons gather in smaller regions separated by a wavelength. This effect is called micro-bunching and improves drastically the coherence and intensity of the generated light. As all electrons inside a micro-bunch emit in phase, the intensity scales with the square of the number of electrons inside the micro-bunch [103, 107]. A stronger light field leads to more interaction; thus, it leads to more bunching and, again, a stronger growth of the intensity. The gain length, L_G , characterises the exponential growth of the radiation intensity and is given by

$$L_G = \frac{\lambda_u}{4\pi\rho} \quad (4.7)$$

where ρ is the dimensionless FEL parameter and for x-ray FELs in the order of 0.001 (what gives $L_G \approx 100 \cdot \lambda_u$) [107]. It is found that the saturation of this process takes about $20L_G$. At this point, the electron bunch is well structured [103, pp. 40-41]. This process of the amplification of spontaneous emission by electron-light interaction is called SASE (self-amplified spontaneous emission).

As mentioned earlier, the difference between the speed of light and the velocity of the electrons is small. Hence, the generated light will slowly advance on front of the electrons. A photon emitted by an electron will slip ahead by about one radiation wavelength over an undulator period [107]. This gives rise to a cooperation length L_C *i.e.*, the distance the emitted light can propagate and still interact with another electron. It is the slippage over a gain length and, hence, both parameters are correlated by $L_C = (\lambda_r/\lambda_u) \cdot L_G$ [107]. This cooperation length is also an approximation for the coherence length (temporal coherence). Over this distance, electrons can interact with each other. This contributes to the build-up of longitudinal coherence during the gain process as electrons can “talk” to other electrons in front of them. Electron (micro-) bunches within the cooperation length gain a phase relation and, hence, coherence. However, the longitudinal coherence remains poor for FELs compared to, for example, HHG. The problem is that the SASE process starts from a white noise spectrum and at the beginning different random peaks (modes) will be amplified. The SASE spectrum, thus, is not a Gaussian like curve but is a rather “spiky” spectrum that is different for every single x-ray pulse. The width of

these spikes in the spectra is inverse proportional to the coherence or cooperation length in the SASE process [107]. These random fluctuations in SASE FELs are a significant disadvantage. Depending on the experiment conducted, it requires detailed knowledge of the shot-to-shot behaviour of the FEL. The stability of the wavelength, however, can be improved by introducing an external seed to initiate the radiation. This is done, for example, at FERMI [94].

After passing the undulator, the electron bunch is deviated and dumped to separate it from the generated x-ray pulses. These are then directed to diagnostics and the actual experiment.

4.3.2 FLASH

The free-electron laser used in parts of the experiments reported in this thesis is the free-electron laser in Hamburg (FLASH) [93]. FLASH, technically, is two FELs (FLASH1/2) that share the same accelerator but have independent undulators. An RF gun creates electron bunch trains with a repetition rate of 10 Hz. These are accelerated and compressed over three stages. The final electron bunch kinetic energy can go up to over 1 GeV. After the acceleration, a kicker system can deflect the full or parts of the bunch to either go to just one or both FELs. FLASH2 – the FEL used during the thesis – uses a variable gap undulator. As the name suggests, the distance between the two rows of magnets can be changed. This parameter affects the magnetic field strength and with that also the generated wavelength (see eqs. 4.5 and 4.6). Hence, wavelength tuning can be done via this parameter. In fixed gap undulator like FLASH1 the wavelength tuning is usually done by changing the energy of the electron bunch.

FLASH2 uses 12, 2.5 m long undulators with a period of 31.4 mm. The wavelength can go down to 4 nm (310 eV) with a spectral width below 2% full width at half maximum (FWHM) in the fundamental. The experiments conducted at FLASH used photon energies up to 270 eV. Thus, the spectral width could be expected to be below 5.5 eV. In fact, we estimated an FWHM of about 1.3% for our experiments which is ca. 3.4 eV [108]. Especially for high resolution photoelectron spectroscopy, such broad bandwidth are a disadvantage because they smear out fine structures such as spin-orbit splitting [39, 109]. In contrast to synchrotrons, FELs provide x-ray light with much higher brilliance. FLASH2 can provide pulse energies up to 1 mJ. For the experiments, however, we restricted ourselves to a couple of μJ [39, 40, 45]. The reasons for that are to avoid flooding the detector with electrons and space charge effects. The pulse duration in our experiments was estimated to 160 fs including some jitter sources [45] what meets the FLASH expectation of <200 fs.

FLASH provides several diagnostics to track beam parameters on a shot-to-shot basis. I want to mention three important ones. The pulse energy is measured at different positions with a gas-monitor detector (GMD) [110]. The idea is that small amount of rare gas is introduced into the light path. The ionization products (electrons and ions) are measured and an estimation for the pulse energy is derived (and also its position). The wavelength is measured with “online photoionization spectrometers” (OPIS) [111].

Again, a small amount of rare gas is introduced. Now, however, four electron time-of-flight spectrometers, aligned perpendicular to the beamline in an “X” shape, are used to determine the photoelectron kinetic energy. From the flight times of the four spectrometers not only the central photon energy is derived but also the beam position (again). Technically, it allows a shot-to-shot determination of the photon energy provided the signal is strong enough. In practice, however, a moving average is applied to the data over several seconds to get more stable wavelength estimations. The last important parameter is the beam arrival time monitor (BAM) [112, 113]. It measures the arrival time of the electron bunch at various stages of the accelerator with respect to a fibre laser reference that is synchronised with a master clock. As the experiments performed involved mostly two pulses, an x-ray and an UV pulse, it is important to know the relative timing between these two. The BAM allows to correct the set delays between the pulses and, thus, improves the temporal resolution [108, 113, 114].

4.3.3 Spectral Resolution in Experiments

As mentioned above, the single-shot spectrum of a SASE FEL is not a smooth curve but shows several sharp spikes above a random background. Averaging several of these spectra results in a broad spectrum that gives an average value for the wavelength at which the FEL is running [103, pp. 117-123]. However, performing electron spectroscopy with such light sources is problematic as the measured spectrum is a convolution of the SASE spectrum and the electron spectrum. This means that the measured electron spectra will show strong shot-to-shot differences and, when averaged, the spectral features from the molecule studied will be broadened significantly due to the SASE spectrum.

In figure 4.6 (a), five consecutive single-shot spectra of the sulfur 2p photoline of 2-tUra are shown. The spectra were taken at FLASH2 using the URSA-PQ apparatus. As mentioned above, FLASH2 is a SASE FEL; thus, its x-ray pulses show strong fluctuations in the photon spectrum on a shot-to-shot basis. This can be seen in the figure as no spectrum looks like the other. The peaks observed in the 2-tUra spectrum are multi-electron events and correspond to the spikes in the SASE spectrum. They are never at the same position as in the previous spectrum and, moreover, their number differs from shot to shot. However, a careful look reveals that the majority of the spikes can be found in the region between 100 and 107 eV kinetic energy. This is the range where the photoline is expected assuming an average photon energy of about 270 eV. Since the number, height and distribution of the peaks changes for every shot, the central wavelength *i.e.*, the centre of gravity of the SASE spectrum, shifts every time and with that the photoline. This is considered the spectral jitter. This jitter broadens the spectral features in addition to the average spectral width of the SASE spectrum.

The average of about 100,000 of these single-shot spectra is shown in fig. 4.6 (b) alongside a spectrum of the S 2p photoline taken at the synchrotron SOLEIL. To match the spectra, the measured kinetic energy has been converted to a binding energy using the (average) photon energy with which the molecule was probed in the respective

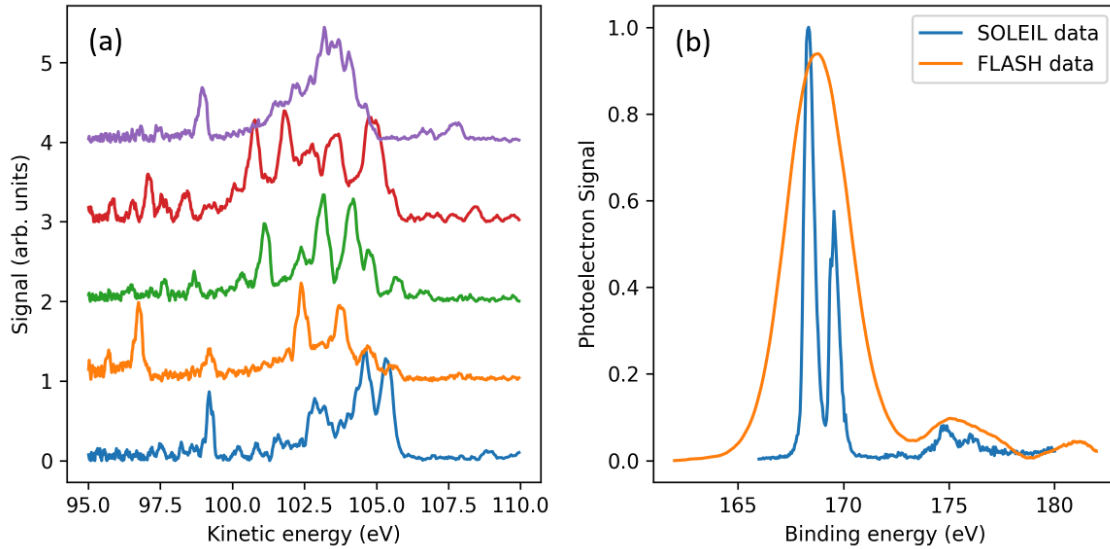


Figure 4.6: (a) Five consecutive single-shot spectra of the sulfur 2p photoline of 2-tUra measured at FLASH2. The fluctuating spikes originate from the SASE spectrum. (b) Comparison of the S 2p photoline of 2-tUra measured at SOLEIL (blue) and FLASH (orange). In the data taken at SOLEIL, the spin-orbit splitting can be observed in the photoline (*ca.* 169 eV) as well as in the satellite feature (*ca.* 175 eV) because monochromatic x-ray light was used. In the FLASH data, the broad spectrum of the x-ray pulse smears out the double peak features and only broad single peaks are observed.

experiments. One can see that both spectra line up very well. However, the synchrotron measurement clearly shows the spin-orbit splitting of the main photoline as well as of its satellite. The two lines are separated by about 1.2 eV. In the measurement at the FEL in contrast, one broad Gaussian-like feature appears accompanied by a broad satellite. The width of the feature is similar to the spectral width of the x-ray pulse used for ionisation. The position of the line lies in-between the two spin-orbit split features³.

To overcome the issues with the spectral jitter of the SASE pulses, as well as their bandwidth, it is best to measure the FEL spectra on a shot-to-shot basis. This would allow one to not only correct mean shifts between the pulses but also to correlate the shape of single-shot electron spectra with its corresponding SASE spectrum [115–117]. However, already with a shot-to-shot mean energy determination one could correct shifts between consecutive shots which would result in a (more or less) bandwidth limited spectral resolution for the electron spectra. In reference [108] (article 4), we discussed the possibilities of energy jitter correction for photoelectron spectra when no shot-to-shot information is available. The used self-referencing approach can theoretically lead to a bandwidth-limited resolution in case for static spectroscopy. For time-resolved data, however, assumptions need to be made in order to properly correct the (UV) pumped

³More precisely: The peak position of the FEL measurement matches the height-weighted average position of the two spin-orbit split peaks.

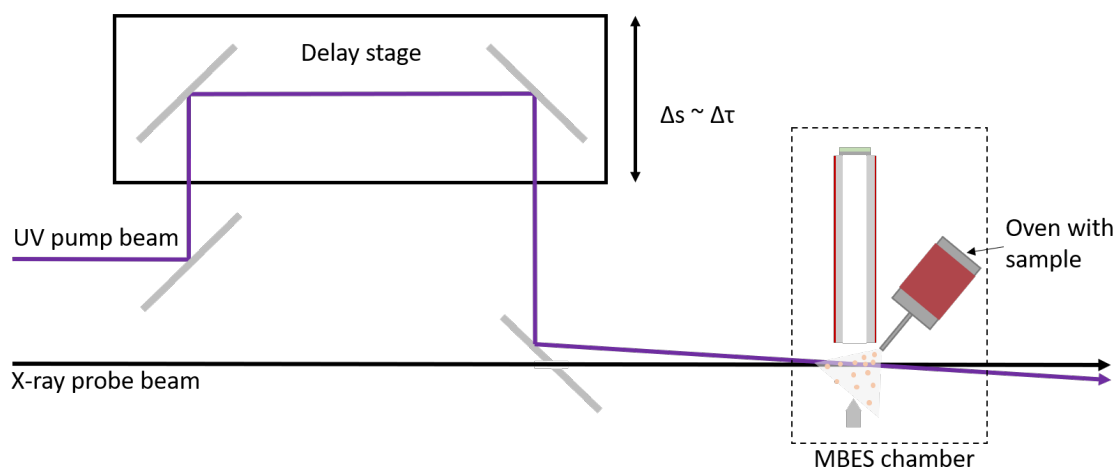


Figure 4.7: Scheme for the UV pump x-ray probe electron spectroscopy. A UV pulse passes a delay stage and crosses with the x-ray pulse in the interaction region. The emitted electrons are collected with a magnetic bottle time-of-flight spectrometer.

spectra. Due to the strong jitter of the SASE FEL, the self-referencing approach needs to rely on averages which flaws the impact on the jitter correction.

4.4 UV Pump - X-ray Probe Electron Spectroscopy

Pump-probe experiments are used to study dynamical effects in samples. In general, two coherent light pulses hit the sample: One pulse initiates the process of interest *e.g.*, a radiationless relaxation in an excited molecule. After a certain time, the second pulse probes the system and one measures an observable that is expected to change during this process. By varying the delay between the pulses, one gets time-dependent information about the observable during the process studied.

During this thesis, we performed UV pump x-ray probe electron spectroscopy on the molecule 2-tUra in the gas-phase at FLASH2. A sketch of the experiment is shown in Figure 4.7. The pump beam consisted of UV pulses with a central wavelength of 269 nm (equal to 4.6 eV photon energy) and excited the molecule 2-tUra resonantly into a $\pi\pi^*$ state. The pulse duration was measured to be 80 fs and the focus in the interaction region of the experiment was about 50 μm . The UV laser at FLASH2 runs in burst mode (as does the FEL). This means it produces pulsetrains of N pulses at a repetition rate of 10 Hz (called “bunch” for now). The repetition rate for the pulses within a bunch was chosen to be 100 kHz and the number of pulses 25. The pulse energy of the UV pulses was continuously tracked by a diode. The delay between pump and probe was set on the UV arm.

Probing was achieved with x-ray pulses at about 270 eV average photon energy that ionised electrons in the molecule down the sulfur L edge. The size of the probe in the

interaction region was measured to be about 100 μm . Similar to the UV laser, the FEL runs in burst mode delivering 50 x-ray pulses per bunch (giving 200 kHz repetition rate). This means that only every second x-ray pulse hit pre-excited molecules. The pulse energy of the x-rays was tracked by the GMD on a shot-to-shot basis and used in the analysis for normalising the spectra. Also, the beam arrival of the electron bunch with respect to the FLASH master oscillator was measured by the BAM on a shot-to-shot basis and was later used to correct the delays between pump and probe.

The sample 2-tUra was inserted via a resistively heated capillary oven (see fig. 4.7) [45, 118]. The solid sample was evaporated at a temperature of 150°C inside the oven body and the gas was introduced in the interaction region via a capillary. The electrons emitted from the molecules were collected with a magnetic bottle time-of-flight spectrometer (the URSA-PQ apparatus) [45]. Here, the time-dependent current on the phosphor anode was measured continuously over a bunch leading to 50 consecutive electron spectra for one trace. These were separated later during the (pre-)analysis. In order to correlate the measured flight times later to kinetic energies the applied voltages for retardation and on the MCPs were recorded as well. One half of the spectra within one bunch trace are pre-excited spectra, the other half are ground-state spectra. As mentioned in sec. 3.5 when we discussed the ESCS, the pre-excited spectra (PS) are a mixture of ground (GS) and excited-state spectra (ES) because only a fraction f of the molecules is excited ($PS = f \cdot ES + (1 - f) \cdot GS$). By analysing the spectra, we estimated that ca. 20 % of the molecules that were hit by the x-ray pulse had been pre-excited [40]. In order to derive the pure excited state contribution, the unpumped spectra are subtracted from pre-excited spectra resulting in difference spectra (DS) given by $DS = f \cdot (ES - GS)$. The difference spectra are then used to evaluate excited state dynamics [39, 40]. With the alternation of pumped and unpumped spectra within a bunch trace, one can reduce the negative effects from the spectral jitter and drift of the SASE FEL as it allows to track these to a certain extent with the unpumped spectra [108].

Transient electron signals are measured by varying the delay between pump and probe pulse. The transients measured in these experiments are convolutions of the actual sample signal, S_{mol} , and the instrument response function, IRF [119]:

$$S_{exp}(\Delta\tau) = \int_{-\infty}^{\infty} IRF(\Delta\tau - t) \cdot S_{mol}(t) dt . \quad (4.8)$$

The IRF is described by the cross-correlation of the pump and probe pulses. Thus, the temporal width of the pulses determines the temporal resolution achieved in the experiment. The shorter the cross-correlation *i.e.*, the shorter the pulses, the better the time-resolution and the more likely very fast processes can be observed. However, a further limit for the temporal resolution is the stability of the pump-probe delay. Variation (jitter) in the delay can originate from different effects. For the FEL experiments at FLASH, there are three different contributions: the intra-train jitter of the X-ray and UV pulses, respectively, within the macro-bunch, and the relative timing jitter of X-ray and UV laser pulses [120]. For our experiments we derived a temporal resolution of about 190 fs [45].

5 | Articles

Article 1: Experimental and theoretical gas-phase absorption spectra of thionated uracils

Dennis Mayer, David Picconi, Matthew S. Robinson, Markus Gühr
Chemical Physics 558, 111500 (2022), DOI: 10.1016/j.chemphys.2022.111500

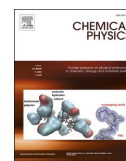
Abstract. We present a comparative study of the gas-phase UV spectra of uracil and its thionated counterparts (2-thiouracil, 4-thiouracil and 2,4-dithiouracil), closely supported by time-dependent density functional theory calculations to assign the transitions observed. We systematically discuss pure gas-phase spectra for the (thio)uracils in the range of 200–400 nm (~ 3.2 – 6.4 eV), and examine the spectra of all four species with a single theoretical approach. We note that specific vibrational modelling is needed to accurately determine the spectra across the examined wavelength range, and systematically model the transitions that appear at wavelengths shorter than 250 nm. Additionally, we find in the cases of 2-thiouracil and 2,4-dithiouracil, that the gas-phase spectra deviate significantly from some previously published solution-phase spectra, especially those collected in basic environments.

Copyright note. © 2022 Elsevier B.V. All rights reserved. The right for the reuse of the article in this dissertation is retained by the author.



Contents lists available at ScienceDirect

Chemical Physics

journal homepage: www.elsevier.com/locate/chemphys

Experimental and theoretical gas-phase absorption spectra of thionated uracils

Dennis Mayer^a, David Picconi^{a,b}, Matthew S. Robinson^{a,c,d,*}, Markus Gühr^a

^a Institut für Physik und Astronomie, Universität Potsdam, 14476 Potsdam, Germany

^b Institut für Chemie, Universität Potsdam, 14476 Potsdam, Germany

^c Center for Free-Electron Laser Science (CFEL), Deutsches Elektronen Synchrotron (DESY), Notkestraße 85, 22607 Hamburg, Germany

^d The Hamburg Centre for Ultrafast Imaging, Universität Hamburg, 22761 Hamburg, Germany

ARTICLE INFO

Keywords:

Thiouracil
Uracil
UV-VIS Spectroscopy
Excited-state calculations
TD-DFT
Gas phase

ABSTRACT

We present a comparative study of the gas-phase UV spectra of uracil and its thionated counterparts (2-thiouracil, 4-thiouracil and 2,4-dithiouracil), closely supported by time-dependent density functional theory calculations to assign the transitions observed. We systematically discuss pure gas-phase spectra for the (thio)uracils in the range of 200–400 nm (~3.2–6.4 eV), and examine the spectra of all four species with a single theoretical approach. We note that specific vibrational modelling is needed to accurately determine the spectra across the examined wavelength range, and systematically model the transitions that appear at wavelengths shorter than 250 nm. Additionally, we find in the cases of 2-thiouracil and 2,4-dithiouracil, that the gas-phase spectra deviate significantly from some previously published solution-phase spectra, especially those collected in basic environments.

1. Introduction

Nucleobases are crucial molecules for life. They encode genetic information and play an important role for cell metabolism. At the same time, nucleobases are known for their high ultraviolet (UV) absorption cross sections, which could in principle be harmful for their important functions, as UV light is energetic enough to alter the chemical bonding of nucleobases within DNA typically via the formation of nucleobase dimers [1]. This dimer formation occurs in the photoexcited states and the nucleobase typical rapid electronic relaxation into the ground state is one of the mechanisms that reduces the occurrence of UV-induced dimers.

Thionated nucleobase analogues result from substituting one or two of the nucleobases' oxygen atoms by sulfur [2]. Thionucleobases have important applications in the context of immunosuppression medication [3], as well as in photoinduced cross-linking [4]. They show two remarkable differences compared to their canonical counterparts. First, the absorption spectra are generally shifted from the UVC into the UVA region; a region that is less absorbed by the earth's atmosphere. Second, thionation causes significant changes in excited potential energy surfaces outside the Franck-Condon region, leading to a different ultrafast relaxation path compared to the canonical analogues. Photoexcited

population undergoes efficient and ultrafast internal conversion into long-lived triplet states [5–8]. These triplet states interact efficiently with the triplet oxygen ground state, which leads to the generation of reactive singlet oxygen molecules. The strong UV-induced triplet yield is thus hazardous in the context of immunosuppression medication, but might turn out to be an important benefit in terms of use in photo-activated cancer therapy [9,10]. Similar to canonical nucleobases, the thionated nucleobases produce photolesions when incorporated into nucleic acids. Among the best studied systems is 4-thiothymidine, leading to intrastrand Dewar isomers [11,12]. In addition, thionucleobases also cause interstrand photo cross-linking [13].

Experimental ultrafast studies on thionated nucleobases, together with calculations of the molecular potential energy surfaces and dynamical excited state relaxation simulations, have helped to unravel the excited state relaxation mechanisms of thionated nucleobases (see Ref. [5,6] and references therein). To date, most of the ultrafast studies have been performed on the thionated uracils, 2-thiouracil (2-tUra) [14–20], and its isomer, 4-thiouracil (4-tUra) [20,21], as well as the doubly thionated variant, 2,4-dithiouracil (2,4-dtUra) [22]. Both gas phase [14,19,21–24] as well as solution phase studies [18,20,23,25] have been performed. Our own studies were conducted with gas-phase samples of 2-tUra, using time-resolved x-ray probing for elucidating

* Corresponding author at: Center for Free-Electron Laser Science (CFEL), Deutsches Elektronen Synchrotron (DESY), Notkestraße 85, 22607 Hamburg, Germany
E-mail address: matthew.robinson@cfel.de (M.S. Robinson).

<https://doi.org/10.1016/j.chemphys.2022.111500>

Available online 9 March 2022
0301-0104/© 2022 Elsevier B.V. All rights reserved.

the molecular ultrafast relaxation [15–17,26]. In performing our studies we have noted that whilst solution-phase UV–Vis spectra for 2-tUra [18,22,27–32], 4-tUra [18,20,22,27,29–31] and 2,4-dtUra [22,27,29–31] are plentiful, we could only find few gas-phase spectra for 2-tUra in the literature [33,34], and none for 4-tUra and 2,4-dtUra (a statement that is seconded for the case of 2,4-dtUra in a recent publication by Mohamadzade and Ullrich [22]).

The absorption spectra of molecules contain important information strongly related to the molecular excited-state dynamics via the Heller autocorrelation formalism [35,36]. In addition, the combination of absorption spectroscopy with calculations of the excited-state energetics in the Franck-Condon region allows for an attribution of absorption features to particular states. Gas-phase spectra allow for a very precise comparison to calculations, as the complexities and differences in spectra resulting from the solvent can be avoided [29,37–39].

In terms of theoretical work, 2-tUra is the most extensively studied among the thionated nucleobases. The electronic structure for the gas phase in the excitation energy range below 5 eV has been investigated using density functional theory (DFT) [40], complete active space perturbation theory (CASPT2) [41], the second-order algebraic diagrammatic construction (ADC(2)) [42], as well as equations-of-motion coupled-cluster [15,17]. All the methods agree in predicting that up to five singlet excited states can contribute to the first absorption band. Among them, two are bright $\pi\pi^*$ transitions and three are dark states of $n\pi^*$ character, which may, however, borrow intensity via vibronic coupling.

4-tUra has been studied using DFT [40,43], CASPT2 [44] and ADC(2) [21] calculations, which suggest that one intense $\pi\pi^*$ transition, in the range 3.90–4.20 eV, dominates the lowest energy absorption band, and a lower lying $n\pi^*$ state, located around 2.8 eV, is essentially dark. Additional weak $\pi\pi^*$ transitions have been obtained for the wavelength range 220–260 nm.

The studies of Refs. [40], [45] and [44] compare the excitation energies of 2-tUra, 4-tUra and 2,4-dtUra using the same level of electronic structure theory (respectively DFT, multi-reference configuration interaction with singles (MR-CIS), and CASPT2) and focuses on the lowest energy absorption band. The different methods agree in predicting an increasing red-shift when going from 2-tUra, to 4-tUra and 2,4-dtUra and point out that a correct estimation of the oscillator strength is important to assess the contribution of each state to the absorption bands. However, the extent of the red-shift, the energy spacing between different electronic states, and the relative intensity varies between different approaches, making it still difficult to understand which states are accessible for a specific photon energy.

Related to this is the fact that vibrational broadening effects and transitions for wavelengths shorter than 250 nm have never been systematically addressed theoretically for thio-uracils. These are indeed the main issues that we aim at solving in this work.

We present the gas-phase UV–Vis spectra of four related systems - Uracil, 2-tUra, 4-tUra, and 2,4-dtUra in gas phase. Our spectra span the full range of 200–400 nm, which explicitly includes the region of 200–240 nm. The latter range is commonly avoided in solution-phase spectra due to absorbing solvent contamination in so-called “UV-cut-off regions” [46]. Interestingly, however, we note that this region holds important, molecule-specific features for the (thio)uracils.

In the rest of this article, we first detail the experimental and computational methods used to perform this work. This is immediately followed by the results, showing gas-phase UV–Vis spectra of the (thio)uracils, and how these compare to our theoretical models. In the discussion we delve deeper into the experimental-theoretical comparisons, whilst highlighting differences that we note in the spectra between the different (thio)uracils. Towards the end of the discussion, we make comparisons to previously obtained solution-phase spectra, and show that in some cases the solvents do indeed have a large effect on the observed spectra.

2. Methods

2.1. Experimental

Samples of Uracil (purity $\geq 99\%$) and 2-thiouracil ($\geq 99\%$) were purchased from Sigma-Aldrich, whilst 4-thiouracil ($\geq 97\%$) was purchased from Biosynth and 2,4-dithiouracil ($\geq 99\%$) from Santa Cruz Biotechnology. Each sample was used without further refinement.

UV gas-phase spectra of the (thio)uracils were recorded on a Cary 5E UV–Vis–NIR Spectrometer, using an in-house developed gas cell - a diagram of which can be seen in Fig. 1. This gas cell consists of a custom-built aluminum tube, with fixtures that allow for viewport flanges (with wedged sapphire windows) and Swagelok components to be attached. Rubber O-rings placed between the viewports and the main body of the cell allow for a vacuum seal to be achieved. A 15 L/s scroll pump was used to evacuate the cell, and a pressure of 1×10^{-1} mbar was measured on a pirani gauge between the cell and pump. Before evacuation, samples are loaded through a port on the top of the cell into a hollowed-out “sample dish” in the base of the cell. Heating tape wrapped around the outside of the cell is used to heat the system and bring the sample into the gas phase. For the experiments described, the main body of the cell was heated to 175 °C to obtain a suitable signal from the (thio)uracils, with the viewports being held at a temperature about 10° higher to prevent sample deposition on the viewport. The temperatures used here are similar to those used in other gas-phase experiments [15–17,21,22,26,47,48] and are below temperatures of degradation [34].

UV absorption scans were performed over the range of 200–400 nm, using a step size of 0.25 nm between each data point, with data being collected for 0.5 s per data point. The spectrometer was calibrated by performing scans on a number of laser-filter windows with sharp band-pass edges before any of the experiments detailed here were performed. It was found that the spectra observed for these filters all matched the manufacturer description to within 1 nm of their expected position - because of this, all experimental peak positions reported below will be given to the nearest 1 nm. In addition to this, background scans of the empty cell were also taken, with the cell heated to a similar temperature to that used in the full experimental measurements. This allowed for the temperature-dependent changes in the transmissive properties of the sapphire windows to be taken into account for the spectra of interest. As we did not determine the partial pressure of the molecules inside the cell, all absorption spectra show relative spectral absorption.

2.2. Theoretical

The ground state structures of the studied (thio)uracils were optimized using density functional theory with the CAM-B3LYP functional [49] and the Def2-TZVP basis [50]. The vibrational frequencies were computed at the same level at the optimized geometries. In agreement with previous studies [41,43,44], for all the molecules a stable planar minimum could be found.

Excited states were computed at the ground-state minima using time-dependent density functional theory (TDDFT) with the same functional and basis set. Indeed, the long-range correction used in the CAM-B3LYP functional can be expected to provide a balanced description of the excitation to high-lying orbitals, Rydberg states, as well as excited states with partial charge-transfer character [49].

A number of excited states, in particular the high-lying ones, turned out to be given as a sum of several Kohn-Sham orbital transitions, with coefficients of similar absolute value. Therefore, to characterize the electronic excited states, the natural transition orbital (NTO) decomposition of the transition density matrix was performed [51]. In this way, it was possible to identify a single dominant pair of NTOs for each transition and assign a specific character. The NTOs for all computed excited states are shown in the [supplementary material](#).

All the electronic structure calculation were performed using the

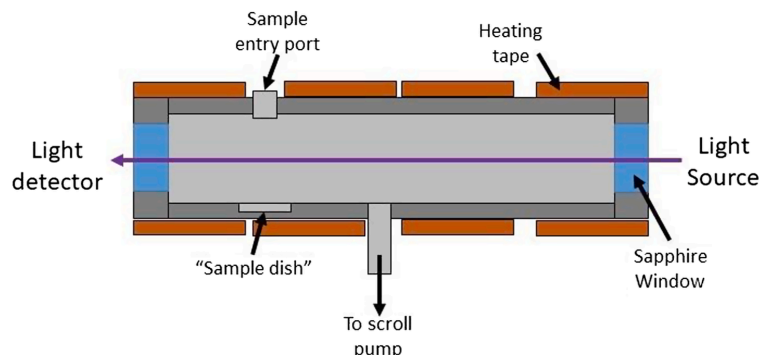


Fig. 1. Diagram showing the set-up of the heated cell used to collect the gas-phase spectra of the (thio)uracils. The cell windows are heated slightly higher than the body to minimized condensation at the windows. The cell sits inside a commercial UV–VIS absorption spectrometer.

Gaussian 16 program [52].

The vibronic band shapes of the UV spectrum were simulated by adopting the Independent Mode Displaced Harmonic Oscillator (IMDHO) approximation [53–55], whereby the ground and excited state potential energy surfaces are approximated as displaced multi-dimensional harmonic oscillators.

The main advantage of the IMDHO approximation is that the excited state potentials can be reconstructed from the evaluation of the geometrical gradient of the energy only at the Franck-Condon point (“vertical gradient” approach). In this way, one does not need to optimize and evaluate the frequencies of the excited states, which can be very cumbersome when many excited states are involved. At the same

the IMDHO Hamiltonian of the n -th excited state [53],

$$\hat{H}_n = T_{e,n} + \sum_r \left[-\frac{\hbar\omega_r}{2} \frac{\partial^2}{\partial Q_r^2} + \frac{\hbar\omega_r}{2} (Q_r - a_{rn})^2 \right]. \quad (2)$$

The quantities $T_{e,n}$ and a_{rn} are the adiabatic electronic excitation energies and the dimensionless displacements along the different normal modes Q_r with frequencies ω_r , and are reconstructed by computing the vertical energy and gradients for each electronic state. The dipole–dipole correlation function can be evaluated analytically. In the Franck-Condon (FC) approximation, i.e. neglecting the dependence of the TDMs on the coordinates ($\mu_{n\alpha} = \mu_{n\alpha,0}$), it is given by [58].

$$\begin{aligned} C_{n,FC}(t) &= \sum_{\alpha=x,y,z} \text{Tr} \left[\mu_{n\alpha,0} e^{-\frac{i}{\hbar} \hat{H}_n t} \mu_{n\alpha,0} e^{\frac{i}{\hbar} \hat{H}_0 (t+i\beta)} \right] \\ &= \left(\sum_{\alpha=x,y,z} \frac{\mu_{n\alpha,0}^2}{2} \right) \exp \left\{ -\frac{i T_{e,n}}{\hbar} t - \sum_r \frac{a_{rn}^2}{2} \left[(1 - \cos(\omega_r t)) (2 \langle n_r \rangle + 1) + i \sin(\omega_r t) \right] \right\}, \end{aligned} \quad (3)$$

time, especially if the vibronic structure is poorly resolved, the approximation allows a good interpretation of the absorption profile [56,57].

The absorption band shape is computed as the half-Fourier transform of the dipole–dipole correlation function,

$$\begin{aligned} \sigma(E) &= CE \sum_{n=1}^{N_{\text{states}}} \sum_{\alpha=x,y,z} \text{Re} \int_0^\infty C_n(t) e^{iEt} dt, \\ C_n(t) &= \text{Tr} \left[\mu_{n\alpha} e^{-\frac{i}{\hbar} \hat{H}_n t} \mu_{n\alpha} e^{\frac{i}{\hbar} \hat{H}_0 (t+i\beta)} \right], \end{aligned} \quad (1)$$

where C is a constant, E is the absorption photon energy, $\mu_{n\alpha}$ ($\alpha = x, y, z$) are the components of the transition dipole moment (TDM) functions for the excitation to the n -th excited state, $\beta = (k_B T)^{-1}$ is the inverse of the product between the temperature and the Boltzmann constant, and \hat{H}_n is

where $\langle n_r \rangle = e^{-\beta \hbar \omega_r} / (1 - e^{-\beta \hbar \omega_r})$ is the thermally averaged number of vibrational quanta for the mode Q_r .

A number of electronic states were found to have a negligible oscillator strength at the Franck-Condon point. These states can, however, borrow intensity from the bright states upon vibrational distortions from the minimum geometry. At the lowest order, the intensity borrowing is modelled using the first-order Herzberg-Teller expansion of the TDM,

$$\mu_{n\alpha} = \mu_{n\alpha,0} + \sum_r \mu_{n\alpha,r} Q_r. \quad (4)$$

Using such Franck-Condon-Herzberg-Teller (FCHT) model, the correlation function is also evaluated analytically as [59].

$$\begin{aligned}
C_{n,\text{FCHT}}(t) &= \sum_{\alpha=x,y,z} \text{Tr} \left[\mu_{n\alpha} e^{-\frac{i}{\hbar} \hat{H}_\alpha t} \mu_{n\alpha} e^{\frac{i}{\hbar} \hat{H}_\alpha (t+i\beta)} \right] \\
&= C_{n,\text{FC}}(t) \sum_{\alpha=x,y,z} \left\{ \mu_{n\alpha,0}^2 + \mu_{n\alpha,0} \sum_r a_{m,n\alpha,r} [1 - \cos(\omega_r t) + i \sin(\omega_r t) (2\langle n_r \rangle + 1)] \right. \\
&\quad \left. + \frac{1}{4} \left[\sum_r a_{m,n\alpha,r} (1 - \cos(\omega_r t) + i \sin(\omega_r t) (2\langle n_r \rangle + 1)) \right]^2 \right. \\
&\quad \left. + \frac{1}{2} \sum_r \mu_{n\alpha,r}^2 [\cos(\omega_r t) (2\langle n_r \rangle + 1) - i \sin(\omega_r t)] \right\}.
\end{aligned} \tag{5}$$

We computed the lowest 12, 12, 12 and 16 excitation energies for Ura, 2-tUra, 4-tUra and 2,4-dtUra, respectively. The FC and FCHT simulations of the absorption spectrum were performed including 10 electronic states for Ura, 2-tUra and 4-tUra, and 12 states for 2,4-dtUra. This was found to be sufficient to cover 200–400 nm range.

The energy-dependent absorption spectrum of Eq. (1) is converted to the wavelength scale as.

$$\begin{aligned}
\bar{\sigma}(\lambda) &= \sigma \left(\frac{2\pi\hbar c}{\lambda} \right) \left| \frac{dE}{d\lambda} \right| \\
&= \sigma \left(\frac{2\pi\hbar c}{\lambda} \right) \frac{2\pi\hbar c}{\lambda^2}.
\end{aligned} \tag{6}$$

The computation of the absorption profile was performed with a self-developed Python script, which reads the gradients of the excited states at the Franck-Condon point directly from the Gaussian 16 output. Denoting as g_n the vertical gradient of the n -th excited state along the mode Q_r , the dimensionless displacement is obtained as $a_m = -g_m / (\hbar\omega_r)$.

3. Results

Fig. 2 shows the background-corrected experimental gas-phase absorption spectra of the (thio)uracils. Uracil (red) shows a strong absorption at 245 nm. The start of an additional absorption band for wavelengths below 200 nm is also observed. Small modulations in the baseline of the uracil spectrum in the region between 300 and 400 nm are ignored, as will be discussed below.

The absorption spectrum of 2-tUra (blue) shows a broad absorption band between 250 and 310 nm, with a peak around 270 nm and a shoulder around 285 nm. A fit using a sum of Gaussian functions within this band reveals that these features are due to two contributions at 261 nm and 286 nm (see SI). Another strong absorption line can be observed at 204 nm and a smaller shoulder at 226 nm.

The absorption spectrum of 4-tUra (green) shows a strong broad maximum, centered at 312 nm. The band around 235 nm can be described by 4 Gaussians, of which one at 244 nm and another one at 223 nm contribute most. The start of another strong absorption can be observed for wavelengths around 200 nm.

The 2,4-dtUra (orange) shows a broad band between 250 and 360 nm. This band consists of a major peak at around 280 nm and a shoulder-like feature at about 325 nm. Three Gaussians are able to describe this

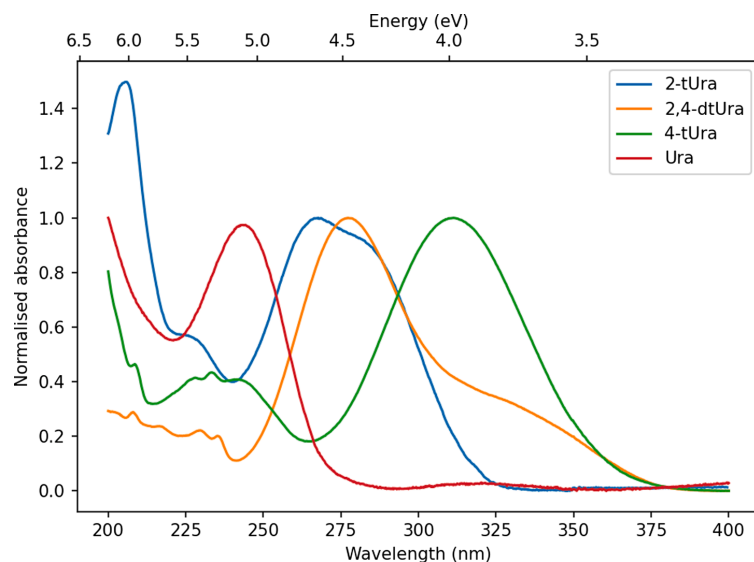


Fig. 2. Gas-phase absorption spectra for 2-thiouracil (blue), 4-thiouracil (green), 2,4-dithiouracil (orange), and uracil (red). Spectra have been normalised with respect to the major peaks that appear within the 225–400 nm range.

Table 1

Vertical excitation energies T_v , oscillator strength f and character of the lowest 10 singlet excited states of uracil, calculated using TDDFT/CAM-B3LYP/Def2-TZVP.

State	T_v [eV]	f	Character
S ₁	5.13	0.000	$n_8\pi_8^*$
S ₂	5.52	0.179	$\pi_{-}\pi_{+}^*$
S ₃	6.43	0.000	$\pi_7\pi_7^*$
S ₄	6.67	0.039	$\pi_{+}\pi_{+}^*$
S ₅	6.85	0.000	$\pi_{-}3s$
S ₆	7.05	0.156	$\pi_{-}\pi_{-}^*$
S ₇	7.20	0.001	$\pi_7\pi_8^*$
S ₈	7.43	0.000	$\pi_{+}\pi_{-}^*$
S ₉	7.93	0.365	$\pi_{+}\pi_{-}^*$
S ₁₀	8.00	0.000	$\pi_{-}3p$

Table 2

Vertical excitation energies T_v , oscillator strength f and character of the lowest 10 singlet excited states of 2-thiouracil, calculated using TDDFT/CAM-B3LYP/Def2-TZVP.

State	T_v [eV]	f	Character
S ₁	3.91	0.000	$\pi_7\pi_7^*$
S ₂	4.76	0.195	$\pi_7\pi_{+}^*$
S ₃	5.00	0.000	$\pi_{-}\pi_8^*$
S ₄	5.25	0.222	$\pi_7\pi_{-}^*$
S ₅	5.53	0.000	$\pi_{-}\pi_8^*$
S ₆	5.84	0.024	$\pi_{+}\pi_{+}^*$
S ₇	6.21	0.003	π_73s
S ₈	6.38	0.001	$\pi_8\pi_7^*$
S ₉	6.40	0.022	$\pi_73s\sigma^*$
S ₁₀	6.68	0.306	$\pi_{+}\pi_{-}^*$

band, the centres of which are located at 275 nm, 306 nm and 343 nm. In contrast to the three previous molecules, there is no strong absorption around 200 nm but only a slight gradual increase from 240 nm on to smaller wavelengths.

The assignment of the observed bands to the different electronic states of the uracils is facilitated by the vibronic spectral calculations based on TDDFT data. The computed vertical excitation energies for the four molecules under investigation are given in Tables 1–4, which also report the oscillator strength and the electronic character of the transition.

The dominant NTOs associated with each transition are illustrated in the [supplementary information](#) and have a n , π , π^* or Rydberg character. To allow a comparison between the transitions of different molecules, we adopted the same atom numbering and a common nomenclature for the orbitals. n and π orbital with a large lobe near the O and S atoms in position 7 and 8 are denoted π_7 , n_8 , π_7 and π_8 . For some transitions the occupied NTOs are delocalized over both positions 7 and 8, as a consequence of the multi-reference character of the excited state, and are approximately given as linear combinations $\pi_{\pm} \approx (\pi_7 \pm n_8)/\sqrt{2}$ and $\pi_{\pm} \approx (\pi_7 \pm \pi_8)/\sqrt{2}$. The dominant virtual NTOs are π^* orbitals for most transitions, having antibonding character along one of the C–O or C–S bonds (π_7^* , π_8^*) or both (π_{\pm}^*). For Rydberg-type excitations, the virtual orbitals have a shape similar to diffuse 3 s or 3p orbitals.

The lowest-excited states of the (thio)uracils have $n\pi^*$ or $\pi\pi^*$ character, and are respectively dark and bright. At higher excitation energies, but within the spectral range of the experiment, TDDFT predicts also Rydberg-type excitations, where virtual 3 s orbital usually has antibonding character along the N₁–H₉ bond.

The absorption profiles computed by Eqs. (1), (5) and (6) are shown in Fig. 3. In order to align the computed spectra to the experimental ones, they had to be red-shifted by 0.5 eV. The CAM-B3LYP functional provides a very accurate prediction of the global spectral shape in the whole 200–400 nm range, and captures precisely the relative positions of the different bands both for the same molecule, and among different molecules. Therefore, we are convinced that the present computations

Table 3

Vertical excitation energies T_v , oscillator strength f and character of the lowest 10 singlet excited states of 4-thiouracil, calculated using TDDFT/CAM-B3LYP/Def2-TZVP.

State	T_v [eV]	f	Character
S ₁	3.07	0.000	$n_8\pi_8^*$
S ₂	4.49	0.381	$\pi_8\pi_8^*$
S ₃	5.34	0.011	$\pi_{-}\pi_8^*$
S ₄	5.69	0.000	$\pi_{-}\pi_{-}^*$
S ₅	5.77	0.057	$\pi_8\pi_{-}^*$
S ₆	6.32	0.002	$\pi_7\pi_8^*$
S ₇	6.46	0.000	$\pi_{-}3s$
S ₈	6.55	0.000	$\pi_7\pi_{-}^*$
S ₉	6.71	0.027	π_83s
S ₁₀	7.21	0.369	$\pi_{+}\pi_{-}^*$

Table 4

Vertical excitation energies T_v , oscillator strength and character of the lowest 12 singlet excited states of 2,4-dithiouracil, calculated using TDDFT/CAM-B3LYP/Def2-TZVP.

State	T_v [eV]	f	Character
S ₁	3.04	0.000	$n_8\pi_8^*$
S ₂	3.86	0.000	$\pi_7\pi_7^*$
S ₃	4.19	0.121	$\pi_{-}\pi_{+}^*$
S ₄	4.57	0.235	$\pi_{+}\pi_8^*$
S ₅	4.69	0.000	$\pi_7\pi_8^*$
S ₆	4.94	0.140	$\pi_{-}\pi_{-}^*$
S ₇	4.94	0.001	$\pi_8\pi_7^*$
S ₈	5.07	0.361	$\pi_{+}\pi_7^*$
S ₉	6.17	0.002	$\pi_{-}3s$
S ₁₀	6.40	0.046	$\pi_{-}3s$
S ₁₁	6.69	0.003	$\pi_{+}3s$
S ₁₂	6.76	0.043	$\pi_{+}3s$

allow a reliable assignment of the experimentally observed bands.

4. Discussion

4.1. Comparison of experimental and theoretical results

The major observation in the absorption spectra in Fig. 2 is the (already well-established) redshift of the lower-energy absorption band due to substituting oxygen with sulfur in each of the thiouracils. Whilst Ura shows its lowest energy absorption maximum around 245 nm, the substitution of the O at the C₂ atom for 2-tUra shifts this band towards 270 nm. In the case of 4-tUra the shift is much stronger and the lowest energy maximum is located at around 310 nm. The substitution of both O atoms in the case of 2,4-dtUra creates a broad band ranging from about 250 to 350 nm, with a major peak at around 275 nm. It overlaps with the first absorption band of 2-tUra suggesting that the part of the band may show contribution from S located at the C₂ atom. The shoulder at around 320 nm overlaps with the spectrum of 4-tUra, which suggests that this part of the absorption band may show significant contributions from S at the C₄ atom.

The oxygen-containing (thio)uracils (i.e. Ura, 2-tUra and 4-tUra) show a strong absorption peak at around 200 nm. In the case of 2,4-dtUra, containing no oxygen atoms, only a weak absorption is observed in this higher-photon energy range. Intuitively, from the experimental spectra alone, one can determine that this absorption in the deep UV region is likely due to the presence of the oxygen atom on the system. This hypothesis is confirmed below in an analysis of the DFT calculations and the orbitals involved in the transitions in this spectral region.

For Ura, Fig. 3(a) shows that the lowest energy absorption band, peaking around 250 nm, is due to the S₂ ($\pi_{-}\pi_{+}^*$) state and the incipient band at 200 nm can be attributed to a mixture of S₅, S₆ and, to a lesser

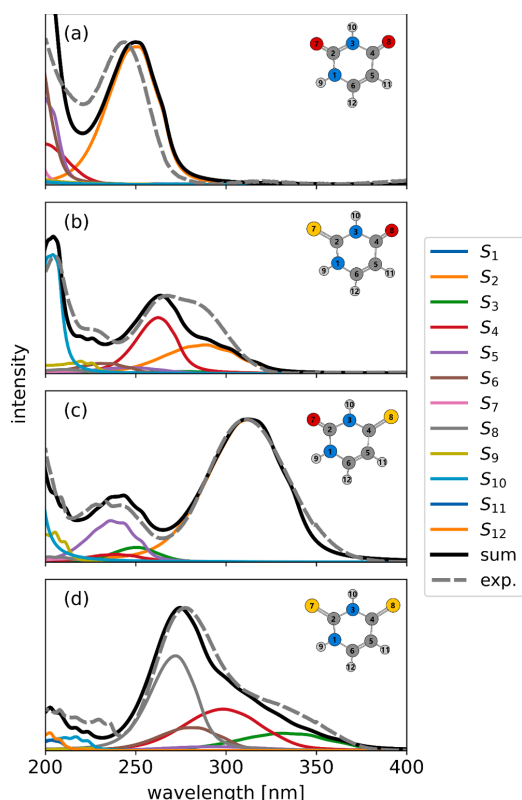


Fig. 3. Comparison between the theoretical (black line) and the experimental (gray, dashed line) absorption spectrum of (a) uracil; (b) 2-thiouracil; (c) 4-thiouracil; (d) 2,4-dithiouracil. For each molecule the contributions of the individual adiabatic electronic states are shown separately with different colors, the nomenclature follows Tables 1–4. The experimental and theoretical spectra are both normalized to the maximum of the lowest energy absorption band. The molecules and atom numbering are shown in the inset (hydrogen: light gray, carbon: dark gray, nitrogen: blue, oxygen: red, sulfur: yellow). The theoretical spectra have been red-shifted by 0.5 eV.

extent, S_4 . In particular, as shown in the SI, the state S_4 originates from a transition out of a π orbital with significant components on the O atoms (π_{+}). The comparison with the FC calculation, given in the SI, shows that the intensity of the S_5 band is due to the Herzberg-Teller mechanism and is slightly overestimated by the CAM-B3LYP functional.

The calculated spectrum for 2-tUra, shown in Fig. 3(b), attributes the lowest energy absorption band to two transitions, to the states S_2 and S_4 , and therefore shows parallels to the double Gaussian fit of the experimental data seen in SI. The discrepancy between theory and experiment suggest that the CAM-B3LYP calculation might underestimate the oscillator strength for the $S_2 \leftarrow S_0$ transition. Indeed, excited state calculations based on wavefunction methods show that the relative intensities of these $\pi\pi^*$ transitions are highly sensitive to the level of electronic structure theory [41]. Additional tests, reported in the supplementary information, show that the intensity pattern also depends on the basis set and the band shape. Interestingly, the agreement with the lowest energy band of the experiment improves when a simple Gaussian envelope is used instead of the FCHT band shape, suggesting that the harmonic model might be not fully adequate for this transition.

As shown in the SI, the π_7 orbital is the same for the S_2 and S_4

transitions and has a large lobe on the S atom; in contrast, the π^* orbitals (π_{+}^* and π_{-}^*) have significant electron density on the ring. Therefore, the partial positive charge on the S atom increases upon photoexcitation to the lowest energy band, as observed in recent x-ray photoelectron studies [17]. The weak band around 220–230 nm is attributed to the states S_6 ($\pi\pi^*$) and S_9 (n -Rydberg), which gain intensity via the Herzberg-Teller mechanism. The band at 204 nm is due to the state S_{10} ($\pi_{+}\pi_{-}^*$), which involves transitions between orbitals with a significant component on the O atom, as previously intuitively hypothesised.

4-tUra is, among the studied (thio)uracils, the one with the absorption maximum peaking at the longest wavelengths. The calculations of Fig. 3(c) show that the main band around 310 nm is due to the S_2 ($\pi\pi^*$) transition. The smaller band observed at 235 nm is mostly due to the S_5 ($\pi\pi^*$) state, where the occupied π_8 orbital is the same as for S_2 (see the SI) and has a large lobe on the C=S bond. The third band, which has higher intensity and starts emerging around 210 nm, is attributed to the states S_9 ($n3s$) and S_{10} ($\pi\pi^*$). The simulation also reproduces nicely the relative intensities of the three bands, as well as the vibrational structure due to vibronic transitions to the states S_5 and S_9 . The analysis of the NTOs shows that the π_{+} orbital, occupied in the $S_{10} \leftarrow S_0$ transition, has a strong contribution on the O atom. This confirms that the intense bands around 200 nm observed in the spectra of Ura, 2-tUra and 4-tUra are due to transitions involving orbitals partially localized on the O atoms.

In 2,4-dtUra, where both oxygen atoms are replaced by sulfur, the “oxygen band” disappears and additional $\pi\pi^*$ bands overlap the transitions in the 250–350 nm region. Indeed, the theoretical analysis of Fig. 3(d) shows that the main absorption band of 2,4-dtUra is composed of four $\pi\pi^*$ transitions, to the states S_3 , S_4 , S_6 , S_8 . The occupied NTOs for these transitions all have a large component on one or both the two S atoms.

For this case, however, an approximation was necessary to reliably simulate the spectrum. As reported in Table 4, the states S_6 and S_7 are nearly degenerate at the Franck-Condon point and, as a consequence, the geometrical derivatives of the respective transition dipole moments diverge [60]. In this case, a more adequate treatment should rely on a vibronic coupling model, based on diabatic electronic states which depend minimally on the nuclear distortions and a potential term to account for the inter-state coupling [61]. However, this would require high-dimensional multi-state quantum dynamical simulations which are much more complex than the analytical approach used here, and beyond the purpose of this work. Indeed, since the FC spectrum already describes the experimental bands quite well, the non-Condon effects for the states S_6 and S_7 are expected to be minor (as for the other thionucleobases) and, therefore, they are simply neglected, i.e. the FC approximation is always used for the bands of S_6 and S_7 .

At wavelengths below 245 nm a broad absorption builds up in the 2,4-dtUra spectrum. In this region rather pronounced vibronic structures are visible. These features are reproduced by the simulations, which attribute the intensity to transitions to S_{10} ($n3s$), S_{12} ($n3s$) and, to a lower extent and due to Herzberg-Teller, S_{11} ($\pi3s$).

4.2. Comparison to previously-published spectra

Unfortunately, gas-phase spectra of (thio)uracils seem to be quite rare. Clark et al. [62] measured the gas-phase spectrum of uracil at temperatures of 166 °C and 228 °C. In agreement with our spectra, they also observe a first absorption band at about 245 nm. In addition, they observe a peak at about 190 nm and a shoulder at 205 nm for a temperature of 166 °C. No data is presented for the 300–400 nm range.

To our knowledge, only two groups have measured gas-phase spectra of 2-tUra so far [33,34]. Despite the fact that these experiments were performed at temperatures of 267 °C and 277 °C, respectively, these spectra are almost identical to the spectrum we present here. This suggests that little change is observed in 2-thiouracil absorption despite the elevated temperatures. This implicitly adds further reassurance that other experiments performed at temperatures above those used here

[19,23,24] are unlikely to have been affected by decomposition effects.

Due to the scarcity of previously published gas-phase data, in the remainder of this section, we will make comparisons to previously published solution-phase spectra of the (thio)uracils.

Most of the reported spectra of uracil in solution show reasonable agreement with those in gas-phase. For neutral and acidic solutions only a red-shift of the first absorption band is observed [20,30,63]. A basic solution seems to not only lead to a strong red shift but also (asymmetrically) broadens the first absorption band [63]. Experiments that cover the range between 300 and 400 nm do not show any signal above background [20,30]. We therefore believe that the subtle changes observed in the baseline in our measurements between 300 and 400 nm result from small changes in the cell background between the measurement performed with and without sample. To test this, we repeated the uracil measurements several times, and found that whilst the noisy, small bumps in the 300–400 nm range varied in position and intensity with respect to the main peak at 245 nm between each run, the 245 nm peak remained constant throughout (i.e. same peak position and width). We therefore attribute these fluctuations in the 300–400 nm region to background noise. Such fluctuations do not affect the absorbance from 2,4-dtUra and 4-tUra, as the absorbance was at least one order of magnitude higher in the non-normalized spectra compared to uracil. Only for wavelength greater than 320 nm in 2-tUra, such a background could play a role.

For 4-tUra, we also find that the solution-based spectra show similar features as the gas-phase spectrum presented here. The biggest difference between the two phases is the position of the major peak, which appears at 312 nm in the gas phase, but is red-shifted by 20–50 nm once in solution, depending on the solution used [20,22,29,30]. Whilst the 4-tUra peak position appears to be solution dependent, it does not, however, appear to be pH dependent [27]. In making comparisons to the work of Zou et al, we see that the smaller gas-phase peak observed here at around 230 nm also appears in the same place for solution, along with the rise in signal as the wavelength tends to 200 nm [20]. It therefore appears in first instances that these higher-energy transitions are less affected by the solvent (explicitly for the cases of water and acetonitrile solvents).

Comparisons for 2-tUra and 2,4-dtUra between the gas-phase and solution phase spectra, however, are more complex than that seen for 4-tUra. A full analysis of how environmental features affect the spectra of the (thio)uracils is outside of the scope of our gas-phase studies. However, some of these differences have not been explicitly mentioned in past studies. We will start with comparisons to experiments that show spectra matching our gas-phase best, before progressively moving to spectra that show more extreme variations.

In the first instance, a large number of acidic nature solution studies (i.e. $\text{pH} < 7$), or those performed in ethanol and methanol, do show similar spectra to those seen here for 2-tUra and 2,4-dtUra in the gas phase. More explicitly: a peak at ~ 275 nm and a shoulder at ~ 285 nm is seen for 2-tUra [27,28,31,32] whilst for 2,4-dtUra a peak is observed at ~ 275 nm with a shoulder at ~ 330 nm [27]. However, as the pH approaches neutral, and then leading on to basic conditions (i.e. $\text{pH} \geq 7$), changes in the spectra of both molecules start to appear. In the case of 2-tUra, two distinct peaks start to appear [27–29], rather than the singular peak with a shoulder seen in the gas-phase and acidic-solution studies. In the case of 2,4-dtUra, when comparing the gas-phase spectrum to those spectra obtained in basic solvents, we note that the main peak at 275 nm remains relatively fixed whilst the shoulder previously at 330 nm is red shifted by up to 70 nm [27,30].

The most interesting comparison to the gas-phase spectra seen here is to the solution-phase work of Mohamadzade et al. [22], as this is one of the few studies in the literature to examine the solution-phase spectra of all three thiouracils simultaneously under the similar conditions. They noted that no gas-phase spectrum of 2,4-dtUra could be found in the literature, and hence the solvent used in their studies was CCl_4 , as it was “a non-polar solvent, [and] can be considered a good approximation of a

gas-phase environment.” In general, we see good agreement between our gas-phase spectra and their solution-phase spectra for 4-tUra and 2,4-dtUra (ignoring peak shifts of a few nm). The 2-tUra spectrum in CCl_4 however, appears to have more in common with the previously discussed basic-solution spectra than what is observed in the gas phase (i.e. peak-splitting is observed). Comparing this spectrum taken by Mohamadzade et al. in CCl_4 further to the spectra measured by Moustafa et al., we find that it has more in common with the spectrum collected in the polar ethanol solution, rather than the spectrum collected in the non-polar 1,2-dichloroethane solution [64]. This suggests that these peak shifts cannot simply be attributed to solvent polarity.

Recent photodissociation spectroscopy studies on iodide ion-thiouracil clusters in the gas phase by Uleanya et al. [29], show results that could be related to this “peak-splitting feature” of 2-tUra. In their work, Uleanya et al. were able to match well the gas-phase photodepletion spectra of Γ -2,4-dtUra and Γ -4-tUra to the aqueous spectra of their respective counterparts, but observed discrepancies between the Γ -2-tUra photodepletion spectrum and the aqueous 2-tUra spectrum (as explicitly noted by Uleanya et al. calling it the “odd-man out”). We compare the Γ -2-tUra photodepletion spectrum collected by Uleanya et al. to the CCl_4 spectra of Mohamadzade et al.. We note similarities between these two, as both show a major peak at ~ 300 nm before a secondary increase in signal as one tends to 270 nm. In contrast, the aqueous spectrum of Uleanya et al., as well as the gas-phase spectrum presented here, has less similarities with the Γ -2-tUra photodepletion spectrum. Therefore, in first instances, it appears that the Γ ion may have a similar effect on the absorption spectra of 2-tUra as the CCl_4 environment.

The only commonality that we can note between the cases involving CCl_4 , 1,2-dichloroethane, acetonitrile, and Γ , where peak splitting of 2-tUra is observed, is the abundant presence of “classic” lone pairs of electrons on each of the systems. Speculatively, it is possible that these solvents/anions are acting in the same fashion as a Lewis base, and are able to share their electrons with 2-tUra, which in turn may affect the observed absorption spectra. Further spectra, as well as simulations, would be needed to understand this better, and in particular, why the 2-tUra presents such a pronounced case.

5. Conclusion

We have presented the collective gas-phase spectra of uracil and its thionated analogues, 2-thiouracil, 4-thiouracil and 2,4-dithiouracil, and accompanied this with a complete theoretical analysis and assignment of the observed transitions in the region of 200–400 nm. Alongside this we have made comparisons of the recorded gas-phase spectra, to those collected in solution in past works. In this we highlight that the (thio)uracils with a sulfur atom on the 2-position of the basic uracil structure (like 2-thiouracil or 2,4-thiouracil) are more sensitive to shifts in the spectrum when in basic conditions. (4)-thiouracil does not appear to be affected by these environmental effects as much.

CRedit authorship contribution statement

Dennis Mayer: Data Curation, Formal analysis, Investigation, Validation, Writing - original draft, Writing - review & editing. **David Picconi:** Data Curation, Formal analysis, Investigation, Methodology, Software, Visualisation, Writing - original draft, Writing - review & editing. **Matthew S. Robinson:** Data curation, Formal analysis, Investigation, Validation, Writing - original draft, Writing - review & editing. **Markus Gühr:** Formal analysis, Funding acquisition, Project administration, Supervision, Validation, Writing - original draft, Writing - review & editing.

Declaration of Competing Interest

The authors declare the following financial interests/personal

D. Mayer et al.

Chemical Physics 558 (2022) 111500

relationships which may be considered as potential competing interests: Markus Guehr reports financial support was provided by Volkswagen Foundation. Markus Guehr reports financial support was provided by German Research Foundation. These funding sources had no input on the research presented here.

Acknowledgements

This paper is dedicated to Peter Saalfrank on the occasion of his 60th birthday. We thank the Volkswagen foundation for funding via a Lichtenberg Professorship. We acknowledge DFG funding via the Grant GU 1478/1-1.

Appendix A. Supplementary material

Supplementary data to this article can be found online at <https://doi.org/10.1016/j.chemphys.2022.111500>. In this supplementary data we reference methods discussed in Ref. [65]

References

- A.C. Kneutinger, G. Kashiwazaki, S. Prill, K. Heil, M. Müller, T. Carell, Formation and Direct Repair of UV-induced Dimeric DNA Pyrimidine Lesions, *Photochem. Photobiol.* 90 (1) (2014) 1–14.
- T. Carell, C. Brandmayr, A. Hienzsch, M. Müller, D. Pearson, V. Reiter, I. Thoma, P. Thumbs, M. Wagner, Structure and Function of Noncanonical Nucleobases, *Angew. Chemie Int. Ed.* 51 (29) (2012) 7110–7131.
- P.F. Swann, T.R. Waters, D.C. Moulton, Y.-Z. Xu, Q. Zheng, M. Edwards, R. Mace, Role of Postreplicative DNA Mismatch Repair in the Cytotoxic Action of Thioguanine, *Science* 273 (5278) (1996) 1109–1111.
- K. Kramer, T. Sachsenberg, B.M. Beckmann, S. Qamar, K.-L. Boon, M.W. Hentze, O. Kohlbacher, H. Urlaub, Photo-cross-linking and high-resolution mass spectrometry for assignment of RNA-binding sites in RNA-binding proteins, *Nat. Methods* 11 (10) (2014) 1064–1070.
- S. Arslançan, L. Martínez-Fernández, I. Corral, Photophysics and photochemistry of canonical nucleobases' thioanalogs: From quantum mechanical studies to time resolved experiments, *Molecules* 22 (6) (2017) 998.
- B. Ashwood, M. Pollum, C.E. Crespo-Hernández, Photochemical and Photodynamical Properties of Sulfur-Substituted Nucleic Acid Bases, *Photochem. Photobiol.* 95 (1) (2019) 33–58.
- S. Bai, M. Barbatti, On the decay of the triplet state of thionucleobases, *Phys. Chem. Chem. Phys.* 19 (20) (2017) 12674–12682.
- M. Pollum, L. Martínez-Fernández, C.E. Crespo-Hernández, Photochemistry of Nucleic Acid Bases and Their Thio- and Aza-Analogues in Solution, in: M. Barbatti, A.C. Borin, S. Ulbrich (Eds.), *Phenomena in Nucleic Acids*, Springer Cham, 2014, p. 245.
- O. Reelfs, P. Karran, A.R. Young, 4-thiothymidine sensitization of DNA to UVA offers potential for a novel photochemotherapy, *Photochem. Photobiol. Sci.* 11 (1) (2012) 148–154.
- M. Pollum, S. Jockusch, C.E. Crespo-Hernández, 2,4-Dithiothymine as a Potent UVA Chemotherapeutic Agent, *J. Am. Chem. Soc.* 136 (52) (2014) 17930–17933.
- L.A. Ortiz-Rodríguez, C.E. Crespo-Hernández, Thionated organic compounds as emerging heavy-atom-free photodynamic therapy agents, *Chem. Sci.* 11 (41) (2020) 11113–11123.
- L.A. Ortiz-Rodríguez, C. Reichardt, S.J. Hoehn, S. Jockusch, C.E. Crespo-Hernández, Detection of the thietane precursor in the UVA formation of the DNA 6–4 photoadduct, *Nat. Commun.* 11 (2020) 3599.
- R. Brem, I. Daehn, P. Karran, Efficient DNA interstrand crosslinking by 6-thioguanine and UVA radiation, *DNA Repair (Amst)*. 10 (8) (2011) 869–876.
- O. Ghafur, S.W. Crane, M. Ryszka, J. Bockova, A. Rebelo, L. Saalbach, S. De Camillis, J.B. Greenwood, S. Eden, D. Townsend, Ultraviolet relaxation dynamics in uracil: Time-resolved photoion yield studies using a laser-based thermal desorption source, *J. Chem. Phys.* 149 (3) (2018) 034301.
- F. Lever, D. Mayer, D. Picconi, J. Metje, S. Alisauskas, F. Calegari, S. Düsterer, C. Ehlert, R. Feifel, M. Niebuhr, B. Manschwetus, M. Kuhlmann, T. Mazza, M. S. Robinson, R.J. Squibb, A. Trabattoni, M. Wallner, P. Saalfrank, T.J.A. Wolf, M. Gühr, Ultrafast dynamics of 2-thiouracil investigated by time-resolved Auger spectroscopy, *J. Phys. B At. Mol. Opt. Phys.* 54 (1) (2020) 014002.
- F. Lever, D. Mayer, J. Metje, S. Alisauskas, F. Calegari, S. Düsterer, R. Feifel, M. Niebuhr, B. Manschwetus, M. Kuhlmann, T. Mazza, M.S. Robinson, R.J. Squibb, A. Trabattoni, M. Wallner, T.J.A. Wolf, M. Gühr, Core-Level Spectroscopy of 2-Thiouracil at the Sulfur L₁- and L_{2,3}-Edges Utilizing a SASE Free-Electron Laser, *Molecules* 26 (21) (2021) 6469, <https://doi.org/10.3390/molecules26216469>.
- D. Mayer, F. Lever, D. Picconi, J. Metje, S. Alisauskas, F. Calegari, S. Düsterer, C. Ehlert, R. Feifel, M. Niebuhr, B. Manschwetus, M. Kuhlmann, T. Mazza, M. S. Robinson, R.J. Squibb, A. Trabattoni, M. Wallner, P. Saalfrank, T.J.A. Wolf, M. Gühr, Following excited-state chemical shifts in molecular ultrafast x-ray photoelectron spectroscopy, *Nat. Commun.* 13 (1) (2022) 198, <https://doi.org/10.1038/s41467-021-27908-y>.
- D. Koyama, M.J. Milner, A.J. Orr-Ewing, Evidence for a Double Well in the First Triplet Excited State of 2-Thiouracil, *J. Phys. Chem. B* 121 (39) (2017) 9274–9280.
- S. Mai, A. Mohamadzade, P. Marquetand, L. González, S. Ulbrich, Simulated and experimental time-resolved photoelectron spectra of the intersystem crossing dynamics in 2-thiouracil, *Molecules* 23 (11) (2018) 2836.
- X. Zou, X. Dai, K. Liu, H. Zhao, D.I. Song, H. Su, Photophysical and Photochemical Properties of 4-Thiouracil: Time-Resolved IR Spectroscopy and DFT Studies, *J. Phys. Chem. B* 118 (22) (2014) 5864–5872.
- A. Mohamadzade, S. Bai, M. Barbatti, S. Ulbrich, Intersystem crossing dynamics in singly substituted thiouracil studied by time-resolved photoelectron spectroscopy: Micro-environmental effects due to sulfur position, *Chem. Phys.* 515 (2018) 572–579.
- A. Mohamadzade, S. Ulbrich, Internal conversion and intersystem crossing dynamics of uracil upon double thionation: a time-resolved photoelectron spectroscopy study in the gas phase, *Phys. Chem. Chem. Phys.* 22 (27) (2020) 15608–15615.
- J.A. Sánchez-Rodríguez, A. Mohamadzade, S. Mai, B. Ashwood, M. Pollum, P. Marquetand, L. González, C.E. Crespo-Hernández, S. Ulbrich, 2-Thiouracil intersystem crossing photodynamics studied by wavelength-dependent photoelectron and transient absorption spectroscopies, *Phys. Chem. Chem. Phys.* 19 (30) (2017) 19756–19766.
- H. Yu, J.A. Sanchez-Rodríguez, M. Pollum, C.E. Crespo-Hernández, S. Mai, P. Marquetand, L. González, S. Ulbrich, Internal conversion and intersystem crossing pathways in UV excited, isolated uracils and their implications in prebiotic chemistry, *Phys. Chem. Chem. Phys.* 18 (30) (2016) 20168–20176.
- M. Pollum, C.E. Crespo-Hernández, Communication: The dark singlet state as a doorway state in the ultrafast and efficient intersystem crossing dynamics in 2-thiothymine and 2-thiouracil, *J. Chem. Phys.* 140 (7) (2014) 071101.
- J. Metje, F. Lever, D. Mayer, R.J. Squibb, M.S. Robinson, M. Niebuhr, R. Feifel, S. Düsterer, M. Gühr, URSA-PQ: A Mobile and Flexible Pump-Probe Instrument for Gas Phase Samples at the FLASH Free Electron Laser, *Appl. Sci.* 10 (2020) 7882.
- G.B. Elion, W.S. Ide, G.H. Hitchings, The Ultraviolet Absorption Spectra of Thiouracils I, *J. Am. Chem. Soc.* 68 (11) (1946) 2137–2140.
- W.H. Miller, R.O. Roblin, E.B. Astwood, Studies in Chemotherapy. XI. Oxidation of 2-Thiouracil and Related Compounds by Iodine, *J. Am. Chem. Soc.* 67 (12) (1945) 2201–2204.
- K.O. Uleanya, C.E.H. Dessent, Investigating the mapping of chromophore excitations onto the electron detachment spectrum: photodissociation spectroscopy of iodide ion–thiouracil clusters, *Phys. Chem. Chem. Phys.* 23 (2) (2021) 1021–1030.
- M. Pollum, S. Jockusch, C.E. Crespo-Hernández, Increase in the photoreactivity of uracil derivatives by doubling thionation, *Phys. Chem. Phys.* 17 (41) (2015) 27851–27861.
- N. Igarashi-Yamamoto, A. Tajiri, M. Hatano, S. Shibuya, T. Ueda, Ultraviolet absorption, circular dichroism and magnetic circular dichroism studies of sulfur-containing nucleic acid bases and their nucleosides, *Biochim. Biophys. Acta - Nucleic Acids Protein Synth.* 656 (1981) 1–15.
- V. Vendrell-Criado, J.A. Sáez, V. Lhiaubet-Vallet, M.C. Cuquerella, M.A. Miranda, Photophysical properties of 5-substituted 2-thiopyrimidines, *Photochem. Photobiol. Sci.* 12 (2013) 1460.
- A. Khvorostov, L. Lapinski, H. Rostkowska, M.J. Nowak, UV-induced generation of rare tautomers of 2-thiouracils: A matrix isolation study, *J. Phys. Chem. A* 109 (2005) 7700–7707.
- H. Rostkowska, A. Barski, K. Szczepaniak, M. Szczesniak, W.B. Person, The tautomeric equilibria of thioanalogs of nucleic acids: spectroscopic studies of 2-thiouracils in the vapour phase and in low temperature matrices, *J. Mol. Struct.* 176 (1988) 137–147.
- E.J. Heller, The semiclassical way to molecular spectroscopy, *Acc. Chem. Res.* 14 (1981) 368–375.
- D.J. Tannor, Introduction to quantum mechanics: a time-dependent perspective, University Science Books, Sausalito, 2007.
- S.F. Mason, The electronic spectra of N-heteroaromatic systems. Part I. The n→π transitions of monocyclic azines, *J. Chem. Soc.* 245 (1959) 1240–1246.
- J.J. Orlando, G.S. Tyndall, Gas phase UV absorption spectra for peracetic acid, and for acetic acid monomers and dimers, *J. Photochem. Photobiol. A Chem.* 157 (2003) 161–166.
- J.Y. Zhang, D.S. Nagra, L. Li, Measurement of gas-phase ultraviolet-visible absorption spectra of thermally labile molecules with a pulsed rapid heating technique for sample vaporization, *Anal. Chem.* 63 (1991) 2995–2999.
- L. Martínez-Fernández, T. Fahleson, P. Norman, F. Santoro, S. Coriani, R. Improta, Optical absorption and magnetic circular dichroism spectra of thiouracils: a quantum mechanical study in solution, *Photochem. Photobiol. Sci.* 16 (2017) 1415–1423.
- S. Mai, P. Marquetand, L. González, A Static Picture of the Relaxation and Intersystem Crossing Mechanisms of Photoexcited 2-Thiouracil, *J. Phys. Chem. A* 119 (2015) 9524–9533.
- S. Mai, F. Plasser, M. Pabst, F. Neese, A. Köhn, L. González, Surface hopping dynamics including intersystem crossing using the algebraic diagrammatic construction method, *J. Chem. Phys.* 147 (2017), 184109.
- M.K. Shukla, J. Leszczynski, Electronic Transitions of Thiouracils in the Gas Phase and in Solutions: Time-Dependent Density Functional Theory (TD-DFT) Study, *J. Phys. Chem. A* 108 (2004) 10367–10375.
- M.K. Shukla, J. Leszczynski, Multiconfigurational Self-Consistent Field Study of the Excited State Properties of 4-Thiouracil in the Gas Phase, *J. Phys. Chem. A* 108 (2004) 7241–7246.

- [45] M. Ruckebauer, S. Mai, P. Marquetand, L. González, Photoelectron spectra of 2-thiouracil, 4-thiouracil, and 2,4-dithiouracil, *J. Chem. Phys.* 144 (2016), 074303.
- [46] C.E. Housecroft, E.C. Constable, Chemistry, Pearson Education Limited, Harlow, 2010.
- [47] H.-W. Jochims, M. Schwell, H. Baumgärtel, S. Leach, Photoion mass spectrometry of adenine, thymine and uracil in the 6–22eV photon energy range, *Chem. Phys.* 314 (2005) 263–282.
- [48] A.R. Katritzky, M. Szafran, G. Pfister-Guillouzo, The tautomeric equilibria of thio analogues of nucleic acid bases. Part 3. Ultraviolet photoelectron spectra of 2-thiouracil and its methyl derivatives, *J. Chem. Soc. Perkin Trans. 2* 871 (1990).
- [49] T. Yanai, D.P. Tew, N.C. Handy, A new hybrid exchange–correlation functional using the Coulomb-attenuating method (CAM-B3LYP), *Chem. Phys. Lett.* 393 (2004) 51–57.
- [50] F. Weigend, R. Ahlrichs, Balanced basis sets of split valence, triple zeta valence and quadruple zeta valence quality for H to Rn: Design and assessment of accuracy, *Phys. Chem. Chem. Phys.* 7 (2005) 3297.
- [51] R.L. Martin, Natural transition orbitals, *J. Chem. Phys.* 118 (2003) 4775–4777.
- [52] M.J. Frisch, G.W. Trucks, H.B. Schlegel, G.E. Scuseria, M.A. Robb, J.R. Cheeseman, G. Scalmani, V. Barone, G.A. Petersson, H. Nakatsuji, X. Li, M. Caricato, A.V. Marenich, J. Bloino, B.G. Janesko, R. Gomperts, B. Mennucci, D.J. Hratch, 2016 Gaussian 16, Revision C.01.
- [53] T. Petrenko, F. Neese, Analysis and prediction of absorption band shapes, fluorescence band shapes, resonance Raman intensities, and excitation profiles using the time-dependent theory of electronic spectroscopy, *J. Chem. Phys.* 127 (2007), 164319.
- [54] S. Banerjee, D. Kröner, P. Saalfrank, Resonance Raman and vibronic absorption spectra with Duschinsky rotation from a time-dependent perspective: Application to β -carotene, *J. Chem. Phys.* 137 (2012) 22A534.
- [55] S. Banerjee, P. Saalfrank, Vibrationally resolved absorption, emission and resonance Raman spectra of diamondoids: a study based on time-dependent correlation functions, *Phys. Chem. Chem. Phys.* 16 (2014) 144–158.
- [56] S. Banerjee, T. Stüker, P. Saalfrank, Vibrationally resolved optical spectra of modified diamondoids obtained from time-dependent correlation function methods, *Phys. Chem. Chem. Phys.* 17 (2015) 19656–19669.
- [57] T. Xiong, P. Saalfrank, Vibrationally Broadened Optical Spectra of Selected Radicals and Cations Derived from Adamantane: A Time-Dependent Correlation Function Approach, *J. Phys. Chem. A* 123 (2019) 8871–8880.
- [58] T. Petrenko, F. Neese, Efficient and automatic calculation of optical band shapes and resonance Raman spectra for larger molecules within the independent mode displaced harmonic oscillator model, *J. Chem. Phys.* 137 (2012), 234107.
- [59] A. Baiardi, J. Bloino, V. Barone, General Time Dependent Approach to Vibronic Spectroscopy Including Franck-Condon, Herzberg-Teller, and Duschinsky Effects, *J. Chem. Theory Comput.* 9 (2013) 4097–4115.
- [60] G. Orlandi, W. Siebrand, Theory of vibronic intensity borrowing. Comparison of Herzberg-Teller and Born-Oppenheimer coupling, *J. Chem. Phys.* 58 (1973) 4513–4523.
- [61] M. Fumanal, F. Plasser, S. Mai, C. Daniel, E. Gindensperger, Interstate vibronic coupling constants between electronic excited states for complex molecules, *J. Chem. Phys.* 148 (2018), 124119.
- [62] L.B. Clark, G.G. Peschel, I. Tinoco, Vapor spectra and heats of vaporization of some purine and pyrimidine bases, *J. Phys. Chem.* 69 (1965) 3615–3618.
- [63] M.M. Stimson, The Ultraviolet Absorption Spectra of Some Pyrimidines. Chemical Structure and the Effect of p H on the Position of λ max, *J. Am. Chem. Soc.* 71 (1949) 1470–1474.
- [64] H. Moustafa, M.F. Shibl, R. Hilal, Electronic Absorption Spectra of Some 2-Thiouracil Derivatives *Phosphorus, Sulfur, Silicon Relat. Elem.* 180 (2005) 459–478.
- [65] M. Haranczyk, M. Gutowski, Visualization of Molecular Orbitals and the Related Electron Densities, *J. Chem. Theory Comput.* 4 (2008) 689–693.

Article 2: URSA-PQ: A Mobile and Flexible Pump-Probe Instrument for Gas Phase Samples at the FLASH Free Electron Laser

Jan Metje, Fabiano Lever, **Dennis Mayer**, Richard James Squibb, Matthew S. Robinson, Mario Niebuhr, Raimund Feifel, Stefan Düsterer and Markus Gühr
Applied Sciences 10, 7882 (2020), DOI: 10.3390/app10217882

Abstract. We present a highly flexible and portable instrument to perform pump-probe spectroscopy with an optical and an X-ray pulse in the gas phase. The so-called URSA-PQ (German for ‘Ultraschnelle Röntgenspektroskopie zur Abfrage der Photoenergiekonversion an Quantensystemen’, Engl. ‘ultrafast X-ray spectroscopy for probing photoenergy conversion in quantum systems’) instrument is equipped with a magnetic bottle electron spectrometer (MBES) and tools to characterize the spatial and temporal overlap of optical and X-ray laser pulses. Its adherence to the CAMP instrument dimensions allows for a wide range of sample sources as well as other spectrometers to be included in the setup. We present the main design and technical features of the instrument. The MBES performance was evaluated using Kr $M_{4,5}$ Auger lines using backfilled Kr gas, with an energy resolution $\Delta E/E$ 1/40 in the integrating operative mode. The time resolution of the setup at FLASH 2 FL 24 has been characterized with the help of an experiment on 2-thiouracil that is inserted via the instruments’ capillary oven. We find a time resolution of 190 fs using the molecular 2p photoline shift and attribute this to different origins in the UV-pump—the X-ray probe setup.

Copyright note. © 2020 by the authors. Licensee MDPI, Basel, Switzerland. This article is an open access article distributed under the terms and conditions of the Creative Commons Attribution (CC BY) license (<http://creativecommons.org/licenses/by/4.0/>).

Article

URSA-PQ: A Mobile and Flexible Pump-Probe Instrument for Gas Phase Samples at the FLASH Free Electron Laser

Jan Metje ¹, Fabiano Lever ¹ , Dennis Mayer ¹ , Richard James Squibb ², Matthew S. Robinson ¹, Mario Niebuhr ¹, Raimund Feifel ², Stefan Düsterer ³ and Markus Gühr ^{1,*}

¹ Institut für Physik und Astronomie, Universität Potsdam, 14476 Potsdam, Germany; jan.metje@uni-potsdam.de (J.M.); fabiano.lever@uni-potsdam.de (F.L.); dennis.mayer@uni-potsdam.de (D.M.); mattrobinson@uni-potsdam.de (M.S.R.); mniebuhr@uni-potsdam.de (M.N.)

² Department of Physics, University of Gothenburg, SE-412 96 Gothenburg, Sweden; richard.squibb@physics.gu.se (R.J.S.); raimund.feifel@physics.gu.se (R.F.)

³ Deutsches Elektronen Synchrotron (DESY), 22607 Hamburg, Germany; stefan.duesterer@desy.de

* Correspondence: mguehr@uni-potsdam.de

Received: 18 October 2020; Accepted: 4 November 2020; Published: 6 November 2020



Abstract: We present a highly flexible and portable instrument to perform pump-probe spectroscopy with an optical and an X-ray pulse in the gas phase. The so-called URSA-PQ (German for ‘Ultraschnelle Röntgenspektroskopie zur Abfrage der Photoenergiekonversion an Quantensystemen’, Engl. ‘ultrafast X-ray spectroscopy for probing photoenergy conversion in quantum systems’) instrument is equipped with a magnetic bottle electron spectrometer (MBES) and tools to characterize the spatial and temporal overlap of optical and X-ray laser pulses. Its adherence to the CAMP instrument dimensions allows for a wide range of sample sources as well as other spectrometers to be included in the setup. We present the main design and technical features of the instrument. The MBES performance was evaluated using Kr $M_{4,5}NN$ Auger lines using backfilled Kr gas, with an energy resolution $\Delta E/E \cong 1/40$ in the integrating operative mode. The time resolution of the setup at FLASH 2 FL 24 has been characterized with the help of an experiment on 2-thiouracil that is inserted via the instruments’ capillary oven. We find a time resolution of 190 fs using the molecular 2p photoline shift and attribute this to different origins in the UV-pump—the X-ray probe setup.

Keywords: X-ray probe; molecular dynamics; gas phase electron spectroscopy

1. Introduction

Photoexcited molecules channel the energy of light into different energetic degrees of freedom, such as vibrational energy, charge transfer and rearrangement of chemical bonds. This process is fast and complex, and often happens in a way that cannot be described within the framework of the Born-Oppenheimer approximation (BOA) [1–4]. In fact, many relevant photoinduced molecular changes, such as retinal isomerization in vision [5], bacterial light harvesting, as well as nucleobase photoprotection [6–9] happen on an ultrafast timescale as non-BOA processes. In order to better understand the molecular dynamics, a close comparison of simulations and experiments is extremely fruitful. Using small and isolated chromophores is advantageous for quantitative comparisons of experiments to simulations, the latter can be performed using the highest level of electronic structure methods under these constraints. Moreover, in the gas phase, experiments can use rather powerful spectroscopic methods for charged particles including highly differential coincidence experiments [10,11]. In addition, quantum manipulation such as molecular nonadiabatic, field-free

alignment [12,13] and quantum state-selection [14] to prepare specific molecular target states are possible in the gas phase.

X-ray probing of molecular dynamics offers substantial new opportunities complementary to well-established optical pump-probe methods. The X-ray-matter-interaction is element selective due to large differences of the inner shell binding energies between different elements and has been demonstrated to be site selective [15]. We have used these advantages in past time resolved UV pump—X-ray probe studies, to investigate the dynamics of isolated nucleobases. The molecular internal conversion from and to $n\pi^*$ states leads to a strong pre-edge feature in the X-ray absorption spectrum of the element at which the n lone-pair orbital is localized [16]. Since both the core-level as well as the lone pair level of one particular atom are having a large overlap, the dipole matrix element and thus the absorption cross section is larger than cross sections involving delocalized molecular orbitals. The method is therefore ideally suited for detection of any $n\pi^*$ states via the spectroscopy at the corresponding heteroatom [17]. Changes in the bond distance manifest themselves as shifts in the Auger kinetic energy of one of the atoms in this bond [18]. This is due to the strongly repulsive, Coulomb-repulsion shape of the final, dicationic states in the Auger decay. In addition, time-resolved Auger probing can also be used to detect the dissociation into a neutral and charged fragment in a time resolved way [19].

In this work, we describe the design and first tests of a new user instrument at the free-electron laser (FEL) facility FLASH (Free Electron Laser in Hamburg), called URSA-PQ (German for ‘Ultraschnelle Röntgenspektroskopie zur Abfrage der Photoenergiekonversion an Quantensystemen’, Engl. ‘ultrafast X-ray spectroscopy for probing photoenergy conversion in quantum systems’), for pump-probe experiments primarily on gas-phase targets.

The new instrument is equipped with a ‘magnetic bottle’ electron spectrometer (MBES) [20], a molecular source, as well as several tools for finding the spatial and temporal overlap of the optical and X-ray laser pulses. The MBES is characterized by a high solid angle collection, ideal for dilute targets. In addition, it is able to measure a large range of kinetic energies, and the resolution at a particular range can be optimized by an electrostatic retardation system. We, furthermore, equipped the present system with a capillary resistively heated oven source for the evaporation of condensed molecular samples [21]. This system works well for fairly small molecules like nucleobases, which can reach an appreciable vapor pressure around 10^{-4} mbar, as for the example of thymine [22], without undergoing pyrolysis or tautomerization. The capillary confines the molecular sample to a beam of small divergence fitted to a narrowly defined interaction region. Tools for spatial and temporal overlap include a cerium doped YAG (Yttrium Aluminium Garnet) screen viewed with magnifying optics as well as diodes for coarse timing, allowing a temporal synchronization of optical and X-ray pulses within about 100 ps.

We present a system that includes all these parts and in addition has a high degree of flexibility. Due to adherence to the flange and distance dimensions set by the so-called CAMP chamber [23], multiple, already existing molecular sources and spectrometers can be integrated with the setup described in this paper.

In what follows, the instrument design and measurement procedures will be described. We will then focus on the energy calibration of the MBES as well as the time resolution in our optical-pump X-ray-probe measurements by using the example of 2-thiouracil.

2. Materials and Methods

2.1. Overview and Vacuum System

Figure 1 shows an overview of the URSA-PQ instrument and its functionalities. In the current version, the sample is introduced by either backfilling the vacuum vessel or using a capillary oven. In this paper, the former is used to characterize the MBES, and the latter is used with 2-thiouracil to evaluate the time resolution. The interaction region is defined by the crossing point of the optical

and X-ray beams overlapping with the region of highest sensitivity of the MBES. Molecules in the interaction region are excited by an optical laser pulse, in this case a 266 nm UV pulse, and subsequently probed by an X-ray pulse. Optical and X-ray pulses are focused by separate mirrors and combined inside the beamline by a mirror having a hole for X-ray transmission. The UV beam is set on side or top of the hole to avoid power losses. The tunable X-rays can induce a resonant core-to-valence excitation and/or non-resonant ionization. The resulting photo- and Auger electrons are then efficiently guided by the MBES's magnetic field arrangement along a flight tube of 1.7 m length to a micro-channel-plate (MCP) detector. The time-of-flight of the electrons is measured and converted to electron kinetic energy. The apparatus is designed in a modular way that also allows upgrades at later times, the usage of different measurement devices from the FLASH environment and other types of sample delivery systems. The desired high flexibility is achieved by designing the central vacuum vessel as a customized six-way cross (see Figure 2), following the most critical dimensions of the permanent CAMP instrument situated at FLASH 1.

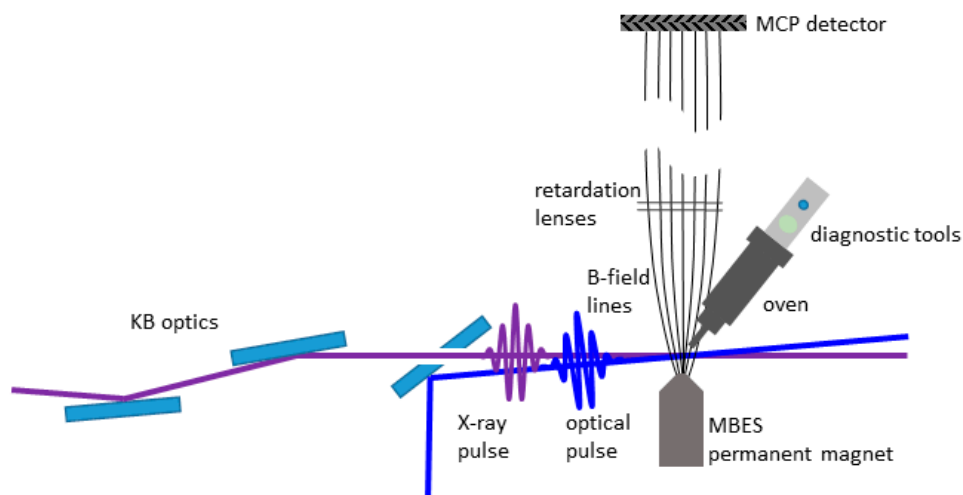


Figure 1. Diagrammatic representation of the URSA-PQ (German for ‘Ultraschnelle Röntgenspektroskopie zur Abfrage der Photoenergiekonversion an Quantensystemen’, Engl. ‘ultrafast X-ray spectroscopy for probing photoenergy conversion in quantum systems’) instrument with its functionalities. The molecular sample is evaporated and guided into the interaction region by a capillary oven. An optical laser pulse excites the sample before a delayed X-ray pulse from the FLASH FEL, focused by a Kirkpatrick-Baez (KB) mirror set, probes the excited molecular ensemble. Photo- and Auger-electrons created by the light-matter interaction are guided by the magnetic field of the magnetic bottle electron spectrometer (MBES) towards a detector. The diagnostic tools for spatial and time-overlap can we driven into the interaction region.

An overview of the instrument is shown in Figure 2. A central cross serves as the light-matter interaction chamber. A manipulator is mounted vertically (z-direction), holding the capillary oven molecular source and diagnostics tools on top of that source. Either one two of the devices (oven or diagnostics tools) can be brought into the center and thus the interaction region of the instrument. Shown in the positive y-direction is the MBES spectrometer flight tube with the MCP detector at the end. The manipulator holding a permanent magnet in the negative y-direction provides the up to 1 Tesla strong B-field of the MBES. The optical and X-ray beams travel in the x-direction, entering by the center flange, through the interaction region in the center of the cross to the center flange at the end.

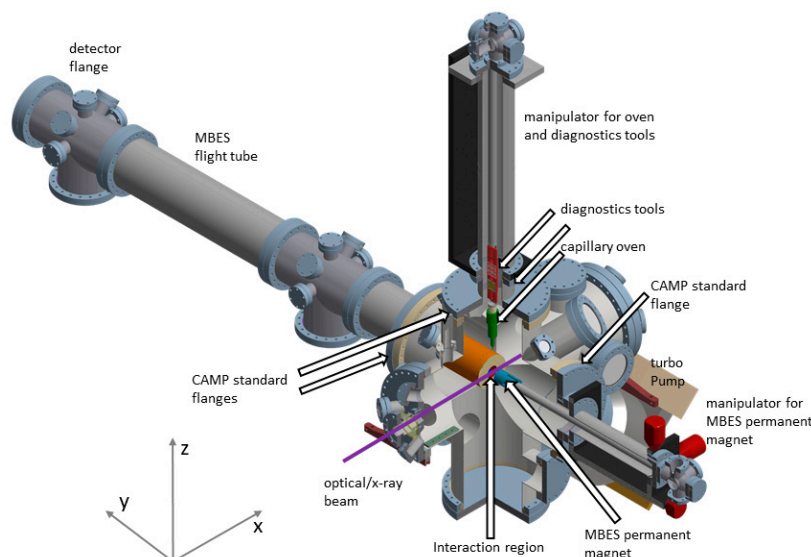


Figure 2. Design-drawing of the URSA-PQ (German for ‘Ultraschnelle Röntgenspektroskopie zur Abfrage der Photoenergiekonversion an Quantensystemen’, Engl. ‘ultrafast X-ray spectroscopy for probing photoenergy conversion in quantum systems’) instrument. The central body contains flanges that adhere to the standard defined by the CAMP-chamber in size as well as distance to the interaction region (marked). The capillary oven and diagnostic tools are mounted on a manipulator allowing for insertion of either device into the beam. The permanent magnet of the magnetic bottle electron spectrometer (MBES) sits on another manipulator to optimally overlap the region of highest sensitivity of the MBES with the interaction region of the optical and X-ray pulses. The 1.7 m long flight tube connects the main body to the detector flange housing the microchannel plate electron detector.

The central cross of the instrument has three flanges (top in z-direction and left, right in $\pm y$ direction) that adhere to the CAMP instrument dimensions concerning flange size (DN 250 CF) and distance of flanges from the interaction region. For the front port where the FEL enters, the chamber is kept at short distance to the interaction region (280 mm) to support short focal lengths of the beamline. Breadboards are welded to the bottom of this port and the rear port to allow the incorporation of in-vacuum equipment such as incoupling optics and diagnosis tools. The floor facing port ($-z$ direction) can be used for a LN_2 cold trap (not shown here). A 1300 l/s turbomolecular pump is attached to a flange facing 45 degrees downwards. A variety of smaller flanges (DN40 to DN100) face the chamber center at the diagonals, or are located at the sides of the cross’s arms. Notably, three DN40 flanges at the entrance arm may be used for baffles. The vacuum apparatus is mounted on a movable frame (not shown here) that allows height and level adjustment by means of four legs. To simplify the alignment of the chamber axis to the FEL beam, the frame is equipped with a motorized x-y-stage and a manual rotation stage with the vertical axis below the connection to the beamline. In this way, the frame can be easily aligned to the path of the FEL beam. The motors of the frame, and the capillary oven magnet manipulators are controlled by a programmable logic controller (PLC).

2.2. Integration at the FLASH FL 24 Beamline

For the results presented here, the URSA-PQ chamber was integrated at FL 24 at FLASH 2 in Deutsches Elektronen Synchrotron (DESY), Hamburg, Germany. The beamline is equipped with bendable Kirkpatrick–Baez (KB) optics [24]. The distance from the KB optics to the interaction region in our experiment is 2.1 m.

The focus position of the X-rays can be manipulated within the chamber by using the KB degrees of freedom. We chose to have the focus beyond the interaction region, as we did want to maximize the number of X-ray photons on target without introducing X-ray nonlinearities. At about 90 cm in front of the interaction region, after the KB optics, the UV beam is coupled in by a 45 degree high reflectivity plane mirror for 266 nm wavelength. This mirror has a central hole for the X-ray beam to pass through. The optical beam is reflected from a position below the center hole, and steered up so that the two beams cross in the interaction region of the MBES.

The control and monitoring of the setup's hardware, such as motor position, oven temperature and chamber pressure is handled by an industrial PLC system working in tandem with a UNIX server. All safety and/or time-sensitive tasks, such as vacuum valves control or high voltage interlocks, are managed by the PLC in a closed loop in order to ensure real-time responsivity. The UNIX server offers a server-client interface that allows multiple operators to monitor and control the system status from different terminals through the use of a purpose-built graphical user interface that connects to the server through a Python API (application program interface).

Integration with the DESY DOOCS (distributed object oriented control system) framework is seamlessly handled by the UNIX server. Experiment parameters such as chamber pressure and MCP voltages are constantly pushed to DOOCS for storage, allowing for later correlation of the chamber parameters with the experimental data. Moreover, the raw experimental data is retrieved from DOOCS and processed in real time. The data is sliced into single-shot traces, separating UV-pumped from non-pumped shots and averaged over a controllable time window. It is then made available to users for visualization (through a purpose built utility) or online analysis (through the python API). A real time calibrated time-of-flight to electron kinetic energy conversion of the measured traces is also provided through the API. After the experiment, all recorded data are available to the user group for offline analysis as hdf5 data files through the standard DESY channels.

2.3. Diagnostics and Oven

We have implemented a diagnostic paddle that is located on top of the oven on the same manipulator (see Figure 2), allowing for precise positioning inside the interaction region of the MBES spectrometer. The diagnostic paddle hosts a number of tools used for spatial as well as temporal characterization.

The spatial diagnostics serve to spatially overlap the UV and X-ray beams in the interaction region, as well as estimating the beam size. We use a 0.2 mm thick, 25 mm diameter YAG screen, possessing a matte, sandblasted surface. The screen is externally viewed through a vacuum window with the aid of a long working distance lens.

For timing diagnostics, we use a fast AXUV-type diode on a subminiature version A (SMA) connector that is not directly illuminated, but by a highly-attenuated beam created using solid filters which are moved in and out. The beam hits the mounting rim of the diode and only scattered light hits the active area in our case. We illuminate it separately with the optical and X-ray pulses. These signals are viewed on a 13 GHz bandwidth oscilloscope. The X-ray induced trace is saved as reference on the scope and the delay of the optical pulse is manipulated by a delay stage such that the rising edges of the two signals overlap. This strategy allows us to temporally overlap the optical and X-ray pulses with a sub 100 ps accuracy. Temporal overlap on the femtosecond scale is achieved using photo or Auger electrons of atoms or molecules shown later in this paper.

We use a resistively-heated capillary oven that we developed some years ago and successfully used before as a sample source at the linac coherent light source (LCLS) [16,18,21,25,26] as well as with high harmonic vacuum ultraviolet sources [27,28]. The oven consists of a body, a cap that is screwed on after filling the main body with a solid molecular sample, and a capillary tip. All components are made from aluminum. The three parts are separately heated using thin-film sheet heaters. The temperatures of the three sections are monitored using thermocouples and we control the heating current using a proportional-integral-derivative PID feedback circuit implemented on the control

computer. The sample density has been once tested with the nucleobase thymine and can reach up to 10^{12} molecules/cm³ [21]. The capillary reduces the angular width of the beam compared to usual effusive sources and we have measured the full width at half maximum (FWHM) of 10 degrees when operating in the 10^{11} molecules/cm³ density regime [21].

2.4. Magnetic Bottle Electron Spectrometer

The magnetic bottle time-of-flight electron spectrometer (MBES) has a high collection efficiency, covering up to the full 4π solid angle [26]. Thus, a large number of electrons can be efficiently detected, which is especially important in experiments with dilute samples. The magnetic bottle spectrometer is characterized by a strong and inhomogeneous magnetic field of about 1 Tesla at the interaction region, which joins onto a much weaker (~ 1 mT), homogeneous magnetic field created by a solenoid around the flight tube. Electrons ejected in the interaction region into any direction are thus confined into the flight tube. The time-of-flight (TOF) of the electrons from the interaction region to detection is determined and subsequently transformed into kinetic energy.

Our specific design is illustrated in Figure 3. A vacuum tube with DN160 flanges houses the flight tube, which is protected from external magnetic fields by a μ -metal shield. Wound onto the flight tube, a solenoid is generating the weak homogeneous field along the electron flight path. The coil has 1450 windings and is fed by a current of 400 mA producing a magnetic field of around 0.4 mT. Winding the coil directly on the flight tube has the advantage that the solenoid can be brought close to the interaction region. In addition, the design allows that the whole instrument can be taken out of the main chamber by unbolting a single DN 250 flange at the central cross. Close to the interaction region, right at the entrance of the flight tube, a stack of electrostatic lenses can be used to retard/repel the electrons. A permanent magnet with a soft iron pole tip generates the strong, inhomogeneous field in the interaction region. The space available at the beamline is used efficiently to maximize the instruments resolution, resulting in an optimal flight tube length of 1.7 m.

The transition from the inhomogeneous to homogeneous field occurs over a short distance of about 10 cm. The lens stack is placed inside the front of the flight tube, at the beginning of the homogeneous part of the magnetic field. At this point, the momentum in direction of the center axis of the flight tube is approximately equal for electrons of equal kinetic energy.

The permanent magnet of the instrument is mounted in a temperature-controlled holder on a manipulator. By this construction, the magnet can be brought close to the interaction region as well as retracted if other equipment is brought into the interaction region, such as a diode or a Ce-YAG screen. Elevated temperatures of 60 °C generally prevent sample building up on the magnet tip and introducing electrostatic inconsistencies.

The detector assembly (purchased from Roentdek Handels GmbH) consists of a grid, followed by a chevron MCP stack with an 80 mm diameter and an anode. The grid is held at the potential of the flight tube (i.e., the retardation potential). The electrons are then accelerated towards the front MCP by a +300 V potential change over 3 mm. Subsequently, the electrons are multiplied by the MCP arrangement using a potential on the MCP backside of 1950 V. The anode, used for picking up the signal is held at 2300 V. The signal is picked up by a high-pass filter and sent to a 12 bit analog-digital converter, which we use at a sample rate of 2Gs. A single electron pulse has a width of 10 ns. The data we present in this paper has been accumulated in the integration mode, i.e., all individual TOF traces have been added. Alternatively, for lower electron yield, individual electron hits can be identified by using a (software) constant fraction discriminator and then added individually to a TOF array.

We transform spectra taken in the TOF domain to the kinetic energy domain by the following procedure. The distance from the interaction region to the detector is divided into three parts. The electric potential in these parts is treated as a step function and the lengths are taken from the CAD drawing of the spectrometer but refined in the calibration by fitting to Auger electron features. In the first part, the electrons are traveling with their original kinetic energy for a distance of 90 mm from the interaction region to the flight tube entrance. In the second part through the flight tube, which is

1694 mm long, their kinetic energy is reduced by the retardation voltage. We fit these distances based on observed electron spectra in the calibration procedure shown below. In the 3-mm-long final part from the flight tube to the detector, their kinetic energy is increased by 300 V.

After axis transformation from TOF to kinetic energy, the signal strength is multiplied by a Jacobian function which corrects for the non-linear mapping of bins from the TOF domain and the kinetic energy domain.

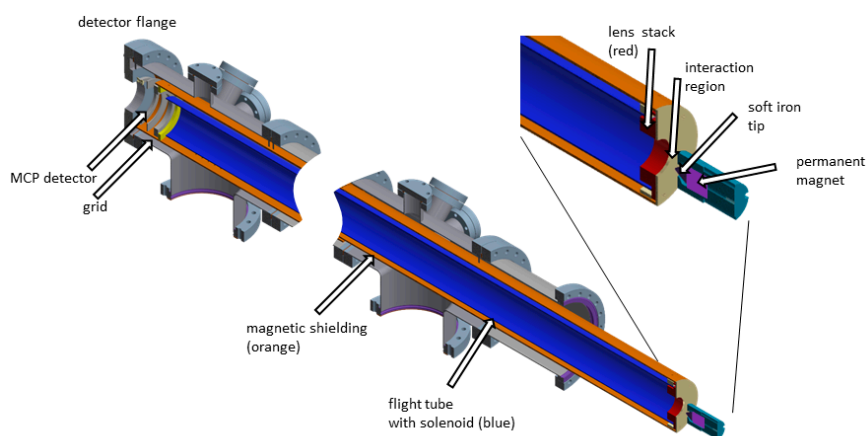


Figure 3. Cut-down scheme of the magnetic bottle time of flight spectrometer, with the magnified area around the interaction region. The interaction region is defined by the overlap of the optical and X-ray pulse with the region of highest sensitivity of the MBES. The magnetic field in the interaction region is dominated by the permanent magnet having a tapered soft-iron pole piece on top. The strong, inhomogeneous magnetic field drops quickly to a weak, homogeneous solenoid field surrounding the flight tube, thus guiding the electrons from the interaction region towards the detector. A μ -metal tube (orange) around the flight-tube and solenoid assembly (blue) shields the long flight region from external magnetic fields. At the entrance of the flight tube, an electrostatic lens stack can be used to retard the electrons to optimally utilize the energy resolution at a mean kinetic energy of choice. The micro-channel-plate (MCP) detector assembly contains a grid at the front to accelerate electrons towards the first plate. The grid and lens stack are equipotential so that the electrons travel through the flight tube with constant velocity.

3. Results and Discussion

3.1. MBES Energy Resolution

The spectrometer has been calibrated with the Kr $M_{4,5}NN$ Auger lines, appearing in the kinetic energy range shown in Figure 4. The background pressure in the interaction region was 2×10^{-7} mbar before filling in Kr, although much lower pressures in the 10^{-9} mbar range have been reached by pumping for longer times and baking. We backfilled the chamber with Kr gas at a pressure of 5.5×10^{-7} mbar for calibration purposes.

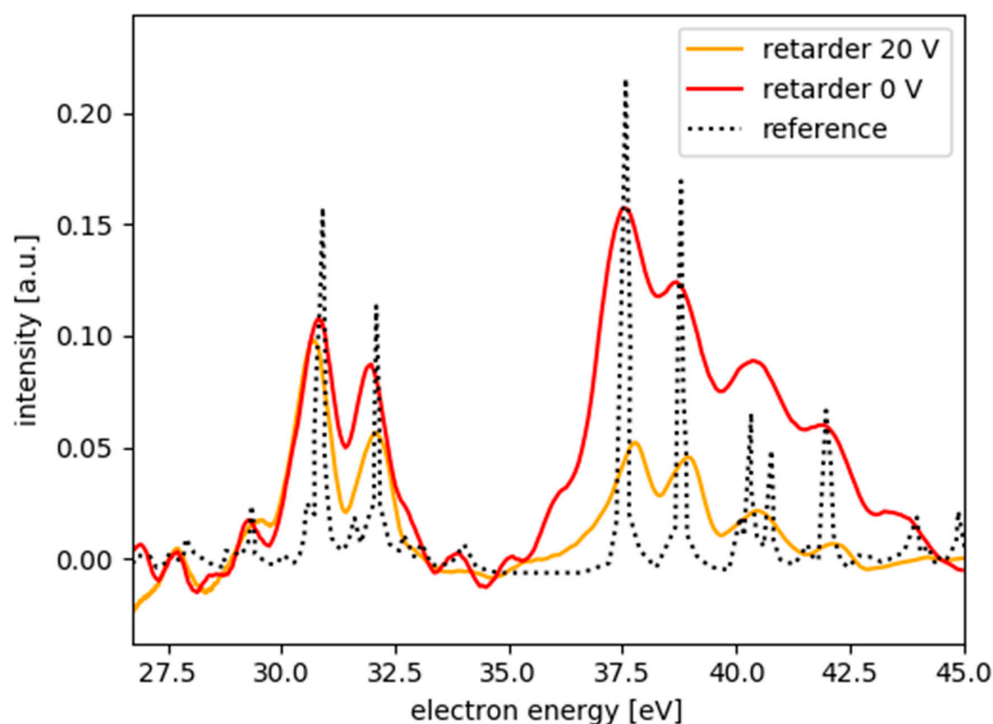


Figure 4. Krypton $M_{4,5}NN$ Auger spectra recorded with the URSA-PQ instrument using 270 eV photons (red spectrum using a retardation of 0 V, orange spectrum using a retardation of 20 V). The spectra are recorded with a back-filled interaction chamber and converted from time-of-flight (TOF) to kinetic energy. The black spectrum from Reference [29] serves as a reference.

We chose an FEL photon energy of 270 eV; the spectral jitter was on the order of 2% as observed by an inline diagnostic instrument at the beamline [30]. The nonresonant Auger lines however are not affected by the spectral jitter of the light source. The permanent magnet of the spectrometer was moved close to the interaction region and scanned vertically to and horizontally along the FEL beam to optimize the position for highest electron signal. A halo of scattered light around the laser focus prohibited distances of the magnet tip to laser focus to be smaller than 4 mm. Even a small amount of scattered light produced many more photoelectrons from the solid magnet tip than from the gas in the real focus because of the orders of magnitude lower density of our gas compared to solid matter.

The Auger spectra used for calibration are shown in Figure 4. The red line is recorded using a retardation potential of 0 V. The black reference spectrum is obtained from Werme et al. [29]. One can clearly identify the two different groups of Kr $M_{4,5}NN$ Auger lines in our spectra. In the higher energy group, we identify the two lines at 37.7 and 38.7 eV as two separate lines. This results in an energy resolution without retardation of $\Delta E/E \cong 1/40$. The kinetic energy spectrum with 20 V retardation voltage (orange) shows deeper modulation indicating higher energy resolution, as the kinetic energy decreased.

We now discuss the resolution-limiting factors in the calibration measurements. We note a large background in the kinetic energy range between 35 and 37.5 eV. This results from a saturation of the detector due to a large amount of electron counts per X-ray pulse. In the TOF-spectrum, the group of Auger electrons between 37 and 42.5 eV hit the detector at early times and thereby produces a long lasting background of several nanoseconds. By the time the next group between 30 and 32 eV hits the detector, this signal has decayed. This memory effect in the detector certainly degrades the resolution as background accumulates in a group of Auger lines. This issue can be easily solved by reducing

the FEL pulse energy or the Kr pressure; in the following experimental runs for 2-thiouracil, we had adjusted pressure as well as FEL pulse energy accordingly.

A single electron pulse coupled out at the detector-anode has a width of 10 ns and is completely symmetric, i.e., the rising edge is not shorter than the falling edge. As mentioned above, we used the system in ‘integration-mode’ by adding up individual traces from the detector. The 10 ns pulse width in TOF corresponds to 0.5 eV of energy resolution in the kinetic energy range around 20 eV. The experimental energy resolution of 1/40 corresponds to a 10 ns time-interval at a TOF of 300 ns (kinetic energy of 101 eV).

A possibility to improve the time resolution would be the reduction of the number of electrons hitting the detector. This would reduce the detector saturation and therefore accumulated background in the different groups. Another important advantage would be the possibility to identify individual electrons hitting the detector. This will allow for edge detection, for instance via a constant fraction discriminator. In this case, the resolution is fundamentally limited by the sample interval of the analog-to-digital converter (ADC), which is 500 ps in our case. In analogy to the resolution limit of 10 ns, the 500 ps would correspond to an energy resolution of 0.03 eV in the energy range of 20 eV. However, there is also the turn-around time of the electrons emitted initially away from the detector, which will also limit the resolution [20].

3.2. Temporal Resolution

We now investigate the temporal resolution in the optical pump—these are X-ray probe experiments. As mentioned above, we initially determined the coarse temporal overlap by monitoring a fast-diode response, induced by UV and X-ray pulses, on an oscilloscope. The setup had an accuracy in the sub-100 ps domain. As 100 ps resolution is not sufficient for the experiments, more accurate information on the temporal overlap, as well as the temporal resolution achievable by this setup, we performed measurements of photoelectron signals of molecules using the URSA instrument. We used the molecule 2-thiouracil ($C_4H_4N_2OS$), as this has been the molecule of interest for our first beamtime utilizing this instrument. Thionucleobases are interesting as they show an efficient relaxation to long-lasting triplet states after UV excitation, thereby showing different behavior compared to canonical nucleobases, which relax relatively quickly to the ground state [31].

Figure 5a shows a core level photoelectron spectrum of 2-thiouracil illuminated by X-ray photons of 272 eV mean-photon-energy. The pulses have less than 1% mean-photon-energy-jitter and a relative bandwidth of 1–1.5%. Shown in this particular part of the spectrum is the 2p-photoline of sulfur at 103.5 eV kinetic energy. This line should be spin-orbit split resulting in the $j = 3/2$ and $1/2$ components with an energy spacing of 1.2 eV [32], however already the photon energy resolution is not sufficient to resolve that splitting. The small shoulder visible on the lower kinetic energy side at 95–97 eV is a satellite structure that accompanies the main 2p photoline (as, for instance, previously documented for sulfur on surfaces [33]).

Upon UV excitation, the main photoline shifts towards lower kinetic energies, due to the molecular dynamics setting in immediately. The molecular origin for this observation will be discussed in detail in a separate paper. Here, we use this feature to determine the temporal overlap with sub-ps precision, and the overall time resolution of the experiment itself. We take here the difference spectrum (not shown), calculate its absolute value $|UV_{on} - UV_{off}|$ as a measure for the UV induced change in the spectrum. This observable as a function of relative delay between UV-pump and X-ray-probe pulse is shown by the blue dots in Figure 5b, together with a theoretical fit shown by the orange line. The fit function includes a Gaussian describing the time-resolution, convoluted with two exponential decays (see for instance Equation (3) in Reference [34]). The second exponential decay is longer than 100 ps and has limited influence on the data in the delay window shown. The faster exponential decay of (230 ± 30) fs describes some molecular dynamics. Most interesting in the context here is the Gaussian time-resolution function. We actually determined the relative time-overlap by the maximum of this

Gaussian, which can be done with a sub-10 fs accuracy. The Gaussian time resolution when correcting data using the beam arrival monitor [35] has a FWHM of $\sigma_{TR} = (190 \pm 10)$ fs.

There are different contributions to the origin of the time-resolution known in the literature which sum up geometrically to the final time resolution $\sigma_{TR} = \sqrt{\sigma_{UVL}^2 + \sigma_{FEL}^2 + \sigma_{FELtrain}^2 + \sigma_{UVLtrain}^2 + \sigma_{FEL-UVLjitter}^2}$, where σ_{UVL} is the UV pulse length, σ_{FEL} the X-ray pulse length, $\sigma_{FELtrain}$ the intra-train jitter of the X-ray pulses within the macro-bunch, $\sigma_{UVLtrain}$ the intra-train jitter of the UV pulses within the macrobunch and $\sigma_{FEL-UVLjitter}$ the relative timing jitter of X-ray and UV laser pulses [36]. The UV pulse duration has been determined to be $\sigma_{UVL} = 80$ fs by a frequency resolved optical gating (FROG) measurement [37]. Subtracting the UV pulse duration geometrically yields 170 fs Gaussian FWHM total for all other components. The other components have been estimated with $\sigma_{FELtrain} = \sigma_{UVLtrain} = 30$ –40 fs and $\sigma_{FEL-UVLjitter} = 70$ fs [38,39]. Subtracting all these components out delivers a remaining X-ray pulse duration in the experiment in the region of about 150 fs. Taking all these components into account results in a remaining X-ray pulse duration in the experiment on the order of 150 fs. However, we would expect a sub-100 fs X-ray pulse duration for this bunch charge. The discrepancy could possibly be attributed to a higher jitter compared to past experiments and longer term drifts.

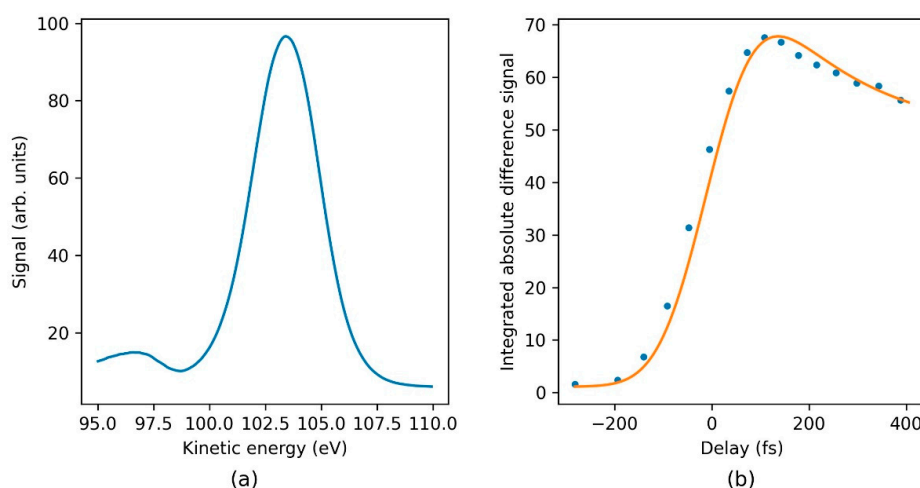


Figure 5. (a) Experimental photoelectron spectrum showing the sulfur-2p photoline of 2-thiouracil taken with a photon energy of ~ 270 eV. (b) Increase of the absolute value in the difference signal $|(UV_{on} - UV_{off})|$ as a function of pump-probe delay (blue dots) and fit by the model explained in the text (orange line).

4. Conclusions

We presented the new URSA-PQ instrument which is now available for general users at the FLASH FEL facility. We described its major design features and its flexibility because of its adherence to CAMP instrument dimensions. The instrument is already equipped with a molecular source and a magnetic bottle spectrometer, allowing for ultrafast X-ray probe studies of photoexcited molecular dynamics. We demonstrated the current spectral resolution of the MBES of 1/40 using the $M_{4,5}NN$ Auger decay of Kr in the range of 30–45 eV electron energy. This can be improved further by treating electron signals digitally using a combination of an edge finder and time-to-digital conversion. We investigated the time-resolution in conjunction with the FLASH 2 pump-probe laser delivering 266 nm pulses at FL 24. For that purpose, we used a UV-induced shift of the sulfur 2p photoelectron line of the molecules 2-thiouracil. We find a temporal resolution of 190 fs using photoelectron features from UV excited 2-thiouracil.

Author Contributions: Instrument design, J.M. and M.G.; MBES design, J.M. with help of R.J.S. and R.F.; realization of the instrument: J.M., D.M., F.L., M.N., M.S.R., S.D., M.G.; instrument software, F.L. with help of J.M., performing experiments, all authors; analyzing data, F.L., D.M. with help of M.G.; writing paper: J.M., F.L., D.M. and M.G.; comments and suggestions on the paper drafts, all authors. All authors have read and agreed to the published version of the manuscript.

Funding: The URSA-PQ instrument and the position of J.M. was funded by the German Federal Ministry for Education and Research (BMBF) under ‘Verbundforschungsprojekt 05K16IP1’. The Potsdam Research Group is funded by a Lichtenberg Professorship of the Volkswagen-Stiftung. We acknowledge DFG funding via grant GU 1478/1-1. We acknowledge DESY (Hamburg, Germany), a member of the Helmholtz Association HGF, for the provision of experimental facilities. Part of this research was carried out at FLASH2. R.F. and R.J.S. received funding from the Swedish Research Council and the Knut and Alice Wallenberg Foundation, Sweden. We acknowledge the support of the Deutsche Forschungsgemeinschaft and Open Access Publishing Fund of University of Potsdam.

Acknowledgments: We acknowledge S. Alisauskas, F. Calegari, B. Manschwetus, M. Kuhlmann, T. Mazza, A. Trabattoni, M. Wallner and T. J. A. Wolf for participating in the experiments on thiouracil.

Conflicts of Interest: The authors declare no conflict of interest. The funders had no role in the design of the study; in the collection, analyses, or interpretation of data; in the writing of the manuscript, or in the decision to publish the results.

References

1. Yarkony, D. Diabolical conical intersections. *Rev. Mod. Phys.* **1996**, *68*, 985–1013. [[CrossRef](#)]
2. Levine, B.G.; Martínez, T.J. Isomerization through Conical Intersections. *Annu. Rev. Phys. Chem.* **2007**, *58*, 613–634. [[CrossRef](#)] [[PubMed](#)]
3. Matsika, S.; Krause, P. Nonadiabatic Events and Conical Intersections. *Annu. Rev. Phys. Chem.* **2011**, *62*, 621–643. [[CrossRef](#)] [[PubMed](#)]
4. Domcke, W.; Yarkony, D.R.; Köppel, H. *Conical Intersections Electronic Structure, Dynamics and Spectroscopy*; World Scientific Publishing Company: Singapore, 2011; ISBN 978-981-4313-45-2.
5. Polli, D.; Altoè, P.; Weingart, O.; Spillane, K.M.; Manzoni, C.; Brida, D.; Tomasello, G.; Orlandi, G.; Kukura, P.; Mathies, R.A.; et al. Conical intersection dynamics of the primary photoisomerization event in vision. *Nature* **2010**, *467*, 440–443. [[CrossRef](#)] [[PubMed](#)]
6. Crespo-Hernández, C.E.; Cohen, B.; Hare, P.M.; Kohler, B. Ultrafast Excited-State Dynamics in Nucleic Acids. *Chem. Rev.* **2004**, *104*, 1977–2020. [[CrossRef](#)]
7. Middleton, C.T.; de La Harpe, K.; Su, C.; Law, Y.K.; Crespo-Hernández, C.E.; Kohler, B. DNA Excited-State Dynamics: From Single Bases to the Double Helix. *Annu. Rev. Phys. Chem.* **2009**, *60*, 217–239. [[CrossRef](#)]
8. Schreier, W.J.; Gilch, P.; Zinth, W. Early Events of DNA Photodamage. *Annu. Rev. Phys. Chem.* **2015**, *66*, 497–519. [[CrossRef](#)] [[PubMed](#)]
9. Improta, R.; Santoro, F.; Blancafort, L. Quantum Mechanical Studies on the Photophysics and the Photochemistry of Nucleic Acids and Nucleobases. *Chem. Rev.* **2016**, *116*, 3540–3593. [[CrossRef](#)]
10. Dörner, R.; Mergel, V.; Jagutzki, O.; Spielberger, L.; Ullrich, J.; Moshhammer, R.; Schmidt-Böcking, H. Cold Target Recoil Ion Momentum Spectroscopy: A “momentum microscope” to view atomic collision dynamics. *Phys. Rep.* **2000**, *330*, 95–192. [[CrossRef](#)]
11. Ullrich, J.; Moshhammer, R.; Dorn, A.; Dörner, R.; Schmidt, L.P.H.; Schmidt-Böcking, H. Recoil-ion and electron momentum spectroscopy: Reaction-microscopes. *Rep. Prog. Phys.* **2003**, *66*, 1463–1545. [[CrossRef](#)]
12. Stapelfeldt, H.; Seideman, T. Colloquium: Aligning molecules with strong laser pulses. *Rev. Mod. Phys.* **2003**, *75*, 543. [[CrossRef](#)]
13. McFarland, B.K.; Farrell, J.P.; Bucksbaum, P.H.; Gühr, M. High Harmonic Generation from Multiple Orbitals in N₂. *Science* **2008**, *322*, 1232. [[CrossRef](#)]
14. Filsinger, F.; Meijer, G.; Stapelfeldt, H.; Chapman, H.N.; Kuepper, J. State- and conformer-selected beams of aligned and oriented molecules for ultrafast diffraction studies. *Phys. Chem. Chem. Phys.* **2011**, *13*, 2076–2087. [[CrossRef](#)]
15. Siegbahn, K. *ESCA Applied to Free Molecules*; North-Holland Pub. Co.: Amsterdam, The Netherlands, 1969; ISBN 0-7204-0160-7.

16. Wolf, T.J.A.; Myhre, R.H.; Cryan, J.P.; Coriani, S.; Squibb, R.J.; Battistoni, A.; Berrah, N.; Bostedt, C.; Bucksbaum, P.; Coslovich, G.; et al. Probing ultrafast $\pi\pi^*/n\pi^*$ internal conversion in organic chromophores via K-edge resonant absorption. *Nat. Commun.* **2017**, *8*, 29. [[CrossRef](#)]
17. Ehlert, C.; Gühr, M.; Saalfrank, P. An efficient first principles method for molecular pump-probe NEXAFS spectra: Application to thymine and azobenzene. *J. Chem. Phys.* **2018**, *149*, 144112. [[CrossRef](#)]
18. McFarland, B.K.; Farrell, J.P.; Miyabe, S.; Tarantelli, F.; Aguilar, A.; Berrah, N.; Bostedt, C.; Bozek, J.D.; Bucksbaum, P.H.; Castagna, J.C.; et al. Ultrafast X-ray Auger probing of photoexcited molecular dynamics. *Nat. Commun.* **2014**, *5*, 4235. [[CrossRef](#)]
19. Wolf, T.; Holzmeier, F.; Wagner, L.; Berrah, N.; Bostedt, C.; Bozek, J.; Bucksbaum, P.; Coffee, R.; Cryan, J.; Farrell, J.; et al. Observing Femtosecond Fragmentation Using Ultrafast X-ray-Induced Auger Spectra. *Appl. Sci.* **2017**, *7*, 681. [[CrossRef](#)]
20. Kruit, P.; Read, F.H. Magnetic field paralleliser for 2π electron-spectrometer and electron-image magnifier. *J. Phys. E Sci. Instrum.* **1983**, *16*, 313–324. [[CrossRef](#)]
21. McFarland, B.K.; Berrah, N.; Bostedt, C.; Bozek, J.; Bucksbaum, P.H.; Castagna, J.C.; Coffee, R.N.; Cryan, J.P.; Fang, L.; Farrell, J.P.; et al. Experimental strategies for optical pump – soft x-ray probe experiments at the LCLS. *J. Phys. Conf. Ser.* **2014**, *488*, 012015. [[CrossRef](#)]
22. Ferro, D.; Bencivenni, L.; Teghil, R.; Mastromarino, R. Vapour pressures and sublimation enthalpies of thymine and cytosine. *Thermochim. Acta* **1980**, *42*, 75–83. [[CrossRef](#)]
23. Strueder, L.; Epp, S.; Rolles, D.; Hartmann, R.; Holl, P.; Lutz, G.; Soltau, H.; Eckart, R.; Reich, C.; Heinzinger, K.; et al. Large-format, high-speed, X-ray pnCCDs combined with electron and ion imaging spectrometers in a multipurpose chamber for experiments at 4th generation light sources. *Nucl. Instrum. Methods Phys. Res. Sect. A-Accel. Spectrom. Detect. Assoc. Equip.* **2010**, *614*, 483–496. [[CrossRef](#)]
24. Raimondi, L.; Manfreda, M.; Mahne, N.; Cocco, D.; Capotondi, F.; Pedersoli, E.; Kiskinova, M.; Zangrando, M. Kirkpatrick-Baez active optics system at FERMI: System performance analysis. *J. Synchrotron Rad.* **2019**, *26*, 1462–1472. [[CrossRef](#)]
25. Zhaunerchyk, V.; Kamińska, M.; Mucke, M.; Squibb, R.J.; Eland, J.H.D.; Piancastelli, M.N.; Frasiniski, L.J.; Grilj, J.; Koch, M.; McFarland, B.K.; et al. Disentangling formation of multiple-core holes in aminophenol molecules exposed to bright X-FEL radiation. *J. Phys. B At. Mol. Opt. Phys.* **2015**, *48*, 244003. [[CrossRef](#)]
26. Sanchez-Gonzalez, A.; Barillot, T.R.; Squibb, R.J.; Kolorenč, P.; Agaker, M.; Averbukh, V.; Bearpark, M.J.; Bostedt, C.; Bozek, J.D.; Bruce, S.; et al. Auger electron and photoabsorption spectra of glycine in the vicinity of the oxygen K-edge measured with an X-FEL. *J. Phys. B At. Mol. Opt. Phys.* **2015**, *48*, 234004. [[CrossRef](#)]
27. Koch, M.; Wolf, T.J.A.; Gühr, M. Understanding the modulation mechanism in resonance-enhanced multiphoton probing of molecular dynamics. *Phys. Rev. A* **2015**, *91*. [[CrossRef](#)]
28. Wolf, T.J.A.; Parrish, R.M.; Myhre, R.H.; Martínez, T.J.; Koch, H.; Gühr, M. Observation of Ultrafast Intersystem Crossing in Thymine by Extreme Ultraviolet Time-Resolved Photoelectron Spectroscopy. *J. Phys. Chem. A* **2019**, *123*, 6897–6903. [[CrossRef](#)] [[PubMed](#)]
29. Werme, L.O.; Bergmark, T.; Siegbahn, K. The High Resolution $L_{2,3}$ MM and $M_{4,5}$ NN Auger Spectra from Krypton and $M_{4,5}$ NN and $N_{4,5}$ OO Auger Spectra from Xenon. *Phys. Scr.* **1972**, *6*, 141–150. [[CrossRef](#)]
30. Braune, M.; Buck, J.; Kuhlmann, M.; Grunewald, S.; Dusterer, S.; Viefhaus, J.; Tiedtke, K. Non-invasive online wavelength measurements at FLASH2 and present benchmark. *J. Synchrotron Rad.* **2018**, *25*, 3–15. [[CrossRef](#)]
31. Arslançan, S.; Martínez-Fernández, L.; Corral, I. Photophysics and Photochemistry of Canonical Nucleobases' Thioanalogs: From Quantum Mechanical Studies to Time Resolved Experiments. *Molecules* **2017**, *22*, 998. [[CrossRef](#)]
32. Giuliano, B.M.; Feyrer, V.; Prince, K.C.; Coreno, M.; Evangelisti, L.; Melandri, S.; Caminati, W. Tautomerism in 4-Hydroxypyrimidine, S-Methyl-2-thiouracil, and 2-Thiouracil. *J. Phys. Chem. A* **2010**, *114*, 12725–12730. [[CrossRef](#)]
33. Föhlisch, A.; Feulner, P.; Hennies, F.; Fink, A.; Menzel, D.; Sanchez-Portal, D.; Echenique, P.M.; Wurth, W. Direct observation of electron dynamics in the attosecond domain. *Nature* **2005**, *436*, 373–376. [[CrossRef](#)] [[PubMed](#)]
34. Beckwith, J.S.; Rumble, C.A.; Vauthey, E. Data analysis in transient electronic spectroscopy—An experimentalist's view. *Int. Rev. Phys. Chem.* **2020**, *39*, 135–216. [[CrossRef](#)]

35. Savelyev, E.; Boll, R.; Bomme, C.; Schirmel, N.; Redlin, H.; Erk, B.; Düsterer, S.; Müller, E.; Höppner, H.; Toleikis, S.; et al. Jitter-correction for IR/UV-XUV pump-probe experiments at the FLASH free-electron laser. *New J. Phys.* **2017**, *19*, 043009. [[CrossRef](#)]
36. Dziarzhytski, S.; Biednov, M.; Dicke, B.; Wang, A.; Miedema, P.S.; Engel, R.Y.; Schunck, J.O.; Redlin, H.; Weigelt, H.; Siewert, F.; et al. The TRIXS end-station for femtosecond time-resolved resonant inelastic x-ray scattering experiments at the soft x-ray free-electron laser FLASH. *Struct. Dyn.* **2020**, *7*, 054301. [[CrossRef](#)] [[PubMed](#)]
37. Trebino, R. *Frequency-Resolved Optical Gating: The Measurement of Ultrashort Laser Pulses*; Springer Science & Business Media: New York, NY, USA, 2000; ISBN 978-1-4613-5432-1.
38. Schulz, S.; Grguraš, I.; Behrens, C.; Bromberger, H.; Costello, J.T.; Czwalińska, M.K.; Felber, M.; Hoffmann, M.C.; Ilchen, M.; Liu, H.Y.; et al. Femtosecond all-optical synchronization of an X-ray free-electron laser. *Nat. Commun.* **2015**, *6*, 5938. [[CrossRef](#)]
39. Schulz, S.; Czwalińska, M.K.; Felber, M.; Predki, P.; Schefer, S.; Schlarb, H.; Wegner, U. Femtosecond-precision synchronization of the pump-probe optical laser for user experiments at flash. In Proceedings of the Advances in X-ray Free-Electron Lasers ii: Instrumentation, Prague, Czech Republic, 17–19 April 2013; Tschentscher, T., Tiedtke, K., Eds.; SPIE Int Soc Optical Engineering: Bellingham, WA, USA, 2013; Volume 8778.

Publisher's Note: MDPI stays neutral with regard to jurisdictional claims in published maps and institutional affiliations.



© 2020 by the authors. Licensee MDPI, Basel, Switzerland. This article is an open access article distributed under the terms and conditions of the Creative Commons Attribution (CC BY) license (<http://creativecommons.org/licenses/by/4.0/>).

Article 3: Core-Level Spectroscopy of 2-Thiouracil at the Sulfur L₁- and L_{2,3}-Edges Utilizing a SASE Free-Electron Laser

Fabiano Lever, **Dennis Mayer**, Jan Metje, Skirmantas Alisauskas, Francesca Calegari, Stefan Düsterer, Raimund Feifel, Mario Niebuhr, Bastian Manschwetus, Marion Kuhlmann, Tommaso Mazza, Matthew Scott Robinson, Richard J. Squibb, Andrea Trabattoni, Måns Wallner, Thomas J. A. Wolf and Markus Gühr

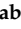



Molecules 26, 6469 (2021), DOI: 10.3390/molecules26216469

Abstract. In this paper, we report X-ray absorption and core-level electron spectra of the nucleobase derivative 2-thiouracil at the sulfur L₁- and L_{2,3}-edges. We used soft X-rays from the free-electron laser FLASH2 for the excitation of isolated molecules and dispersed the outgoing electrons with a magnetic bottle spectrometer. We identified photoelectrons from the 2p core orbital, accompanied by an electron correlation satellite, as well as resonant and non-resonant Coster–Kronig and Auger–Meitner emission at the L₁- and L_{2,3}-edges, respectively. We used the electron yield to construct X-ray absorption spectra at the two edges. The experimental data obtained are put in the context of the literature currently available on sulfur core-level and 2-thiouracil spectroscopy.

Copyright note. © 2021 by the authors. Licensee MDPI, Basel, Switzerland. This article is an open access article distributed under the terms and conditions of the Creative Commons Attribution (CC BY) license (<https://creativecommons.org/licenses/by/4.0/>).

Article

Core-Level Spectroscopy of 2-Thiouracil at the Sulfur L₁- and L_{2,3}-Edges Utilizing a SASE Free-Electron Laser

Fabiano Lever¹, Dennis Mayer¹ , Jan Metje¹, Skirmantas Alisauskas², Francesca Calegari^{3,4,5}, Stefan Düsterer², Raimund Feifel⁶, Mario Niebuhr¹ , Bastian Manschwetus², Marion Kuhlmann², Tommaso Mazza⁷, Matthew Scott Robinson^{1,2,3,4}, Richard J. Squibb⁶, Andrea Trabattoni³ , Måns Wallner⁶, Thomas J. A. Wolf⁸  and Markus Gühr^{1,*}

- ¹ Institut für Physik und Astronomie, Universität Potsdam, 14476 Potsdam, Germany; fabiano.lever@uni-potsdam.de (F.L.); dmayer@uni-potsdam.de (D.M.); metje.jan@gmail.com (J.M.); mniebuhr@uni-potsdam.de (M.N.); matthew.robinson@desy.de (M.S.R.)
- ² Deutsches Elektronen Synchrotron (DESY), 22607 Hamburg, Germany; skirmantas.alisauskas@desy.de (S.A.); stefan.duesterer@desy.de (S.D.); bastian.manschwetus@desy.de (B.M.); marion.kuhlmann@desy.de (M.K.)
- ³ Center for Free-Electron Laser Science (CFEL), Deutsches Elektronen Synchrotron (DESY), Notkestraße 85, 22607 Hamburg, Germany; francesca.calegari@desy.de (F.C.); andrea.trabattoni@desy.de (A.T.)
- ⁴ The Hamburg Centre for Ultrafast Imaging, Universität Hamburg, 22761 Hamburg, Germany
- ⁵ Institut für Experimentalphysik, Universität Hamburg, 22761 Hamburg, Germany
- ⁶ Department of Physics, Gothenburg University, SE-41296 Gothenburg, Sweden; raimund.feifel@physics.gu.se (R.F.); richard.squibb@physics.gu.se (R.J.S.); mans.wallner@physics.gu.se (M.W.)
- ⁷ European XFEL, 22869 Schenefeld, Germany; tommaso.mazza@xfel.eu
- ⁸ Stanford PULSE Institute, SLAC National Accelerator Laboratory, Menlo Park, CA 94025, USA; thomas.wolf@stanford.edu
- * Correspondence: mguehr@uni-potsdam.de



Citation: Lever, F.; Mayer, D.; Metje, J.; Alisauskas, S.; Calegari, F.; Düsterer, S.; Feifel, R.; Niebuhr, M.; Manschwetus, B.; Kuhlmann, M.; et al. Core-Level Spectroscopy of 2-Thiouracil at the Sulfur L₁- and L_{2,3}-Edges Utilizing a SASE Free-Electron Laser. *Molecules* **2021**, *26*, 6469. <https://doi.org/10.3390/molecules26216469>

Academic Editor: R. Daniel Little

Received: 6 October 2021

Accepted: 22 October 2021

Published: 26 October 2021

Publisher's Note: MDPI stays neutral with regard to jurisdictional claims in published maps and institutional affiliations.



Copyright: © 2021 by the authors. Licensee MDPI, Basel, Switzerland. This article is an open access article distributed under the terms and conditions of the Creative Commons Attribution (CC BY) license (<https://creativecommons.org/licenses/by/4.0/>).

Abstract: In this paper, we report X-ray absorption and core-level electron spectra of the nucleobase derivative 2-thiouracil at the sulfur L₁- and L_{2,3}-edges. We used soft X-rays from the free-electron laser FLASH2 for the excitation of isolated molecules and dispersed the outgoing electrons with a magnetic bottle spectrometer. We identified photoelectrons from the 2p core orbital, accompanied by an electron correlation satellite, as well as resonant and non-resonant Coster–Kronig and Auger–Meitner emission at the L₁- and L_{2,3}-edges, respectively. We used the electron yield to construct X-ray absorption spectra at the two edges. The experimental data obtained are put in the context of the literature currently available on sulfur core-level and 2-thiouracil spectroscopy.

Keywords: X-ray; photoelectron; sulfur; thiouracil; nucleobases; Coster–Kronig; Auger–Meitner; NEXAFS; FLASH

1. Introduction

Recent years have seen increasing interest in the study of sulfur-substituted nucleobases, known as thionucleobases, for applications in medicine and biochemistry [1,2]. They differ from their canonical counterparts in their response to UV radiation. The substitution of an oxygen atom with the much heavier sulfur atom significantly changes the potential energy landscape, affecting how the molecules interact with light. The absorption spectrum is shifted from UVC into the UVA range, and the resulting excitation produces long-lived triplet states [3–8]. Their reactive triplet state makes thionucleobases useful as cross-linking agents [9,10], as well as candidates for photoinduced cancer treatment [11,12].

Ultrafast radiationless transitions are crucial in funneling the molecular population from the initially excited ¹ππ* states into the long-lived ³ππ* states. The details of these dynamics have been the topic of theoretical and experimental efforts (see Ref. [8] and the references therein). The particular thionucleobase 2-thiouracil (2-tUra) is among the most studied systems. Its static potential energy landscape properties indicate the existence

of several conical intersection (CI) seams [13]. Dynamical simulations predict how an initially UV-excited population traverses the CI regions to end up in the lowest $^3\pi\pi^*$ state. Experiments using UV pump and visible-ultraviolet probe pulses in solvents [4,14] and in the gas phase [14–16] confirm the ultrafast nature of the molecular transitions. The combination of dynamics predictions with experimental transient spectra present a powerful approach to deduce molecular dynamics. These combined studies suggested ultrafast sub-picosecond transitions from the $^1\pi\pi^*$ to a $^1n\pi^*$ ‘doorway’ state, from which the lower-lying triplet states are accessed [14,16].

Using ultrafast X-ray pulses to probe molecular dynamics via core-electron excitations provides insight into the molecular dynamics, a process which is complementary to the well-established probe methods that utilize valence electron transitions [17]. X-rays provide an element-sensitive probe as the core-level electron binding energies differ strongly among elements. The tight binding afforded also makes this method highly spatially selective. This particular advantage has been used to examine the $^1n\pi^*$ channel via UV-pump X-ray probe studies on thymine [18,19]. For 2-tUra, we used the sulfur L-edges to probe the local dynamics at the C-S bond using time-resolved Auger–Meitner spectroscopy [20]. In addition, we could attribute electronic states using the excited-state chemical shift (ESCS) resulting from the local charge at the sulfur atom probed in time-resolved X-ray photoelectron studies [21].

In this paper, we present a static X-ray spectroscopic study of 2-tUra performed at the sulfur L-edge. Our work includes near-edge absorption fine structure (NEXAFS) spectra at the L_{1-} and $L_{2,3-}$ edges, as well as photoelectron spectra involving the 2s and 2p core-holes. We furthermore investigate the Auger–Meitner spectra induced by sulfur 2p vacancies and the Coster–Kronig decay of the sulfur 2s core-hole as a function of X-ray energy.

2. Results

We first investigated the photon-energy range of the sulfur $L_{2,3-}$ edge creating a sulfur 2p core hole through either resonant transitions to core-valence excited states or non-resonant promotion of the core electron into the continuum. The FEL photon energy $h\nu$ was scanned over the ionization edge region from $h\nu = 155$ to 175 eV, with 0.75 eV steps in randomized order; the averaged FEL bandwidth was about 4 eV. For each photon energy setting, a full electron spectrum of 2-tUra was recorded. The electron time-of-flight spectra were converted to the kinetic energy scale by taking the Jacobian correction in the binning process into account. The results are shown in Figure 1a, with electron spectral intensity shown in the form of grayscale false-color code as a function of electron kinetic energy and photon energy.

The 2D spectrum shows two qualitatively different groups of features. First, we discerned a group of maxima that did not change their kinetic energy as the photon energy was varied. We refer to these as ‘non-dispersing’ lines or bands. The strongest is a broad line at 140 eV with a width of ~ 9 eV, which appears from photon energies of 167 eV and higher. This component is accompanied by a weaker one at $E_{\text{kin}} = 130$ eV and a smaller background towards lower kinetic energies.

The second group of features are ‘dispersing’, meaning they change their kinetic energy with $h\nu$. In the photon energy range of 155–163 eV, we observed several such lines which changed E_{kin} linearly with $h\nu$ in the kinetic energy range above 120 eV. The highest kinetic energy lines also continued to be visible for larger photon energies up to 175 eV. A further dispersing line starting at $E_{\text{kin}} = 48$ eV at $h\nu = 155$ eV also linearly changed its kinetic energy with $h\nu$. This line is not part of the molecule and we discuss it further in the discussion below. An additional transition region was visible around $h\nu = 165$ eV to 167 eV, where dispersive features convert into non-dispersive bands. In this region, a line with ‘negative’ dispersion seems to change from high to lower kinetic energies around $E_{\text{kin}} = 140$ eV. We integrated the full two-dimensional spectrum over the kinetic energy range and present it as a function of photon energy in Figure 1b. The NEXAFS spectrum obtained in this way

shows a decreasing electron yield (absorption) from the lowest $h\nu$ to about 165 eV, where the absorption rises. This rise occurs over a photon energy interval of ~ 2 eV.

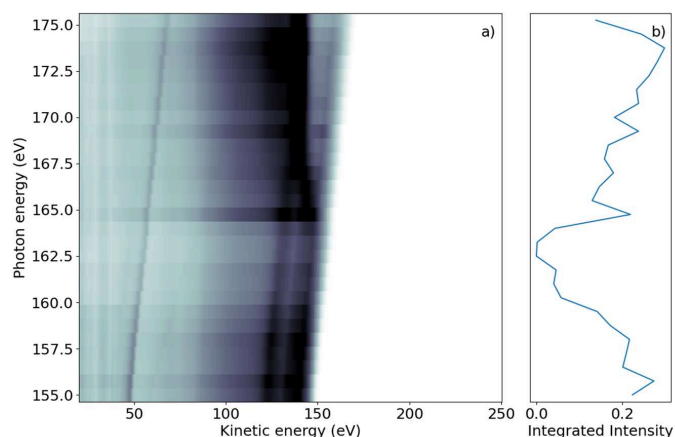


Figure 1. (a) Photon energy vs. electron kinetic energy for the 2-tUra sulfur 2p edge. The valence emission can be discerned as dispersing diagonal lines. Resonant and non-resonant Auger–Meitner emission splits off from the valence signal when the photon energy reaches the 2p binding energy. (b) NEXAFS spectrum obtained by integrating the electron emission intensity over the whole kinetic energy range. The 2p edge marks an increase in emitted signal, with some spectral features visible as peaks in the NEXAFS.

We subsequently demonstrate the energy range around the sulfur L_1 -edge, which creates features connected to a sulfur 2s core-hole. We scanned the photon energy in the range of 206 eV to 240 eV, with 1 eV steps. Figure 2a shows a false-color 2D spectrum of electron yield as a function of kinetic energy and photon energy. Similar to the $L_{2,3}$ spectrum, we again identified dispersing and non-dispersing lines. The most prominent dispersing feature changes E_{kin} linearly with $h\nu$ from $E_{kin} = 38.5$ eV to 75 eV over the full range shown in Figure 2a. The line is accompanied by a weaker dispersing line shifted by 6 eV towards lower kinetic energy. In addition, weaker dispersing features from valence ionization are visible for kinetic energies over 150 eV and up to 200 eV for the lowest photon energy.

In the lower kinetic energy range, we observed a non-dispersing broad line centered around $E_{kin} = 42.5$ eV. At higher kinetic energies, we observed a non-dispersing band around $E_{kin} = 140$ eV with a tail towards lower energies. Analogous to the $L_{2,3}$ -edge, we generated a NEXAFS spectrum from the integrated electron yield, shown in Figure 2b. In addition to the decrease in intensity from lower to higher photon energies, an absorption increase starting at $h\nu = 222$ eV with a maximum at $h\nu = 227$ eV was observed.

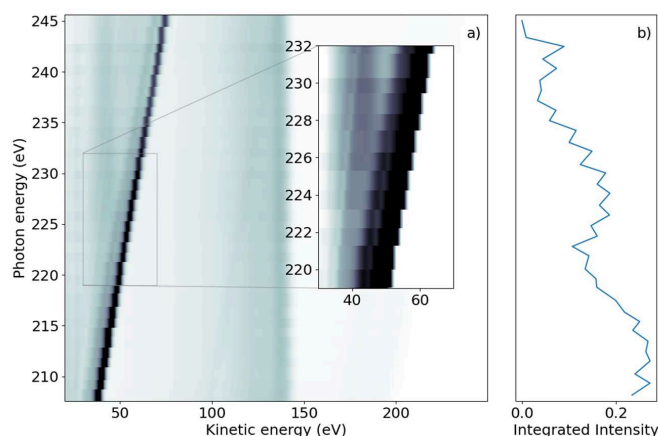


Figure 2. (a) Photon energy vs. kinetic energy for the 2-tUra sulfur 2s edge, with the photon energy varying from 208 eV to 245 eV. The bright diagonal feature is the dispersing 2p photoelectron line. A satellite photoelectron line is visible to the left of the main feature. Non-resonant 2p Auger–Meitner electron emission can be seen in the 100 eV to 150 eV range. Coster–Kronig electrons from the 2p → 2s decay are visible at 40 eV for photon energies above 220 eV. The dispersing dip overlapping the Coster–Kronig feature visible in the inset is an artifact of the readout electronics. (b) NEXAFS spectrum obtained by integrating the emission intensity over the whole kinetic energy range.

3. Discussion

We first discuss the spectra at the sulfur $L_{2,3}$ -edge. According to calculations [22], the ionization potential of sulfur is given as 162.5 eV and 163.6 eV for the two spin-orbit split components $2p_{3/2}$ and $2p_{1/2}$, respectively. Photoelectron measurements of 2-tUra found the ionization potential values to be 168.17 eV and 169.37 eV for the spin-orbit split components [23]. The photon energy window from $h\nu = 155$ eV to 176 eV in Figure 1 thus spans from well below to above the ionization potential.

At the lowest photon energies, the spectrum must be dominated by valence emission, and we can clearly identify dispersing features with a high energy edge around 150 eV kinetic energy. We thus compare the electron spectrum to the He-lamp induced valence photoemission spectrum taken over a range of only 10 eV (from 8 to 18 eV binding energy) [24]. Figure 3 shows a photoelectron spectrum taken at FLASH2 at $h\nu = 155.75$ eV (blue line). The inset of Figure 3 compares a small region of that spectrum with the photoelectron spectrum obtained using the He (I) line at $h\nu = 21.2$ eV. While the He spectrum shows rich detail attributed to photoemission from different valence orbitals [24], our spectrum at FLASH2 is only weakly modulated as a function of E_{kin} . The ionization potential overlaps with the measured ionization potential of 8.8 eV [24]. The poor modulation of the FLASH2 valence photoelectron spectrum in Figures 1 and 3 is a combined effect of the photon energy bandwidth of 4 eV and the reduced resolution of the magnetic bottle spectrometer at these comparatively high kinetic energies. The magnetic bottle was operated at retardation of only 5 eV; taking the measured 1/40 resolution [25], we arrive at a feature width of about 4 eV at $E_{kin} = 150$ eV. The valence features disperse with a slope of one in $h\nu$ per eV in E_{kin} throughout the whole measurement range, confirming the use of fundamental undulator radiation.

A second dispersive feature, starting at $E_{kin} = 47.9$ eV, has a binding energy of 108 eV (see also Figure 2). The slope, equal to the slope of the valence lines, indicates its origin from photoemission with the fundamental of the undulator. We suggest that this line stems from the Al tip of the oven, sitting at a distance of a few mm from the interaction region but still being hit by some halo of the X-ray beam. The 2s line of Al is nominally expected

to be around 120 eV, but due to patch charges at the oxidized tip, this line might be shifted by a few eV towards its apparent binding energy of 108 eV.

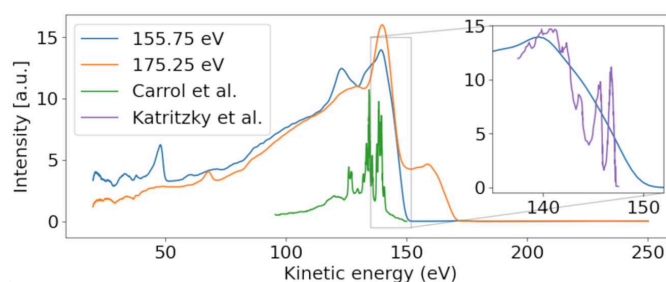


Figure 3. Photoelectron spectra for photon energies above (175.25 eV) and below (155.75 eV) the sulfur 2p binding energy. A dispersive behavior of the valence band is visible, moving from ~140 to ~160 eV with increasing photon energy. Our valence spectrum at $h\nu = 155.75$ eV is compared with a He-lamp-induced valence photoelectron spectrum (purple) from Ref. [24] in the inset, which is scaled in kinetic energy according to the difference of photon energies used in the experiments. Conversely, the Auger–Meitner feature is only present for the higher photon energy. The Auger–Meitner data are compared with the sulfur Auger–Meitner spectrum of OCS (green) from Ref. [26].

We now concentrate on the non-dispersive features. At the limit of the highest photon energy in Figure 1, we observe a non-dispersive band peaking at 140 eV, shown in the orange line in Figure 3. As the photon energy of 175.25 eV is above the ionization limit for the sulfur 2p electrons, we assume that these features belong to non-resonant Auger–Meitner (NAM) decay of 2-tUra. An Auger–Meitner spectrum of the molecule is not available; we therefore compare the features with a sulfur L-MM Auger–Meitner spectrum of OCS (green line Figure 3) from Ref. [26]. The OCS reference shows four dominant groups of lines, which are attributed to different bands of dicationic final states in Ref. [26]. Generally, we observe less resolved features than in the OCS reference. This is due to the reduced resolution of our magnetic bottle spectrometer. On the other hand, larger species such as 2-tUra tend to not show resolved features on the eV scale. This argument can be made in analogy to thymine and its fragment isocyanic acid (HNCO). While the Auger–Meitner spectrum of the latter shows details on an eV scale in analogy to OCS, thymine only exhibits broad bands about 10 eV wide [27]. This effect is due to the increased density of final dicationic states in NAM decay for growing molecular size. The different bands at 140 and 130 eV correspond to broadened bands in the OCS spectrum. We do not know the exact electronic configuration of the valence dicationic states after Auger decay of the sulfur core-hole. However, the sulfur atom has two valence orbitals that must be strongly involved in the sulfur core hole decay: a strongly bound 3s and a shallow bound 3p valence orbital. A decay involving strongly bound valence orbitals in dicationic states leads to less kinetic energy of the Auger electron. Therefore, a very coarse interpretation can attribute the different band ‘humps’ at 140, 130, and 105 eV to dicationic decays with two valence holes dominated by sulfur $3p^{-2}$, $3p^{-1}3s^{-1}$, and $3s^{-2}$ configurations, respectively. The hole-character refers to the sulfur atomic orbital contained in the molecular orbitals.

The NEXAFS spectrum in Figure 1b shows an intensity decrease from lower $h\nu$ up to about 164 eV, where the integrated electron yield in the spectrum increases. This is about 4 eV below the first sulfur 2p binding energy and thus in the region of core-to-valence resonances from 2p core levels to unoccupied valence levels. The valence state in the transition needs to fulfill symmetry requirements, meaning it needs to contain either atomic sulfur s or d orbitals. As we do not observe any fine structure because of the comparatively large bandwidth, we have not pursued any calculations of the unoccupied valence electronic states. The lowest unoccupied states of 2-tUra, the so-called π^* resonances, are dominated

by sulfur atomic character. As in every NEXAFS spectrum, a dense series of Rydberg states with many different atomic contributions spans from the lowest resonances up to the ionization limit. There is currently no NEXAFS reference data available for 2-tUra. We thus compare our data to NEXAFS spectra of OCS and CS₂ at the sulfur L_{2,3}-edge [28], as well as on dimethyl disulfide at the sulfur L_{2,3}- and also L₁-edges [29]. In CS₂ as well as OCS, the first resonances are described by 2p_{3/2} and 2p_{1/2} to π* transitions, located around 163–164 eV and 164–165 eV for CS₂ and OCS, respectively. Higher resonances are attributed to Rydberg-transitions with 4s and 3d sulfur character. Above the ionization limit, the spectra of CS₂ and OCS show a broad shape resonance.

The kinetic energy-resolved region of the core-valence resonances shows so-called resonant Auger–Meitner processes. The resonant Auger–Meitner (RAM) decay [30] has been studied in several molecules, from diatomic to quadratomic [31,32]. Part of our group has studied RAM decay in the nucleobase thymine, where it has been used to infer molecular excited state dynamics [33]. In RAM decay, the initial core-excited neutral state decays into a cationic state, in contrast to decay to dicationic states, as is the case for core-ionized states in a NAM process. We clearly see the effect of the final state in the transition of the RAM to the NAM decay of 2-tUra. At the 1s-π* resonance, the most prominent feature in the RAM sits at 146 eV, which then transforms into the NAM feature at 140 eV kinetic energy. The shift results from a more attractive dicationic potential for the outgoing Auger–Meitner electron in NAM as compared with the cationic potential in RAM. The transition region of RAM to NAM in thymine shows a very similar shift, appearing as dispersion in the wrong direction, i.e., the kinetic energy decreases as the photon energy increases (see Figure 2 in Ref. [33]). The spectrum in Figure 1 does not possess sufficient kinetic energy resolution to distinguish participator (final states are identical to outer valence ionized final states) and spectator decay (final states possess an excited valence electron corresponding to inner valence ionized final states), in contrast to Ref. [33].

We now discuss features at the L₁-edge, which implies a sulfur 2s hole being created upon X-ray interaction. Unlike the L_{2,3}-edges, only one core-hole state is created here due to the absence of spin-orbit coupling. According to calculations, the binding energy of the sulfur 2s-ionized state is 230 eV [22]. The photon energy window in Figure 2, therefore, contains the sulfur L₁-edge.

For the discussion, we first concentrate on the most prominent feature in Figure 2: the dispersive line presented more prominently in the inset. Figure 4 presents some lineouts of kinetic energy spectra at specific photon energies. We find a kinetic energy of 39.8 eV at the photon energy of 209.35 eV, corresponding to a binding energy of 169.5 eV. The linewidth is about 4 eV, masking any splitting below that width. We thus conclude that the dispersive feature must be the sulfur 2p photoelectron line at the binding energies of 168.17 eV and 169.37 eV for the 2p_{3/2} and 2p_{1/2} spin-orbit split components, respectively [23]. The experimentally found dispersion fits to ionization by the first order of undulator radiation from FLASH2.

Parallel to the main photoelectron line, a correlation satellite line [34] appears 5 eV below in kinetic energy, most clearly visible in the hν = 240 eV spectrum (orange line in Figure 4) at a kinetic energy of 68 eV. In an orbital picture, the structure corresponds to a shake-up process from an occupied to an unoccupied valence orbital induced by the sulfur 2p photoionization. Thus, the photoelectron has the energy of the main line reduced by the energy to accomplish that shake-up. Satellite structures of the sulfur 2p photoelectron line have also been documented for comparatively small molecules such as SF₆ [35] or sulfur atoms on a metal surface [36]. For the latter, a similar shift is observed.

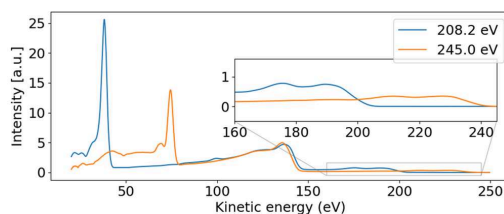


Figure 4. Photoelectron spectra for photon energies above (~ 245 eV) and below (~ 208 eV) the 2s binding energy. The dispersive behavior of the 2p photoelectron line is visible, moving from 39.8 to 74.4 eV with increasing photon energy. The 2p non-resonant Auger–Meitner band from 100 eV to 144 eV remains stable and is independent of the photon energy. The dispersive valence features are visible in the inset.

The non-dispersive part is composed of the sulfur 2p NAM decay in the 100 to 150 eV kinetic energy range. For photon energies above the 2s binding energy, we also see a non-dispersive feature with a kinetic energy of about 40 eV. We attribute this second feature to the Coster–Kronig spectrum of the 2s hole, which is dominated by one broad peak at 42.5 eV kinetic energy, visible in the orange line of Figure 4. Photon energies above the 2s binding energy are able to create a 2s core hole, which is rapidly filled by a 2p electron in the form of Coster–Kronig decay, ejecting a valence electron in the process. The observed kinetic energy is therefore given by the 2s–2p energy gap, minus the valence binding energy, and is independent of the photon energy that produced the 2s core hole. To our knowledge, there are no S 2s Coster–Kronig spectra documented for molecules. We thus compare the spectra to those of sulfur atoms on surfaces from Ref. [36], showing two bands at 40 and 50 eV kinetic energy, which falls energetically within our observed broad band. Those bands are attributed to $2s^{-1}$ Coster–Kronig decays with a $2p^{-1} 3s^{-1}$ and $2p^{-1} 3p^{-1}$ final state accompanied by a charge transfer from the sulfur atom into the substrate.

The 2p induced NAM decay is visible in both the blue and orange lines of Figure 4, where a slight shift in the peak position is observed. At low photon energies, the 2p decay is induced by 2p photoelectron emission. For the higher photon energies, however, the 2p NAM decay can be induced by both 2p and 2s photoelectron emission. In case of 2s ionization, the 2s Coster–Kronig decay will create a valence hole and 2p-core hole; the latter will then decay via NAM channels. We suggest that the Auger spectra of NAM and Coster–Kronig induced NAM are different because of the additional valence hole. Thus, the shift is caused by photon energy-dependent changes in the relative intensities of the NAM decay channels originating from either 2s or 2p ionization.

For the L_1 -NEXAFS spectrum, we observed the peak of the absorption feature as being between $h\nu = 225$ and 230 eV. The ‘generic’ binding energy of the 2s electron of 230 eV likely needs to be shifted upwards in the molecule by a few eV in analogy to the 2p electron. Thus, we end up with $2s-\pi^*$ transitions at the maximum of the NEXAFS spectrum. Again, because of a lack of molecular NEXAFS spectra, we point to Ref. [36] for comparison, where the maximum of the $2s-3p_z$ absorption was observed at 225 eV.

The relatively large bandwidth of the X-rays—of up to 2%—limits the energy resolution in NEXAFS and resonant Auger–Meitner and photoelectron spectroscopy. Nevertheless, we were able to discern features that are attributed to core-valence resonances and core-level electron binding energies. The non-resonant Auger–Meitner and Coster–Kronig features are independent of the initial photon energy and bandwidth. Their shape is therefore governed by the resolution of the electron spectrometer and the number of electronic states accessible by Auger–Meitner and Coster–Kronig decay in large molecules.

4. Materials and Methods

The data were obtained at the FL24 beamline of the FLASH2 free-electron laser (FEL) [37,38] as part of a more extensive investigation of the dynamics following UV excita-

tion [20,21]. An instrument containing sample injection and a magnetic bottle-type electron spectrometer (URSA-PQ, German: Ultraschnelle Röntgenspektroskopie zur Abfrage der Photoenergiekonversion in Quantensystemen, English: Ultrafast X-ray spectroscopy for probing photoenergy conversion in quantum systems)—designed and built by the group at University of Potsdam—was connected to the beamline [25].

At the FLASH FEL, the X-rays are produced by self-amplified spontaneous emission (SASE), and we used photon energies at the FLASH2 branch in the range of 150 eV to 250 eV tuned by variable gap undulators. Rare-gas photoelectron spectrometers built in the beamline, the OPIS (Online Photoionization Spectrometer) [39], were used to determine the wavelength and spectrum of the emitted light; for the machine settings used in this study, the average bandwidth (including jitter) was found to be 4 eV. This kind of spectrometer does not provide shot-to-shot resolved data. We instead averaged the OPIS spectra for a complete run with minutes of data to determine the average photon energy value for each photon energy bin. The different step sizes for the two energy scans (1 eV and 0.75 eV) were chosen to allow for efficient use of experimental time; a finer step size of about 4 eV effective bandwidth would not improve the data. We scanned with a slightly larger step size at the L_1 -edge, as we expected wider features at the L_1 -edge compared with the $L_{2,3}$ -edge.

The FEL delivers the radiation in trains of pulses with a repetition rate of 10 Hz [40]. Each train consists of 50 pulses at 200 kHz internal repetition rate, with an estimated pulse duration of 150 fs [25]. Pulse energy scans were carried out to avoid X-ray saturation of the obtained electron spectra. During the data collection, the average pulse energy used was 5 μ J. The X-rays are focused by means of Kirkpatrick–Baez (KB) mirrors to a spot of ~ 100 μ m size, located in the interaction region of our magnetic bottle electron spectrometer (MBES) [41]. The X-rays are linearly polarized parallel to the axis of the spectrometer.

Figure 5 presents a sketch of the URSA-PQ apparatus. The use of an MBES allows for high collection efficiency. A permanent magnet with a soft iron pole produces a high magnetic field in the interaction region, which adiabatically changes into a homogeneous solenoid field that guides the confined electrons through an almost 2 m long flight tube [41]. The emitted electrons are detected by a multi-channel plate (MCP) assembly at the end of the flight tube. Their kinetic energy can then be obtained from the time-of-flight measurements. A time-of-flight spectrum was recorded for each pulse of the FEL, and the results were subsequently averaged. An electrostatic lens was used to apply a retardation potential to the electrons as they enter the flight tube, slowing them down and thus increasing the time-of-flight resolution. Calibration of the spectrometer was carried out using Kr-MNN Auger–Meitner electrons [25]. Using the calibration data together with a geometric model of the flight tube, a time-of-flight to kinetic energy conversion function was developed. This function was then adapted to enable the conversion of data acquired under different retardation settings. Specifically, we used recorded krypton spectra to construct a model of the spectrometer and extrapolated it to other retardation settings/energy ranges. The resolution ($E/\Delta E$) was found to be around 40 under the chosen settings [25]. For each X-ray pulse, FLASH provides a shot-to-shot measurement of the pulse energy (photon number) through the use of gas-monitor detectors (GMD). We used these data to normalize our electron spectra.

The 2-tUra sample (acquired from Sigma-Aldrich (St. Louis, MO, USA) and used without further processing) was delivered by a capillary oven [42] heated to 150°C and located near the tip of the permanent magnet of the spectrometer. At this oven temperature, the only tautomer is the oxo-form [23], as noted in a comparison of gas-phase 2-tUra experiments [15,23].

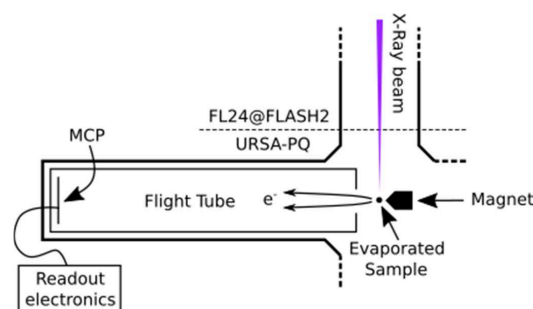


Figure 5. Sketch of the experimental setup. The soft X-rays from FLASH2 are focused into the interaction region of the magnetic bottle spectrometer, where the sample is provided by means of a capillary oven (located above the spectrometer, out of plane of the diagram). The emitted photoelectrons enter the flight tube and are detected by an MCP detector.

5. Conclusions

Here, we present the results of an X-ray sulfur core-level investigation of 2-thiouracil. The data obtained—primarily covering previously unobserved energy ranges—provide novel information about this molecule which is complementary to the currently available literature.

The valence and 2p photoelectron features present a dispersive character, with the electron kinetic energy linearly following the changes in photon energy. However, the Auger–Meitner and Coster–Kronig decay channels are associated with constant kinetic energies and do not show dispersion.

The previously measured value for the sulfur 2p binding energy in 2-tUra of 168 eV [23] is consistent with our observations for both the 2p photoelectron line kinetic energy and the onset of the 2p Auger–Meitner features. Moreover, our NEXAFS spectra show a similar position of the sulfur-2p edge as the already available ion-yield NEXAFS spectra of related sulfur-containing compounds [28], although with a significantly lower resolution in the finer details of our spectrum. This is due to the large bandwidth of the FEL radiation used, acting to broaden the observed features. The future use of a monochromator would help to increase the energy resolution, as in [19]. It increases the shot-to-shot fluctuations when used with SASE sources, but this can be corrected for on a single-shot basis.

To our knowledge, this work is the first available NEXAFS spectrum of 2-tUra at the sulfur 2p and 2s edges.

The observed 2p Auger–Meitner spectrum does not present any fine structure or discernable lines. In other cases, such as OCS, pronounced features in the sulfur Auger–Meitner spectra were observed [26]. We attribute the lack of fine structure to the relatively high number of atoms forming 2-tUra, leading to a high density of dicationic states and thus leading to spectral congestion [27].

Resonant and non-resonant Auger–Meitner emissions can be distinguished by their kinetic energy, with resonant electrons showing a shift of about 10 eV toward higher kinetic energies. Similar shifts are observed in other molecules [32], and are attributed to the spectating electron affecting the energy landscape in which the decay takes place.

At the sulfur L_1 -edge, we observe the dispersive 2p photoline as well as a broad non-dispersing Coster–Kronig band at around 40 eV. Comparisons to a core level spectroscopy study of sulfur atoms on a metal surface confirm our interpretation of the features in the absence of comparable molecular data for this spectral region.

Author Contributions: Data collection: all authors. Data analysis: F.L. and D.M. with the help of M.G. Instrument design/construction: J.M., F.L., D.M. and M.G. with the help of S.D., M.N., M.S.R., R.F. and R.J.S. Paper text: F.L. and M.G. Comments and suggestions on the paper drafts: all authors. All authors have read and agreed to the published version of the manuscript.

Funding: We acknowledge the Volkswagen foundation for a Lichtenberg Professorship. We thank the BMBF for URSA-PQ apparatus funding and for funding J.M. and F.L. via Verbundforschungsprojekt 05K16IP1 and 05K19IP1. Furthermore, we acknowledge DFG funding via grant GU 1478/1-1. T.J.A.W was supported by the US Department of Energy, Office of Science, Basic Energy Sciences, Chemical Sciences, Geosciences, and Biosciences Division. F.C. acknowledges support from the European Research Council under ERC-2014-StG STARLIGHT (grant agreement No. 637756). R.F. acknowledges funding from the Swedish Research Council and the Knut and Alice Wallenberg Foundation, Sweden. T.M. acknowledges the support by the SFB 925, Project A3 of the University of Hamburg.

Institutional Review Board Statement: Not applicable.

Informed Consent Statement: Not applicable.

Data Availability Statement: Data is available upon request.

Acknowledgments: We acknowledge DESY (Hamburg, Germany), a member of the Helmholtz Association HGF, for the provision of experimental facilities. Part of this research was carried out at FLASH2.

Conflicts of Interest: The authors declare no conflict of interest.

Sample Availability: Samples of the compounds are available from Sigma-Aldrich.

References

- Swann, P.F.; Waters, T.R.; Moulton, D.C.; Xu, Y.-Z.; Zheng, Q.; Edwards, M.; Mace, R. Role of Postreplicative DNA Mismatch Repair in the Cytotoxic Action of Thioguanine. *Science* **1996**, *273*, 1109–1111. [[CrossRef](#)] [[PubMed](#)]
- Kramer, K.; Sachsenberg, T.; Beckmann, B.M.; Qamar, S.; Boon, K.-L.; Hentze, M.W.; Kohlbacher, O.; Urlaub, H. Photo-Cross-Linking and High-Resolution Mass Spectrometry for Assignment of RNA-Binding Sites in RNA-Binding Proteins. *Nat. Methods* **2014**, *11*, 1064–1070. [[CrossRef](#)]
- Ashwood, B.; Pollum, M.; Crespo-Hernández, C.E. Photochemical and Photodynamical Properties of Sulfur-Substituted Nucleic Acid Bases. *Photochem. Photobiol.* **2019**, *95*, 33–58. [[CrossRef](#)] [[PubMed](#)]
- Pollum, M.; Jockusch, S.; Crespo-Hernández, C.E. Increase in the Photoreactivity of Uracil Derivatives by Doubling Thionation. *Phys. Chem. Chem. Phys.* **2015**, *17*, 27851–27861. [[CrossRef](#)]
- Matsika, S. Modified Nucleobases. In *Photoinduced Phenomena in Nucleic Acids I*; Barbatti, M., Borin, A.C., Ullrich, S., Eds.; Springer International Publishing: Cham, Switzerland, 2014; Volume 355, pp. 209–243. ISBN 978-3-319-13370-13376.
- Bai, S.; Barbatti, M. Spatial Factors for Triplet Fusion Reaction of Singlet Oxygen Photosensitization. *J. Phys. Chem. Lett.* **2017**, *8*, 5456–5460. [[CrossRef](#)]
- Bai, S.; Barbatti, M. On the Decay of the Triplet State of Thionucleobases. *Phys. Chem. Chem. Phys.* **2017**, *19*, 12674–12682. [[CrossRef](#)]
- Arslançan, S.; Martínez-Fernández, L.; Corral, I. Photophysics and Photochemistry of Canonical Nucleobases' Thioanalogs: From Quantum Mechanical Studies to Time Resolved Experiments. *Molecules* **2017**, *22*, 998. [[CrossRef](#)]
- Brem, R.; Daehn, I.; Karran, P. Efficient DNA Interstrand Crosslinking by 6-Thioguanine and UVA Radiation. *DNA Repair* **2011**, *10*, 869–876. [[CrossRef](#)]
- Zhang, X.; Jeffs, G.; Ren, X.; O'Donovan, P.; Montaner, B.; Perrett, C.M.; Karran, P.; Xu, Y.-Z. Novel DNA Lesions Generated by the Interaction between Therapeutic Thiopurines and UVA Light. *DNA Repair* **2007**, *6*, 344–354. [[CrossRef](#)] [[PubMed](#)]
- Massey, A.; Xu, Y.-Z.; Karran, P. Photoactivation of DNA Thiobases as a Potential Novel Therapeutic Option. *Curr. Biol.* **2001**, *11*, 1142–1146. [[CrossRef](#)]
- Reelfs, O.; Karran, P.; Young, A.R. 4-Thiothymidine Sensitization of DNA to UVA Offers Potential for a Novel Photochemotherapy. *Photochem. Photobiol. Sci.* **2012**, *11*, 148–154. [[CrossRef](#)] [[PubMed](#)]
- Mai, S.; Marquetand, P.; González, L. A Static Picture of the Relaxation and Intersystem Crossing Mechanisms of Photoexcited 2-Thiouracil. *J. Phys. Chem. A* **2015**, *119*, 9524–9533. [[CrossRef](#)]
- Sánchez-Rodríguez, J.A.; Mohamadzade, A.; Mai, S.; Ashwood, B.; Pollum, M.; Marquetand, P.; González, L.; Crespo-Hernández, C.E.; Ullrich, S. 2-Thiouracil Intersystem Crossing Photodynamics Studied by Wavelength-Dependent Photoelectron and Transient Absorption Spectroscopies. *Phys. Chem. Chem. Phys.* **2017**, *19*, 19756–19766. [[CrossRef](#)] [[PubMed](#)]
- Mohamadzade, A.; Bai, S.; Barbatti, M.; Ullrich, S. Intersystem Crossing Dynamics in Singly Substituted Thiouracil Studied by Time-Resolved Photoelectron Spectroscopy: Micro-Environmental Effects Due to Sulfur Position. *Chem. Phys.* **2018**, *515*, 572–579. [[CrossRef](#)]
- Mai, S.; Mohamadzade, A.; Marquetand, P.; González, L.; Ullrich, S. Simulated and Experimental Time-Resolved Photoelectron Spectra of the Intersystem Crossing Dynamics in 2-Thiouracil. *Molecules* **2018**, *23*, 2836. [[CrossRef](#)]
- Stolow, A.; Bragg, A.E.; Neumark, D.M. Femtosecond Time-Resolved Photoelectron Spectroscopy. *Chem. Rev.* **2004**, *104*, 1719–1758. [[CrossRef](#)]

18. McFarland, B.K.; Farrell, J.P.; Miyabe, S.; Tarantelli, F.; Aguilar, A.; Berrah, N.; Bostedt, C.; Bozek, J.D.; Bucksbaum, P.H.; Castagna, J.C.; et al. Ultrafast X-Ray Auger Probing of Photoexcited Molecular Dynamics. *Nat. Commun.* **2014**, *5*, 4235. [CrossRef]
19. Wolf, T.J.A.; Myhre, R.H.; Cryan, J.P.; Coriani, S.; Squibb, R.J.; Battistoni, A.; Berrah, N.; Bostedt, C.; Bucksbaum, P.; Coslovich, G.; et al. Probing Ultrafast $\Pi\pi^*$ / $N\pi^*$ Internal Conversion in Organic Chromophores via K-Edge Resonant Absorption. *Nat. Commun.* **2017**, *8*, 29. [CrossRef] [PubMed]
20. Lever, F.; Mayer, D.; Picconi, D.; Metje, J.; Alisaukas, S.; Calegari, F.; Düsterer, S.; Ehlert, C.; Feifel, R.; Niebuhr, M.; et al. Ultrafast Dynamics of 2-Thiouracil Investigated by Time-Resolved Auger Spectroscopy. *J. Phys. B At. Mol. Opt. Phys.* **2020**, *54*, 014002. [CrossRef]
21. Mayer, D.; Lever, F.; Picconi, D.; Metje, J.; Alisaukas, S.; Calegari, F.; Düsterer, S.; Ehlert, C.; Feifel, R.; Niebuhr, M.; et al. Following UV-Induced Electronic Dynamics of Thiouracil by Ultrafast x-Ray Photoelectron Spectroscopy. Available online: <https://arxiv.org/abs/2102.13431> (accessed on 25 September 2021).
22. Thompson, A.; Vaughan, D. *X-RAY Data Booklet*; Center for X-ray Optics and Advanced Light Source Lawrence, Berkeley National Laboratory: Berkeley, CA, USA, 2009.
23. Giuliano, B.M.; Feyer, V.; Prince, K.C.; Coreno, M.; Evangelisti, L.; Melandri, S.; Caminati, W. Tautomerism in 4-Hydroxypyrimidine, S-Methyl-2-Thiouracil, and 2-Thiouracil. *J. Phys. Chem. A* **2010**, *114*, 12725–12730. [CrossRef] [PubMed]
24. Katritzky, A.R.; Szafran, M.; Pfister-Guillouzo, G. The Tautomeric Equilibria of Thio Analogues of Nucleic Acid Bases. Part 3. Ultraviolet Photoelectron Spectra of 2-Thiouracil and Its Methyl Derivatives. *J. Chem. Soc.* **1990**, *6*, 871–876. [CrossRef]
25. Metje, J.; Lever, F.; Mayer, D.; Squibb, R.J.; Robinson, M.S.; Niebuhr, M.; Feifel, R.; Düsterer, S.; Gühr, M. URSA-PQ: A Mobile and Flexible Pump-Probe Instrument for Gas Phase Samples at the FLASH Free Electron Laser. *Appl. Sci.* **2020**, *10*, 7882. [CrossRef]
26. Carroll, T.X.; Ji, D.; Thomas, T.D. Carbon and Oxygen K α and Sulfur L α Auger Spectra of OCS. *J. Electron. Spectrosc. Relat. Phenom.* **1990**, *51*, 471–486. [CrossRef]
27. Wolf, T.; Holzmeier, F.; Wagner, I.; Berrah, N.; Bostedt, C.; Bozek, J.; Bucksbaum, P.; Coffee, R.; Cryan, J.; Farrell, J.; et al. Observing Femtosecond Fragmentation Using Ultrafast X-ray-Induced Auger Spectra. *Appl. Sci.* **2017**, *7*, 681. [CrossRef]
28. Ankerhold, U.; Esser, B.; von Busch, F. Ionization and Fragmentation of OCS and CS₂ after Photoexcitation around the Sulfur 2p Edge. *Chem. Phys.* **1997**, *220*, 393–407. [CrossRef]
29. Schnorr, K.; Bhattacharjee, A.; Oosterbaan, K.J.; Delcey, M.G.; Yang, Z.; Xue, T.; Attar, A.R.; Chatterley, A.S.; Head-Gordon, M.; Leone, S.R.; et al. Tracing the 267 Nm-Induced Radical Formation in Dimethyl Disulfide Using Time-Resolved X-Ray Absorption Spectroscopy. *J. Phys. Chem. Lett.* **2019**, *10*, 1382–1387. [CrossRef] [PubMed]
30. Armen, G.B.; Aksela, H.; Åberg, T.; Aksela, S. The Resonant Auger Effect. *J. Phys. B At. Mol. Opt. Phys.* **2000**, *33*, R49–R92. [CrossRef]
31. Feifel, R.; Piancastelli, M.N. Core-Level Spectroscopy and Dynamics of Free Molecules. *J. Electron. Spectrosc. Relat. Phenom.* **2011**, *183*, 10–28. [CrossRef]
32. Holzmeier, F.; Wolf, T.J.A.; Gienger, C.; Wagner, I.; Bozek, J.; Nandi, S.; Nicolas, C.; Fischer, I.; Gühr, M.; Fink, R.F. Normal and Resonant Auger Spectroscopy of Isocyanic Acid, HNCO. *J. Chem. Phys.* **2018**, *149*, 034308. [CrossRef] [PubMed]
33. Wolf, T.J.A.; Paul, A.C.; Folkestad, S.D.; Myhre, R.H.; Cryan, J.P.; Berrah, N.; Bucksbaum, P.H.; Coriani, S.; Coslovich, G.; Feifel, R.; et al. Transient Resonant Auger–Meitner Spectra of Photoexcited Thymine. *Faraday Discuss.* **2021**, *228*. [CrossRef] [PubMed]
34. Svensson, S.; Eriksson, B.; Mårtensson, N.; Wendin, G.; Gelius, U. Electron Shake-up and Correlation Satellites and Continuum Shake-off Distributions in X-Ray Photoelectron Spectra of the Rare Gas Atoms. *J. Electron. Spectrosc. Relat. Phenom.* **1988**, *47*, 327–384. [CrossRef]
35. Decleva, P.; Fronzoni, G.; Kivimäki, A.; Álvarez Ruiz, J.; Svensson, S. Shake-up Transitions in S 2p, S 2s and F 1s Photoionization of the SF₆ Molecule. *J. Phys. B At. Mol. Opt. Phys.* **2009**, *42*, 055102. [CrossRef]
36. Föhlisch, A.; Feulner, P.; Hennies, F.; Fink, A.; Menzel, D.; Sanchez-Portal, D.; Echenique, P.M.; Wurth, W. Direct Observation of Electron Dynamics in the Attosecond Domain. *Nature* **2005**, *436*, 373–376. [CrossRef] [PubMed]
37. Faatz, B.; Baboi, N.; Ayvazyan, V.; Balandin, V.; Decking, W.; Düsterer, S.; Eckoldt, H.-J.; Feldhaus, J.; Golubeva, N.; Honkavaara, K.; et al. FLASH II: Perspectives and Challenges. *Nucl. Instrum. METHODS Phys. Res. Sect.-Accel. Spectrometers Detect. Assoc. Equip.* **2011**, *635*, S2–S5. [CrossRef]
38. Kuhlmann, M.; Ploenjes, E. FLASH2 Phontondiagnostics and Beamline Concepts. In *Advances in X-ray Free-Electron Lasers II: Instrumentation*; Tschentscher, T., Tiedtke, K., Eds.; SPIE-International Society of Optical Engineering: Bellingham, WA, USA, 2013; Volume 8778.
39. Braune, M.; Buck, J.; Kuhlmann, M.; Grunewald, S.; Düsterer, S.; Viefhaus, J.; Tiedtke, K. Non-Invasive Online Wavelength Measurements at FLASH2 and Present Benchmark. *J. Synchrotron Radiat.* **2018**, *25*, 3–15. [CrossRef]
40. Faatz, B.; Plönjes, E.; Ackermann, S.; Agababyan, A.; Asgekar, V.; Ayvazyan, V.; Baark, S.; Baboi, N.; Balandin, V.; Von Bargen, N.; et al. Simultaneous Operation of Two Soft X-Ray Free-Electron Lasers Driven by One Linear Accelerator. *New J. Phys.* **2016**, *18*, 062002. [CrossRef]
41. Kruit, P.; Read, F.H. Magnetic Field Paralleliser for 2π Electron-Spectrometer and Electron-Image Magnifier. *J. Phys. [E]* **1983**, *16*, 313–324. [CrossRef]
42. McFarland, B.K.; Berrah, N.; Bostedt, C.; Bozek, J.; Bucksbaum, P.H.; Castagna, J.C.; Coffee, R.N.; Cryan, J.P.; Fang, L.; Farrell, J.P.; et al. Experimental Strategies for Optical Pump–Soft x-Ray Probe Experiments at the LCLS. *J. Phys. Conf. Ser.* **2014**, *488*, 012015. [CrossRef]

Article 4: Data analysis procedures for time-resolved photoelectron spectroscopy at a SASE free electron laser

Dennis Mayer, Fabiano Lever, Markus Gühr

Journal of Physics B: Atomic, Molecular and Optical Physics 55, 054002 (2022), DOI: 10.1088/1361-6455/ac3c91

Abstract. The random nature of self-amplified spontaneous emission (SASE) is a well-known challenge for x-ray core level spectroscopy at SASE free-electron lasers (FELs). Especially in time-resolved experiments that require a combination of good temporal and spectral resolution the jitter and drifts in the spectral characteristics, relative arrival time as well as power fluctuations can smear out spectral-temporal features. We present a combination of methods for the analysis of time-resolved photoelectron spectra based on power and time corrections as well as self-referencing of a strong photoelectron line. Based on sulfur 2p photoelectron spectra of 2-thiouracil taken at the SASE FEL FLASH2, we show that it is possible to correct for some of the photon energy drift and jitter even when reliable shot-to-shot photon energy data is not available. The quality of pump–probe difference spectra improves as random jumps in energy between delay points reduce significantly. The data analysis allows to identify coherent oscillations of 1 eV shift on the mean photoelectron line of 4 eV width with an error of less than 0.1 eV.

Copyright note. © 2022 by the authors. Licensee IOP Publishing. This article is an open access article distributed under the terms and conditions of the Creative Commons Attribution (CC BY) license (<https://creativecommons.org/licenses/by/4.0/>).

Data analysis procedures for time-resolved x-ray photoelectron spectroscopy at a SASE free-electron-laser

Dennis Mayer* , Fabiano Lever  and Markus Gühr* 

Institut für Physik und Astronomie, Universität Potsdam, 14476 Potsdam, Germany

E-mail: dmayer@uni-potsdam.de and mguehr@uni-potsdam.de

Received 9 September 2021

Accepted for publication 22 November 2021

Published 21 March 2022



CrossMark

Abstract

The random nature of self-amplified spontaneous emission (SASE) is a well-known challenge for x-ray core level spectroscopy at SASE free-electron lasers (FELs). Especially in time-resolved experiments that require a combination of good temporal and spectral resolution the jitter and drifts in the spectral characteristics, relative arrival time as well as power fluctuations can smear out spectral-temporal features. We present a combination of methods for the analysis of time-resolved photoelectron spectra based on power and time corrections as well as self-referencing of a strong photoelectron line. Based on sulfur 2p photoelectron spectra of 2-thiouracil taken at the SASE FEL FLASH2, we show that it is possible to correct for some of the photon energy drift and jitter even when reliable shot-to-shot photon energy data is not available. The quality of pump–probe difference spectra improves as random jumps in energy between delay points reduce significantly. The data analysis allows to identify coherent oscillations of 1 eV shift on the mean photoelectron line of 4 eV width with an error of less than 0.1 eV.

Keywords: free-electron laser, photoelectron spectroscopy, FLASH

(Some figures may appear in colour only in the online journal)


1. Introduction

Absorption of light in molecules often triggers complex ultrafast relaxation processes [1–3]. In the course of this, the molecule converts light energy into a variety of other energetic forms such as molecular vibration or rotation, photoisomerisation or bond dissociation. A standard technique to study the dynamics of isolated molecules in gas phase is time-resolved photoelectron spectroscopy [4, 5]. Here, a first light pulse, often in the visible or UV range, promotes electrons into an excited state and triggers the ultrafast relaxation process.

A second, delayed UV pulse ionises valence electrons of the excited molecule. The emitted photoelectrons are detected and the time-dependent spectrum as well as angular distribution help to unravel the coupled electron-nuclear dynamics using valence ionization. Probing time-resolved core-electron spectra via ultrafast x-ray pulses offers a fundamentally different and new view on the molecular dynamics [6–11] due to the x-ray-typical element- and site-selectivity [12, 13] together with the high localization of core-electrons.

Free electron lasers (FEL) have developed as promising tools to study the electronic structure and dynamics of matter with x-ray light due to their high brilliance and pulse durations in the femtosecond range [14–20]. However, the pulse characteristics of the FEL sources based on SASE show strong fluctuations in time-structure, pulse energy as well as spectral characteristics. A seeded free-electron laser like FERMI [17] does not exhibit these problems, however seeding techniques like HGHG [21, 22] and EEHG [23, 24] can only realistically

* Authors to whom the correspondence should be addressed.

 Original content from this work may be used under the terms of the [Creative Commons Attribution 4.0 licence](https://creativecommons.org/licenses/by/4.0/). Any further distribution of this work must maintain attribution to the author(s) and the title of the work, journal citation and DOI.

be implemented up to the oxygen K-edge with current technology. At higher photon energies, self-seeding schemes might be used as a more standard way in future to reduce at least the spectral jitter of a SASE source, as demonstrated in the hard x-ray [25] and soft x-ray spectral regions [26].

Currently, jitter-problems of SASE FELs are to some extent eased using single-shot detection of all relevant pulse parameters and appropriate binning and filtering of the experimental observables with respect to this multidimensional pulse-jitter-space. This scheme has been used since the very first FEL experiments for the correction of pulse-energy and pulse arrival jitter with respect to an optical (excitation) laser pulse [27–29].

Spectral jitter is mostly avoided by inserting monochromators, such as the PG at FLASH [30] or the SXR monochromator at LCLS [31]. Those devices however decrease the available flux, elongate the pulse duration, if not designed in a pulse tilt compensation way [32], and convert spectral jitter into pulse energy jitter. Alternatively, an accurate detection of the spectral fluctuations on a single shot basis can be used to deduce the average photon energy and thus a single shot correction of the spectra [33]. Newer correlation based approaches using all features in the detected spectra can result in a full spectral reconstruction of the x-ray induced observable [34–37].

In this paper we present some data analysis methods for time-resolved x-ray photoelectron spectroscopy (TR-XPS) at a SASE FEL source. The molecular sample 2-thiouracil (2-tUra) is excited by a femtosecond-duration ultraviolet (UV) pulse and probed by a SASE FEL pulse at around 270 eV photon energy. We use the known single shot correction methods with respect to x-ray pulse energy and arrival time. For our experiment at FLASH2, we had no single-shot spectral tool at hand. The online photoionization spectrometer (OPIS) spectral tool [38] implemented at this FEL currently only delivers spectral information averaged over a few ten to hundred shot range. We developed a method for the correction of x-ray photon energy drifts and jitter in time-resolved photoelectron spectra. The method is based on correcting the UV-pumped molecular XPS using intermittent non-UV pumped spectra. This allows to reduce the influence of drifts and jitter on the final averaged spectrum and helps to make relative changes between non-excited and excited spectra more distinct.

2. Methods

2.1. Experiment

The data for this publication was collected during a FLASH2 beamtime in 2019. The 2-tUra sample was studied by means of time-resolved UV pump x-ray probe photoelectron spectroscopy using the URSA-PQ apparatus [6, 39, 40]. The molecule was excited with 269 nm light and probed with a delayed x-ray pulse with a photon energy of 272 eV, which is above the sulfur L_1 edge. The emitted electrons were slowed down by a retardation voltage of 80 V and their kinetic energy was measured using a magnetic-bottle time-of-flight spectrometer [41]. The retardation allowed the detection of the sulfur 2p

photo and Auger electrons without being interfered by other spectral features. The FEL delivered pulse trains that consist of 50 shots with a 5 μ s intra-train spacing, at a 10 Hz rate. The UV laser for molecular excitation ran in burst mode synchronized to the FEL so that every second x-ray pulse hit an excited molecular ensemble. The shots with odd shot index did not have a UV laser active, whereas the shots with even shot index were coincident with the UV laser firing.

We took time-dependent data by scanning the delay between the UV pulse and the x-ray pulse. Delays were chosen in a randomized manner and several of the random-delay datasets were collected to improve statistics.

The FLASH data-acquisition system provided measurements of different x-ray and UV beam parameters. Pulse energies were detected by a gas-monitor detector (GMD) for the x-ray and a photodiode for the UV. The OPIS measured the averaged photon energy of the x-ray pulses [38]. The temporal jitter of the x-ray pulses with respect to the FLASH master clock was measured by a bunch arrival monitor (BAM) [27, 42].

2.2. Analysis methods

2.2.1. Data preparation. Before analysing the data, the raw data set was ‘reshaped’ for easier access. The electron time-of-flight spectra were originally saved/delivered by FLASH bunch-wise, which means that the 50 spectra for a pulse-train were saved in a single trace. In this reshaping step, the trace was split into 50 spectra of equal size and saved in a separate HDF (hierarchical data format) file along with important parameters such as GMD, UV pulse energy, OPIS, BAM, retardation and others. The data was indexed by FLASH’s internal bunch number and an index between 0 and 49 representing the pulse position within the pulse train. The latter number is from now on called shot number.

2.2.2. Delay correction and binning. The delays set during the experiment were corrected by the bunch arrival time i.e., the BAM values are subtracted from the delays. The resulting change in the distribution of delays was also used to define the delay bins such that all bins have similar statistics.

2.2.3. Spectral correction. In contrast to the well-established delay correction, the self-referencing spectral correction scheme is novel and thus a careful step-by-step analysis is presented. To start, the self-referencing was applied to unpumped spectra only. All spectra were first converted from time-of-flight to kinetic energy and their spectral intensity rescaled using the Jacobian. In addition, the spectra were normalised by their corresponding GMD value. The first moment of the spectrum was calculated within a close area around the expected S 2p photoline position (100–106 eV kinetic energy). The spectra were then shifted to a reference position which was defined by the first processed (averaged) spectrum. The spectra were then summed up to calculate the first and second moment and compared to the values for an uncorrected averaged spectrum.

For the UV-pumped molecular spectra, the data handling begins exactly like in the unpumped case. The spectra were normalised to GMD and converted to kinetic energy. In the

pump–probe case, it needs to be considered that the photoelectron line is altered by a UV pulse, which is exactly the effect we want to analyse. We thus developed a method to deduce this UV-induced change on top of a statistical SASE fluctuation without having the raw SASE spectrum available. We tried two options to correct the UV altered spectra for the SASE jitter effects:

- (a) Assuming that the jitter of the FEL photon energy between consecutive pulses is negligible, one can use the photoline position of unpumped shots for correcting consecutive UV-pumped spectra.
- (b) Make use of photon energy correlations within a pulse train. A certain number of spectra is binned by shot number (resulting in 50 average traces) and the photoline position of these averaged spectra is determined. The position trend of the unaltered spectra over the pulse train is then fitted by a low order polynomial to interpolate for the intermediate altered spectra.

Regardless of the approach used, the determined (average) position was used to shift the raw spectra towards a reference position. With the shifted electron spectra, shot-to-shot difference spectra were calculated.

2.3. Simulation

A simulation serves to better understand how the spectral correction method works in the static case. Raw photoelectron spectra were simulated by summing a certain number of ‘electron hits’ together. These electron hits in the kinetic energy domain were defined by a product of a Heaviside function and an exponential decay. The appearance position of an electron hit was randomly selected based on a normal distribution. The centre and width of this normal distribution were based on the values from the S 2p photoline from the experiment, but varied slightly for each spectrum within a small window around the mean value (to simulate jitter). On top of a random variation a shot-to-shot drift could be applied to the central position either as a linear drift or as an oscillation. The generated spectra then underwent the same correction algorithm as described in section 2.2.3.

The following scenarios were simulated: jitter only, jitter + drift, and jitter + oscillation. For each scenario, 10 runs of the simulation were done with 50 000 spectra per run. The number of electron hits per spectrum was set to 50 and the decay constant to 0.1 eV. The mean of the normal distribution was set to 103 eV and the width to 1.42 eV. The mean was randomised within a window ($\Delta E/E$) of 0.125% and the width within a 5% window ($\Delta w/w$). The period of the applied oscillation was 50 spectra and the relative amplitude 0.25% of the mean central position. The slope of the linear drift was 10 μeV per spectrum giving a drift of the mean of 0.5 eV after 50 000 spectra.

3. Results and discussion

3.1. Spectral correction of unpumped spectra

Figure 1(a) shows raw and averaged experimental S 2p photoelectron spectra of 2-tUra. The raw trace already shows a

significant signal within the expected area of the photoline (100–106 eV). High-resolution S2p XPS in 2-tUra shows two lines of 0.5 eV width which are spin–orbit split by 1.2 eV [43]. Previous experiments predict a resolution below 1 eV for our experimental settings [39]. The appearance of signal out of this narrow interval of 2 eV is thus due to the spectrum of the x-ray pulses produced by the SASE process. The experimental resolution is not sufficient to resolve the spin–orbit splitting. The spikes disappear with increasing number of spectra in the average. After about 50 to 100 averaged raw spectra, the spectrum follows a fairly smooth Gaussian-like profile. The smaller peak on the lower kinetic energy side (~ 96 eV) is a correlation satellite feature.

The mean of the photoline distribution is shown for a 5 shot average over a one-hour time window in figure 1(b). The fast jitter of the photoline centre covers a range of about 1–2 eV. A slow drift can be identified, which is in the order of about 0.5 to 1 eV. Both contribute significantly to the photoline width when the spectra are averaged and thus limit spectral resolution.

We judge the effectiveness of the spectral correction the photoelectron-line width for different datasets without molecular pre-excitation. In figure 1(c), the width of the corrected photoline is shown for different average sizes (solid line) and compared to the value of the uncorrected case (dashed line of same colour). Here, averaged shots mean the number of spectra averaged to determine the position of the photoline before correcting the spectra. Three example data sets of about 700 000 shots are shown. The corrected spectral widths are a few percent below the uncorrected case which tells us that the correction algorithm works towards the right direction. Furthermore, the width decreases continuously when decreasing the average towards the shot-to-shot correction ($x = 1$), which is giving the best results there. In the best case, the corrected width is lying $\sim 3\%$ under the uncorrected case. Within the average size of 1–10 the change in width is very steep. Above, the change is fairly flat and the offset between corrected and uncorrected data reduces slowly within the shown window. All three datasets also show outliers at ~ 5 , ~ 10 and ~ 25 . These numbers are (close to) integer divisors of 50 which is the length of the FEL pulse train. It appears that the algorithm picks up harmonics of this length. A fast Fourier-transform of a time series of the photoline (not shown here) does indeed show peaks at frequencies that coincide with the size of the FEL pulse train and its sub-harmonics ($50/n$).

For figure 1(d), the correction algorithm has been applied to simulated (electron) spectra to systematically understand the features shown in figure 1(c). Three different scenarios were studied. In the first scenario the spectra only show a jitter in the mean photon energy as well as in the width (blue line). It can be seen that the width for the corrected spectra rapidly approaches the uncorrected mean value. Thus, the steep change for low averages in figure 1(c) can be attributed to the correction of the fast FEL jitter. The second scenario included a linear drift of the mean energy of the photoline (orange). At the beginning, the curve behaves exactly as the jitter-only curve. However, after it flattens out it still shows a significant offset towards the uncorrected value. The offset we observe in figure 1(c) thus likely results from longer term drift of the FEL. In the third

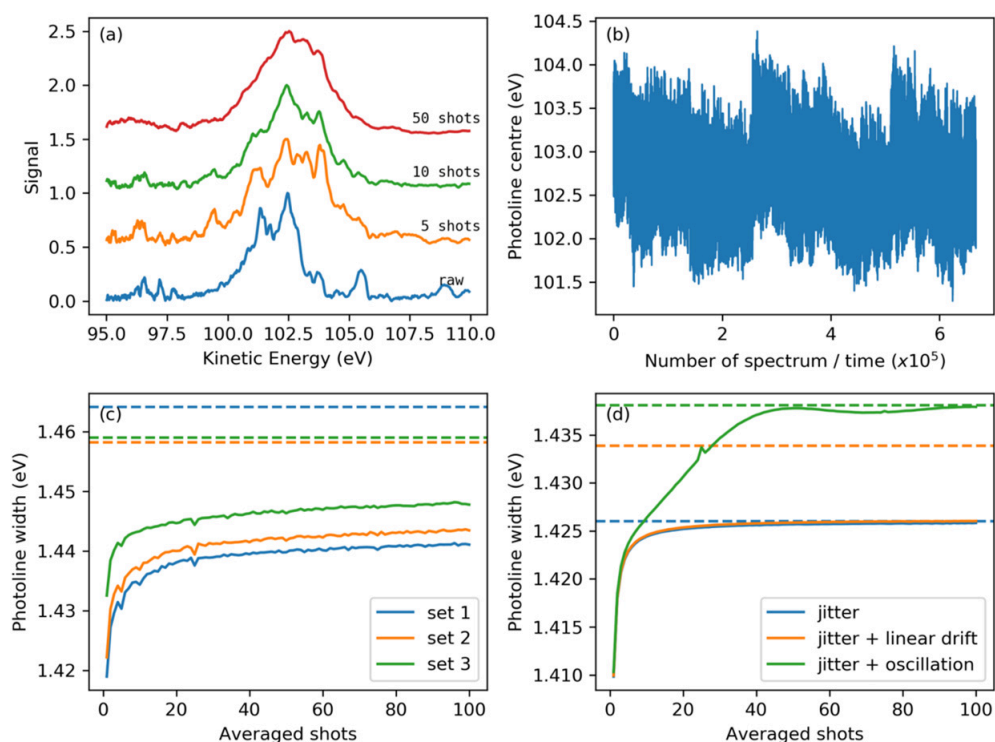


Figure 1. (a) Raw and averaged photoelectron spectra of sulfur 2p line of 2-tUra. (b) Time-series of the photoline centre over time (5 shot average). (c) Width of drift-corrected spectra for different sampling averages (solid lines) for three 1 h long data sets (~700 000 shots each) compared to the width of the uncorrected spectra (dashed lines). (d) Simulations for averaging of photoelectron spectra with different origins for photoline broadening.

scenario an oscillation with a period of 50 shots was applied instead of a linear drift to check if periodical features lead to outliers in the graph. Indeed, a peak at 25 can be observed. It has the opposite direction compared to the experiment, which might just be due to the random phase of the oscillation. Apart from this outlier, the curve looks quite different compared to the other two simulated scenarios. There is a less steep increase of the width up to the uncorrected value and after that the width ‘bounces back’ slightly giving another local minimum. These features are, however, not observed in the experimental data so that we can exclude a phase stable, long term oscillation of the central photon energy of the FEL.

We can summarise at this point that correcting the raw spectra by means of the photoline position does improve the spectral width on the few percent level. We could identify that jitter and drift of the FEL have a major impact on the photoline but can be corrected using the self-referencing method. However, the method requires a strong photoelectron signal in order to properly determine the centre of mass of the photoline spectrum. If noise or a strong background dominates the raw spectra, a shot-to-shot determination of the photoline position may fail and will make the shot-to-shot corrected spectra worse than spectra that were corrected based on an average. Also, the spectral resolution is still limited by the bandwidth

of the SASE radiation. Based on figure 1 and the assumption that in the static case both jitter and drift are properly corrected, it can be estimated that the bandwidth in the experiment was in the order of 1.3% or 3.5 eV FWHM. With this it is not possible to resolve the spin-orbit splitting of the S2p photoelectrons which is 1.2 eV [43]. We have to note that a large bandwidth of the FEL is also a drawback for this self-referencing approach when it comes to reducing the average spectral width. The width reduction introduced by the correction of jitter and drift depends highly on the ratio between mean spectral width of the single traces and their distance towards the mean/reference position. If the bandwidth of the FEL would have been smaller i.e., below 1 eV the relative improvement in spectral width would have been much stronger after the correction.

3.2. Correction for pump-probe spectra

The UV pre-excitation alters the spectral shape, the effect which we are trying to isolate. For the pump-probe spectra one needs to exploit the spectra without UV-excitation and their correlations in order to correct the UV pumped spectra. Figure 2(a) shows the photoline centre in the pulse train consisting of 50 spectra, binned according to shot index. The underlying dataset consists of over 8000 pulse trains. The filled symbols show the photoline positions for unpumped spectra

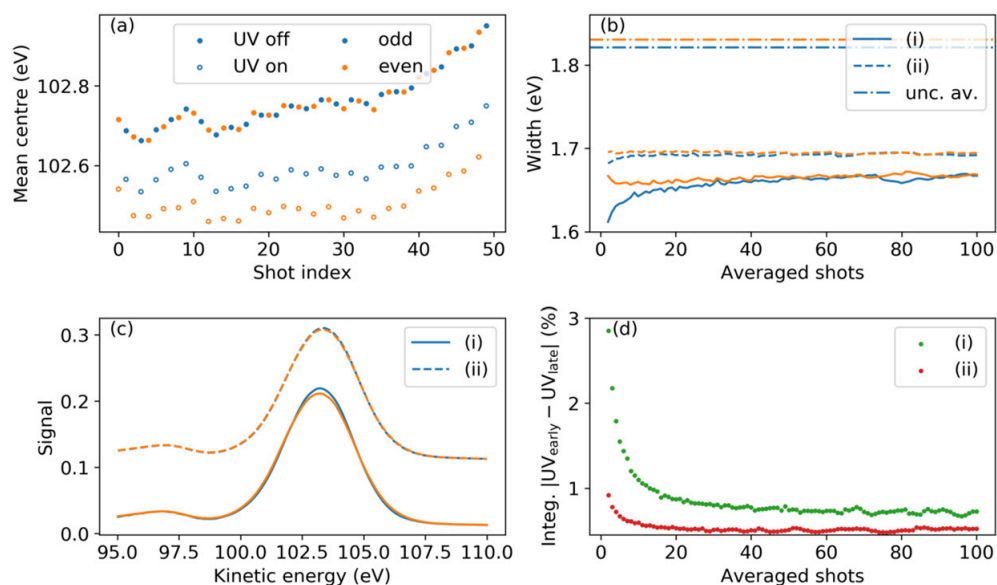


Figure 2. (a) Average photoline position binned by shot-index in a pulse train for spectra without ('UV off', solid symbols) and with UV pre-excitation ('UV on', open symbols) on every second shot. Odd shots are blue, even ones orange. (b) Width of the corrected average UV-off spectra for different intermediate averages and correction separated in even and odd shots. The dash-dot lines (labelled with 'unc. av.') show the width of the uncorrected average spectra. (i) and (ii) Indicate the method used to determine photoline position of pumped shots (see methods). (c) Corrected photoelectron spectra for even and odd shots. The spectra are vertically offset on purpose. (d) Integrated difference between corrected even and odd spectra normalised to the integral of the odd spectra. The colour code in (a) applies also for (b) and (c).

only ('UV off'), for the opened symbols every second shot is pumped with UV light ('UV on'). Even and odd shots (meaning pumped and non-pumped spectra) are coloured differently. From 0 to 49, the spectral position is gradually increasing with the shot number by about 250 meV while the shot-to-shot difference is in the order of 10 meV. In contrast, the pumped data shows a strong offset between even (UV-pumped) and odd (not UV-pumped) shots. The curve for both, however, looks similar to the fully non-pumped case. The fact that the unpumped (odd) shots of the two datasets do not coincide is due to the fact that the FEL drifted in between the two datasets chosen here. Two ways for correction can be considered here. (i) Similar to the correction of the x-ray-only spectra, the photoline is determined either from shot-to-shot or by averaging consecutive *odd* shots and the values are used also for the intermediate UV-pumped spectra. (ii) The spectra are binned by shot number and the trend as shown in figure 2(a) is fitted for the odd spectra in order to interpolate the centre position for the even spectra. The latter option will reduce the width of the photoline less because the interpolation via fitting gives another layer of averaging. However, the first option will suffer from shot-to-shot jitter a lot. The jitter is also the reason why both options will not show the best width for the shot-to-shot correction. In the following we will concentrate on the non-pumped spectra only to understand how the correction methods alter the spectra.

Figure 2(b) shows the width of the corrected spectra for both even and odd shots in the case of non-pumped dataset

(molecules not excited before the x-ray probe) and compares both approaches. The solid line shows the width for (i) and the dashed line for (ii). In both cases, the blue curve (odd, x-ray-only spectra) reproduces the major trend as shown in figure 1(c). Though, the fast jitter correction i.e., the steep width change for low averages, is much more pronounced when an average over consecutive shots is used. Additionally, the width is slightly larger for option (ii) than for (i). The orange lines represent the even spectra and show a significantly different behaviour. In contrast to their odd counterparts a jitter correction cannot be observed. Instead, the curves show a minimum for low average at about 2–5 shots. We keep in mind that only odd shots were used for correction. Thus, this difference between the blue and the orange line results from the shot-to-shot jitter. With a weak average it is possible to correct for the slow drifts in the FEL which is the same for even and odd shots. When even shots are corrected on a single-shot base the jitter contributes more strongly to width as it is now not averaged out. For both correction options though, the curves for even and odd are close together latest after an average of 50 shots.

If not UV-pumped, the (averaged) photoelectron spectra for even and odd FEL shots should be very similar before and after correcting the FEL jitter and drift. However, figure 2(b) indicates that for weak averages the spectra resulting from even and odd shots, respectively, appear not to be similar due to the problem that the fast jitter in the even spectra cannot be corrected. However, it is necessary for a reasonable data analysis that the spectra are fairly similar so that the correction does not

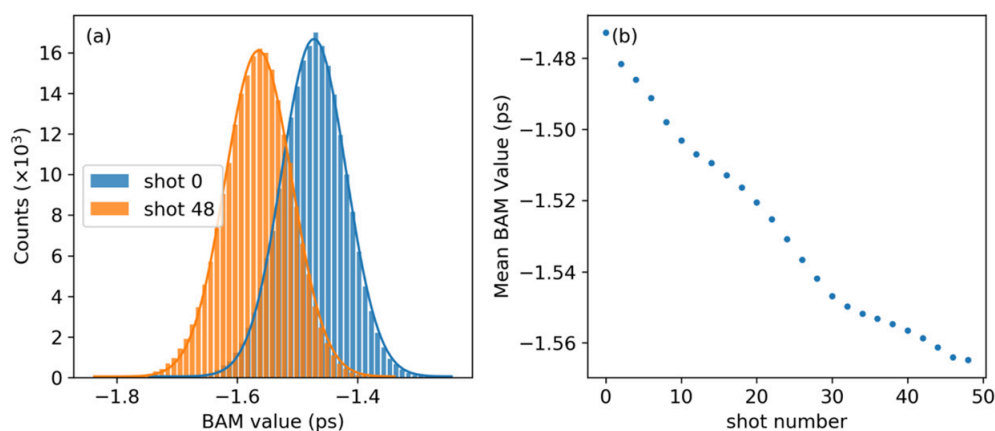


Figure 3. (a) Histograms of the BAM data for the first and second to last pulse in the FEL pulsetrain. (b) Central positions of the BAM distributions for pulses with even shot number.

introduce additional artifacts. Figure 2(c) shows the corrected electron spectra for a 2-shot intermediate average. For method (i), even and odd spectra show an obvious difference in the centre and on the sides. The even spectrum is broader than the odd spectrum but has a similar signal strength. In contrast, the spectra for the (ii) case do not show pronounced differences on the same scale. This difference between the even and odd non-pumped spectra is thus an important criterion to find a reasonable value for the intermediate average. Figure 2(d) shows the integrated difference signal between even and odd spectra for different averages normalised to the respective integral of the corrected odd spectrum. In both cases a weak average increases the difference between even and odd spectrum. The increase for (i) is stronger than for (ii) as the latter has an additional layer of averaging due to the pulse train fit. For (i) the difference reaches a value of $<1\%$ for an average of at least 13 spectra. At the same point, the value for (ii) is $<0.6\%$. A roughly constant value is reached at about 50 shots for (i) and about 20 shots for (ii).

From the perspective of avoiding additional artifacts in the difference signal between pumped and unpumped spectra it appears to be more reasonable to use method (ii). The difference is less than 1% of the original photoelectron spectrum and at least major drifts of the FEL can be corrected. However, an appropriate value for the correction induced difference must be considered against the UV induced difference signal. In our particular case of 2-tUra, the UV-induced excited-state signal is in the order of 15%–20% of the ground-state photoelectron spectrum. With 20 averaged spectra for (ii), the induced difference signal is 0.55% and thus about 30 times weaker than UV induced signal.

3.3. Time-resolved difference spectra

Before we come to the effect of the spectral correction on the difference spectra, we want to focus on the BAM correction for the delay between the UV pump and x-ray probe pulses. The BAM tracks the arrival time of the x-ray pulse (or more

precisely the electron beam) with respect to the FLASH master clock to which the UV laser is synchronized [27, 28]. This allows for a correction of the UV-pump x-ray probe delay and also rebinning of the delays different to the values set during the experiment. Figure 3(a) shows histograms of the measured BAM values for the first and second to last pulse in the pulse train. The distribution is Gaussian in both cases. The centre for the first pulse is -1.47 ps and for the other -1.56 ps as determined with a Gaussian fit (solid line). The width σ (the arrival time jitter) is (53.6 ± 0.3) fs and (55.2 ± 0.4) fs, respectively. In figure 3(b) the mean BAM values are shown for all even pulses of the pulsetrain i.e., pulses that are accompanied by an UV pulse. A clear trend to lower values is visible from first to the last pulse. Even though it is only 90 fs in the mean this can have significant impact on delays that are separated with steps below 100 fs [28] which is the case for delays around time-zero in our experiment.

We now turn to the experimental difference spectra. The molecular dynamics behind them are investigated in reference [6]. Figure 4 shows the delay dependent ‘UV on’–‘UV off’ difference spectra of the S2p photoline of 2-tUra in a false colour plot (a)–(c) in addition with further analysis (d)–(i). For the left column (a), (d) and (g) the data was only corrected by the pulse energy of the x-ray pulses (GMD) and the Jacobian renormalisation as the data was converted from time-of-flight to kinetic energy. In general, the difference spectrum has two main contributions i.e., a negative depletion feature (blue) at about 103 eV kinetic energy and a positive gain feature (red) at about 100 eV. The false-colour plot (a) shows sudden jumps in the spectral position of these features. In figure 4(d) a sum of two Gaussian functions was fitted to the difference spectra and the resulting mean positions for the negative and positive lobe were plotted vs delay. Especially for the positive lobe the values scatter strongly and no transient features can be observed there. Also, the values for the negative lobe scatter but one could guess an increase in kinetic energy there. The integrated signal for the two contributions (in part (g)) show a clear

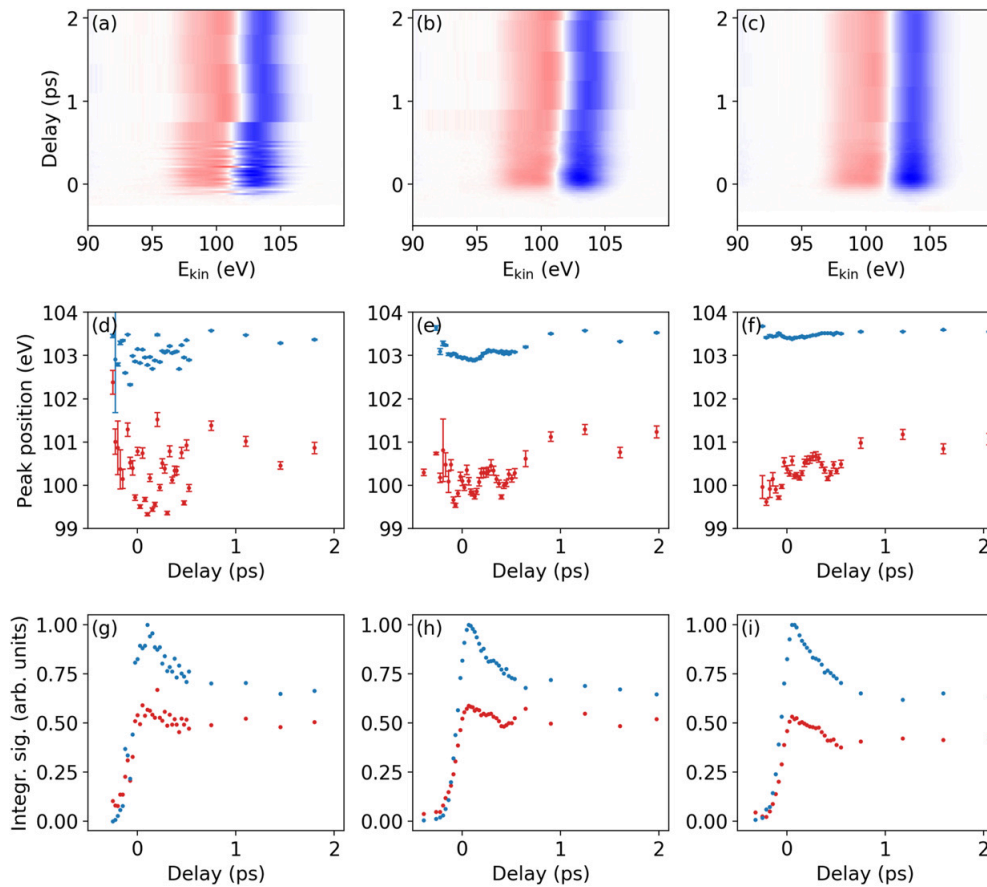


Figure 4. Difference spectra of 2-tUra and analysis with different correction steps applied. (a) and (b) Delay dependent false-colour plot of S2p difference spectra. (d)–(f) Centre positions of the positive and negative lobe from a double Gaussian fit to the data in (a)–(c). (g)–(i) Integrate absolute signal of the positive and negative contribution to the difference spectrum. The left column (a), (d) and (g) includes only a GMD normalisation of the raw spectra and Jacobian renormalisation due to conversion from time-of-flight to kinetic energy. The delay bins are fixed according to experiment. The middle column (b), (e) and (h) adds a BAM correction to the delays and the bins are chosen in such a way to have equal statistics. The right column (c), (f) and (i) adds the previously discussed spectral correction.

delay-dependent behaviour. The signal rises and parts of the signal quickly decay. However, the dots scatter considerably.

The spectral jumps result from various issues with the FEL photon energy. First, jitter and drift of the FEL photon energy introduce different mean photon energies for each delay which results in a jitter or even drift in the spectra. Picking up spectral drift as a systematic error was suppressed by randomly scanning the delays during the measurement. Second, the jitter effect is increased by the fact that the FEL pulsetrain shows a trend in both the photon energy (figure 2(a)) as well as in the BAM data (figure 3(a)) and both are correlated. The first pulse of the train has a slightly lower energy than the last one, while the first pulse arrives about 90 fs earlier than the last one. This means that especially around time-zero where finer delay steps were chosen the binning of the spectra is wrong and thus the spectral position of the features is off.

In the second column of figure 4 (panels (b), (e) and (h)) the BAM values are included in the analysis on a single shot basis. The arrival times were subtracted from the delays and the new more precise delays were binned so that each bin has about the same number of the spectra. The false-colour plot in figure 4(b) appears much smoother which means that the number of sudden spectral shifts between the delays has reduced significantly. The central positions from the Gaussian fit in panel (e) now show clear transients for each lobe as the scattering has reduced. Interestingly, the positive lobe does not only show a trend but an oscillation in the vicinity of time-zero. This is an interesting improvement in the data quality. Also, the dots in the intensity curve in figure 4(h) scatter less as all bins now have equal statistics. A delay-dependent decay can now be clearly observed in the negative lobe and to a much weaker extent in the positive lobe.

However, we still observe spectral jumps, best visible in the difference spectra shown in panel (b), resulting from spectral jitter and drift of the FEL. We now apply the spectral correction routines, developed above, on top of all other corrections. An average of 50 pulses was used to determine the photoline positions within the pulsetrain. The false-colour plot becomes even more smooth as most of the sudden jumps are corrected. The trend in the position of the negative lobe has significantly reduced and the values appear nearly as a straight line. This suggests that most of the spectral movement seen in figures 4(d) and (e) arises from the FEL. The oscillation in the positive lobe's position is still visible which suggests that it is indeed a real molecular response. The noise on the integrated signal in figure 4(g) has nearly disappeared in figure 4(i). An ultrafast decay is now clearly visible in both contributions.

4. Conclusion

We have presented analysis methods for (time-resolved) photoelectron spectra that utilise beam arrival times and the photoline itself to correct delays between the pump and probe pulse as well as instabilities and drifts in the FEL photon energy when shot-to-shot photon energy data is not available. We could show that the method optimises the spectral width of the sulfur 2p photoline in the static case, verifying that effects from jitter and drift in the photon energy are reduced by the correction. Utilising the trend of the kinetic energy of the photoline over the pulse train allowed to correct also the UV altered spectra and in consequence improved the time-resolved difference spectra.

Referencing the photoline on itself is a fairly simple approach to correct for instabilities in the FEL photon energy resulting from e.g., the SASE process. However, it is only possible to correct both jitter and drift of the FEL in the static case because here the method does not need to rely on correlation within the FEL parameters. In the pump-probe case, the shot-to-shot jitter cannot be corrected because adjusting the UV altered spectra relies on correlations in the photon energy between the x-ray pulses which requires at least a weak averaging of the spectra.

Sub-bandwidth resolution cannot be achieved with this approach and since the spectra are a convolution of the spin-orbit split S2p line and the SASE spectrum it would require full information about the latter. It is possible to achieve sub-bandwidth resolution with additional information about the SASE spectrum was recently demonstrated by Li *et al* [34–37]. Li *et al* could show that this approach works for one- [34] and two-dimensional [37] static Auger and photoelectron spectroscopy and delivers sub-bandwidth resolution for the studied spectral features. They also adapted the method to an x-ray pump-probe experiment [35] and could show that the 'spooktroscopy' approach is able to separate overlapping signals from pump and probe pulses.

Further improvement for tracking and correcting SASE related instabilities in the data collected might come from machine learning (ML) and the usage of (deep) neural networks (NN). Over the last years and with increasing general

interest in this field, first studies have been conducted to investigate how ML and NN may help data analysis. At LCLS, a study showed that a combination of fast and slow measurements of FEL beam parameters can be used to predict parameters such as intensity, spectrum or temporal profile on a shot-to-shot basis [44]. A different study showed that using simulated SASE spectra to train a deep NN allows to identify the SASE fluctuations in electron spectra and to extract the sample response [45].

Acknowledgments

We thank the Volkswagen foundation for funding via a Lichtenberg Professorship. We thank the BMBF for funding the URSA-PQ apparatus and for funding FL via Verbundforschungsproject 05K16IP1 and 05K19IP1. We acknowledge DFG funding via Grant GU 1478/1-1 (MG). We acknowledge DESY (Hamburg, Germany), a member of the Helmholtz Association HGF, for the provision of experimental facilities. Part of this research was carried out at FLASH2. The experiment data underlying this data-analysis study was performed at FLASH2 by the authors together with J Metje, S Alisauskas, F Calegari, S Düsterer, R Feifel, M Niebuhr, B Manschwetus, M Kuhlman, T Mazza, M S Robinson, R J Squibb, A Trabattoni, M Wallner and T J A Wolf.

Data availability statement

The data that support the findings of this study are available upon reasonable request from the authors.

ORCID iDs

Dennis Mayer  <https://orcid.org/0000-0002-1858-6818>

Fabiano Lever  <https://orcid.org/0000-0002-8448-7594>

Markus Gühr  <https://orcid.org/0000-0002-9111-8981>

References

- [1] Michl J and Bonacic-Koutecky V 1990 *Electronic Aspects of Organic Photochemistry* (New York: Interscience (Wiley-Interscience))
- [2] Klessinger M and Michl J 1995 *Excited States and Photochemistry of Organic Molecules* (New York: VCH)
- [3] Domcke W, Yarkony D R and Köppel H 2011 *Conical Intersections: Theory, Computation and Experiment* vol 17 (Singapore: World Scientific)
- [4] Stolow A, Bragg A E and Neumark D M 2004 *Chem. Rev.* **104** 1719–58
- [5] Stolow A 2003 *Annu. Rev. Phys. Chem.* **54** 89–119
- [6] Mayer D *et al* 2022 *Nat. Commun.* **13** 198
- [7] Brauße F *et al* 2018 *Phys. Rev. A* **97** 043429
- [8] Inhester L, Li Z, Zhu X, Medvedev N and Wolf T J A 2019 *J. Phys. Chem. Lett.* **10** 6536–44
- [9] Bennett K, Kowalewski M and Mukamel S 2016 *J. Chem. Theory Comput.* **12** 740–52
- [10] Neville S P, Averbukh V, Patchkovskii S, Ruberti M, Yun R, Chergui M, Stolow A and Schuurman M S 2016 *Faraday Discuss.* **194** 117–45

- [11] Leitner T et al 2018 *J. Chem. Phys.* **149** 044307
- [12] Siegbahn K 1969 *ESCA Applied to Free Molecules* (Amsterdam: North-Holland)
- [13] Gelius U 1974 *Phys. Scr.* **9** 133–47
- [14] Ackermann W et al 2007 *Nat. Photon.* **1** 336–42
- [15] Emma P et al 2010 *Nat. Photon.* **4** 641–7
- [16] Ishikawa T et al 2012 *Nat. Photon.* **6** 540–4
- [17] Allaria E et al 2012 *Nat. Photon.* **6** 699–704
- [18] Nam I et al 2021 *Nat. Photon.* **15** 435–41
- [19] Rouxel J R et al 2021 *Nat. Photon.* **15** 499–503
- [20] Yan J et al 2021 *Phys. Rev. Lett.* **126** 084801
- [21] Yu L-H et al 2000 *Science* **289** 932–4
- [22] Doyuran A et al 2001 *Phys. Rev. Lett.* **86** 5902–5
- [23] Stupakov G 2009 *Phys. Rev. Lett.* **102** 074801
- [24] Rebernik Ribič P et al 2019 *Nat. Photon.* **13** 555–61
- [25] Amann J et al 2012 *Nat. Photon.* **6** 693–8
- [26] Ratner D et al 2015 *Phys. Rev. Lett.* **114** 054801
- [27] Schulz S et al 2015 *Nat. Commun.* **6** 5938
- [28] Savelyev E et al 2017 *New J. Phys.* **19** 043009
- [29] McFarland B K et al 2014 *J. Phys.: Conf. Ser.* **488** 012015
- [30] Wellhöfer M, Martins M, Wurth W, Sorokin A A and Richter M 2007 *J. Opt. A: Pure Appl. Opt.* **9** 749–56
- [31] Heimann P et al 2011 *Rev. Sci. Instrum.* **82** 093104
- [32] Poletto L, Villorosi P, Benedetti E, Ferrari F, Stagira S, Sansone G and Nisoli M 2007 *Opt. Lett.* **32** 2897
- [33] Svetina C, Cocco D, Mahne N, Raimondi L, Ferrari E and Zangrando M 2016 *J. Synchrotron Radiat.* **23** 35–42
- [34] Driver T et al 2020 *Phys. Chem. Chem. Phys.* **22** 2704–12
- [35] Li S, Driver T, Alexander O, Cooper B, Garratt D, Marinelli A, Cryan J P and Marangos J P 2021 *Faraday Discuss.* **228** 488–501
- [36] Ratner D, Cryan J P, Lane T J, Li S and Stupakov G 2019 *Phys. Rev. X* **9** 011045
- [37] Li S et al 2021 *J. Phys. B: At. Mol. Opt. Phys.* **54** 144005
- [38] Braune M, Buck J, Kuhlmann M, Grunewald S, Düsterer S, Viefhaus J and Tiedtke K 2018 *J. Synchrotron Radiat.* **25** 3–15
- [39] Metje J, Lever F, Mayer D, Squibb R J, Robinson M S, Niebuhr M, Feifel R, Düsterer S and Gühr M 2020 *Appl. Sci.* **10** 7882
- [40] Lever F et al 2020 *J. Phys. B: At. Mol. Opt. Phys.* **54** 014002
- [41] Kruit P and Read F H 1983 *J. Phys. E: Sci. Instrum.* **16** 313–24
- [42] Löhl F et al 2010 *Phys. Rev. Lett.* **104** 144801
- [43] Giuliano B M, Feyer V, Prince K C, Coreno M, Evangelisti L, Melandri S and Caminati W 2010 *J. Phys. Chem. A* **114** 12725–30
- [44] Sanchez-Gonzalez A et al 2017 *Nat. Commun.* **8** 15461
- [45] Kumar Giri S, Saalman U and Rost J M 2020 *Phys. Rev. Lett.* **124** 113201

Article 5: Following excited-state chemical shifts in molecular ultrafast x-ray photoelectron spectroscopy

Dennis Mayer, Fabiano Lever, David Picconi, Jan Metje, Skirmantas Alisauskas, Francesca Calegari, Stefan Düsterer, Christopher Ehlert, Raimund Feifel, Mario Niebuhr, Bastian Manschwetus, Marion Kuhlmann, Tommaso Mazza, Matthew S. Robinson, Richard J. Squibb, Andrea Trabattoni, Mans Wallner, Peter Saalfrank, Thomas J. A. Wolf and Markus Gühr

Nature Communications 13, 198 (2022), DOI: 10.1038/s41467-021-27908-y

Abstract. The conversion of photon energy into other energetic forms in molecules is accompanied by charge moving on ultrafast timescales. We directly observe the charge motion at a specific site in an electronically excited molecule using time-resolved x-ray photoelectron spectroscopy (TR-XPS). We extend the concept of static chemical shift from conventional XPS by the excited-state chemical shift (ESCS), which is connected to the charge in the framework of a potential model. This allows us to invert TR-XPS spectra to the dynamic charge at a specific atom. We demonstrate the power of TR-XPS by using sulphur 2p-core-electron-emission probing to study the UV-excited dynamics of 2-thiouracil. The method allows us to discover that a major part of the population relaxes to the molecular ground state within 220–250 fs. In addition, a 250-fs oscillation, visible in the kinetic energy of the TR-XPS, reveals a coherent exchange of population among electronic states.

Copyright note. © The Author(s) 2022. This article is an open access article distributed under the terms and conditions of the Creative Commons Attribution (CC BY) license (<https://creativecommons.org/licenses/by/4.0/>).

ARTICLE



<https://doi.org/10.1038/s41467-021-27908-y>

OPEN

Following excited-state chemical shifts in molecular ultrafast x-ray photoelectron spectroscopy

D. Mayer^{1,11}, F. Lever^{1,11}, D. Picconi^{2✉}, J. Metje¹, S. Alisauskas³, F. Calegari^{4,5,6}, S. Düsterer³, C. Ehlert⁷, R. Feifel⁸, M. Niebuhr¹, B. Manschwetus³, M. Kuhlmann³, T. Mazza⁹, M. S. Robinson^{1,4,5}, R. J. Squibb⁸, A. Trabatttoni⁴, M. Wallner⁸, P. Saalfrank², T. J. A. Wolf¹⁰ & M. Gühr^{1✉}

The conversion of photon energy into other energetic forms in molecules is accompanied by charge moving on ultrafast timescales. We directly observe the charge motion at a specific site in an electronically excited molecule using time-resolved x-ray photoelectron spectroscopy (TR-XPS). We extend the concept of static chemical shift from conventional XPS by the excited-state chemical shift (ESCS), which is connected to the charge in the framework of a potential model. This allows us to invert TR-XPS spectra to the dynamic charge at a specific atom. We demonstrate the power of TR-XPS by using sulphur 2*p*-core-electron-emission probing to study the UV-excited dynamics of 2-thiouracil. The method allows us to discover that a major part of the population relaxes to the molecular ground state within 220–250 fs. In addition, a 250-fs oscillation, visible in the kinetic energy of the TR-XPS, reveals a coherent exchange of population among electronic states.

¹Institut für Physik und Astronomie, Universität Potsdam, 14476 Potsdam, Germany. ²Institut für Chemie, Universität Potsdam, 14476 Potsdam, Germany. ³Deutsches Elektronen Synchrotron (DESY), 22607 Hamburg, Germany. ⁴Center for Free-Electron Laser Science (CFEL), Deutsches Elektronen Synchrotron (DESY), 22607 Hamburg, Germany. ⁵The Hamburg Centre for Ultrafast Imaging, Universität Hamburg, 22761 Hamburg, Germany. ⁶Institut für Experimentalphysik, Universität Hamburg, 22761 Hamburg, Germany. ⁷Heidelberg Institute for Theoretical Studies, HITS gGmbH, 69118 Heidelberg, Germany. ⁸Department of Physics, University of Gothenburg, SE-41296 Gothenburg, Sweden. ⁹European XFEL, 22869 Schenefeld, Germany. ¹⁰Stanford PULSE Institute, SLAC National Accelerator Laboratory, Menlo Park, CA 94025, USA. ¹¹These authors contributed equally: D. Mayer, F. Lever. ✉email: david.picconi@uni-potsdam.de; mguehr@uni-potsdam.de

Light-induced charge flow in molecules forms the basis to convert photon energy into other energetic forms. The excitation of valence electrons by light triggers a change in charge density that eventually couples to nuclear motion. The complex interplay of nuclear and electronic degrees of freedom in the electronically excited states continues to move charge on an ultrafast time-scale by nonadiabatic couplings¹. This in turn gives rise to phenomena like photoisomerization² and proton-coupled electron transfer³ with rich applications in light-harvesting and photocatalysis⁴. Finding a way to image the charge flow in electronically excited systems, including organic molecules, on its natural timescale and with atomic precision would provide new ground for understanding molecular photophysics and excited-state (ES) reactivity.

X-ray photoelectron spectroscopy (XPS) is a proven tool to obtain information about local charge with atomic specificity in electronic ground states⁵. The tight localisation of core orbitals makes the method site selective. The ionisation potential (IP) measures the difference between neutral state and core-ionised state at a particular atom in a molecule. The so-called chemical shift (CS) of the IP reflects the charge at, and in close vicinity of, the probed atom. Within the potential approximation, the CS can be directly converted into local charge⁶.

In this paper we generalise the CS concept known from conventional, static XPS to electronically excited states, introducing the excited-state chemical shift (ESCS, not to be confused with the ESCS in nuclear magnetic resonance). We test this on the thionucleobase 2-thiouracil (2-tUra), which is photoexcited to a $\pi\pi^*$ state by an ultraviolet (UV) light pulse (Fig. 1). The S 2*p* photoionization with a soft x-ray pulse, of photon energy $h\nu$,

leads to a photoelectron with kinetic energy $E_{\text{kin}} = h\nu - E_{\text{bind}}$. The molecular UV photoexcitation changes the local charge density at the probed atom (Fig. 1b bottom), which leads to a specific ESCS. We find a direct relation between the ESCS and the local charge at the probe site in analogy to the potential model for the CS in static XPS⁶. This allows one to circumvent complex calculations of IPs, while allowing for an interpretation based on chemical intuition. We show that the largest effect on the ESCS is due to electronic relaxation, especially if the local charge at the probed atom is grossly changed in the process. A smaller, but non-negligible effect, stems from geometry changes, which can also alter local charge at the probed atom.

Our studies extend existing theoretical^{7–10} and experimental^{11–13} time-resolved (TR)-XPS by the demonstration of direct local charge recovery from ESCS. The x-ray typical element- and site-specific responses^{14,15} are also accomplished using the now well-established TR x-ray absorption spectroscopy (TR-XAS) method. In the soft x-ray range, TR-XAS has the capability to monitor electronic and nuclear dynamics^{16–18}, which has been demonstrated in ring-opening reactions¹⁹, dissociation²⁰, intersystem-crossing²¹, ionisation²² as well as the interplay between $\pi\pi^*$ and $n\pi^*$ valence electronic states^{23,24}. Hard x-ray absorption and emission spectroscopy is highly sensitive to charge and spin states, however, only on metal atoms within molecules^{25,26}. The novel TR-XPS extends this characteristic to lighter atoms and has the advantage that a fixed x-ray wavelength can be used to address several elements and sites. In addition, the use for molecules in thick solvent jets can also be accomplished by employing harder x-rays for increased penetration depth of the radiation as well as escape depth of the photoelectrons for light-element XPS.

We demonstrate the opportunities provided by TR-XPS on electronically excited states of a thionucleobase. Photoexcited thionucleobases are interesting because of efficient relaxation into long-lived triplet states (see Ref. 27,28 and references therein) triggering applications as photoinduced cross-linkers^{29,30} and photoinduced cancer therapy²⁸. Among those, 2-tUra is one of the most-studied cases on an ultrafast scale²⁷, both experimentally, using transient absorption³¹ and photoelectron spectroscopy^{31–33}, and theoretically in static calculations³⁴ and surface hopping trajectory simulations^{35,36}. The latter predict coherent population exchange among electronic states. The model emerging from joint experimental-theoretical investigations includes ultrafast internal conversion from the photoexcited S_2 $\pi\pi^*$ state into the S_1 $n\pi^*$ state, followed by a sub-picosecond intersystem crossing³². Relaxation from the triplet states to the ground state has previously been observed with a time constant of several ten picoseconds³² while also indirect evidence for an ultrafast direct ground-state (GS) relaxation from the photoexcited state has been reported³⁷.

In this work, we show that TR-XPS on electronically excited states allows us to identify the relaxation paths of 2-tUra by direct analysis of the ESCS and in addition comparisons to the calculated binding energy of different states and geometries. Most interestingly, we identify a ground state relaxation and the predicted coherent electronic population oscillation modulating the sulphur 2*p* binding energy periodically.

Results

Difference spectra. Figure 2a shows a photoelectron spectrum of 2-tUra obtained at the FLASH2 free-electron laser (FEL)³⁸ using a nominal photon energy of 272 eV and an average bandwidth of 1–2%. The electron spectra are taken with a magnetic-bottle electron spectrometer (MBES). We identify the sulphur 2*p*-photoelectron line (blue) at a kinetic energy of 103.5 eV in agreement with the literature³⁹. The width of about 4 eV does prevent us from distinguishing the spin-orbit splitting^{39,40}. The photoelectron line is accompanied by shake-up satellites at around 91 and

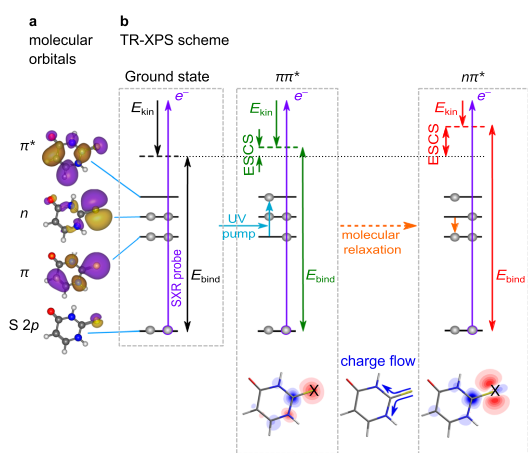


Fig. 1 Schematic picture of TR-XPS and ESCS in 2-thiouracil in a molecular orbital representation. **a** Molecular valence (π , n , π^*) orbitals and a core (sulphur 2*p*) orbital. **b** Probe of the S 2*p* core level with a binding energy E_{bind} by means of a soft x-ray (SXR) light pulse, leading to a photoelectron with a kinetic energy, E_{kin} . A UV pump pulse (cyan arrow) excites the 2-thiouracil from its electronic ground state (S_0) to a $\pi\pi^*$ state (S_2) which then relaxes further, for instance into the S_1 ($n\pi^*$) state shown here. The difference in E_{bind} with respect to the ground state is the excited-state chemical shift (ESCS = $E_{\text{bind}}^{\text{excited state}} - E_{\text{bind}}^{\text{ground state}}$). The molecular structures in the lower part of the panel represent the difference in charge density between the ground state and the respective excited states (red: decreased electron density, blue: increased electron density). Increase in positive charge at the sulphur site (marked with X) increases E_{bind} and the ESCS.

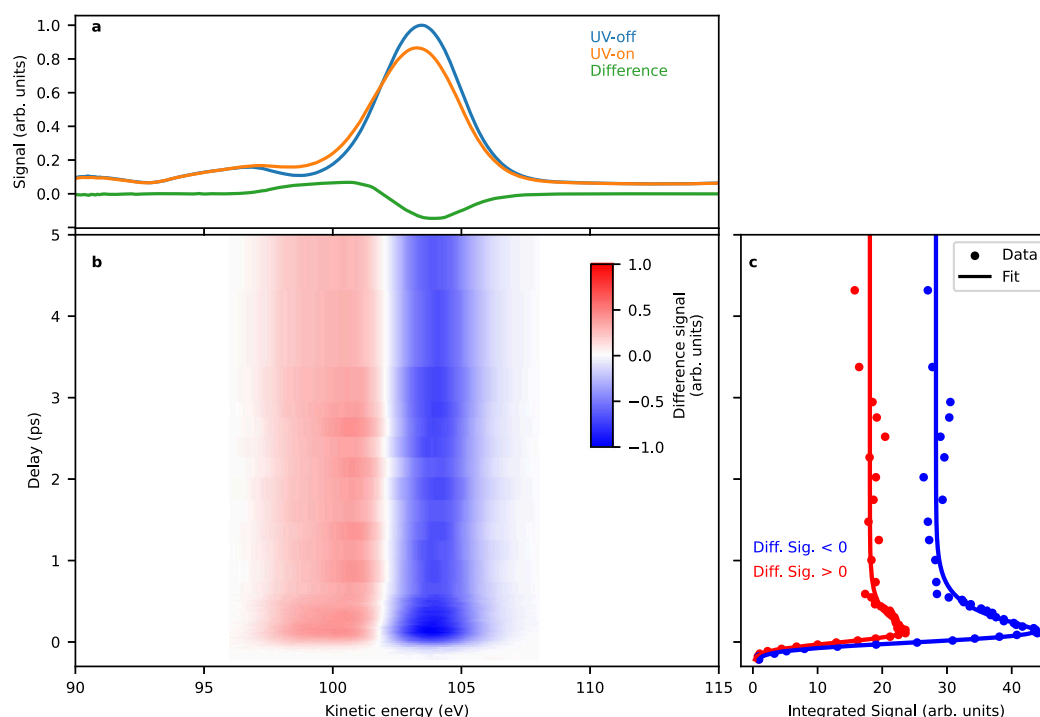


Fig. 2 Experimental time-resolved XPS spectra of 2-thiouracil. **a** UV-on (orange) and UV-off (blue) photoelectron spectra as well as the difference spectrum (green) between UV-on and UV-off at a delay of 200 fs. **b** False-colour plot of time-dependent difference XPS with red indicating UV-induced increase of the photoelectron spectrum and blue a UV-induced decrease. **c** Integrated signal of the positive (red) and negative (blue) parts of the difference spectra (dots) and fit to the data (solid line). Source data are provided as Source Data file.

96 eV⁴¹. Upon UV excitation (“UV-on”, orange line), the 2*p*-photoelectron line shifts towards lower kinetic energies. The difference spectrum (“UV-on” - “UV-off”, green line at a delay of 200 fs) is equal to the difference between GS and ES spectra times the fraction, *f*, of excited molecules (*f* · (ES-GS)). Part of the main photoelectron line is shifted into the region of the upper shake-up satellite, but the main part of the satellite line at 96 eV and the satellite at 91 eV remains unaffected. Figure 2b shows a time-dependent false-colour plot of the difference spectra. Temporal overlap has been determined by analysing the integrated absolute difference signal. The integrated signal under the positive/negative lobe in the difference spectrum is given in Fig. 2c.

The difference feature keeps its characteristic lineshape over the timescale of our measurement shown in Fig. 2b, indicating a persistent kinetic energy shift to smaller values over the whole range. The difference-amplitude changes significantly during the first picosecond. We use an exponential model function convoluted with a Gaussian time-uncertainty function of 190 (±10) fs FWHM (see Supplementary Discussion 1). We observe an exponential decay of 250 (±20) fs to 75% of the maximal signal for the negative part and 220 (±40) fs to 65% of the maximal signal for the positive part. The positive amplitude is always smaller than the negative amplitude. Systematic investigations of the difference spectra for various experimental settings exhibit the influence of so-called cyclotron resonances on the relative amplitudes in the MBES (see Supplementary Discussion 2). We therefore abstain from interpreting further the relative strength of the positive and negative features.

Spectral oscillations at small delays. Figure 3a shows a magnified part of the difference spectrum in Fig. 2b. To enhance the visibility of the spectral dynamics, we normalised each delay-slice on the area of the positive lobe. Despite the spectral width of about 4 eV, we identify oscillatory features in the positive part of the difference spectrum within the first ~600 fs. From zero delay to 150 fs, the spectrum shifts to lower kinetic energies and the peak of the spectrum widens. The shifts are most clearly visible in the spectral region from 99 to 101 eV. In the ground state, the shake-up peak at 96 eV has some spectral wing in this region. However, we do not observe a UV-induced change on the shake-up peak in its main part and lower energy wing. We thus assume that the main spectral effects in the 99–101 eV range are solely due to the UV-altered main photoelectron line.

After reaching minimal kinetic energies at 150 fs, the spectrum shifts towards higher kinetic energies by about 0.5 eV and the peak narrows reaching its extreme in the range between 200 and 300 fs. Subsequently, the spectrum shifts and widens again to reach its other extreme at 400 fs. For larger delays, the spectrum shifts again to higher kinetic energies. Further oscillations are not observed, however, for reasons of scarce experimental time, the delay steps are too coarse to follow additional oscillations (for more details see Supplementary Discussion 3). The negative lobe does not show systematic trends in this region and is therefore not shown in Fig. 3.

Difference spectra simulations. We will interpret the experimental results, casting them in the context of the rich literature

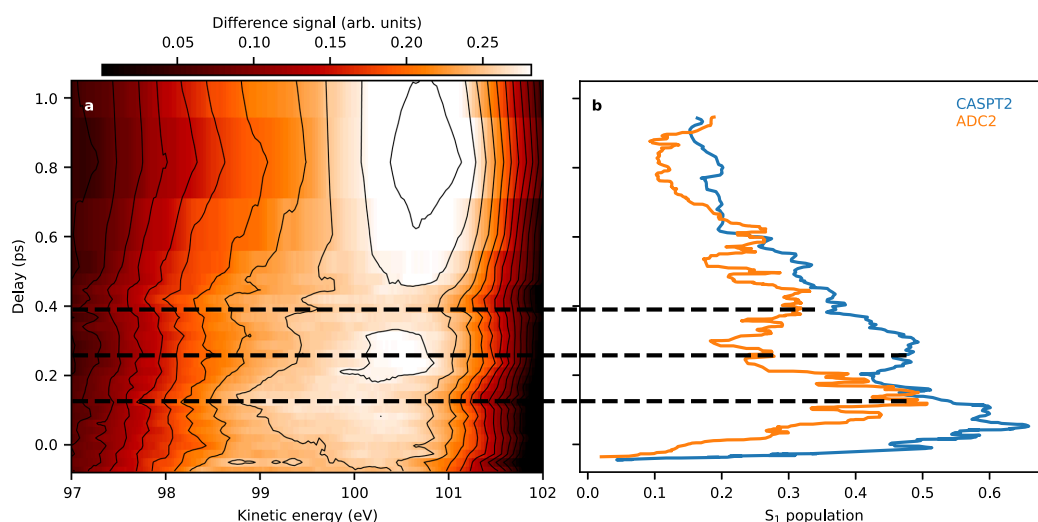


Fig. 3 Experimental shifts and theoretical predictions on state population. **a** False-colour contour plot of the positive lobe in Fig. 2b, normalised on the time-dependent area under the lobe. An oscillatory dynamic in the lineshape and position is visible for the first ~600 fs. At 150 fs and 400 fs delay, the spectrum is shifted to lower kinetic energy, while it is shifted to higher kinetic energies in between and afterwards. **b** Comparison of the oscillation dynamics with trajectory simulations. The population of the S_1 ($n\pi^*$) state, obtained from CASPT2 calculations of Ref. ³⁵ (blue line) and ADC(2) calculations of Ref. ³⁶ (orange line) are plotted. The dashed lines highlight the extrema of the oscillation observed in the experiment. The theoretical simulations do not include finite time-resolution and we shifted them by 50 fs to smaller delays to induce a transient rise of the signal around zero delay. The experimental 250 fs oscillation features have their counterparts in the simulated S_1 population, indicating the observation of a population exchange between the S_1 state and other electronic states. Source Data (for a) are provided as Source Data file.

on this molecule. Conclusions will also be drawn based on non-relativistic quantum chemical coupled-cluster calculations of the ground, valence-excited and core-ionised states of 2-tUra.

Previous calculations in the gas phase³⁴ or in the presence of water solvent molecules⁴² identified global, non-planar minima, as well as nearly planar minima, which can be potentially visited by the photoinduced wave packet.

Along the same lines, we optimised the geometry of the lowest valence singlet (S_0 , S_1 , S_2) and triplet (T_1 , T_2 , T_3) states with and without the constraint of planarity. Since the S_0 minimum is nearly planar, the excited state (unstable) planar minima are likely to play a role in the short time dynamics and are marked with an asterisk in Figs. 4 and 5. Fully-optimised, stable non-planar minima could be found for the S_1 , S_2 and T_1 states. The computational details are given in the Methods section and more extended in Supplementary Discussion 4. For all the geometries considered in this work the states S_1 , S_2 , T_1 , T_2 and T_3 have $n\pi^*$, $\pi\pi^*$, $\pi\pi^*$, $n\pi^*$ and $\pi\pi^*$ character, respectively.

For each optimised geometry and each valence state we calculated the binding energy of the electrons in the three $2p$ core orbitals of the S atom. We estimated the ionisation cross sections as proportional to the norm of the associated Dyson orbitals and used this data to simulate pump-probe photoelectron spectra at different geometries. The stick spectrum (shown in the Supplementary Discussion 5) was convoluted with a Gaussian of a FWHM of 3.5 eV, to match the width of the experimental bands.

Discussion

We first discuss the experimental data without reference to the XPS simulations. The difference spectra of Fig. 2, with their shift towards lower kinetic energies, indicate an increased E_{bind} of the

UV excited states. The classical static XPS connects the E_{bind} of a particular element on a particular site within a molecule to the total charge at the probed atom, which is related to the electro-negativity of the nearest neighbour atoms⁵. This connection is known as a 'chemical shift'. Accordingly, we anticipate that the CS can be generalised to a dynamic context as an ESCS in form of the difference of excited and ground state binding energy. The long-lasting shift of the kinetic energy would then indicate that the net effect of the photoexcitation is charge redistribution away from the sulphur atom (see Fig. 1). The electronic states inducing the strongest charge changes at the sulphur heteroatom are the $n\pi^*$ states. This is because the n (lone-pair orbital) is strongly localised at the sulphur heteroatom (see Fig. 1b) and in the $n\pi^*$ states n is singly occupied with respect to double occupation in the electronic ground state. Overall, this will lead to a strong ESCS to higher binding energies. The $^1n\pi^*$ state is generally considered a doorway state, leading from the UV excited $^1\pi\pi^*$ to the triplet states³⁷ and accordingly, we would expect an ESCS induced by this state.

The π orbitals are less localised at the sulphur atom. Intuitively removal of an electron from a π orbital would not induce as strong an ESCS as the n removal, but it will still lead to some ESCS. These relative strengths of the ESCS can also be estimated by a simple charge analysis of the molecular wavefunctions, a method that can even be implemented with simple Hartree-Fock orbitals. We performed a Löwdin-population-analysis on the wavefunctions of the different electronic states at different geometries, which yields partial charges on the atoms of the molecule. In Fig. 4b, the calculated partial charge on the S atom is plotted against the calculated ESCS, which we will not use in the discussion yet as it is a much more complex entity to calculate. We clearly identify the strongest local positive charge on the sulphur atom with respect to the ground

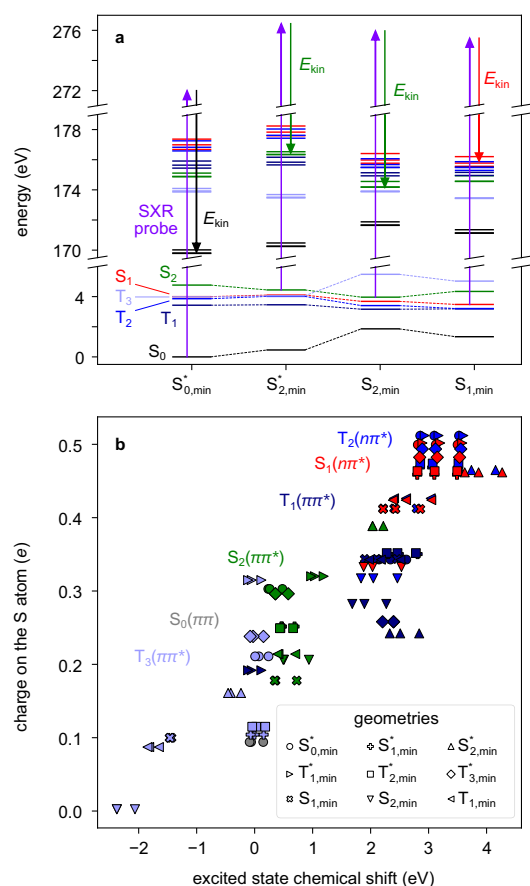


Fig. 4 Soft x-ray photoelectron probing of the excited-state dynamics of 2-thiouracil in a multi-electron picture. **a** Calculated electronic energies of the valence excited states, in the range 0–6 eV, and the core ionised states, in the range of 170–179 eV, for four geometries relevant in the short time dynamics. The arrows illustrate the $2p^{-1}$ ionisation process associated with the most intense transition. The core ionised states are grouped into sets of three states, which follow the colour coding of the valence states, meaning that their valence configuration is maintained with a $2p_x$, $2p_y$ or $2p_z$ core hole. Accordingly, the electron kinetic energy E_{kin} refers to ionisations out of S_0 , S_1 ($n\pi^*$) and S_2 ($\pi\pi^*$), depending on the geometry. **b** Partial charges on the S atom are plotted against the excited state chemical shift of the $2p$ electrons, calculated for the valence states at nine different geometries. For each geometry, the graph includes three markers for each excited state (S_1 , S_2 , T_1 , T_2 , T_3); in addition, three dots are included for the ionisation from S_0 at $S_{0,min}^*$, for a total of $9 \times 3 \times 5 + 3 = 138$ markers. Asterisks denote restriction in the calculation of the states to planar geometries. Source Data are provided as a Source Data file.

states in the S_1 ($1n\pi^*$) and T_2 ($3\pi\pi^*$) states, confirming the intuitive arguments given above. The S_2 ($1\pi\pi^*$) state is characterised by a relatively low positive charge on the sulphur atom and the lowest T_1 ($3\pi\pi^*$) state in its minimum geometry, generally considered as the long-lasting state^{31,34}, is lying in between the $n\pi^*$ and S_2 ($1\pi\pi^*$) states. Thus, the permanent ESCS to lower kinetic energies (higher binding energies) is consistent with a relaxation cascade from the initially excited S_2

($1\pi\pi^*$) over the S_1 ($1n\pi^*$) and possibly also T_2 ($3\pi\pi^*$) states into the lowest T_1 ($3\pi\pi^*$) state.

Closer inspection of the short-time dynamics in Fig. 3a provides extraordinary experimental details on the molecular relaxation dynamics. In the spectral shift dynamics, the strongest ESCS to lower kinetic energies (higher binding energies) is found at 150 and 400 fs, interrupted with an interval and followed by delays of smaller ESCS. Intuition based on the lone-pair orbital localisation, as well as the simple local charge analysis at the sulphur atom mentioned above, indicate that this spectral shift reflects changes in the electronic state of the molecule with maximal $n\pi^*$ contributions at 150 and 400 fs and consequently minimal $n\pi^*$ contributions in between and after. We compare theoretical predictions of the S_1 ($1n\pi^*$) state population dynamics from the trajectory surface-hopping calculations of Mai et al.^{35,36} in Fig. 3b. The S_1 populations calculated using CASPT2 and ADC(2) potentials show indeed dynamics that fit well to the experimentally observed shifts. The oscillation period depends on the theoretical approach, and the timing of the second S_1 population maximum fits the experimental data better in the case of the ADC(2) approach. The simulations of Mai et al. predict a population transfer among the S_1 , S_2 and triplet states in a coherent fashion and the details of states participating in the population dynamics depends on the applied electronic structure method. However, in both cases, the S_1 state, having the highest IP of all states, carries the largest oscillation. This comparison strongly supports the experimental arguments for observing population dynamics entering and leaving the S_1 state in a coherently modulated fashion.

Similar coherent modulations have been observed in the transient spectra for 4-tUra and 2-tUra and in liquid phase^{42,43}. In case of 4-tUra, much faster, sub-100 fs, coherent modulations have been observed in fs transient absorption spectra and attributed to particular vibrational modes in the electronically excited state of 4-tUra⁴³. For the case of 2-tUra, the same experimental methods exhibit oscillations with a period very similar to ours⁴², which are however not interpreted. We also checked the assignment to a purely vibrational coherence by performing a normal mode analysis at the calculated excited state minima. Only at the nonplanar minimum of the S_2 ($\pi\pi^*$) state we found a mode with a frequency of 131 cm^{-1} , thus compatible with a 250 fs modulation. However, this would mean that the molecular population should be dominated by the S_2 state for the 600 fs of our modulated time-interval, which is in contrast to all current literature suggestions. Also, for short times, we suggest that the molecule remains mostly planar on the S_2 state, as will be shown below by comparison to calculated difference spectra. Remarkably, valence photoelectron spectra of 2-tUra in the gas phase do not show these modulations³¹, demonstrating that the ESCS in XPS is able to pick up molecular dynamics beyond reach for valence electron photoemission.

On top of the coherently modulated signal, we find an amplitude decay with a time-constant of 220–250 fs, being equal on the positive and negative lobe of the difference spectra within the error bars. Similar short decays have been observed in liquid and gas phase studies of 2-tUra. In valence photoelectron spectroscopy, a time constant of around 300 fs is observed for the excitation wavelength corresponding to the one used here³¹. Based on the calculated valence IPs of the different states⁴⁴, the decay is attributed to relaxation from the S_1 ($1n\pi^*$) to the triplet state manifold. Liquid-phase transient absorption spectra of 2-tUra in the same work show similar time constants and the same interpretation is applied³¹. This is supported by a recent joint experimental-theoretical investigation that includes calculated transient absorption windows at some of the molecule's crucial excited state positions⁴². The observed vanishing contrast in our TR-XPS might need to be interpreted in a different way

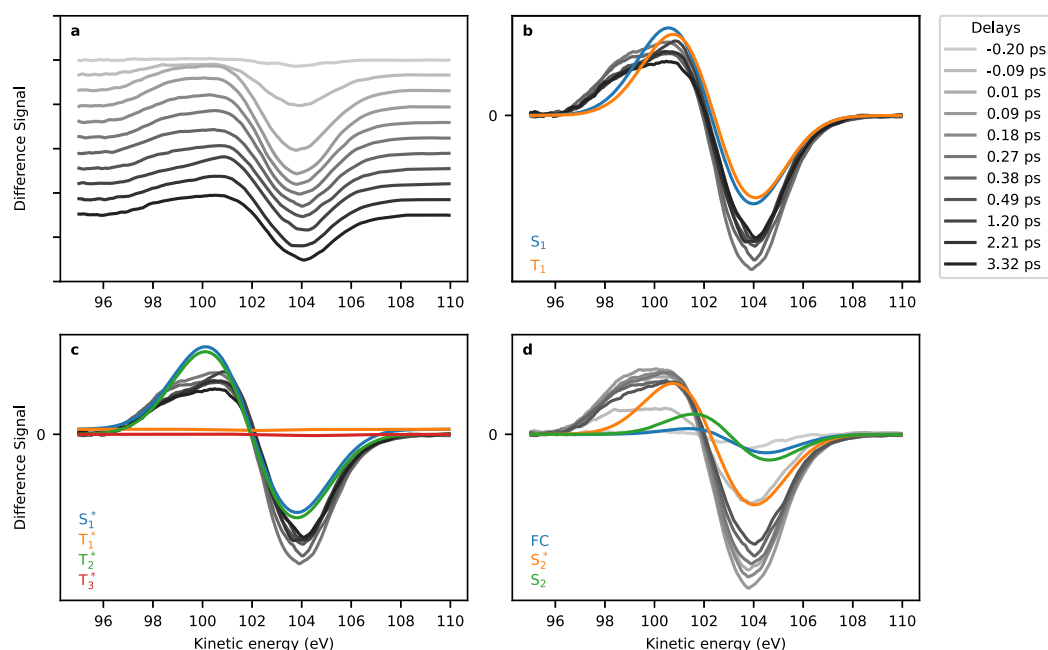


Fig. 5 Comparison between experimental and theoretical difference spectra. **a** Ridgeline plot of experimental difference spectra for different pump-probe delays between -0.2 and 3.32 ps. **b–d** Comparison of experiment (greyscale lines) with theoretical (coloured lines) difference spectra computed at the coupled-cluster level of theory. All calculated difference spectra are shifted lower in kinetic energy by 1.3 eV. **b** and **c** Spectra with delays in the range 0.27 – 3.32 ps, **(d)** spectra with delays -0.2 – 0.49 ps. The theoretical spectra use the energies at the minima (S_2 is the nonplanar, S_2^* is the restricted geometry) and the Franck-Condon geometry. Asterisks denote restriction in the calculation of the states to planar geometries. Source Data are provided as a Source Data file.

than the $S_1(1n\pi^*)$ —triplet state relaxation, as we would expect to still observe a ESCS leading to different features in the triplet manifold. The state diminishing the modulation contrast of the difference spectra would have to show a small ESCS with respect to the ground state, and thus be electronically similar—or identical—to the ground state. We thus suggest an ultrafast molecular decay of part of the population into the electronic ground state and check it further by comparison to ESCS simulations below.

We now discuss the calculated ESCS and its connection to the charge on the sulphur atom in the photoexcited states. We observe the remarkable linear relation between binding energy and charge, closely resembling the potential model introduced in static XPS⁶. While many effects such as final-state charge relaxation and core-hole screening^{13,45} shape the calculated binding energy, the linear trend prevails. This provides a generalised concept for deducing local charge changes in electronically excited states from the ESCS. Further well-established corrections known from static XPS to this plot make the E_{bind} - charge connection even more obvious (Supplementary Discussion 6).

In addition, we can clearly distinguish drivers behind the charge and ESCS shifts. The colours in Fig. 4 indicate the electronic state while the different symbols indicate geometries, corresponding to minima or saddle points on different potential energy surfaces. We clearly observe clustering according to electronic state, although very widely differing geometries have been used. Thus, the main factor for local charge and therefore binding energy is the electronic state of the molecule. This in turn gives core-level photoelectron spectroscopy high electronic state sensitivity. The exceptions of one S_2 and T_1 geometry are explained

in the Supplementary Discussion 7. The data for the S_1 and T_2 states ($n\pi^*$) are very well clustered in the upper right corner of Fig. 4b, with the highest ESCS. As explained above, these states have $n\pi^*$ character and possess a high positive charge on the sulphur atom, which is also illustrated in Fig. 1.

In Fig. 5, we assess details of the TR-XPS spectra by comparison with the calculated spectra, extending our discussion of the purely experimental features. The onset of the experimental difference feature around time-zero is shown in more detail in the ridgeline plot of Fig. 5a. The difference signal gets stronger with delay indicating an increasing f over the time-resolution of 191 fs. We initially identify the development of the negative feature sitting stable at 104 eV and a comparatively broader positive feature at lower kinetic energies. The relative position of the positive and negative bands is very well captured by the simulation. Since similar Dyson norms were predicted for the different initial valence excited states, the calculated spectra essentially integrate to zero. According to model and intuition, the positive feature should be attributed to electronic states with higher positive charge on the sulphur atom.

We continue discussing the picosecond difference spectra, comparing them to calculated difference spectra in Fig. 5b and c. Among the states with highest local charge and thus highest E_{bind} are the $S_1(n\pi^*)$, $T_1(\pi\pi^*)$ and $T_2(n\pi^*)$ states. The unstable, restricted planar minima/saddle points of S_1 and T_2 (Fig. 5c) could be responsible for parts of the difference spectra for a limited time until relaxation into a non-planar geometry. Among these non-planar geometries, both the S_1 and T_1 show agreement with the experimental difference spectra (Fig. 5b). The missing low-energy wing from 97 to 98.5 eV in the theoretical spectra can

likely be attributed to the fact that we neglect wave-packet and incoherent thermal distribution effects resulting in extended geometry coverage. The shake-up phenomena are also not modelled. However, we do not observe a change of the shake-up peaks and we would expect that the observation of UV-induced effects on the weaker satellite lines requires better signal-to-noise ratio. The theoretical simulations strengthen the arguments given in the context of Fig. 3, showing that a strong ESCS due to the S_1 coherent dynamics is followed by a state with less ESCS. We note that simulations/experiments on the pyrimidine nucleobases call for the S_1 $1\pi\pi^*$ state to be occupied first after S_2 relaxation⁴⁶. Only thereafter will the triplet states gain population. Based on the experimental features, we can exclude the planar geometries of the T_1 and T_3 states to play a major role in the relaxation process. A comparison to the ESCS in Fig. 4b implies that the charge at the sulphur atom has reached about half a positive value due to the molecular relaxation.

We now return to the initial 220–250 fs decay of the difference feature, which can be an indication of relaxation of the charge back to the ground state distribution, into states with negligible photoionisation cross section, or into states with an IP equal to the electronic ground state before photoexcitation. To obtain more insight, we compare the experimental XPS to simulations in Fig. 5b–d. Figure 5d shows the S_2 ($\pi\pi^*$) state difference spectra in three different molecular geometries. Figure 5c shows spectra with ‘unstable’ planar geometries. The most important is the S_1 ($\pi\pi^*$) state, others are expected to play a minor role in the dynamics for short times^{35,36}. Figure 5b shows difference spectra for the S_1 and T_1 states at their respective potential energy minimum geometry. The unstable T_1^* and T_3^* spectra are indeed flat on our scale and could in principle explain the observed decay in difference amplitude. However, these geometries cannot be stable, and cannot explain the long-lasting reduction in amplitude with the 220–250 fs exponential decay. In addition, the remaining calculated non-flat difference spectra do not exhibit a large enough difference. We therefore attribute the observed decay to an ultrafast relaxation into the electronic ground state with net zero charge change with a 220–250 fs time-constant.

Ground-state (GS) relaxation has been discussed before in the solution as well as in the gas phase^{31,37,47}. In earlier solution-phase work, a remark on an incomplete triplet yield could be interpreted in favour of an ultrafast ground state decay channel³⁷. More recent work in the gas phase has attributed time-constants from 50 to 200 ps to ground state relaxation³¹. Our ground state channel is close to the 300 fs decay observed in Ref. 31, which was attributed to intersystem crossing previously.

We now compare early difference spectra to the calculated spectra of the directly photoexcited S_2 ($\pi\pi^*$) state in different geometries in Fig. 5d. The best representation is given by the S_2^* planar geometry. The Franck-Condon spectrum should be included in the difference spectra, however, the short lifetime of this point as compared to our time-resolution makes it a minor contributor. We can, however, exclude a relaxation with major contributions from the S_2 out-of-plane minimum (green line), as this would mean a shift in the zero-crossing feature by about 1 eV to higher kinetic energies, which is not observed in the experiment. This observation agrees with the predictions of trajectory calculations when using a CASPT2 approach to electronic structure³⁵ but is in contrast to trajectory calculations with an ADC(2) electronic structure approach³⁶. While in the first reference the S_2 lifetime is below 100 fs and thus too short for the molecule to effectively reach out of plane geometries, the latter predicts an S_2 lifetime of 250 fs which allows for out of plane geometries.

In a recent theoretical-experimental solution phase study, two $1\pi\pi^*$ states with a slight energy gap are assumed to be populated

and while the upper one is predicted to relax via out-of-plane geometries, the lower one is suggested to relax via planar geometries⁴². We find that our calculated geometries are very similar to the ones from Ref. 42. (see the Supplementary Discussion 4 for a full comparison) and thus our analysis above would clearly advocate for initial planar geometries in the relaxation path. However, as our study is performed on isolated molecules instead of in solution phase it is not clear if we have any appreciable admixture of the higher lying $1\pi\pi^*$ state.

We have introduced the concept of ESCS in TR-XPS and shown that this powerful concept can be applied to deduce charge distribution changes in excited molecules. We observe rich dynamics on a sub-ps timescale. Based on intuitive arguments, we can assign the spectral features to coherent population exchange of the $\pi\pi^*$ state, inducing a strong ESCS, with other electronic states of less ESCS. In addition, we identify an ultrafast ground state relaxation path based on decaying amplitude in the differential signal. The calculated ESCS as a function of electronic state and geometry help in interpreting the geometric changes of the molecule after UV excitation in terms of a planar relaxation path on the photoexcited $1\pi\pi^*$ state. The connection between charge change at the probe site and the exactly calculated ESCS can be well approximated by a potential model, as in ground state XPS. This will provide a methodological basis for an intuitive understanding of charge dynamics in photoexcited isolated molecules on the femto- and attosecond timescale but also for photocatalytic systems. In a next step, one can address more than one site of the molecule using TR-XPS and map the charge flow induced by photoexcitation over the whole molecule.

Methods

Time-resolved UV pump soft x-ray probe (photo-) electron spectroscopy. The experiment was performed at the FL24 beamline of the FLASH2 facility at DESY using the newly built URSA-PQ apparatus. A detailed description of the apparatus and the experiment can be found elsewhere^{48,49}. In short, the apparatus includes a magnetic bottle time-of-flight electron spectrometer (MBES), a capillary oven to evaporate the 2-thiouracil samples at 150 °C and a paddle with beam diagnostics on top of the oven. UV pump pulses of 269 nm centre wavelength, 80 fs duration and an energy around 1 μ J were focused to a 50 μ m focus to pre-excite the molecules into the $\pi\pi^*$ state. Power scans on the time-dependent spectral features were performed to assure that the signal is not over-pumped by the UV pulses (Supplementary Discussion 8).

Tunable soft x-ray pump pulses were produced in form of SASE (self-amplified spontaneous emission) radiation. Every second x-ray pulse was delivered without UV excitation for obtaining a reference on the non-excited molecule. The mean x-ray photon energy was set to 272 eV with a bandwidth of 1–2% (including jitter). The x-ray probe was linearly polarised parallel to the axis of the magnetic bottle spectrometer and the UV polarisation. The focal size of the x-ray beam was slightly larger than the UV spot size. Systematic power scans were performed to exclude nonlinear effects in the x-ray induced electron spectra (see Supplementary Discussion 8). To increase energy resolution of the spectrometer, the speed of the ejected electrons was reduced by an -80 V retardation voltage on an electrostatic lens in front of the 1.7 m long flight tube which was kept at a constant potential. The energy resolving power of the MBES ($E/\Delta E$) has been determined with Kr MNN Auger lines to be 40 at 0 V retardation. Based on the sulphur 2p-photoelectron line, we estimate the resolution to be better than 30 with respect to the total kinetic energy. The time-dependent spectra were measured for a series of delays. In each scan, the delays were set randomly to avoid systematic effects. We measure the difference spectra of UV excited to non-excited shots. The data evaluation is described in Supplementary Discussion 9.

Theoretical calculations. The geometry optimisation of ground state 2-thiouracil was performed using coupled-cluster theory with singles and doubles (CCSD) with the 6-311++G** basis set^{50,51}. Valence excited state optimisations and energy calculations at specific geometries were performed using the equation-of-motion formalism (EOM-CGSD) with the same basis set. All calculations were performed using the package Q-Chem 4.4⁵². At all computed geometries the valence excited states' wavefunctions are dominated by a singly-excited configuration. For the states S_1 , T_2 ($\pi\pi^*$) and S_2 , T_1 ($\pi\pi^*$) the involved orbitals at the Franck-Condon point are shown in Fig. 1. The structural parameters of the optimised planar and non-planar geometries on the different electronic states are reported in the Supplementary Discussion 4.

The binding energy of the electrons in the 2*p* orbitals of the sulphur atom were calculated using the equation-of-motion coupled-cluster method for IPs (EOM-IP-CCSD)⁵³ with the 6-311++G** basis set for the S atom and the 6-31++G basis for all other atoms. Photoelectron intensities were approximated as the geometric mean of the norms of the left and right Dyson orbitals associated with the ionisation process¹⁰. The target core-excited states of the cation were identified as the eigenstates which have the largest overlap with initial guess states, obtained by applying the annihilation operator of the three 2*p* electrons on reference CCSD wavefunctions, according to the procedure implemented in Q-Chem. To this end, reference CCSD wavefunctions for the different electronic states of the neutral molecule were calculated starting from unrestricted Hartree-Fock wavefunctions, which were optimised using the maximum overlap method, in order to mimic the (singly excited) orbital occupancy of the excited states. A similar strategy has been recently validated by Coriani et al. to model pump-probe x-ray absorption spectra of nucleobases at the coupled-cluster level⁵⁴. Spin-orbit coupling, leading to a splitting of the core-ionised states of the order of 1 eV (not resolved due to spectral broadening) is not included in the calculations.

Data availability

Source data are provided with this paper. The FEL raw data, several TB in size, that support the findings of this study are available from the corresponding authors upon request. The processed photoelectron spectra are provided in the Source Data File. The results of the theoretical calculations i.e. optimised geometries, ionisation potentials, state energies and partial charges, are provided in the Source Data File. Source data are provided with this paper.

Code availability

The codes used to generate the computational results of this study are highly adapted to the hdf5 output of the FLASH free-electron laser. They are available from the corresponding authors upon request.

Received: 8 August 2021; Accepted: 20 December 2021;

Published online: 11 January 2022

References

- Domcke, W., Yarkony, D. R. & Köppel, H. *Conical intersections: theory, computation and experiment*. Advanced Series in Physical Chemistry 17 (World Scientific, 2011).
- Levine, B. G. & Martínez, T. J. Isomerization Through Conical Intersections. *Ann. Rev. Phys. Chem.* **58**, 613–634 (2007).
- Weinberg, D. R. et al. Proton-Coupled Electron Transfer. *Chem. Rev.* **112**, 4016–4093 (2012).
- Tian, H., Boschloo, G. & Hagfeldt, A. *Molecular devices for solar energy conversion and storage*. (Springer Berlin Heidelberg, 2017).
- Siegbahn, K. *ESCA applied to free molecules*. (North-Holland Pub. Co, 1969).
- Gelius, U. Binding Energies and Chemical Shifts in ESCA. *Phys. Scr.* **9**, 133–147 (1974).
- Bennett, K., Kowalewski, M. & Mukamel, S. Nonadiabatic Dynamics May Be Probed through Electronic Coherence in Time-Resolved Photoelectron Spectroscopy. *J. Chem. Theory Comput.* **12**, 740–752 (2016).
- Neville, S. P., Chergui, M., Stolow, A. & Schuurman, M. S. Ultrafast X-Ray Spectroscopy of Conical Intersections. *Phys. Rev. Lett.* **120**, 243001 (2018).
- Inhester, L., Li, Z., Zhu, X., Medvedev, N. & Wolf, T. J. A. Spectroscopic Signature of Chemical Bond Dissociation Revealed by Calculated Core-Electron Spectra. *J. Phys. Chem. Lett.* **10**, 6536–6544 (2019).
- Vidal, M. L., Krylov, A. I. & Coriani, S. Dyson orbitals within the fc-CVS-EOM-CCSD framework: theory and application to X-ray photoelectron spectroscopy of ground and excited states. *Phys. Chem. Chem. Phys.* **22**, 2693–2703 (2020).
- Siefermann, K. R. et al. Atomic-Scale Perspective of Ultrafast Charge Transfer at a Dye-Semiconductor Interface. *J. Phys. Chem. Lett.* **5**, 2753–2759 (2014).
- Brauß, F. et al. Time-resolved inner-shell photoelectron spectroscopy: from a bound molecule to an isolated atom. *Phys. Rev. A* **97**, 043429 (2018).
- Leitner, T. et al. Time-resolved electron spectroscopy for chemical analysis of photodissociation: photoelectron spectra of Fe(CO)₅, Fe(CO)₄, and Fe(CO)₃. *J. Chem. Phys.* **149**, 44307 (2018).
- Bergmann, U., Yachandra, V. & Yano, J. *X-ray free electron lasers: applications in materials, chemistry and biology*. Energy and Environment Series (Royal Society of Chemistry, 2017).
- Young, L. et al. Roadmap of ultrafast x-ray atomic and molecular physics. *J. Phys. B - Mol. Opt. Phys.* **51**, 032003 (2018).
- Neville, S. P. et al. Beyond structure: Ultrafast X-ray absorption spectroscopy as a probe of non-adiabatic wavepacket dynamics. *Faraday Discuss.* **194**, 117–145 (2016).
- Neville, S. P. et al. Excited state X-ray absorption spectroscopy: Probing both electronic and structural dynamics. *J. Chem. Phys.* **145**, 144307 (2016).
- Segatta, F. et al. Exploring the capabilities of optical pump X-ray probe NEXAFS spectroscopy to track photo-induced dynamics mediated by conical intersections. *Faraday Discuss.* **221**, 245–264 (2020).
- Attar, A. R. et al. Femtosecond x-ray spectroscopy of an electrocyclic ring-opening reaction. *Science* **356**, 54–59 (2017).
- Pertot, Y. et al. Time-resolved x-ray absorption spectroscopy with a water window high-harmonic source. *Science* **355**, 264–267 (2017).
- Bhattacharjee, A. et al. Ultrafast Intersystem Crossing in Acetylacetone via Femtosecond X-ray Transient Absorption at the Carbon K-Edge. *J. Am. Chem. Soc.* **139**, 16576–16583 (2017).
- Loh, Z.-H. et al. Observation of the fastest chemical processes in the radiolysis of water. *Science* **367**, 179–182 (2020).
- Wolf, T. J. A. et al. Probing ultrafast ππ*/ππ* internal conversion in organic chromophores via K-edge resonant absorption. *Nat. Comm.* **8**, 29 (2017).
- Ehlert, C., Gühr, M. & Saalfrank, P. An efficient first principles method for molecular pump-probe NEXAFS spectra: Application to thymine and azobenzene. *J. Chem. Phys.* **149**, 144112 (2018).
- Bressler, C. & Chergui, M. Ultrafast X-ray Absorption Spectroscopy. *Chem. Rev.* **104**, 1781–1812 (2004).
- Zhang, W. et al. Tracking excited-state charge and spin dynamics in iron coordination complexes. *Nature* **509**, 345–348 (2014).
- Arslançan, S., Martínez-Fernández, L. & Corral, I. Photophysics and photochemistry of canonical nucleobases' thioanalogs: from quantum mechanical studies to time resolved experiments. *Molecules* **22**, 998 (2017).
- Ashwood, B., Pollum, M. & Crespo-Hernández, C. E. Photochemical and Photodynamical Properties of Sulfur-Substituted Nucleic Acid Bases. *Photochem. Photobiol.* **95**, 33–58 (2019).
- Zhang, X. et al. Novel DNA lesions generated by the interaction between therapeutic thiopurines and UVA light. *DNA Repair* **6**, 344–354 (2007).
- Brem, R., Daehn, I. & Karran, P. Efficient DNA interstrand crosslinking by 6-thioguanine and UVA radiation. *DNA Repair* **10**, 869–876 (2011).
- Sánchez-Rodríguez, J. A. et al. 2-Thiouracil intersystem crossing photodynamics studied by wavelength-dependent photoelectron and transient absorption spectroscopies. *Phys. Chem. Chem. Phys.* **19**, 19756–19766 (2017).
- Mohamadzade, A., Bai, S., Barbatti, M. & Ullrich, S. Intersystem crossing dynamics in singly substituted thiouracil studied by time-resolved photoelectron spectroscopy: Micro-environmental effects due to sulfur position. *Chem. Phys.* **515**, 572–579 (2018).
- Mai, S., Mohamadzade, A., Marquetand, P., González, L. & Ullrich, S. Simulated and Experimental Time-Resolved Photoelectron Spectra of the Intersystem Crossing Dynamics in 2-Thiouracil. *Molecules* **23**, 2836 (2018).
- Mai, S., Marquetand, P. & González, L. A Static Picture of the Relaxation and Intersystem Crossing Mechanisms of Photoexcited 2-Thiouracil. *J. Phys. Chem. A* **119**, 9524–9533 (2015).
- Mai, S., Marquetand, P. & González, L. Intersystem Crossing Pathways in the Noncanonical Nucleobase 2-Thiouracil: a time-dependent picture. *J. Phys. Chem. Lett.* **7**, 1978–1983 (2016).
- Mai, S. et al. Surface hopping dynamics including intersystem crossing using the algebraic diagrammatic construction method. *J. Chem. Phys.* **147**, 184109 (2017).
- Pollum, M. & Crespo-Hernández, C. E. Communication: The dark singlet state as a doorway state in the ultrafast and efficient intersystem crossing dynamics in 2-thiothymine and 2-thiouracil. *J. Chem. Phys.* **140**, 071101 (2014).
- Faatz, B. et al. Simultaneous operation of two soft x-ray free-electron lasers driven by one linear accelerator. *N. J. Phys.* **18**, 062002 (2016).
- Giuliano, B. M. et al. Tautomerism in 4-Hydroxypyrimidine, 5-Methyl-2-thiouracil, and 2-Thiouracil. *J. Phys. Chem. A* **114**, 12725–12730 (2010).
- Plekan, O. et al. Functionalisation and immobilisation of an Au(110) surface via uracil and 2-thiouracil anchored layer. *Phys. Chem. Chem. Phys.* **17**, 15181–15192 (2015).
- Föhlich, A. et al. Direct observation of electron dynamics in the attosecond domain. *Nature* **436**, 373–376 (2005).
- Teles-Ferreira, D. C. et al. A Unified Experimental/Theoretical Description of the Ultrafast Photophysics of Single and Double Thionated Uracils. *Chem. - A Eur. J.* **26**, 336–343 (2020).
- Borrego-Varillas, R. et al. Observation of the Sub-100 Femtosecond Population of a Dark State in a Thio base Mediating Intersystem Crossing. *J. Am. Chem. Soc.* **140**, 16087–16093 (2018).
- Ruckenbauer, M., Mai, S., Marquetand, P. & González, L. Photoelectron spectra of 2-thiouracil, 4-thiouracil, and 2,4-dithiouracil. *J. Chem. Phys.* **144**, 074303 (2016).
- Mårtensson, N. & Nilsson, A. On the origin of core-level binding energy shifts. *J. Electr. Spectr. Rel. Phen.* **75**, 209–223 (1995).

46. Improta, R., Santoro, F. & Blancafort, L. Quantum Mechanical Studies on the Photophysics and the Photochemistry of Nucleic Acids and Nucleobases. *Chem. Rev.* **116**, 3540–3593 (2016).
47. Yu, H. et al. Internal conversion and intersystem crossing pathways in UV excited, isolated uracils and their implications in prebiotic chemistry. *Phys. Chem. Chem. Phys.* **18**, 20168–20176 (2016).
48. Metje, J. et al. URSA-PQ: A Mobile and Flexible Pump-Probe Instrument for Gas Phase Samples at the FLASH Free Electron Laser. *Appl. Sci.* **10**, 7882 (2020).
49. Lever, F. et al. Ultrafast dynamics of 2-thiouracil investigated by time-resolved Auger spectroscopy. *J. Phys. B. Mol. Opt. Phys.* **54**, 014002 (2020).
50. Shavitt, I. & Bartlett, R. J. *Many – Body Methods in Chemistry and Physics: MBPT and Coupled-Cluster Theory*. (Cambridge University Press, 2009).
51. Bartlett, R. J. & Musial, M. Coupled-cluster theory in quantum chemistry. *Rev. Mod. Phys.* **79**, 291–352 (2007).
52. Shao, Y. et al. Advances in molecular quantum chemistry contained in the Q-Chem 4 program package. *Mol. Phys.* **113**, 184–215 (2015).
53. Krylov, A. I. Equation-of-Motion Coupled-Cluster Methods for Open-Shell and Electronically Excited Species: The Hitchhiker’s Guide to Fock Space. *Annu. Rev. Phys. Chem.* **59**, 433–462 (2008).
54. Tsuru, S. et al. An assessment of different electronic structure approaches for modeling time-resolved x-ray absorption spectroscopy. *Struct. Dyn.* **8**, 24101 (2021).

Acknowledgements

We thank the Volkswagen foundation for funding via a Lichtenberg Professorship. We thank the BMBF for funding the URSA-PQ apparatus and for funding J.M. via Verbundforschungsprojekt 05K161P1. We acknowledge DFG funding via Grants GU 1478/1-1 (M.G.) and SA 547/17-1 (P.S.). T.J.A.W. was supported by the US Department of Energy, Office of Science, Basic Energy Sciences, Chemical Sciences, Geosciences, and Biosciences Division. R.F. thanks the Swedish Research Council (VR) and the Knut and Alice Wallenberg Foundation, Sweden, for financial support. We acknowledge DESY (Hamburg, Germany), a member of the Helmholtz Association HGF, for the provision of experimental facilities. Part of this research was carried out at FLASH2. F.C. acknowledges support from the European Research Council under the ERC-2014-StG STAR-LIGHT (Grant Agreement No. 637756).

Author contributions

J.M. and M.G. did the conceptual design for the experimental apparatus. J.M. designed and built the apparatus. The magnetic bottle spectrometer was designed by J.M. with help of R.F. and R.J.S. and M.G. J.M., D.M., F.L. and S.D. integrated the apparatus into the FLASH beamline. F.L. designed and executed the data interfacing between the experiment and the FLASH data infrastructure. D.M., F.L., J.M., S.A., F.C., S.D., R.F., M.N.,

B.M., M.K., T.M., M.S.R., R.J.S., A.T., M.W., T.J.A.W. and M.G. performed the experiment. D.M. and F.L. analysed the data. D.P. performed the calculations and discussed the theoretical methods with C.E. and P.S. D.M., F.L., D.P. and M.G. discussed the data and theory and prepared the paper. All authors contributed to the final version of the paper by discussions and/or edits. M.G. wrote the beamtime proposal for this experiment and serves as spokesperson for the collaboration.

Funding

Open Access funding enabled and organized by Projekt DEAL.

Competing interests

The authors declare no competing interests.

Additional information

Supplementary information The online version contains supplementary material available at <https://doi.org/10.1038/s41467-021-27908-y>.

Correspondence and requests for materials should be addressed to D. Picconi or M. Gühr.

Peer review information *Nature Communications* thanks the anonymous reviewers for their contribution to the peer review of this work. Peer reviewer reports are available.

Reprints and permission information is available at <http://www.nature.com/reprints>

Publisher’s note Springer Nature remains neutral with regard to jurisdictional claims in published maps and institutional affiliations.



Open Access This article is licensed under a Creative Commons Attribution 4.0 International License, which permits use, sharing, adaptation, distribution and reproduction in any medium or format, as long as you give appropriate credit to the original author(s) and the source, provide a link to the Creative Commons license, and indicate if changes were made. The images or other third party material in this article are included in the article’s Creative Commons license, unless indicated otherwise in a credit line to the material. If material is not included in the article’s Creative Commons license and your intended use is not permitted by statutory regulation or exceeds the permitted use, you will need to obtain permission directly from the copyright holder. To view a copy of this license, visit <http://creativecommons.org/licenses/by/4.0/>.

© The Author(s) 2022, corrected publication 2022

Article 6: Ultrafast dynamics of 2-thiouracil investigated by time-resolved Auger spectroscopy

Fabiano Lever, **Dennis Mayer**, David Picconi, Jan Metje, Skirmantas Alisauskas, Francesca Calegari, Stefan Dusterer, Christopher Ehlert, Raimund Feifel, Mario Niebuhr, Bastian Manschwetus, Marion Kuhlmann, Tommaso Mazza, Matthew S. Robinson, Richard J. Squibb, Andrea Trabattoni, Mans Wallner, Peter Saalfrank, Thomas J. A. Wolf and Markus Gühr

Journal of Physics B: Atomic, Molecular and Optical Physics 54, 014002 (2020), DOI: 10.1088/1361-6455/abc9cb

Abstract. We present time-resolved ultraviolet-pump x-ray probe Auger spectra of 2-thiouracil. An ultraviolet induced shift towards higher kinetic energies is observed in the sulfur 2p Auger decay. The difference Auger spectra of pumped and unpumped molecules exhibit ultrafast dynamics in the shift amplitude, in which three phases can be recognized. In the first 100 fs, a shift towards higher kinetic energies is observed, followed by a 400 fs shift back to lower kinetic energies and a 1 ps shift again to higher kinetic energies. We use a simple Coulomb-model, aided by quantum chemical calculations of potential energy states, to deduce a C–S bond expansion within the first 100 fs. The bond elongation triggers internal conversion from the photoexcited S2 to the S1 state. Based on timescales, the subsequent dynamics can be interpreted in terms of S1 nuclear relaxation and S1-triplet internal conversion.

Copyright note. © IOP Publishing. Reproduced with permission. All rights reserved

Ultrafast dynamics of 2-thiouracil investigated by time-resolved Auger spectroscopy

F Lever^{1,**}, D Mayer^{1,**}, D Picconi^{2,*}, J Metje¹, S Alisauskas³,
F Calegari^{3,4,5,6}, S Düsterer³, C Ehlert⁷, R Feifel⁸, M Niebuhr¹,
B Manschwetus³, M Kuhlmann³, T Mazza⁹, M S Robinson¹, R J Squibb⁸,
A Trabattoni^{3,4}, M Wallner⁸, P Saalfrank², T J A Wolf¹⁰ and M Gühr^{1,*}

¹ Institut für Physik und Astronomie, Universität Potsdam, 14476 Potsdam Germany

² Institut für Chemie, Universität Potsdam, 14476 Potsdam Germany

³ Deutsches Elektronen Synchrotron (DESY), 22607 Hamburg, Germany

⁴ Center for Free-Electron Laser Science (CFEL), DESY, 22607 Hamburg, Germany

⁵ The Hamburg Centre for Ultrafast Imaging, Universität Hamburg, 22761 Hamburg, Germany

⁶ Institut für Experimentalphysik, Universität Hamburg, 22761 Hamburg, Germany

⁷ Heidelberg Institute for Theoretical Studies, HITS gGmbH, 69118 Heidelberg, Germany

⁸ Department of Physics, Gothenburg University, SE-41296 Gothenburg, Sweden

⁹ European XFEL GmbH, 22869 Schenefeld, Germany

¹⁰ Stanford PULSE Institute, SLAC National Accelerator Laboratory, 94025 Menlo Park, United States of America

E-mail: david.picconi@uni-potsdam.de and mguehr@uni-potsdam.de

Received 31 July 2020, revised 19 October 2020

Accepted for publication 12 November 2020

Published 17 December 2020



CrossMark

Abstract

We present time-resolved ultraviolet-pump x-ray probe Auger spectra of 2-thiouracil. An ultraviolet induced shift towards higher kinetic energies is observed in the sulfur 2p Auger decay. The difference Auger spectra of pumped and unpumped molecules exhibit ultrafast dynamics in the shift amplitude, in which three phases can be recognized. In the first 100 fs, a shift towards higher kinetic energies is observed, followed by a 400 fs shift back to lower kinetic energies and a 1 ps shift again to higher kinetic energies. We use a simple Coulomb-model, aided by quantum chemical calculations of potential energy states, to deduce a C–S bond expansion within the first 100 fs. The bond elongation triggers internal conversion from the photoexcited S_2 to the S_1 state. Based on timescales, the subsequent dynamics can be interpreted in terms of S_1 nuclear relaxation and S_1 -triplet internal conversion.

Keywords: time-resolved x-ray spectroscopy, Auger spectroscopy, thionucleobases

(Some figures may appear in colour only in the online journal)

1. Introduction

Nucleobases are strong absorbers in the ultraviolet (UV) domain and show ultrafast processes after photoexcitation. Canonical nucleobases exhibit ultrafast relaxation to the singlet and triplet ground states after UV excitation through

internal conversion and intersystem crossing [1–4]. Electronic energy is efficiently transferred into vibrational excitation, a process that likely contributes to the remarkable stability of nucleic acids against UV-induced damage [1–3]. The processes underlying the ultrafast transitions violate the Born–Oppenheimer–Approximation (BOA), which allows for separate treatment of the electronic and nuclear degrees of freedom of a molecule, and is an important tool in

** Contributed equally.

* Author to whom any correspondence should be addressed.

modeling many molecular phenomena. In the case of close-lying potential energy surfaces such as avoided crossings or conical intersections, non-adiabatic coupling elements, which are neglected in the BOA, become large and lead to mixing of different Born–Oppenheimer electronic states. This redistributes the molecular population over initially unexcited potential energy surfaces [4, 5, 6]. The study of nucleobase dynamics, that cannot be described within the framework of the BOA, presents challenges both for theory as well as experiments that have been faced in the past by many systematic theoretical and experimental studies, reviewed for example in references [1–3, 7].

Thionucleobases are obtained by replacing one or two oxygen atoms by sulfur in canonical nucleobases, and exhibit two major differences compared to their canonical counterparts. The absorption spectrum is shifted from the UVC region into the UVA region [8, 9], which is much more abundant on the earth surface. In addition, photoexcitation produces long living triplet states in thionucleobases, leading to cross linking [10, 11] and the creation of reactive singlet oxygen via a reaction with the triplet oxygen molecules in the vicinity [12, 13]. These properties create on one hand a higher skin cancer risk for patients treated with thionucleobase medication for immunosuppression [14], on the other hand they might open the path for targeted photoinduced tumor therapy [15, 16].

The special case of thiouracil can be used for sketching the reaction pathway following UV excitation. The system is initially excited to the S_2 state, with $^1\pi\pi^*$ electronic character. In solution, intersystem crossing has been determined to be on a few hundred femtosecond timescale in 2-thiouracil and 4-thiouracil, as well as doubly thionated 2–4-thiouracil [9]. The S_1 $^1n\pi^*$ state has been suggested to act as a doorway state to the lower lying triplet states in excited-state absorption studies in 2-thiouracil [13] as well as for 4-thiouracil. For the latter, the lifetime of the $^1n\pi^*$ state has been indirectly determined to be 225 fs in solution [13, 17] by looking at the mismatch between the $^1\pi\pi^*$ singlet decay and triplet rise times. In contrast, time-resolved photoelectron studies in the gas phase deduce an $^1n\pi^*$ lifetime in 4-thiouracil of several picoseconds via fit of the photoelectron spectra [18]. This discrepancy is unlikely a solvent effect, as similar comparisons of gas and condensed phase techniques in 2-thiouracil give good agreements [19]. For 2-thiouracil, a joint theoretical-experimental investigation using Dyson orbitals in conjunction with gas-phase photoelectron spectroscopy [20] deduced a very fast time constant of 50 fs for $^1\pi\pi^* \rightarrow ^1n\pi^*$ internal conversion and 500 fs for the $^1n\pi^*$ lifetime; excited state absorption studies in condensed phase report on a similar $^1n\pi^*$ lifetime [9].

We now concentrate on the case of 2-thiouracil (2-TU), on which we perform our studies. The mechanism for sub-100 fs decay out of the initially photoexcited S_2 state as well as the ultrafast intersystem crossing from the S_1 $^1n\pi^*$ state into triplet states are illuminated by theoretical investigations (see reference [21] for a concise review). Cui and Fang suggest electronic states as well as crucial geometries for three different pathways, one of which includes the $^1n\pi^*$ state, while the other

paths involve transitions directly from the S_2 to triplet states. Calculations by Mai, Marquetand and González predict two different pathways for $S_2 \rightarrow S_1$ internal conversion, involving two different minima of the photoexcited state of 2-thiouracil [22]. One minimum is attributed to a $^1\pi_s\pi_6^*$ electronic character possessing a nearly planar geometry, while the other minimum is attributed to a $^1\pi_s\pi_2^*$ electronic character and it is reached via elongation and out-of-plane pyramidalization of the C–S bond. In nonadiabatic surface-hopping calculations at the CASPT2 level by the same group, both minima are predicted to be transiently populated, although the majority of the molecular photoexcited population is predicted to pass through the $^1\pi_s\pi_6^*$ minimum within 60 fs to a conical intersection connecting it to the $^1n\pi^*$ state, which then is populated for around 500 fs before decaying into triplet states [23]. A second dynamics paper from the same group on this topic using ADC(2) comes to very similar results but a longer 250 fs $^1\pi\pi^* \rightarrow ^1n\pi^*$ transition time due to pyramidalization occurring in the $^1\pi\pi^*$ state [24].

In this paper, we investigate the dynamics of 2-thiouracil using ultrashort x-ray probe pulses. Generally, time-resolved x-ray spectroscopy has been proven to be a useful tool for the study of structural changes in isolated molecules [25]. The x-rays interact with core electrons of the molecule, whose binding energies are strongly dependent on the element. Thus, x-rays offer the advantage of an element-selective spectroscopic view on molecular dynamics. In addition, due to the narrow spatial confinement of core-electronic wavefunctions, the transitions are highly site-specific. In the gas phase, these advantages have been used to follow for instance nucleobase internal conversion [26], fragmentation [27], ring-opening [28] as well as dissociation [29].

We use ultrafast x-ray induced Auger decay to investigate 2-thiouracil. This method has been applied before to investigate the internal conversion of thymine [30]. The key feature in this study was the change in molecular geometry on the photoexcited state. This can be deduced from the delay-dependent kinetic energy shift in the Auger spectrum. We used the fact that the kinetic energy of emitted Auger electrons depends strongly on the local bond distance of the molecule around the core hole created by the x-ray probe pulse. Auger electron spectroscopy is particularly suited for the use with free-electron lasers (FELs), since nonresonant Auger processes are insensitive to the energy of the probing photon, rendering the method immune against the energy fluctuation inherent in the self-amplified spontaneous emission (SASE) process. Moreover, for a given x-ray energy, several Auger decays of different elements can be addressed separately by analyzing different kinetic energy ranges, allowing the simultaneous study of the dynamics for different locations in the molecule.

We use ultrashort x-ray pulses to probe the sulfur 2p core electrons of UV-photoexcited 2-thiouracil. We measure a general shift of the 2p Auger spectrum towards higher kinetic energies. By comparison to simulations, we deduce that the molecule does not return to the molecular ground state for the maximal delay of our measurements of 2 ps. On the transient Auger signal, we identify three different dynamic features.

A first, sub-100 fs shift of the Auger band towards higher energies, followed by a 500 fs period with a slight shift towards lower energies and finally a picosecond modulation with a shift to higher kinetic energies. We show that the initial sub-100 fs modulation in the Auger spectrum can be clearly attributed to a C–S local bond elongation in the photoexcited S_2 state as predicted in the theoretical literature [22–24]. The high-energy edge shifts to lower kinetic energies in this time interval and we show that an effective theoretical model can reproduce this trend. The later modulations in the Auger spectrum fit dynamics previously attributed to the S_1 relaxation and S_1 -triplet intersystem crossing.

2. Methods

The experiment was performed at the FLASH2 facility at DESY, where the newly built URSA-PQ (German: Ultraschnelle Röntgenspektroskopie zur Abfrage der Photoenergiekonversion in Quantensystemen, engl. Ultrafast x-ray spectroscopy for probing photoenergy conversion in quantum systems) experimental chamber [31] built by the Potsdam group was connected to the FEL beamline FL24 (see figure 1).

The sample was introduced via a capillary oven [32], heated to a temperature of 150 °C, creating a molecular gas jet that crosses the x-ray beam in the interaction region of the TOF spectrometer. We have not observed degradation of the sample in previous experiments with our capillary oven under the conditions used. The 150 °C for sample evaporation have also been used in other studies on 2-thiouracil [18, 33] as tautomerization can be neglected in this regime [33].

The molecule is preexcited with a 269 nm laser pulse at the maximum of its $^1\pi\pi^*$ absorption band [18]. The pulse duration was about 80 fs as determined with an FROG (frequency resolved optical gating) setup. In the interaction region, the pulse was focused to a spot size of 50 μm by means of a focusing mirror. Inside the beamline, the x-ray beam passed unperturbed through the center of a holey mirror, while the UV beam was directed onto the reflective section of the holey mirror (just off to the side from the hole) to produce near-collinear trajectories for the two beams, as seen in figure 1. The UV laser power was adjusted by means of a $\lambda/2$ plate–polarizer combination. In the experiments, the UV laser pulse energy was set below 1 μJ . We performed systematic power scans on the time-dependent spectral features to make sure that the UV induced signal is not over-pumped.

The FEL produces frequency-tunable x-ray pulses via SASE radiation. We used a mean photon energy of 272 eV with a spectral bandwidth of 1%–2% (including jitter), as determined by the photoemission of rare gases in electron time-of-flight spectrometers ($e\text{TOF}$) integrated into the beamline [34]. The x-ray beam was linearly polarized parallel to the axis of our magnetic bottle spectrometer and parallel to the UV polarization. The x-ray pulses were focused by means of Kirkpatrick–Baez mirrors to a spot size slightly larger than the UV spot. We used systematic power scans to make sure that the x-ray induced electron spectra did not exhibit nonlinear phenomena.

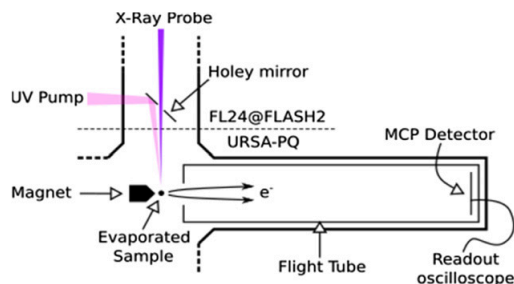


Figure 1. Experimental setup at the FL24 beamline of FLASH2. The UV pump and x-ray probe beams from FLASH2 are focused into the URSA-PQ chamber and hit the sample in the interaction region of the magnetic bottle spectrometer. The sample is evaporated using a capillary oven (located above the interaction region, out of the plane of the diagram) [31]. The photo- and Auger electrons generated by the x-ray interaction are guided into the flight tube by the magnetic bottle, detected using a multi-channel-plate (MCP) and their time of flight is measured by a fast analogue-digital converter (ADC).

The URSA-PQ setup contains a magnetic bottle electron spectrometer (MBES), providing high angular collection efficiency for electrons [35]. We used a permanent magnet and soft iron cone to reach a high magnetic field at the interaction region, which adiabatically transforms into a homogeneous magnetic field of a solenoid in a 1.7 m long flight tube. The magnet defines a small volume from which the electrons are guided into the flight tube. This volume is smaller than the optical beam overlap along the beam propagation axis. A retardation potential of 80 V was applied to the electrons using an electrostatic lens in front of the flight tube, diminishing their speed and increasing the time of flight and thus energy resolution.

The flight tube is kept at constant potential. At the very end, electrons are accelerated on the multi-channel-plate detector by a 300 V potential drop over 3 mm. The amplified electron signal trace is fully digitized using a 12 bit analog-to-digital converter (ADC) with 2 Gs s^{-1} sample rate. The amplified electron pulses have an FWHM of 10 ns, typical flight times are on the order of 250 ns for the fast valence electrons and 410 ns for the slower Auger electrons. We chose to integrate the ADC-traces to obtain our spectra, as individual electron hits could not be distinguished in TOF regions of high signal strength. The spectra were subsequently converted to a kinetic energy scale.

Tests on the Kr MNN Auger lines at 0 V retardation demonstrated an MBES resolution ($E/\Delta E$) of 40. This is not yet the maximum achievable resolution, as some x-ray beam-halo problems at the beamline prevented us from positioning the magnet closer to the interaction region which would allow for a better optimised signal. We did not check the resolution at the retardation used further below (80 V). We estimate the resolution based on the sulfur 2p photoline with 3.5 eV width at 103.5 eV to be better than 30 with respect to the total kinetic energy or 7 relative to the retarded kinetic energy. The photoline itself is considerably broadened due to the FEL linewidth and therefore our estimate is really an upper limit.

Spatial overlap of the UV-pump and x-ray probe pulses was obtained by viewing a YAG screen inserted in the interaction region through a large work-distance microscope lens. Temporal overlap was established coarsely on a 50 ps scale using a fast photodiode and high-bandwidth (13 GHz) oscilloscope checking the rising flank of the UV and x-ray induced signals. Fine temporal overlap was found with the use of the sample itself, utilizing the time-dependent behavior of Auger and 2p-photoelectron lines. The width of the time-uncertainty function is 180 fs, time zero can be found with an accuracy of ± 20 fs.

The FLASH2 FEL delivers pulse-trains with a frequency of 10 Hz; we used 50 pulses at a 200 kHz repetition rate in each pulse-train [36]. An eTOF spectrum is recorded and saved for each FEL pulse. The UV laser is set to run at 100 kHz intraburst rep-rate, such that every second x-ray shot is pumped by the optical laser, allowing the calculation of shot-by-shot difference spectra. This results in 500 x-ray pulses per second, with 250 pulses UV pumped. In the rest of the discussion, we will refer to UV pumped shots as UV-on, while x-ray only shots will be referred to as UV-off. FLASH2 instruments also provide a shot-by-shot measurement of the x-ray pulse power by means of a combined ion–electron detector. This data has been used to rescale each eTOF spectra, therefore correcting for fluctuations in the SASE pulse power.

A bunch arrival monitor (BAM) at the FEL measures the time of arrival of each electron bunch, giving information on the jitter of the x-ray arrival time [37, 38]. The width of the arrival time distribution has been measured to be 140 fs. The length of the x-ray pulse plus non-corrected jitter was estimated to be 160 fs. Pump-probe delays have been corrected with the BAM data and rebinned, exploiting the jitter and allowing finer delay binning than the time steps chosen during the measurement. The bin sizes are chosen by dividing the shot distribution in discrete parts, so that each bin is populated by the same number of shots. That is, the delay length of each bin is adjusted so that all bins have the same statistics. The delay points have been measured by random scans in repeated cycles over many hours. Thus any systematic drifts in the data-acquisition would average out.

To facilitate the interpretation of the experimental data, we make use of *ab initio* quantum chemical calculations to explore the potential energy surfaces (PESs) of the neutral (2-TU), core-ionized (2-TU+) and dicationic (2-TU++) molecule. The ground and excited states of 2-TU and 2-TU++ were computed using ground state coupled cluster theory with singles and doubles (CCSD) and the equation-of-motion formalism for the excitation energies (EOM-EE-CCSD) with the 6–311++G** basis set [39]. In order to explore the high lying states of 2-TU++, potential energy cuts along the C–S bond distance were performed using time-dependent density functional theory (TDDFT) with the B3LYP functional and the 6–311++G** basis set. Geometry optimizations for the ground and excited states of 2-TU were also performed at the (EOM-)CCSD/6–311++G** level without geometrical constraints using Q-chem, and the stability was verified by frequency calculations with the smaller 6–31++G** basis set. Stable minima were found for the states S_0 , S_1 , S_2 and T_1 .

The minimum of S_0 has a nearly planar structure. Furthermore, optimizations where the molecule was constrained to be planar were also carried out and additional (unstable) stationary points could be located for the states S_0 , S_1 , S_2 , T_1 and T_2 . The core-ionized states were computed using the equation-of-motion ionization potential formalism (EOM-IP-CCSD) with the 6–311++G** basis set for the S atom and the 6–31++G basis for all other atoms; in order to simulate the ionization from the excited states of 2-TU, the reference (neutral) CCSD wavefunction was obtained starting from an unrestricted Hartree–Fock wavefunction optimized using the maximum-overlap-method (MOM) [40]. All calculations were performed using the package Q-chem 4.4 [41]. Spin–orbit coupling, leading to a splitting of the core ionized states of about 1 eV is not included in the calculations, instead we model photoionization from the px, py, pz orbitals.

3. Results

The 272 eV photons used in the experiment allow for an element and site-specific investigation of the molecular dynamics from the perspective of the sulfur atom. An overview of the electron kinetic energy spectrum without UV pre-excitation is shown in figure 2. Various features are visible in the graph. A sharp line at 103 eV in kinetic energy, corresponding to a binding energy of 169 eV, is attributed to photoemission from the sulfur 2p ($j = 3/2$ and $1/2$) levels according to reference [33]. The ~ 1 eV spin–orbit splitting [33, 42] cannot be resolved due to insufficient spectral resolution determined by the bandwidth of the SASE FEL and the MBES energy resolution. The neighboring feature, spanning the range 115–150 eV is attributed to the Auger emission caused by the 2p core vacancy. Scanning the photon energy does not change this feature, as it is typical for Auger decay. Furthermore, the energy levels with 2p core hole binding energies around 170 eV and ten to a few ten eV valence binding energies result in Auger features at this energy band. No detailed structure is visible, even at higher MBES resolution with higher retardations, due to many broad Auger decay channels overlapping. Coarsely, the atomic Auger spectrum should divide into three larger groups belonging to sulfur $3p3p \rightarrow 2p$ (highest energy), $3p3s \rightarrow 2p$ and $3s3s \rightarrow 2p$ (lowest energy) type Auger decays. For molecules with mixed atomic orbitals resulting in molecular orbitals, these groups can still be identified in case of oxygen Auger decay [30], here it is less pronounced.

In figure 3(a), we show the pump-probe difference spectra in the energy range of the Auger features in false color-representation. The spectra are obtained by subtracting UV-off shots from the UV-on shots, accumulating data from ~ 16 million FEL shots over all delays. A positive differential signal (rendered with red color in the figures) signifies that UV pumping leads to more emitted electrons for that specific kinetic energy, while negative values (rendered with blue color in the figures) stand for a UV-induced depletion of the electron signal. Time zero was determined by maximizing the cross-correlation between a step function and the differential signal intensity. The delay values should therefore be regarded as relative to the appearance time of this feature.

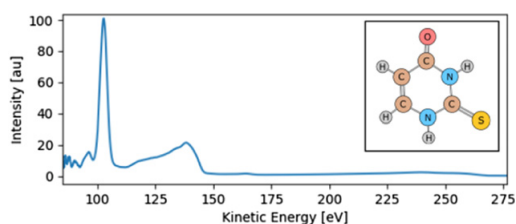


Figure 2. Overview of the photoemission spectrum of 2-thiouracil at 272 eV photon energy on an electron kinetic energy axis. Two main features are visible; the sulfur 2p photoline centered at 103 eV and the Auger band in the 115-150 eV range. Inset: structure of 2-thiouracil.

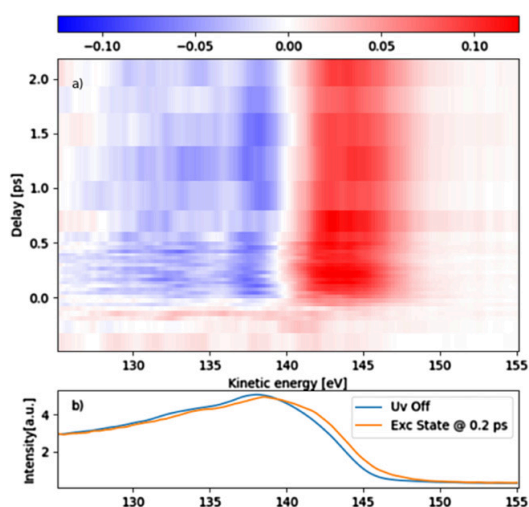


Figure 3. (a) False-color representation of time resolved differential Auger spectrum (UV-on–UV-off) for 2-thiouracil (red: positive signal, blue: negative signal). A differential feature appears at $t \sim -60$ fs and remains visible for all recorded delays. The Auger emission shifts to higher kinetic energies with UV-illumination and ultrafast changes in the shape are visible around time zero. (b) Spectra without UV excitation (UV off, blue) and spectrum of the excited state at 0.2 ps delay (orange) recovered by the procedure described in the text.

For positive delays, a general shift of the Auger spectrum toward higher kinetic energies is visible. This coarse shift of intensity in the difference spectrum related to the UV excitation is about 4 eV, however, the shift undergoes dynamics on an eV scale, as we will show below. We first investigate the coarse shift closer. The UV-on spectrum is given as $fES + (1 - f)GS$, where ES and GS are the excited state and ground state Auger spectra respectively and f is the fraction of excited molecules. The UV-off spectrum is given as GS. The difference UV-on minus UV-off is thus $f(ES - GS)$. In the process of photoexcitation, the f changes.

An estimate of the excited state Auger spectrum is shown in figure 3(b). It has been obtained from the UV-on and UV-off data. We need to model f as a function of delay to obtain ES. Assuming that the fraction of excited molecules, f introduced

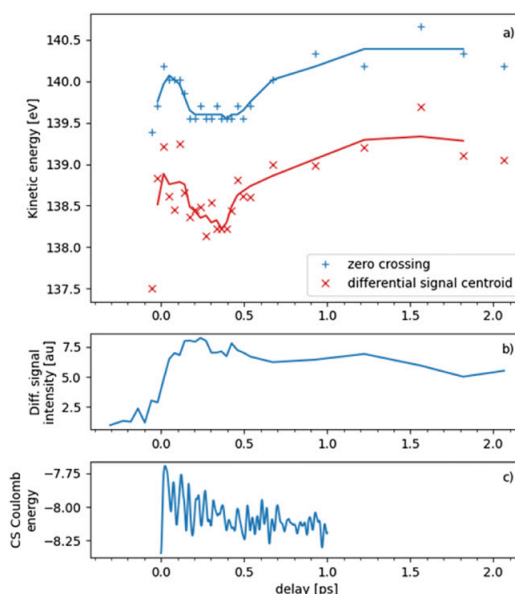


Figure 4. (a) Zero crossing and differential signal centroid positions vs delay. Ultrafast dynamics is visible after time zero, with changes occurring on timescales from 100 fs to 1 ps. Solid lines are 3 point moving averages. (b) Differential signal intensity, calculated from the cumulative sum of positive plus absolute of negative data points for each delay value. (c) Negative Coulomb energy constructed from the trajectory set of reference [24] using a simple Coulomb potential as a function of C–S distance.

above, in the ensemble rises as an error function from 0 to 0.22 we succeeded to reconstruct the ES spectrum. The final f of 0.22 was chosen as the minimum possible value that does not lead to negative amplitudes in the reconstructed excited spectrum ES. We identify that the shape of the Auger spectrum changes by comparing the UV-off spectrum with the reconstructed ES spectrum at 200 fs delay. The maximum in the UV-off spectra is located at 138 eV. For the excited state spectrum at 200 fs, the region around the maximum flattens up to about 142 eV, for higher energies the excited state spectrum drops. This leads to the observed gross shift in the difference spectra with a bleach at 138 eV and an increase from 140 eV on with its maximum at 142 eV. The edge itself shifts only by about 1 eV in the center of the edge and about 2 eV at the very high energy region. Assuming that the ES spectrum is completely static (no molecular dynamics after photoexcitation), the difference spectrum would not show any dynamics, apart from a changing scaling factor f . We however observe a fine shift visible in the zero line, thus indicating the presence of ultrafast processes in the relaxation pathway of the molecule.

In order to quantify the shift dynamics, the zero-crossing position of the differential signal (white line in between blue and red features) needs to be analyzed for each time delay. We estimated this parameter by maximizing the cross-correlation of the kinetic energy spectrum with a sign function. This method delivers the blue datapoints in figure 4(a). In addition,

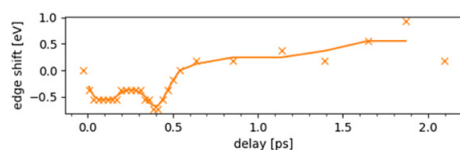


Figure 5. Auger edge shift as a function of pump-probe delay. Edge values are taken at the point where the signal rises over 20% of the peak intensity. Data points are shown for delays where the excited state population is above 1% of the final value. Solid line is a 3 point moving average.

we calculated the center of mass of the positive and negative contributions and averaged their value (red datapoints in figure 4(a)). The analysis of the centroid positions allows us to be sensitive to changes in the overall spectral distribution that might not affect the zero crossing point.

The aforementioned analysis technique does not give meaningful results when no differential features are present as it would be noise dominated. Therefore, we use the absolute intensity of the differential signal in figure 4(b)) (positive contribution + absolute of negative contribution) to select the delay regions that can be interpreted. The onset of the differential feature is found at delay ~ -60 fs, and we clearly identify the typical lineshape in this time bin in the false color plot of figure 3(a).

The Auger dynamics shows three phases (see figure 4(a)). First, a fast shift towards higher kinetic energies on a ~ 100 fs scale is visible, shifting the centroid difference as well as the zero crossing up by about 1 eV in kinetic energy. Since the time resolution of the experiment is in this regime, we cannot give more precise estimates of the dynamics. After this initial rise in the kinetic energy, a transient dip of ~ 0.5 eV is visible, lasting for about 400 fs. This is followed by a 1 ps rise in centroid/zero crossing energy by 1 eV.

We now concentrate on the shift in the edge of the excited state Auger spectrum at high kinetic energies. We therefore analyze the time dependent ES spectra with the dynamic f described above. Figure 5 shows the edge-position, defined by the ES signal being above 20% of the peak signal for each delay bin. The shifts are evaluated relative to the ES spectrum at zero delay. Ultrafast dynamics on the same time scales as presented above can be discerned here, with some differences in the shift amplitudes.

The three phases mentioned above are discernible here again. The initial 100 fs dynamics is characterized by a shift of the edge position of -0.5 eV (relative to the first datapoint), which is the opposite trend as shown in the zero position and centroid. This is followed by a plateau and a further dip at the 400 fs mark. After the dip, a fast 1 eV blue shift is observed, persisting for the remaining of the time evolution. The different signs of spectral shift in the edge and at zero crossing in the beginning actually indicate that the excited state Auger spectrum undergoes changes in its shape.

4. Discussion

First, we discuss the results of the calculations. Table 1 reports our calculated energies at different stationary points on the excited states surfaces, and the corresponding value for the C–S bond distance. Geometry optimizations have been carried out with and without the constraint of planarity. Local and global minima on the singlet and triplet potential energy surfaces of 2-TU have been located by Mai *et al* using multistate complete active space perturbation theory calculations and in the present study using EOM–CCSD theory [22]. The calculated energies as well as geometry parameters are close to those of Mai *et al* [21]. Surface-hopping trajectories calculated by Mai *et al* predict that in the first 50 fs the molecule retains a near-planar geometry, and so do many trajectories at subsequent times and after transitions from S_2 to other states.

In order to investigate the initial behavior of the Auger signal at photoexcitation, we computed the energies of the valence-excited, core-ionized and dicationic states in the Franck–Condon region (see figure 6). We also calculated PESs along a reaction pathway which linearly interpolates between the unrestricted optimized minima of S_0 (reaction coordinate = 0) and the initially photoexcited S_2 (reaction coordinate = 1) states. This will help later in the interpretation of the high kinetic energy Auger edge.

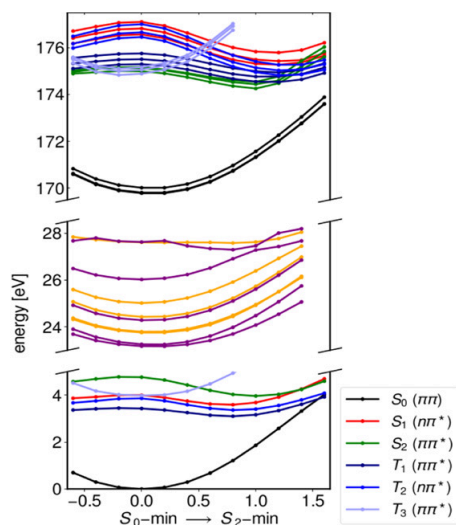
The data in the Franck–Condon region allows us to estimate the change in the kinetic energy of emitted Auger electrons, as Auger kinetic energy is equal to the difference between the core ionized state (one electron missing from the sulfur 2p shell) and the dicationic manifold (with two electrons missing in the valence orbitals). Auger emission from the non-UV excited molecule occurs from the ground core-excited state (black around 170 eV) to many different dicationic states, of which only the lowest ones are calculated. Auger emission from the UV excited molecule occurs from the core ionized $S_2-^1\pi\pi^*$ state (green with an energy of 175 eV in the Franck–Condon region). Assuming that the rates for the Auger transitions do not change upon UV excitation, the model predicts a general shift towards higher kinetic energy of the Auger spectrum in the range of 5 eV.

Molecular dynamics on the core-ionized states can be neglected within the few fs-Auger decay timescale. All the states visited by the molecule after UV excitation show a gap with respect to the ground state. If efficient coupling to the ground state is absent on our measured timescales, as predicted by many previous papers [9, 20, 21], the measured Auger spectra must show a long lasting blue shift that begins at time zero and remains present for all probed delays. This is in general agreement with the spectral trend observed in our measurements, and thus serves as a confirmation of excited state lifetimes longer than a few picoseconds.

The assumption of no Auger rate changes upon UV excitation however is oversimplified. As the valence occupation of

Table 1. Calculated electronic energies and C–S bond distances at planar (*) and non-planar minima of 2-thiouracil, optimized at the EOM–CCSD/6–311++G** level.

Minimum	Planar geometries					Non-planar geometries		
	S ₀ *	S ₁ *	S ₂ *	T ₁ *	T ₂ *	S ₁	S ₂	T ₁
Energy (eV)	0.00	3.78	4.44	3.17	3.65	3.48	3.96	3.00
C–S distance (Å)	1.65	1.74	1.76	1.67	1.73	1.77	1.90	1.77

**Figure 6.** Calculated energy values for different electronic levels and for various nuclear configurations interpolated between the S₀ and S₂ minima. The energy scale is divided in ground and valence excited states (lower portion), 10 lowest energy dicationic states (middle) and core ionized (2p⁻¹) states (upper). The core excited states follow the color coding of the valence states, meaning that their valence configuration is maintained with a 2p core hole. The core ionized states of each valence state are divided into three states, according to px, py, pz ionization. SO coupling, leading to an observed core-ionized state splitting of 1 eV, is not included in our calculation. Singlet and triplet dicationic states are shown in orange and violet, respectively. Auger features with the highest observable kinetic energy can be calculated from the energy gap between core excited and dicationic states.

two of the highest valence orbitals changes, there will be rate changing effects. Similar to the resonant-Augur language, one can define spectator and participator channels here but the calculation of those rates is beyond the scope of this paper. We expect the valence reorganization effects induced by the UV excitation to be most effective at the high energy edge of the Auger spectrum, with participation from the highest orbitals. A comparison with the reconstructed ES spectrum (figure 3(b)) serves to support this point. The edge of the spectrum shows a UV induced shift of only 1–2 eV. In the region around the maximum, the redistribution of population is larger indicating shifts closer to those predicted by the gap between ground cationic state and excited cationic states, thus rate changes due to UV are less important in this region.

In order to interpret the initial ultrafast changes of the shift in the Auger spectrum, we include a model for the more energetic states of the dicationic manifold. The previously presented calculations on the lowest dicationic states will be used further below in a comparison to the edge features presented in figure 5. Upon sulfur 2p Auger decay, dicationic states with electrons missing in orbitals localized at the sulfur atom will be preferentially populated, as the decay matrix element is sensitive on the overlap of core and valence holes [30, 43]. Those orbitals promote the C–S bonding and thus the Auger decay kinetic energy will be sensitive to the C–S bond [30]. Since the missing valence electrons expose the nuclear charges, the Auger manifold will be dominated by Coulomb repulsion. The lowest energy dicationic states often show a binding character as seen in figure 6. We performed a Löwdin population analysis on the dicationic states of figure 6. Indeed, for most states the computed charge on the S atom is in the range 0.8–1.0 e. The electron hole on the S atom is present for all geometries, suggesting that Coulomb repulsion should be present, at least at longer C–S distances. From the kinetic energy difference between the maximum and the edge of the Auger band, the Coulomb repulsive states should be located 7–8 eV above the lowest (bound) states of 2-TU²⁺, therefore they are not covered by our EOM–CCSD calculations. Repulsive potential energy curves in this energy range are predicted by TDDFT scans we performed along the C–S bond distance (not shown here). Indeed, with higher potential energy, dicationic states are increasingly dominated by Coulomb repulsion [44]. All statements below are therefore valid for the majority of the Auger decay channels, apart from the highest kinetic energy ones. Figure 7 shows a sketch of the electrostatic energy e^2/R for a dicationic state as a function of C–S bond stretch R . Qualitatively speaking, this can be seen as the central energy of the final state in the Auger decay process. Therefore, the decrease of Coulomb energy with increasing C–S bond distance will lead to an increase in Auger kinetic energy, given that the core ionized starting state remains approximately constant in energy along the reaction coordinate as seen in figure 6.

The data on the zero-crossing as well as the centroid in figure 4 indicates an initial dynamic shift towards higher kinetic energies around time zero by less than 1 eV. Assuming that the ground and excited state spectra have similar shape, the overall spectral shift will be double the zero crossing shift, so between 1 and 2 eV. According to figure 7, the simple Coulomb-potential model predicts a bond expansion. At the Franck–Condon point, the molecule possesses a C–S bond distance of 1.65 Å (table 1). The experimentally observed shift

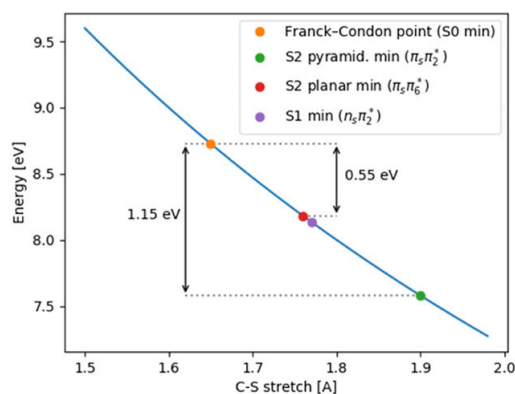


Figure 7. Electrostatic energy for a dicationic state for various bond lengths. Numerical values for the bond lengths as in table 1. In the suggested dynamics, the electrostatic contribution to the molecular energy follows the highlighted path, caused by an ultrafast stretch and subsequent contraction of the C–S bond.

would predict an expansion of the C–S bond by nuclear relaxation into an interval from 1.85 to over 2 Å within a delay range limited essentially by our temporal resolution. This interval does not include the calculated planar minimum at 1.76 Å. Our planar minimum has a structure similar to the (slightly non-planar) $\pi_5\pi_6^*$ minimum found by Mai *et al* [23], and predicted to be the dominant pathway for nuclear relaxation out of the Franck–Condon region on the S_2 surface at short times. The experimentally found interval includes the unrestricted minimum at 1.90 Å. This minimum has a structure similar to the $\pi_5\pi_2^*$ minimum found by Mai *et al* [22]. It is predicted to be populated, however with much less amplitude compared to the other minimum. The ADC(2) calculations by the same group however predict the internal conversion mostly occurring through a pyramidal deformation [24].

Shortly after the maximum in spectral shift, there is a reverse shift in the zero crossing and centroid towards lower kinetic energies by about 0.5 eV, as observed in figure 4. The feature is then stable for about 400 fs. The ADC(2) based trajectory calculations indeed show a reverse trend. In order to compare the results to our data, Mai *et al* kindly sent us the C–S distance of their trajectories [24]. We used those to calculate the dicationic energies and show them in figure 4(c). We clearly identify the reverse trend indicating shrinking C–S bond length over 400 fs. In the framework of the ADC(2) calculations, this period is dominated by dynamics on the S_2 state [24]. In comparison to these simulations, we seem to pick up the trends in the bond extension well. The rising kinetic energy after 400 fs does not find its counterpart in any of the calculated C–S bond data of [24]. Thus it would need to be attributed to electronic state effects. On this timescale the triplet T_1 state is predicted to take over in referene [24].

The CASPT2 trajectory calculations of Mai *et al* [23], display a S_2 – S_1 internal conversion on the order of 60 fs (below our time-resolution), with an S_1 state lifetime of 400–500 fs [23]. This interpretation is also chosen in previous experiments [18, 19, 40]. Afterwards, the T_1 and T_2 states become popu-

lated via an intersystem crossing with the S_1 . In this framework, the fitting time scales suggests that the pump-probe Auger signal in the interval between 50 fs and 400 fs is most likely due to the population in the S_1 ($^1n\pi^*$) state. According to the Coulomb-potential model, the decrease in kinetic energy should be associated with a slight contraction of the C–S bond. However, at the S_1 minimum, optimized at the EOM–CCSD level, the C–S distance is 1.77 Å, i.e. very similar to the bond length at the S_2 planar minimum. Therefore, the C–S bond contraction could be explained by allowing that a relevant fraction of molecules on the S_2 surface either evolve towards the $^1\pi_5\pi_2^*$ minimum (a barrierless pathway as shown in figure 6, but less relevant according to the simulations of reference [23]) or undergo a large C–S elongation while retaining planarity, before undergoing the internal conversion. On the other hand, many of the nonadiabatic dynamics trajectories of reference [23] evolve along planar configurations also on the S_1 surface. Optimizing the S_1 state with the constraint of planarity we obtained a stationary point with a shorter C–S distance (1.74 Å), which might also explain the observed decrease in kinetic energy. This model of course neglects all changes in the Auger spectra induced by electronic transitions. While our assumptions are justified on the initially photoexcited state, a transition from S_2 to S_1 can equally alter the Auger kinetic energies on the eV level. In order to make more precise statements about the competition of electronic vs nuclear relaxation in shaping the Auger spectrum, further simulations need to be accomplished, which are beyond the scope of this work.

As stated above, we assumed that only nuclear geometry is able to influence the Auger kinetic energy. This is certainly justified for the initial relaxation of the molecular vibrational wave packet out of the Franck–Condon window. At later times, there might be an increasing influence of the electronic state changes on the Auger spectrum, and the argument will become more intertwined. However, we note that for Auger decay of the lighter oxygen, we have observed this strong electronic state dependence before as a massive redshift of the Auger band [30]. This is obviously lacking in our current experiment. We thus speculate, that the Auger decay of the much heavier sulfur, due to its increased density of states on the dicationic manifold will be less susceptible to those electronic state effects.

Regarding the dynamics of the high energy Auger edge, we can compare the excited state spectrum inferred from the experimental data to a synthetically constructed spectrum from the calculated potential energy curves of figure 6. It is important to note, that the computational results do not give us any information on the relative strengths of the various transitions; therefore, the constructed spectrum should be regarded as a qualitative guideline, and not as a predictive tool. Assuming a linear relaxation along the S_2 potential surface on a time scale of 60 fs, a time dependent excited state spectrum from the data in figure 6 can be constructed. The energy difference between the core excited S_2 state and each of the calculated dicationic states is taken as a function of time, and all the contributions are broadened and summed together to generate the time dependent spectrum. Convoluting the result with an error function in order to model the non-simultaneous excitation of

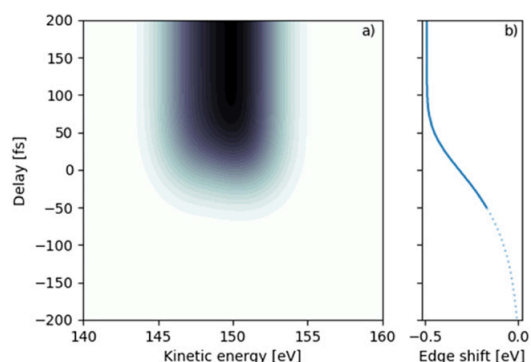


Figure 8. (a) Reconstructed high kinetic energy band of the Auger spectrum for the calculated energy levels, convoluted with an error function to account for non-simultaneous excitation of the molecular ensemble. (b) Auger edge shift in the reconstructed spectrum as a function of pump-probe delay. Dashed line shows values where the excited fraction is below 1% (compare to figure 4(b)).

the ensemble, we obtain an estimate for the dynamics of the Auger edge.

The calculated spectrum is shown in figure 8(a). Analyzing the edge shift in the same way as in figure 5, we deduce a redshift of the edge position (figure 8(b)) in agreement with the experimental result in figure 5. The calculated value is 0.3 eV, while the experimental shift in the edge is 0.5 eV with a discrete bin interval of 0.2 eV. According to the simulation, the energies of the lowest dicationic states and of the core-ionized states accessed from S_2 increase and decrease respectively, along the reaction pathway of figure 6. This is associated with a highest kinetic energy of the Auger electrons. Therefore, the short-time observed redshift of the Auger band edge provides further evidence for an ultrafast nuclear relaxation of the molecule out of the Franck–Condon region on a sub 100 fs timescale.

On a longer time scale, for delays in the range 0.4 to 1.5 ps, the shift to higher kinetic energies observed on both the zero crossing and the edge position points to further ultrafast processes in the molecular dynamics (figures 4 and 5). The detailed interpretation of those features however requires a deeper understanding of the Auger processes in the molecule, due to the aforementioned electronic state effects.

5. Summary

In this work, we have used Auger spectroscopy to investigate the ultrafast dynamics of 2-thiouracil after UV excitation, using a UV pump–x-ray probe setup. The experiment has been carried out at beamline FL24 at the FLASH2 free electron laser. We observe a shift in the overall Auger emission pattern, as well as ultrafast dynamics in the shift amplitude, providing evidence for ultrafast processes in the molecule. The dynamics of the zero-crossing/centroid of figure 4 in conjunction with our quantum chemical calculations and the trajectory simulations by Mai *et al* [23, 24] strongly suggests that the

time-resolved Auger signal is capable of capturing the main relaxation pathway of 2-thiouracil, which involves three steps: (i) an ultrafast, <100 fs, process likely associated with an overstretching of the C–S bond, which leads to the S_2 – S_1 internal conversion; (ii) an intermediate evolution on the S_1 surfaces, for approximately 400 fs [23] or alternatively a shrinking C–S bond dominated by S_2 dynamics [24]; (iii) the final intersystem crossing and subsequent relaxation in the triplet manifold. The C–S bond elongation in step (i) can be deduced from the observed zero line/centroid Auger shift towards higher kinetic energies using a simple Coulomb-model for dicationic states. Additional support for this behavior is delivered by an observed edge shift towards lower kinetic energies, which is predicted by our model using the lowest dicationic states. Experimental evidence for (ii) and (iii) comes from an agreement of timescales in the zero line/centroid Auger shift, the details of the shift required additional Auger spectrum modeling involving electronic and nuclear dynamics, which is beyond the scope of this work.

Acknowledgments

We thank S Mai (González group, Theoretical Chemistry, University of Vienna) for generously sending us trajectory data from reference [24] used in figure 4(c). We thank the Volkswagen foundation for funding via a Lichtenberg Professorship. We thank the BMBF for funding the URSA-PQ apparatus and for funding JM via Verbundforschungsproject 05K16IP1. We acknowledge DFG funding via Grants GU 1478/1-1 (MG) and SA 547/17-1 (PS). TJAW was supported by the US Department of Energy, Office of Science, Basic Energy Sciences, Chemical Sciences, Geosciences, and Biosciences Division. We acknowledge DESY (Hamburg, Germany), a member of the Helmholtz Association HGF, for the provision of experimental facilities. Part of this research was carried out at FLASH2. FC acknowledges support from the European Research Council under the ERC-2014-StG STARLIGHT (Grant Agreement No. 637756).

ORCID iDs

F Lever <https://orcid.org/0000-0002-8448-7594>
 D Mayer <https://orcid.org/0000-0002-1858-6818>
 D Picconi <https://orcid.org/0000-0001-6468-1595>
 B Manschwetus <https://orcid.org/0000-0001-6165-9560>
 A Trabattoni <https://orcid.org/0000-0002-0187-9075>
 T J A Wolf <https://orcid.org/0000-0002-0641-1279>
 M Gühr <https://orcid.org/0000-0002-9111-8981>

References

- [1] Barbatti M, Borin A C and Ulbrich S (ed) 2015 *Nucleobases in the Gas Phase and in Solvents* (Berlin: Springer)
- [2] Middleton C T, de La Harpe K, Su C, Law Y K, Crespo-Hernández C E and Kohler B 2009 *Annu. Rev. Phys. Chem.* **60** 217

- [3] Crespo-Hernández C E, Cohen B, Hare P M and Kohler B 2004 *Chem. Rev.* **104** 1977
- [4] Wolf T J A, Parrish R M, Myhre R H, Martínez T J, Koch H and Gühr M 2019 *J. Phys. Chem. A* **123** 6897
- [5] Levine B G and Martínez T J 2007 *Annu. Rev. Phys. Chem.* **58** 613
- [6] Yarkony D R 1996 *Rev. Mod. Phys.* **68** 985
- [7] Improta R, Santoro F and Blancafort L 2016 *Chem. Rev.* **116** 3540
- [8] Ashwood B, Pollum M and Crespo-Hernández C E 2019 *Photochem. Photobiol.* **95** 33
- [9] Pollum M, Jockusch S and Crespo-Hernández C E 2015 *Phys. Chem. Chem. Phys.* **17** 27851
- [10] Brem R, Daehn I and Karran P 2011 *DNA Repair* **10** 869
- [11] Zhang X, Jeffs G, Ren X, O'Donovan P, Montaner B, Perrett C M, Karran P and Xu Y-Z 2007 *DNA Repair* **6** 344
- [12] Kuramochi H, Kobayashi T, Suzuki T and Ichimura T 2010 *J. Phys. Chem. B* **114** 8782
- [13] Pollum M, Martínez-Fernández L and Crespo-Hernández C E 2014 *Photoinduced Phenom: Nucleic Acids I* ed M Barbatti, A C Borin and S Ullrich (Berlin: Springer) pp 245–327
- [14] Euvrard S, Kanitakis J and Claudy A 2003 *N. Engl. J. Med.* **348** 1681
- [15] Massey A, Xu Y-Z and Karran P 2001 *Curr. Biol.* **11** 1142
- [16] Reelfs O, Karran P and Young A R 2012 *Photochem. Photobiol. Sci.* **11** 148
- [17] Borrego-Varillas R, Teles-Ferreira D C, Nenov A, Conti I, Ganzer L, Manzoni C, Garavelli M, Maria de Paula A and Cerullo G 2018 *J. Am. Chem. Soc.* **140** 16087
- [18] Mohamadzade A, Bai S, Barbatti M and Ullrich S 2018 *Chem. Phys.* **515** 572
- [19] Sánchez-Rodríguez J A, Mohamadzade A, Mai S, Ashwood B, Pollum M, Marquetand P, González L, Crespo-Hernández C E and Ullrich S 2017 *Phys. Chem. Chem. Phys.* **19** 19756
- [20] Mai S, Mohamadzade A, Marquetand P, González L and Ullrich S 2018 *Molecules* **23** 2836
- [21] Arslançan S, Martínez-Fernández L and Corral I *et al* 2017 *Molecules* **22** 998
- [22] Mai S, Marquetand P and González L 2015 *J. Phys. Chem. A* **119** 9524
- [23] Mai S, Marquetand P and González L 2016 *J. Phys. Chem. Lett.* **7** 1978
- [24] Mai S, Plasser F, Pabst M, Neese F, Köhn A and González L 2017 *J. Chem. Phys.* **147** 184109
- [25] Young L *et al* 2018 *J. Phys. B: At. Mol. Opt. Phys.* **51** 032003
- [26] Wolf T J A *et al* 2017 *Nat. Commun.* **8** 29
- [27] Pertot Y *et al* 2017 *Science* **355** 264
- [28] Attar A R, Bhattacharjee A, Pemmaraju C D, Schnorr K, Closser K D, Prendergast D and Leone S R 2017 *Science* **356** 54
- [29] Brauße F *et al* 2018 *Phys. Rev. A* **97** 043429
- [30] McFarland B K *et al* 2014 *Nat. Commun.* **5** 4235
- [31] Metje J 2020 *Applied Sci.* **10** 7882
- [32] McFarland B K *et al* 2014 *J. Phys.: Conf. Ser.* **488** 012015
- [33] Giuliano B M, Feyer V, Prince K C, Coreno M, Evangelisti L, Melandri S and Caminati W 2010 *J. Phys. Chem. A* **114** 12725
- [34] Braune M, Buck J, Kuhlmann M, Grunewald S, Düsterer S, Viefhaus J and Tiedtke K 2018 *J. Synchrotron Radiat.* **25** 3
- [35] Kruit P and Read F H 1983 *J. Phys. E: Sci. Instrum.* **16** 313
- [36] Faatz B *et al* 2016 *New J. Phys.* **18** 062002
- [37] Schulz S *et al* 2015 *Nat. Commun.* **6** 5938
- [38] Savelyev E *et al* 2017 *New J. Phys.* **19** 043009
- [39] Krylov A I 2008 *Annu. Rev. Phys. Chem.* **59** 433
- [40] Besley N A, Gilbert A T B and Gill P M W 2009 *J. Chem. Phys.* **130** 124308
- [41] Shao Y *et al* 2015 *Mol. Phys.* **113** 184
- [42] Thompson A C and Vaughan D 2009 *X-RAY Data Booklet* (Washington DC: GPO - United States Government Publishing Office)
- [43] Siegbahn H, Asplund L and Kelfve P 1975 *Chem. Phys. Lett.* **35** 330
- [44] Cryan J P *et al* 2012 *J. Phys. B: At. Mol. Opt. Phys.* **45** 055601



6 | Conclusions & Outlook

In this thesis based on six publications, I summarize my contributions in the field ultrafast molecular dynamics. It covers the x-ray and UV spectroscopy of thionated uracil as well as the relaxation dynamics of 2-thiouracil as studied with time-resolved x-ray spectroscopy.

Understanding photoinduced dynamics is crucial as biomolecules like 2-tUra are used for medical and research purposes. However, it is challenging to decipher the ultrafast relaxation mechanism in molecules as the time-scales are incredibly short (fs) and the response of the molecule is not necessarily due to one singular mechanism. The method of choice to address this problem during this work was ultrafast UV-pump x-ray probe electron spectroscopy. Using ultrashort pulses on the natural time-scales of the process of interest provides the temporal resolution necessary to study them. The UV serves for the direct excitation of the molecule 2-tUra and initiates the relaxation process. The x-ray pulses deliver site- and element-specific probing reducing the problem to a specific atom and its surrounding (here: the only sulfur atom in the molecule).

In order to do those experiments, one needs to establish first the states that are involved in the process (article 1). Then, a suitable apparatus needs to be built that provides the requirements for UV-pump x-ray probe spectroscopy (article 2). With that one can establish the x-ray spectroscopy of the molecule (article 3) to understand the features that are going to be studied in time-resolved experiments. These reveal that time-resolved XPS is best to track the charge flow over the molecule (article 4 & 5). However, the molecular dynamics is made up by the coupled electron and nuclear dynamics. Auger spectroscopy can give insight into these nuclear dynamics to a certain extent (article 6).

In more detail, we present in article 1 the experimental as well as theoretical UV absorption spectra of thionated uracil in the gas-phase. For 4-thiouracil and 2,4-dithiouracil, these are the first experimental gas-phase spectra published. By comparing the experimental spectra, it is possible to predict the localisation of certain orbital transitions. The coupled-cluster calculations performed compare well to the experimental spectra and back the prediction made from the experimental data. A comparison to literature spectra shows that some solution phase spectra that are supposed to resemble the pure gas-phase spectrum show significant differences to our measurements. A further comparison shows that basic environments tend to affect each thiouracil differently while acidic and neutral environments don't.

In article 2, I present the apparatus used at the beamtimes at FLASH. We describe the details of the magnetic bottle time-of-flight spectrometer which is the heart of the

instrument. With measurements on krypton, we determine a resolution of 40 for our MBES at a retardation of 0 V. Using the 2-thiouracil S 2p line, we determine temporal resolution of 200 fs in the pump-probe measurements.

The NEXAFS and core-level electron spectra of the sulfur L edge of 2-tUra are presented in article 3. Within a photon energy window from 150 to 250 eV, main sulfur related features emerge *i.e.*, the dispersing S 2p photoline and the corresponding Auger-Meitner band as well as the S 2p photoline and the corresponding Coster-Kronig decay. By scanning the above window, we determined the first NEXAFS (x-ray absorption) spectra at the sulfur L-edges.

Article 4 and 5 cover the x-ray photoelectron spectroscopy performed on the 2-tUra molecule. Technical aspects concerning the data analysis are described in article 4. Here, we show the influence of different FEL jitters *i.e.*, photon energy and timing jitter, on the photoelectron spectra of 2-tUra. We describe how shot-to-shot measurements of beam arrival times and self-referencing of a photoline in absence of shot-to-shot photon energy measurements can improve the data quality.

Based on these analysis techniques, article 5 covers the observed relaxation behaviour of the S 2p photoline. We introduce the model of the excited-state chemical shift to connect the observed UV-induced shift of the photoline with the electronic charge flow during the relaxation. Coupled-cluster calculations verify this model and show, further, that the partial charge on the sulfur atom is dominated by the character of the electronic state the molecule is in. Observed oscillations in the binding energy shifts are attributed to coherent oscillations between electronic states and an ultrafast decay in the intensity of the signal gives rise to a ground-state relaxation channel. In summary, we prove in this article that ultrafast x-ray photoelectron spectroscopy gives insight into the electronic character of the states involved in a relaxation process.

The corresponding time-resolved Auger-Meitner spectroscopy is covered in article 6. Similar to the XPS, a shift is observed in the S 2p Auger-Meitner band. With a simple Coulomb model, we are able to correlate the shift within the first couple of 100 fs to an elongation in the C=S bond distance. Previously performed ADC calculations by S. Mai *et al.* confirm the prediction from the Coulomb model. Thus, we show that time-resolved Auger-Meitner spectroscopy can give insight into geometrical changes at early stages of the relaxation process.

The static spectroscopy performed in article 3 suffers from large bandwidth of the FEL as well as jitter correlated issues and for these measurements it is more reasonable to perform them at a synchrotron source as shown in chapter 3 and 4. However, article 5 and 6 show the capabilities FELs provide for time-resolved x-ray electron spectroscopy. The site and element selectivity allows one to focus on very specific regions of the molecules *e.g.*, a single atom as shown here with the spectroscopy at the sulfur L edge. In combination with the short fs pulses, it is possible to concentrate on geometric and electronic changes at a particular site of the molecule of interest. The (photon energy) stability issues of SASE FELs as FLASH are starting to be addressed *e.g.*, by seeding mechanism in the SASE process [94] and a more thorough shot-to-shot tracking of FEL parameters. Improving the

control over the experiment creates also more opportunities for the data analysis as new techniques can be applied such as “spooktroscopy” [115–117] or machine learning [121, 122]. These can help to improve the resolution of the experiments and thus one may gain even more insight into molecular dynamics by utilising x-ray (electron) spectroscopy.

Further, the thesis shows that – from the point of view of the sulfur atom – we can follow the charge flow over the molecule that is associated with its internal conversion and can even reflect great details on the oscillatory character of this. The reasonable step forward would now be to investigate where the charge that is abstracted from the sulfur in the $n\pi^*$ state actually flows. Follow-up experiments that point on atoms on the pyrimidine ring (C and N) and track the charge flow there can provide a full picture on the redistribution of electrons during the molecular relaxation.

Bibliography

- ¹A. C. Kneuttinger, G. Kashiwazaki, S. Prill, K. Heil, M. Müller and T. Carell, 'Formation and Direct Repair of UV-induced Dimeric DNA Pyrimidine Lesions', *Photochemistry and Photobiology* **90**, 1–14 (2014).
- ²W. J. Schreier, T. E. Schrader, F. O. Koller, P. Gilch, C. E. Crespo-Hernandez, V. N. Swaminathan, T. Carell, W. Zinth and B. Kohler, 'Thymine dimerization in dna is an ultrafast photoreaction', *Science* **315**, 625–629 (2007).
- ³G. Ackermann, 'Photophysikalische Grundlagen zur Fluoreszenzdiagnostik von Tumoren der Haut', Dissertation (Universität Regensburg, 2001).
- ⁴A. P. Castano, T. N. Demidova and M. R. Hamblin, 'Mechanisms in photodynamic therapy: part one—photosensitizers, photochemistry and cellular localization', *Photodiagnosis and Photodynamic Therapy* **1**, 279–293 (2004).
- ⁵A. P. Castano, T. N. Demidova and M. R. Hamblin, 'Mechanisms in photodynamic therapy: part two—cellular signaling, cell metabolism and modes of cell death', *Photodiagnosis and Photodynamic Therapy* **2**, 1–23 (2005).
- ⁶A. P. Castano, T. N. Demidova and M. R. Hamblin, 'Mechanisms in photodynamic therapy: Part three—Photosensitizer pharmacokinetics, biodistribution, tumor localization and modes of tumor destruction', *Photodiagnosis and Photodynamic Therapy* **2**, 91–106 (2005).
- ⁷A. J. McLean, D. J. McGarvey, T. G. Truscott, C. R. Lambert and E. J. Land, 'Effect of oxygen-enhanced intersystem crossing on the observed efficiency of formation of singlet oxygen', *J. Chem. Soc., Faraday Trans.* **86**, 3075–3080 (1990).
- ⁸P. R. Ogilby, 'Singlet oxygen: there is indeed something new under the sun', *Chemical Society Reviews* **39**, 3181–3209 (2010).
- ⁹L. A. Ortiz-Rodríguez and C. E. Crespo-Hernández, 'Thionated organic compounds as emerging heavy-atom-free photodynamic therapy agents', *Chemical Science* **11**, 11113–11123 (2020).
- ¹⁰S. Arslançan, L. Martínez-Fernández and I. Corral, 'Photophysics and photochemistry of canonical nucleobases' thioanalogs: From quantum mechanical studies to time resolved experiments', *Molecules* **22**, 998 (2017).
- ¹¹B. Ashwood, M. Pollum and C. E. Crespo-Hernández, 'Photochemical and Photodynamical Properties of Sulfur-Substituted Nucleic Acid Bases', *Photochemistry and Photobiology* **95**, 33–58 (2019).

- ¹²S. Bai and M. Barbatti, 'On the decay of the triplet state of thionucleobases', *Physical Chemistry Chemical Physics* **19**, 12674–12682 (2017).
- ¹³M. Pollum, L. Martínez-Fernández and C. E. Crespo-Hernández, 'Photochemistry of Nucleic Acid Bases and Their Thio- and Aza-Analogues in Solution', in *Photoinduced phenomena in nucleic acids i*, edited by M. Barbatti, A. C. Borin and S. Ullrich (Springer International, Cham, 2014), pp. 245–327.
- ¹⁴T. Carell, C. Brandmayr, A. Hienzsch, M. Müller, D. Pearson, V. Reiter, I. Thoma, P. Thumbs and M. Wagner, 'Structure and Function of Noncanonical Nucleobases', *Angewandte Chemie International Edition* **51**, 7110–7131 (2012).
- ¹⁵P. F. Swann, T. R. Waters, D. C. Moulton, Y.-Z. Xu, Q. Zheng, M. Edwards and R. Mace, 'Role of Postreplicative DNA Mismatch Repair in the Cytotoxic Action of Thioguanine', *Science* **273**, 1109–1111 (1996).
- ¹⁶E. B. Astwood, 'Treatment of hyperthyroidism with thiourea and thiouracil', *Journal of the American Medical Association* **122**, 78 (1943).
- ¹⁷E. B. Astwood and W. P. Vanderlaan, 'Thiouracil Derivatives of Greater Activity for the Treatment of Hyperthyroidism', *The Journal of Clinical Endocrinology & Metabolism* **5**, 424–430 (1945).
- ¹⁸A. Palumbo and M. D'Ischia, 'Thiouracil Antithyroid Drugs as a New Class of Neuronal Nitric Oxide Synthase Inhibitors', *Biochemical and Biophysical Research Communications* **282**, 793–797 (2001).
- ¹⁹L. A. Ortiz-Rodríguez, C. Reichardt, S. J. Hoehn, S. Jockusch and C. E. Crespo-Hernández, 'Detection of the thietane precursor in the UVA formation of the DNA 6-4 photoadduct', *Nature Communications* **11**, 3599 (2020).
- ²⁰R. Brem, I. Daehn and P. Karran, 'Efficient DNA interstrand crosslinking by 6-thioguanine and UVA radiation', *DNA Repair* **10**, 869–876 (2011).
- ²¹O. Ghafur, S. W. Crane, M. Ryszka, J. Bockova, A. Rebelo, L. Saalbach, S. De Camillis, J. B. Greenwood, S. Eden and D. Townsend, 'Ultraviolet relaxation dynamics in uracil: Time-resolved photoion yield studies using a laser-based thermal desorption source', *The Journal of Chemical Physics* **149**, 034301 (2018).
- ²²S. Mai, A. Mohamadzade, P. Marquetand, L. González and S. Ullrich, 'Simulated and experimental time-resolved photoelectron spectra of the intersystem crossing dynamics in 2-thiouracil', *Molecules* **23**, 2836 (2018).
- ²³J. A. Sánchez-Rodríguez, A. Mohamadzade, S. Mai, B. Ashwood, M. Pollum, P. Marquetand, L. González, C. E. Crespo-Hernández and S. Ullrich, '2-Thiouracil intersystem crossing photo-dynamics studied by wavelength-dependent photoelectron and transient absorption spectroscopies', *Physical Chemistry Chemical Physics* **19**, 19756–19766 (2017).
- ²⁴H. Yu, J. A. Sanchez-Rodriguez, M. Pollum, C. E. Crespo-Hernández, S. Mai, P. Marquetand, L. González and S. Ullrich, 'Internal conversion and intersystem crossing pathways in UV excited, isolated uracils and their implications in prebiotic chemistry', *Physical Chemistry Chemical Physics* **18**, 20168–20176 (2016).

- ²⁵M. Pollum and C. E. Crespo-Hernández, 'Communication: The dark singlet state as a doorway state in the ultrafast and efficient intersystem crossing dynamics in 2-thiothymine and 2-thiouracil', *The Journal of Chemical Physics* **140**, 071101 (2014).
- ²⁶S. Mai, P. Marquetand and L. González, 'A Static Picture of the Relaxation and Intersystem Crossing Mechanisms of Photoexcited 2-Thiouracil', *Journal of Physical Chemistry A* **119**, 9524–9533 (2015).
- ²⁷S. Mai, P. Marquetand and L. González, 'Intersystem Crossing Pathways in the Noncanonical Nucleobase 2-Thiouracil: A Time-Dependent Picture', *Journal of Physical Chemistry Letters* **7**, 1978–1983 (2016).
- ²⁸S. Mai, F. Plasser, M. Pabst, F. Neese, A. Köhn and L. González, 'Surface hopping dynamics including intersystem crossing using the algebraic diagrammatic construction method', *Journal of Chemical Physics* **147**, 184109 (2017).
- ²⁹J. P. Gobbo and A. C. Borin, '2-Thiouracil deactivation pathways and triplet states population', *Computational and Theoretical Chemistry* **1040-1041**, 195–201 (2014).
- ³⁰D. C. Teles-Ferreira, I. Conti, R. Borrego-Varillas, A. Nenov, I. H. M. Van Stokkum, L. Ganzer, C. Manzoni, A. M. Paula, G. Cerullo and M. Garavelli, 'A Unified Experimental/Theoretical Description of the Ultrafast Photophysics of Single and Double Thionated Uracils', *Chemistry - A European Journal* **26**, 336–343 (2020).
- ³¹D. Koyama, M. J. Milner and A. J. Orr-Ewing, 'Evidence for a Double Well in the First Triplet Excited State of 2-Thiouracil', *Journal of Physical Chemistry B* **121**, 9274–9280 (2017).
- ³²X. Zou, X. Dai, K. Liu, H. Zhao, D. Song and H. Su, 'Photophysical and Photochemical Properties of 4-Thiouracil: Time-Resolved IR Spectroscopy and DFT Studies', *The Journal of Physical Chemistry B* **118**, 5864–5872 (2014).
- ³³A. Mohamadzade, S. Bai, M. Barbatti and S. Ullrich, 'Intersystem crossing dynamics in singly substituted thiouracil studied by time-resolved photoelectron spectroscopy: Micro-environmental effects due to sulfur position', *Chemical Physics* **515**, 572–579 (2018).
- ³⁴R. Borrego-Varillas, D. C. Teles-Ferreira, A. Nenov, I. Conti, L. Ganzer, C. Manzoni, M. Garavelli, A. M. de Paula and G. Cerullo, 'Observation of the Sub-100 Femtosecond Population of a Dark State in a Thiobase Mediating Intersystem Crossing', *Journal of the American Chemical Society* **140**, 16087–16093 (2018).
- ³⁵A. Mohamadzade and S. Ullrich, 'Internal conversion and intersystem crossing dynamics of uracil upon double thionation: a time-resolved photoelectron spectroscopy study in the gas phase', *Physical Chemistry Chemical Physics* **22**, 15608–15615 (2020).
- ³⁶P. Chakraborty, Y. Liu, S. McClung, T. Weinacht and S. Matsika, 'Time Resolved Photoelectron Spectroscopy as a Test of Electronic Structure and Nonadiabatic Dynamics', *The Journal of Physical Chemistry Letters* **12**, 5099–5104 (2021).
- ³⁷K. Siegbahn, *ESCA applied to free molecules* (North-Holland Pub. Co, Amsterdam, London, 1969).
- ³⁸F. Brauße et al., 'Time-resolved inner-shell photoelectron spectroscopy: From a bound molecule to an isolated atom', *Physical Review A* **97**, 043429 (2018).

- ³⁹D. Mayer et al., ‘Following excited-state chemical shifts in molecular ultrafast x-ray photoelectron spectroscopy’, *Nature Communications* **13**, 198 (2022).
- ⁴⁰F. Lever et al., ‘Ultrafast dynamics of 2-thiouracil investigated by time-resolved Auger spectroscopy’, *Journal of Physics B: Atomic, Molecular and Optical Physics* **54**, 014002 (2020).
- ⁴¹S. M. Cavaletto, D. Keefer and S. Mukamel, ‘Electronic coherences in nonadiabatic molecular photophysics revealed by time-resolved photoelectron spectroscopy’, *Proceedings of the National Academy of Sciences* **119**, 1–8 (2022).
- ⁴²T. J. A. Wolf et al., ‘Probing ultrafast $\pi\pi^*/n\pi^*$ internal conversion in organic chromophores via K-edge resonant absorption’, *Nature Communications* **8**, 1–6 (2017).
- ⁴³T. J. A. Wolf et al., ‘Transient resonant Auger–Meitner spectra of photoexcited thymine’, *Faraday Discussions* **228**, 555–570 (2021).
- ⁴⁴F. Segatta, A. Nenov, S. Orlandi, A. Arcioni, S. Mukamel and M. Garavelli, ‘Exploring the capabilities of optical pump X-ray probe NEXAFS spectroscopy to track photo-induced dynamics mediated by conical intersections’, *Faraday Discussions* **221**, 245–264 (2019).
- ⁴⁵J. Metje, F. Lever, D. Mayer, R. J. Squibb, M. S. Robinson, M. Niebuhr, R. Feifel, S. Düsterer and M. Gühr, ‘URSA-PQ: A Mobile and Flexible Pump-Probe Instrument for Gas Phase Samples at the FLASH Free Electron Laser’, *Applied Sciences* **10**, 7882 (2020).
- ⁴⁶E. Schrödinger, ‘Quantisierung als Eigenwertproblem I’, *Annalen der Physik* **384**, 361–376 (1926).
- ⁴⁷E. Schrödinger, ‘Quantisierung als Eigenwertproblem II’, *Annalen der Physik* **384**, 489–527 (1926).
- ⁴⁸E. Schrödinger, ‘Über das Verhältnis der Heisenberg-Born-Jordanschen Quantenmechanik zu der meinem’, *Annalen der Physik* **384**, 734–756 (1926).
- ⁴⁹E. Schrödinger, ‘Quantisierung als Eigenwertproblem III’, *Annalen der Physik* **385**, 437–490 (1926).
- ⁵⁰E. Schrödinger, ‘Quantisierung als Eigenwertproblem IV’, *Annalen der Physik* **386**, 109–139 (1926).
- ⁵¹W. Demtröder, *Molekülphysik* (Oldenbourg Wissenschaftsverlag GmbH, München, 2013).
- ⁵²J. Franck and E. G. Dymond, ‘Elementary processes of the photochemical reactions’, *Transactions of the Faraday Society* **21**, 536–542 (1926).
- ⁵³E. U. Condon, ‘A theory of intensity distribution in band systems’, *Physical Review* **28**, 1182–1201 (1926).
- ⁵⁴E. U. Condon, ‘Nuclear motions associated with electron transitions in diatomic molecules’, *Physical Review* **32**, 858–872 (1928).
- ⁵⁵M. S. Schuurman and A. Stolow, ‘Dynamics at Conical Intersections’, *Annual Review of Physical Chemistry* **69**, 427–450 (2018).
- ⁵⁶G. J. Atchity, S. S. Xantheas and K. Ruedenberg, ‘Potential energy surfaces near intersections’, *The Journal of Chemical Physics* **95**, 1862–1876 (1991).
- ⁵⁷F. Hund, ‘Zur Deutung der Molekelspektren. I’, *Zeitschrift für Physik* **40**, 742–764 (1927).

- ⁵⁸J. von Neumann and E. P. Wigner, 'Über das Verhalten von Eigenwerten bei adiabatischen Prozessen', in *The Collected Works of Eugene Paul Wigner* (Springer, Berlin, Heidelberg, 1993), pp. 294–297.
- ⁵⁹H. C. Longuet-Higgins, 'The intersection of potential energy surfaces in polyatomic molecules', *Proceedings of the Royal Society of London. A. Mathematical and Physical Sciences* **344**, 147–156 (1975).
- ⁶⁰G. J. Hatton, W. L. Lichten and N. Ostrove, 'Non-non-crossings in molecular potential energy curves', *Chemical Physics Letters* **40**, 437–440 (1976).
- ⁶¹J. Stöhr, *NEXAFS spectroscopy*, 1st ed. (Springer, Berlin; New York, 1996).
- ⁶²H. G. Kümmel, 'A biography of the coupled cluster method', *International Journal of Modern Physics B* **17**, 5311–5325 (2003).
- ⁶³C. D. Sherrill and H. F. Schaefer, 'The configuration interaction method: advances in highly correlated approaches', in , Vol. 34, edited by P.-O. Löwdin, J. R. Sabin, M. C. Zerner and E. Brändas, *Advances in Quantum Chemistry* (Academic Press, London, Oxford, Boston, New York, San Diego, 1999), pp. 143–269.
- ⁶⁴F. Neese, 'The ORCA program system', *WIREs Computational Molecular Science* **2**, 73–78 (2012).
- ⁶⁵F. Neese, 'Software update: the ORCA program system, version 4.0', *WIREs Computational Molecular Science* **8**, 10.1002/wcms.1327 (2018).
- ⁶⁶F. Neese, F. Wennmohs, U. Becker and C. Riplinger, 'The ORCA quantum chemistry program package', *The Journal of Chemical Physics* **152**, 224108 (2020).
- ⁶⁷F. Weigend and R. Ahlrichs, 'Balanced basis sets of split valence, triple zeta valence and quadruple zeta valence quality for h to rn: design and assessment of accuracy', *Phys. Chem. Chem. Phys.* **7**, 3297 (2005).
- ⁶⁸M. Ruckebauer, S. Mai, P. Marquetand and L. González, 'Photoelectron spectra of 2-thiouracil, 4-thiouracil, and 2,4-dithiouracil', *The Journal of Chemical Physics* **144**, 074303 (2016).
- ⁶⁹D. Mayer, D. Picconi, M. S. Robinson and M. Gühr, 'Experimental and theoretical gas-phase absorption spectra of thionated uracils', *Chemical Physics* **558**, 111500 (2022).
- ⁷⁰M. Richter, S. Mai, P. Marquetand and L. González, 'Ultrafast intersystem crossing dynamics in uracil unravelled by ab initio molecular dynamics', *Phys. Chem. Chem. Phys.* **16**, 24423–24436 (2014).
- ⁷¹H. Rostkowska, A. Barski, K. Szczepaniak, M. Szczesniak and W. Person, 'The tautomeric equilibria of thioanalogues of nucleic acids: spectroscopic studies of 2-thiouracils in the vapour phase and in low temperature matrices', *Journal of Molecular Structure* **176**, 137–147 (1988).
- ⁷²A. Khvorostov, L. Lapinski, H. Rostkowska and M. J. Nowak, 'UV-induced generation of rare tautomers of 2-thiouracils: A matrix isolation study', *Journal of Physical Chemistry A* **109**, 7700–7707 (2005).
- ⁷³M. Barbatti, A. C. Borin and S. Ullrich, *Nucleobases in the gas phase and in solvents* (Springer International, Cham, 2015), p. 362.

Bibliography

- ⁷⁴B. M. Giuliano, V. Feyer, K. C. Prince, M. Coreno, L. Evangelisti, S. Melandri and W. Caminati, 'Tautomerism in 4-hydroxypyrimidine, S-methyl-2-thiouracil, and 2-thiouracil', *Journal of Physical Chemistry A* **114**, 12725–12730 (2010).
- ⁷⁵L. Aarons, M. Barber, M. Guest, I. Hillier and J. McCartney, 'Satellite peaks in the high energy photoelectron spectra of some small first row molecules', *Molecular Physics* **26**, 1247–1256 (1973).
- ⁷⁶M. A. Brisk and A. D. Baker, 'Shake-up satellites in X-ray photoelectron spectroscopy', *Journal of Electron Spectroscopy and Related Phenomena* **7**, 197–213 (1975).
- ⁷⁷R. L. Martin and D. A. Shirley, 'Theory of the neon 1 s correlation-peak intensities', *Physical Review A* **13**, 1475–1483 (1976).
- ⁷⁸R. L. Martin and D. A. Shirley, 'Theory of core-level photoemission correlation state spectra', *The Journal of Chemical Physics* **64**, 3685–3689 (1976).
- ⁷⁹S. Süzer, S. T. Lee and D. A. Shirley, 'Correlation satellites in the atomic photoelectron spectra of group-IIA and -IIB elements', *Physical Review A* **13**, 1842–1849 (1976).
- ⁸⁰R. L. Martin, S. P. Kowalczyk and D. A. Shirley, 'The relation between satellite peaks in x-ray emission and x-ray photoemission spectra', *The Journal of Chemical Physics* **68**, 3829–3836 (1977).
- ⁸¹M. H. Wood, 'On the calculation of the satellite peaks observed in the high energy photoelectron spectra of small molecules', *Chemical Physics* **5**, 471–477 (1974).
- ⁸²V. Feyer et al., 'Tautomerism in Cytosine and Uracil: An Experimental and Theoretical Core Level Spectroscopic Study', *The Journal of Physical Chemistry A* **113**, 5736–5742 (2009).
- ⁸³K. Siegbahn, 'A Discussion on photoelectron spectroscopy - Electron spectroscopy for chemical analysis (e.s.c.a.)', *Philosophical Transactions of the Royal Society of London. Series A, Mathematical and Physical Sciences* **268**, 33–57 (1970).
- ⁸⁴U. Gelius, 'Binding Energies and Chemical Shifts in ESCA', *Physica Scripta* **9**, 133–147 (1974).
- ⁸⁵D. Coster and R. D. L. Kronig, 'New type of auger effect and its influence on the x-ray spectrum', *Physica* **2**, 13–24 (1935).
- ⁸⁶E. H. S. Burhop, *The Auger effect and other radiationless transitions* (R. E. Krieger Pub. Co, Huntington, N.Y, 1980).
- ⁸⁷W. E. Moddeman, T. A. Carlson, M. O. Krause, B. P. Pullen, W. E. Bull and G. K. Schweitzer, 'Determination of the K–LL Auger Spectra of N_2 , O_2 , CO , NO , H_2O , and CO_2 ', *The Journal of Chemical Physics* **55**, 2317–2336 (1971).
- ⁸⁸P. Kruit and F. H. Read, 'Magnetic field paralleliser for 2π electron-spectrometer and electron-image magnifier', *Journal of Physics E: Scientific Instruments* **16**, 313–324 (1983).
- ⁸⁹J. H. D. Eland, O. Vieuxmaire, T. Kinugawa, P. Lablanquie, R. I. Hall and F. Penent, 'Complete Two-Electron Spectra in Double Photoionization: The Rare Gases Ar, Kr, and Xe', *Physical Review Letters* **90**, 053003 (2003).
- ⁹⁰M. Mucke, M. Förstel, T. Lischke, T. Arion, A. M. Bradshaw and U. Hergenhahn, 'Performance of a short "magnetic bottle" electron spectrometer', *Review of Scientific Instruments* **83**, 63106 (2012).

- ⁹¹D. Oepts, A. van der Meer and P. van Amersfoort, 'The Free-Electron-Laser user facility FELIX', *Infrared Physics & Technology* **36**, Proceedings of the Sixth International Conference on Infrared Physics, 297–308 (1995).
- ⁹²W. Schöllkopf et al., 'First lasing of the IR FEL at the Fritz-Haber-Institut, Berlin', in Proceedings of the 34th International Free-Electron Laser Conference, edited by T. Tanaka and V. R. W. Schaa (2012).
- ⁹³W. Ackermann et al., 'Operation of a free-electron laser from the extreme ultraviolet to the water window', *Nature Photonics* **1**, 336–342 (2007).
- ⁹⁴E. Allaria et al., 'Highly coherent and stable pulses from the FERMI seeded free-electron laser in the extreme ultraviolet', *Nature Photonics* **6**, 699–704 (2012).
- ⁹⁵P. Emma et al., 'First lasing and operation of an ångström-wavelength free-electron laser', *Nature Photonics* **4**, 641–647 (2010).
- ⁹⁶T. Ishikawa et al., 'A compact X-ray free-electron laser emitting in the sub-ångström region', *Nature Photonics* **6**, 540–544 (2012).
- ⁹⁷I. Nam et al., 'High-brightness self-seeded X-ray free-electron laser covering the 3.5 keV to 14.6 keV range', *Nature Photonics* **15**, 435–441 (2021).
- ⁹⁸J. R. Rouxel et al., 'Hard X-ray transient grating spectroscopy on bismuth germanate', *Nature Photonics* **15**, 499–503 (2021).
- ⁹⁹J. Yan et al., 'Self-Amplification of Coherent Energy Modulation in Seeded Free-Electron Lasers', *Physical Review Letters* **126**, 084801 (2021).
- ¹⁰⁰R. Spitzeneifel et al., 'Enhancing the brilliance of high-harmonic generation', *Applied Physics A* **96**, 69–81 (2009).
- ¹⁰¹G. Geloni, Z. Huang and C. Pellegrini, 'CHAPTER 1. The Physics and Status of X-ray Free-electron Lasers', in *X-ray free electron lasers: applications in materials, chemistry and biology*, edited by U. Bergmann, V. Yachandra and J. Yano (Royal Society of Chemistry, Cambridge, 2017) Chap. 1, pp. 1–44.
- ¹⁰²T. Popmintchev et al., 'Bright coherent ultrahigh harmonics in the keV x-ray regime from mid-infrared femtosecond lasers', *Science* **336**, 1287–1291 (2012).
- ¹⁰³P. Schmüser, M. Dohlus, J. Rossbach and C. Behrens, *Free-Electron Lasers in the Ultraviolet and X-Ray Regime*, 2nd ed. (Springer International, Cham, Heidelberg, New York, Dordrecht, London, 2014).
- ¹⁰⁴P. K. Maroju et al., 'Attosecond pulse shaping using a seeded free-electron laser', *Nature* **578**, 386–391 (2020).
- ¹⁰⁵J. Duris et al., 'Tunable isolated attosecond x-ray pulses with gigawatt peak power from a free-electron laser', *Nature Photonics* **14**, 30–36 (2020).
- ¹⁰⁶E. J. Jaeschke, S. Khan, J. R. Schneider and J. B. Hastings, *Synchrotron light sources and free-electron lasers: Accelerator physics, instrumentation and science applications*, edited by E. J. Jaeschke, S. Khan, J. R. Schneider and J. B. Hastings (Springer International Publishing, Cham, 2016), pp. 1–1840.

Bibliography

- ¹⁰⁷C. Pellegrini, A. Marinelli and S. Reiche, 'The physics of x-ray free-electron lasers', *Reviews of Modern Physics* **88**, 015006 (2016).
- ¹⁰⁸D. Mayer, F. Lever and M. Gühr, 'Data analysis procedures for time-resolved x-ray photoelectron spectroscopy at a SASE free-electron-laser', *Journal of Physics B: Atomic, Molecular and Optical Physics* **55**, 054002 (2022).
- ¹⁰⁹F. Lever et al., 'Core-Level Spectroscopy of 2-Thiouracil at the Sulfur L₁- and L_{2,3}-Edges Utilizing a SASE Free-Electron Laser', *Molecules* **26**, 6469 (2021).
- ¹¹⁰K. Tiedtke et al., 'Gas detectors for x-ray lasers', *Journal of Applied Physics* **103**, 094511 (2008).
- ¹¹¹M. Braune, G. Brenner, S. Dziarzhytski, P. Juranić, A. Sorokin and K. Tiedtke, 'A non-invasive online photoionization spectrometer for FLASH2', *Journal of Synchrotron Radiation* **23**, 10–20 (2016).
- ¹¹²F. Löhler et al., 'Electron Bunch Timing with Femtosecond Precision in a Superconducting Free-Electron Laser', *Physical Review Letters* **104**, 144801 (2010).
- ¹¹³S. Schulz et al., 'Femtosecond all-optical synchronization of an X-ray free-electron laser', *Nature Communications* **6**, 5938 (2015).
- ¹¹⁴E. Savelyev et al., 'Jitter-correction for IR/UV-XUV pump-probe experiments at the FLASH free-electron laser', *New Journal of Physics* **19**, 43009 (2017).
- ¹¹⁵S. Li et al., 'Two-dimensional correlation analysis for x-ray photoelectron spectroscopy', *Journal of Physics B: Atomic, Molecular and Optical Physics* **54**, 144005 (2021).
- ¹¹⁶S. Li, T. Driver, O. Alexander, B. Cooper, D. Garratt, A. Marinelli, J. P. Cryan and J. P. Marangos, 'Time-resolved pump-probe spectroscopy with spectral domain ghost imaging', *Faraday Discussions* **228**, 488–501 (2021).
- ¹¹⁷T. Driver et al., 'Attosecond transient absorption spooktscopy: a ghost imaging approach to ultrafast absorption spectroscopy', *Physical Chemistry Chemical Physics* **22**, 2704–2712 (2020).
- ¹¹⁸B. K. McFarland et al., 'Experimental strategies for optical pump – soft x-ray probe experiments at the LCLS', *Journal of Physics: Conference Series* **488**, 012015 (2014).
- ¹¹⁹J. S. Beckwith, C. A. Rumble and E. Vauthey, 'Data analysis in transient electronic spectroscopy – an experimentalist's view', *International Reviews in Physical Chemistry* **39**, 135–216 (2020).
- ¹²⁰S. Dziarzhytski et al., 'The TRIXS end-station for femtosecond time-resolved resonant inelastic x-ray scattering experiments at the soft x-ray free-electron laser FLASH', *Structural Dynamics* **7**, 054301 (2020).
- ¹²¹S. Kumar Giri, U. Saalman and J. M. Rost, 'Purifying Electron Spectra from Noisy Pulses with Machine Learning Using Synthetic Hamilton Matrices', *Physical Review Letters* **124**, 113201 (2020).
- ¹²²A. Sanchez-Gonzalez et al., 'Accurate prediction of X-ray pulse properties from a free-electron laser using machine learning', *Nature Communications* **8**, 1–9 (2017).

Appendix

A Supplementary Information to Article 1

The following pages include the supplementary information from Article 1:

Experimental and theoretical gas-phase absorption spectra of thionated uracils, Dennis Mayer, David Picconi, Matthew S. Robinson, Markus Gühr, *Chemical Physics* **558**, 111500 (2020), DOI: 10.1016/j.chemphys.2022.111500

Copyright note. © 2022 Elsevier B.V. All rights reserved. The right for the reuse of the article in this dissertation is retained by the author.

Supplementary Information: Experimental and theoretical gas -phase absorption spectra of thionated uracils

Dennis Mayer,[1] David Picconi,[1,2] Matthew S. Robinson,[1,3,4]* Markus Gühr.[1]

- 1) Institut für Physik und Astronomie, Universität Potsdam, 14476 Potsdam, Germany
 - 2) Institut für Chemie, Universität Potsdam, 14476 Potsdam Germany
 - 3) Center for Free-Electron Laser Science (CFEL), Deutsches Elektronen Synchrotron (DESY), Notkestraße 85, 22607 Hamburg, Germany
 - 4) The Hamburg Centre for Ultrafast Imaging, Universität Hamburg, 22761 Hamburg, Germany
- *Corresponding Author

1 Fitting of the thiouracil spectra

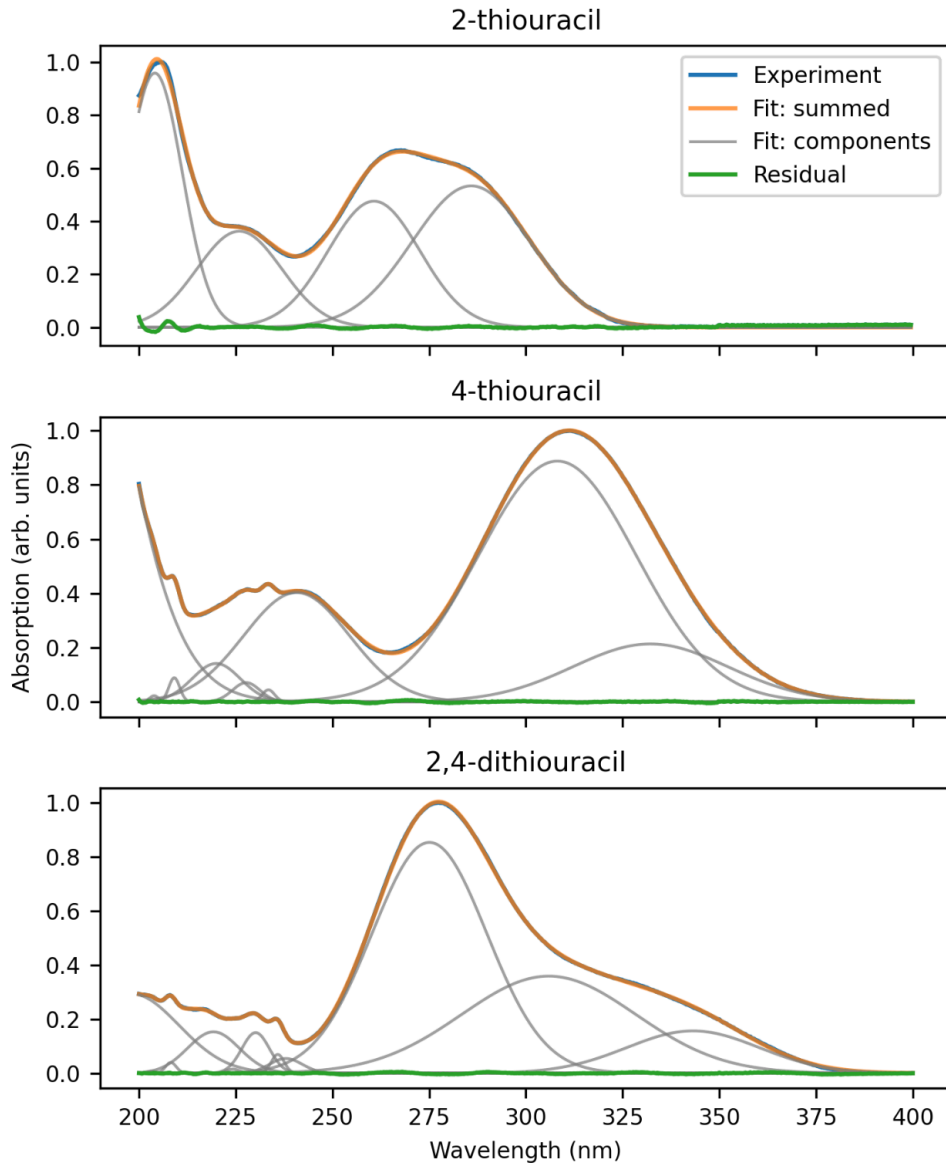


Figure S1: Gaussian fits of the thiouracil spectra. Contributing components are shown in grey. The sum of the components (orange) matches well with the measured spectrum (blue) as can be seen by the flat residual (green).

Table S1: Fitted Gaussian parameters for 2-thiouracil.

amplitude	centre (nm)	width (nm)
0.9588 +/- 0.0041	204.091 +/- 0.029	7.134 +/- 0.045
0.3623 +/- 0.0013	225.93 +/- 0.12	11.00 +/- 0.19
0.4756 +/- 0.0088	260.74 +/- 0.16	11.86 +/- 0.15
0.5332 +/- 0.0055	285.89 +/- 0.29	15.27 +/- 0.13

Table S2: Fitted Gaussian parameters for 4-thiouracil.

amplitude	centre (nm)	width (nm)
4 +/- 10	170 +/- 52	17 +/- 14
0.039 +/- 0.017	203.99 +/- 0.17	1.5245 +/- 0.3732
0.0966 +/- 0.0093	209.034 +/- 0.051	1.472 +/- 0.083
0.225 +/- 0.051	221.2 +/- 1.7	8.65 +/- 0.99
0.0397 +/- 0.0081	227.66 +/- 0.23	3.03 +/- 0.45
0.0417 +/- 0.0036	233.43 +/- 0.12	1.56 +/- 0.13
0.3863 +/- 0.0054	242.26 +/- 0.34	12.22 +/- 0.16
1.0000 +/- 0.0005	311.667 +/- 0.019	22.191 +/- 0.025
0.0315 +/- 0.0010	353.32 +/- 0.31	10.00 +/- 0.33

Table S3: Fitted Gaussian parameters for 2,4-dithiouracil.

amplitude	centre (nm)	width (nm)
0.293 +/- 0.022	198.0 +/- 4.7	12 +/- 13
0.0074 +/- 0.0074	203.11 +/- 0.39	1.16 +/- 0.76
0.0398 +/- 0.0049	208.2310 +/- 0.099	1.38 +/- 0.13
0.15 +/- 0.17	219.2 +/- 1.6	6.7 +/- 2.8
0.0153 +/- 0.0076	224.31 +/- 0.29	1.69 +/- 0.41
0.150 +/- 0.025	230.14 +/- 0.31	3.58 +/- 0.33
0.0696 +/- 0.0085	235.861 +/- 0.062	1.653 +/- 0.092
0.055 +/- 0.014	238.0 +/- 1.5	4.25 +/- 0.68
0.853 +/- 0.055	275.07 +/- 0.16	14.82 +/- 0.19
0.359 +/- 0.022	305.9 +/- 1.1	22.5 +/- 3.3
0.156 +/- 0.035	343.2 +/- 1.6	17.11 +/- 0.48

2 Natural transition orbitals

Table S4. Natural transition orbitals for uracil.

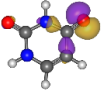
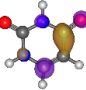
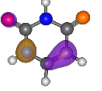

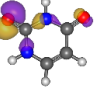
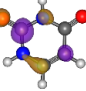
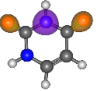

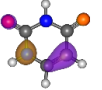

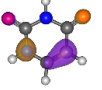
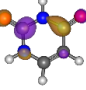
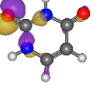

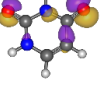
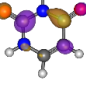
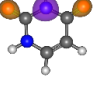
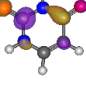
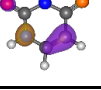

State	Occupied NTO	Virtual NTO
$S_1 (n\pi^*)$		
$S_2 (\pi\pi^*)$		
$S_3 (n\pi^*)$		
$S_4 (\pi\pi^*)$		
$S_5 (\pi\sigma^*)$		
$S_6 (\pi\pi^*)$		
$S_7 (n\pi^*)$		
$S_8 (n\pi^*)$		
$S_9 (\pi\pi^*)$		
$S_{10} (\pi\sigma^*)$		

Table S5. Natural transition orbitals for 2-thiouracil.

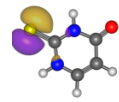
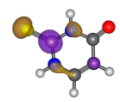
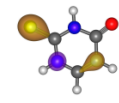
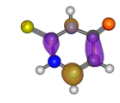
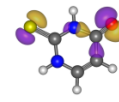
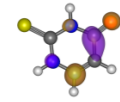
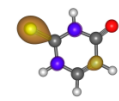
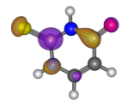

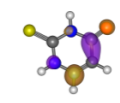
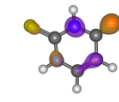
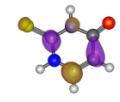
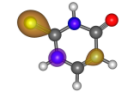
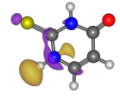
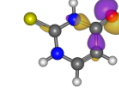
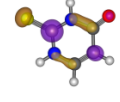
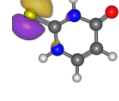
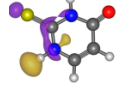
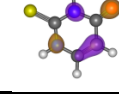
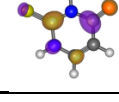
State	Occupied NTO	Virtual NTO
$S_1 (n\pi^*)$		
$S_2 (\pi\pi^*)$		
$S_3 (n\pi^*)$		
$S_4 (\pi\pi^*)$		
$S_5 (n\pi^*)$		
$S_6 (\pi\pi^*)$		
$S_7 (\pi\sigma^*)$		
$S_8 (n\pi^*)$		
$S_9 (n\sigma^*)$		
$S_{10} (\pi\pi^*)$		

Table S6. Natural transition orbitals for 4-thiouracil.

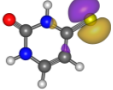
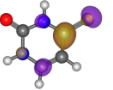
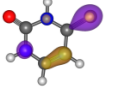
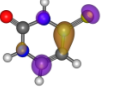
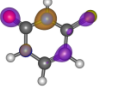
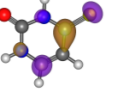
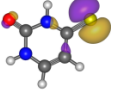
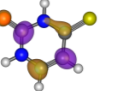
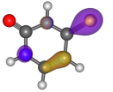
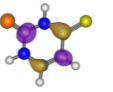
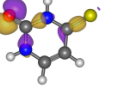
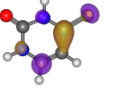
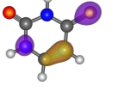
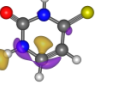
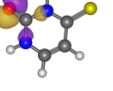
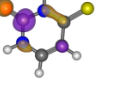
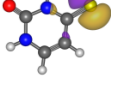
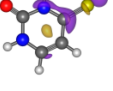
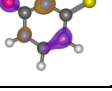
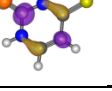
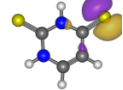
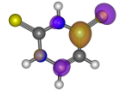
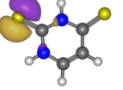
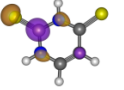
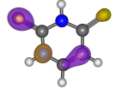
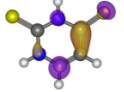

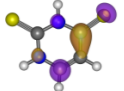
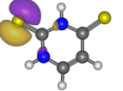
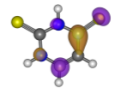
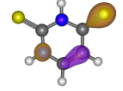
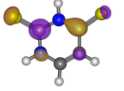
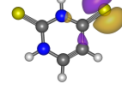
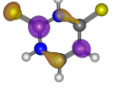

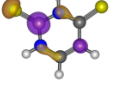
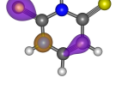
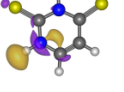
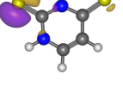
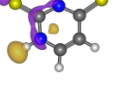
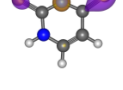
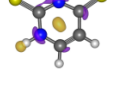
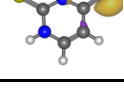
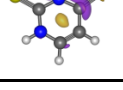
State	Occupied NTO	Virtual NTO
$S_1 (n\pi^*)$		
$S_2 (\pi\pi^*)$		
$S_3 (\pi\pi^*)$		
$S_4 (n\pi^*)$		
$S_5 (\pi\pi^*)$		
$S_6 (n\pi^*)$		
$S_7 (\pi\sigma^*)$		
$S_8 (n\pi^*)$		
$S_9 (n\sigma^*)$		
$S_{10} (\pi\pi^*)$		

Table S7. Natural transition orbitals for 2,4-dithiouracil.

State	Occupied NTO	Virtual NTO
$S_1 (n\pi^*)$		
$S_2 (n\pi^*)$		
$S_3 (\pi\pi^*)$		
$S_4 (\pi\pi^*)$		
$S_5 (n\pi^*)$		
$S_6 (\pi\pi^*)$		
$S_7 (n\pi^*)$		
$S_8 (\pi\pi^*)$		
$S_9 (\pi\sigma^*)$		
$S_{10} (n\sigma^*)$		
$S_{11} (\pi\sigma^*)$		
$S_{12} (n\sigma^*)$		

3 Calculated spectra in the Franck-Condon approximation

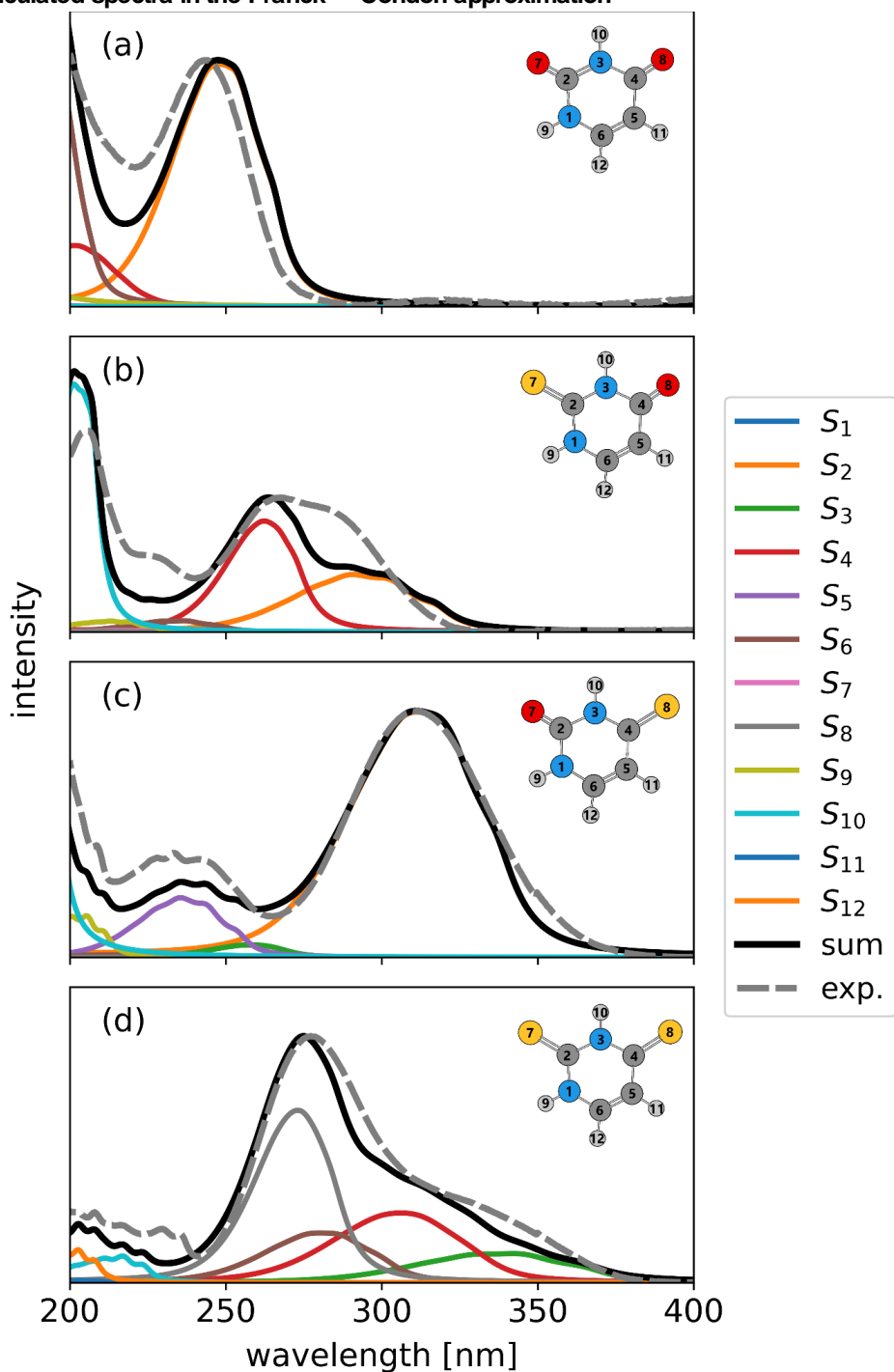


Figure S2. Comparison between the theoretical Franck-Condon (black line) and the experimental (gray dashed line) absorption spectrum of (a) Uracil; (b) 2-thiouracil; (c) 4-thiouracil; (d) 2,4-dithiouracil. For each molecule the contributions of the individual electronic states are shown separately with different colors. The theoretical spectra are computed at the TD-CAM-B3LYP/Def2-TZVP level with the Franck-Condon approximation.

Figure S2 shows the theoretical spectra computed without including the Herzberg-Teller (HT) contribution, i.e. using the Franck-Condon (FC) approximation. Comparison with Figure 3 of the main paper shows that HT terms have little relevance for Ura and 2,4-dtUra. For 2-tUra, the FC approximation fails to reproduce the minor band around 230 nm, which is due to intensity borrowing of the states S_6 ($\pi\pi^*$) and S_9 ($n\sigma^*$). For 4-tUra, the HT contribution corrects the too low intensity for wavelengths < 260 nm.

4 Cartesian coordinates of the ground state structures [Angstrom], optimized at the CAM-B3LYP/Def2-TZVP level

Uracil

O	-2.278390	0.944443	0.000000
O	2.260594	1.075575	-0.000000
N	-0.000000	0.984757	-0.000000
N	-1.133894	-1.018512	0.000000
C	-1.223620	0.360432	0.000000
C	1.266681	0.390081	-0.000000
C	0.054469	-1.695320	0.000000
C	1.231445	-1.062709	-0.000000
H	-0.021364	1.994596	-0.000000
H	-2.014603	-1.504939	0.000000
H	-0.026050	-2.773260	0.000000
H	2.167794	-1.595161	-0.000000

2-Thiouracil

S	-0.453077	2.450209	0.000000
O	-1.472490	-2.354521	0.000000
N	-0.873437	-0.172939	0.000000
N	1.310808	0.482668	0.000000
C	-0.000000	0.868403	0.000000
C	-0.578225	-1.545085	0.000000
C	1.717442	-0.822450	0.000000
C	0.843699	-1.834034	0.000000
H	-1.855126	0.066101	0.000000
H	1.979769	1.234950	0.000000
H	2.787768	-0.972824	0.000000
H	1.157651	-2.864507	0.000000

4-Thiouracil

O	-2.091986	1.766836	0.000000
S	2.514925	0.102217	-0.000000
N	0.000000	0.868101	-0.000000
N	-1.858338	-0.494827	0.000000
C	-1.376321	0.797543	0.000000
C	0.899613	-0.176147	-0.000000
C	-1.045148	-1.593499	0.000000
C	0.289243	-1.479574	-0.000000

H	0.382858	1.803316	-0.000000
H	-2.861103	-0.580545	0.000000
H	-1.548699	-2.549715	0.000000
H	0.928073	-2.346068	-0.000000

2,4-Dithiouracil

S	2.648906	0.810211	0.000000
S	-2.601781	1.024763	0.000000
N	0.000000	0.657935	0.000000
N	1.108270	-1.338762	0.000000
C	1.206454	0.022944	0.000000
C	-1.258878	0.087743	0.000000
C	-0.083723	-2.006240	0.000000
C	-1.251273	-1.349578	0.000000
H	0.036563	1.668023	0.000000
H	1.984519	-1.834773	0.000000
H	-0.015620	-3.084554	0.000000
H	-2.192815	-1.871703	0.000000

B Supplementary Information to Article 5

The following pages include the supplementary information from Article 5:

Following excited-state chemical shifts in molecular ultrafast x-ray photoelectron spectroscopy, Dennis Mayer, Fabiano Lever, David Picconi, Jan Metje, Skirmantas Alisauskas, Francesca Calegari, Stefan Düsterer, Christopher Ehlert, Raimund Feifel, Mario Niebuhr, Bastian Manschwetus, Marion Kuhlmann, Tommaso Mazza, Matthew S. Robinson, Richard J. Squibb, Andrea Trabattoni, Mans Wallner, Peter Saalfrank, Thomas J. A. Wolf and Markus Gühr, *Nature Communications* **13**, 198 (2022), DOI: 10.1038/s41467-021-27908-y

Copyright note. © The Author(s) 2022. This article is an open access article distributed under the terms and conditions of the Creative Commons Attribution (CC BY) license (<https://creativecommons.org/licenses/by/4.0/>).

Supplementary information

Following excited π -state chemical shifts in molecular ultrafast x-ray photoelectron spectroscopy

D. Mayer¹⁺, F. Lever¹⁺, D. Picconi^{2,*}, J. Metje¹, S. Alisauskas³, F. Calegari^{4,5,6}, S. Düsterer³, C. Ehlert⁷, R. Feifel⁸, M. Niebuhr¹, B. Manschwetus³, M. Kuhlmann³, T. Mazza⁹, M. S. Robinson^{1,4,5}, R. J. Squibb⁸, A. Trabattoni⁴, M. Wallner⁸, P. Saalfrank², T. J. A. Wolf¹⁰ and M. Gühr^{1,*}

1 Institut für Physik und Astronomie, Universität Potsdam, 14476 Potsdam, Germany

2 Institut für Chemie, Universität Potsdam, 14476 Potsdam, Germany

3 Deutsches Elektronen Synchrotron (DESY), 22607 Hamburg, Germany

4 Center for Free Electron Laser Science (CFEL), Deutsches Elektronen Synchrotron (DESY), 22607 Hamburg, Germany

5 The Hamburg Centre for Ultrafast Imaging, Universität Hamburg, 22761 Hamburg, Germany

6 Institut für Experimentalphysik, Universität Hamburg, 22761 Hamburg, Germany

7 Heidelberg Institute for Theoretical Studies, HITS gGmbH, 69126 Heidelberg, Germany

8 Department of Physics, University of Gothenburg, 41346 Gothenburg, Sweden

9 European XFEL, 22869 Schenefeld, Germany

10 Stanford PULSE Institute, SLAC National Accelerator Laboratory, 94025 Menlo Park, United States of America

+ Contributed equally

* correspondence should be addressed david.picconi@unipotsdam.de and mguehr@unipotsdam.de

Contents

Supplementary Discussion 1: Fits of the delay π-dependent signals	2
Supplementary Discussion 2: Magnetic bottle sensitivity	4
Supplementary Discussion 3: Spectral oscillations	6
Supplementary Discussion 4: Quantum chemical results	7
Supplementary Discussion 5: Calculated state π- and geometry π-dependent pump π-probe XPS spectra	13
Supplementary Discussion 6: Potential model fits	15
Supplementary Discussion 7: Exceptions in the clustering according to electronic state	17
Supplementary Discussion 8: Pulse energy scans	18
Supplementary Discussion 9: Data handling	19
Supplementary References	20

Supplementary Discussion 1: Fits of the delay -dependent signals

The integral of the difference signal and the amplitudes from the double Gaussian fit show similar delay-dependent behaviour and have thus been fitted with the same function:

$$S(t) = \sum_{i=1}^2 A_i \cdot \exp\{-\tau_i^{-1} \cdot (t - t_0)\} \exp\{0.5 \cdot \tau_i^{-2} \cdot \sigma^2\} \cdot \left[1 + \operatorname{erf}\left(\frac{t - t_0 - \tau_i^{-1} \cdot \sigma^2}{\sqrt{2}\sigma}\right) \right] \quad (1)$$

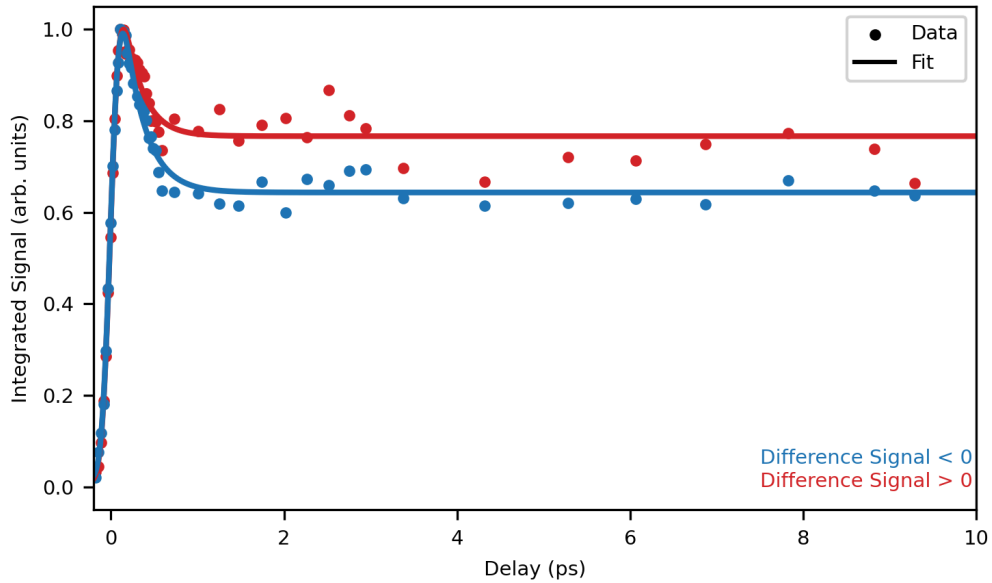
The equation represents a Gaussian time-uncertainty function convoluted with two exponential decays. Here, A_i and τ_i are the amplitude and decay constant of the i -th component. t_0 is the time-zero i.e., the overlap between pump and probe pulse, and σ describes the temporal resolution (with σ^2 being the variance of the Gaussian function). The erf is the Gauss error function. The fitting range was restricted to -0.2 to +10 ps.

First, the integral of the absolute difference signal ($S_{\text{int}}^{\text{abs}}$) was fitted. The fitted t_0 value was used to correct the delays. Then, the integral of the positive (S_{int}^+) and negative (S_{int}^-) contributions to the difference spectra were fitted with a fixed time uncertainty using the value from $S_{\text{int}}^{\text{abs}}$. The results of all five fits are summarised in Supplementary Table 1.

The full width at half maximum of the Gaussian time-uncertainty function is 190 ± 10 fs. This value includes the pulse duration of the UV pump and the x-ray probe pulse as well as temporal jitter^{1,2}. The time constant of the first decay component τ_1 lies between 200 and 300 fs for all fits with an average value of 235 ± 10 fs. For the second decay constant τ_2 , only two fits give values within the picosecond range (~ 200 ps). The other values are within nano- or even microsecond range with similarly large fitting errors (noted with >1000 in table S1). Increasing the delay range for the fit does not improve the values for τ_2 . The values for τ_1 stay similar. A normalized plot in Supplementary Figure 1, allowing for a better comparison of the positive and negative signal decay, confirms that the observed decays on the positive and negative lobe are equal.

	$S_{\text{int}}^{\text{abs}}$	S_{int}^-	S_{int}^+
σ / fs	81 ± 5	-	-
t_0 / fs	-56 ± 4	$2.0 \pm 4.0^*$	$-6 \pm 6^*$
A_1	43 ± 4	31 ± 2	12 ± 2
τ_1 / fs	225 ± 30	250 ± 20	220 ± 40
A_2	46.5 ± 2	28.2 ± 0.8	17.5 ± 0.6
τ_2 / ps	200 ± 140	>1000	>1000
offset	1.8 ± 1.0	1.0 ± 0.6	0.70 ± 0.6

Supplementary Table 1 . Fitted parameters of delay dependent amplitudes and integrals. “-” indicates that the value from $S_{\text{int}}^{\text{abs}}$ has been used. t_0 values with an asterisk (*) are evaluated after correcting the delays with t_0 value from $S_{\text{int}}^{\text{abs}}$.



Supplementary Figure 1. Integrated (absolute) signal for positive (red) and negative lobe (blue) of the S 2p difference spectrum normalized on the maximum.

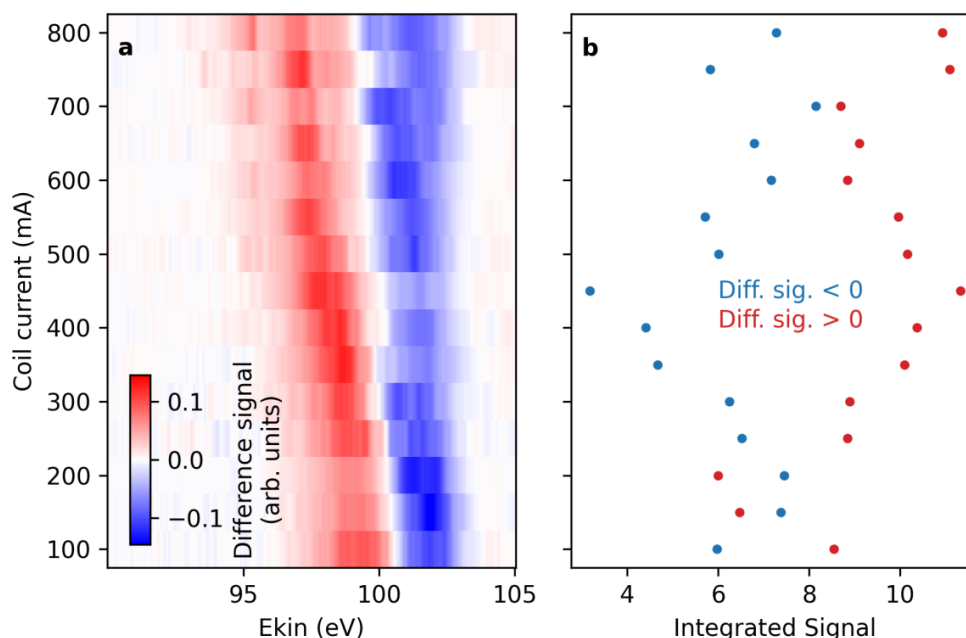
Supplementary Discussion 2: Magnetic bottle sensitivity

The data shown in the following plots (Suppl. Fig. 2 to 4) were recorded on a follow up beamtime to investigate the influence of different experimental parameters on the photoelectron spectra.

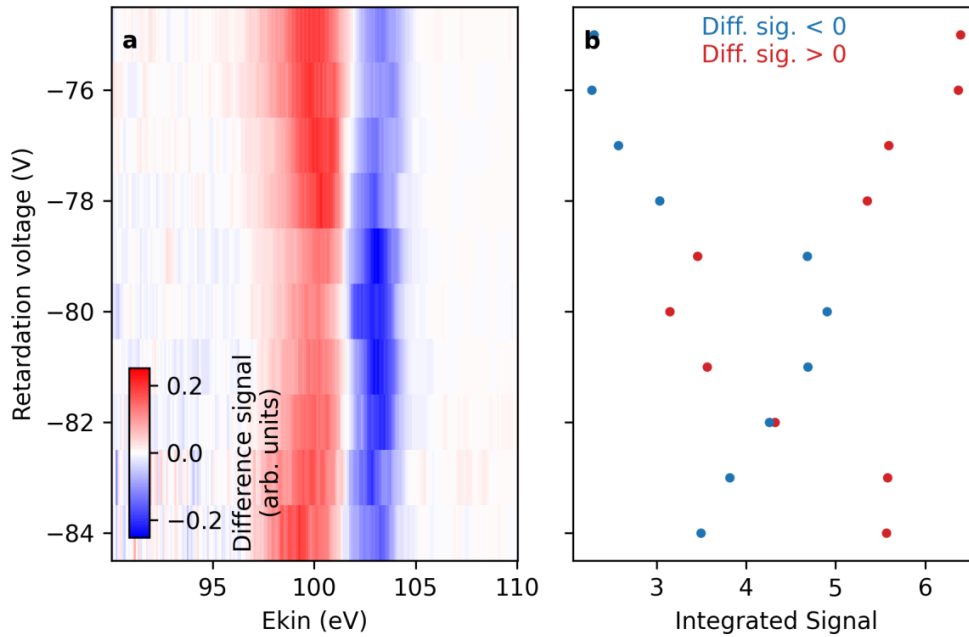
In Suppl. Fig. 2, the solenoid (coil) current and thus the magnetic field inside the flight tube was changed. The electron spectra were recorded with a photon energy of 272 eV at a delay of 200 ps and a retardation voltage of -80 V. Panel a) shows the normalised difference spectra of the sulphur $2p$ photoline. The positive (red) and negative (blue) contributions broaden with increasing magnetic field and also shift towards lower kinetic energy. Additionally, panel b) shows the integrals of the positive and negative contributions of the spectra. The two lobes change signal strength in a counter-oscillatory way. Especially the negative lobe is stronger than the positive one at 200 mA which was the value also used for the data presented in this paper.

In Suppl. Fig. 3, the coil current was kept constant at 200 mA and instead the retardation voltage was scanned across -80 V, while the kinetic energy is corrected for the change in retardation potential. Again, panel a) shows the difference spectra and b) the integrals of the positive and negative contributions. The counter-oscillation of the two lobe integrals is again observed. This is also the case for a photon energy scan around 272 eV shown in Suppl. Fig. 4 where the coil current and retardation voltage are kept constant at values of 200 mA and -80 V, respectively.

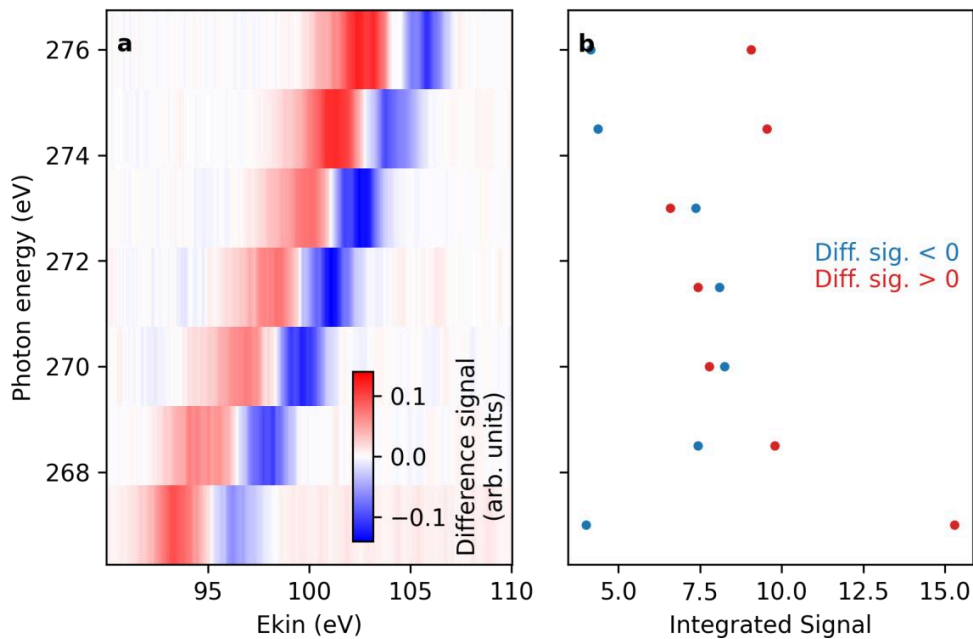
Our systematic investigations of the difference spectra for various experimental settings exhibit the influence of cyclotron resonances on the relative amplitudes in the MBES, an aspect which is well known for this kind of electron spectrometer¹. In future runs, the characterisation might be used to calibrate the MBES sensitivity.



Supplementary Figure 2. Scan of the coil current on the flight tube at 272 eV x-ray photon energy and -80 V retardation. a: false-color representation of the difference spectra of the photoline. b: integrated signal of positive (red) and negative (blue) contributions.



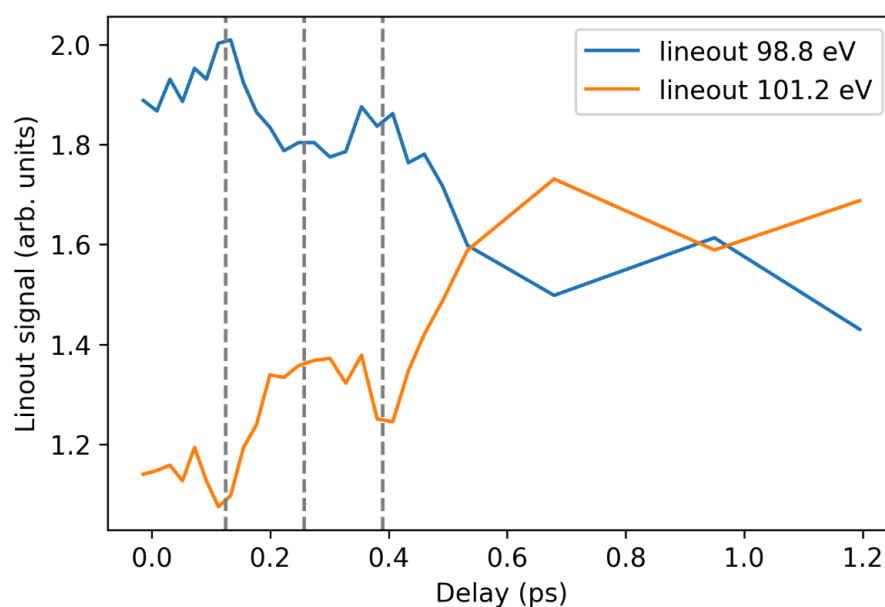
Supplementary Figure 3. Scan of the retardation voltage at 272 eV and 200 mA coil current. a: false-color representation of the difference spectra of the photoline. b: integrated signal of positive (red) and negative (blue) contributions.



Supplementary Figure 4. Scan of the photon energy at 80V retardation and 200mA coil current. a: false-color representation of the difference spectra of the photoline. b: integrated signal of positive (red) and negative (blue) contributions.

Supplementary Discussion 3: Spectral oscillations

To reduce the complexity of the data shown in Fig. 3, we show lineouts at the positive lobe's low and high kinetic energy edges at 98.8 eV (blue) and 101.2 eV (orange) in Suppl. Fig. 5. In the delay region described above, both lineouts show an oscillation. They occur with opposite phase as expected for spectral shifts. At 150 and 400 fs, the underlying photoelectron signal shifts to lower kinetic energies, increasing the lineout at 98.8 eV while decreasing the lineout at 101.2 eV. In between these times, the photoelectron signal shifts to higher kinetic energies, reducing the lineout at 98.8 eV and increasing the 101.2 eV lineout. At higher delays, the step size is too coarse to resolve such oscillation.



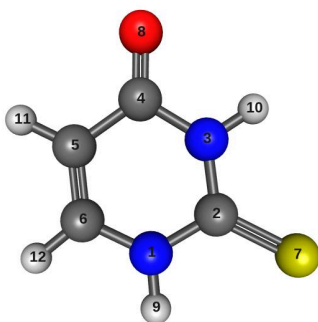
Supplementary Figure 5 . Lineouts for the delay-dependent difference signal at 98.8 eV (blue line) and 101.2 eV (orange line). The two curves show out-of-phase oscillation within the first 600fs. The grey dashed vertical lines mark the same positions as the dashed lines in Fig. 3.

Supplementary Discussion 4: Quantum chemical results

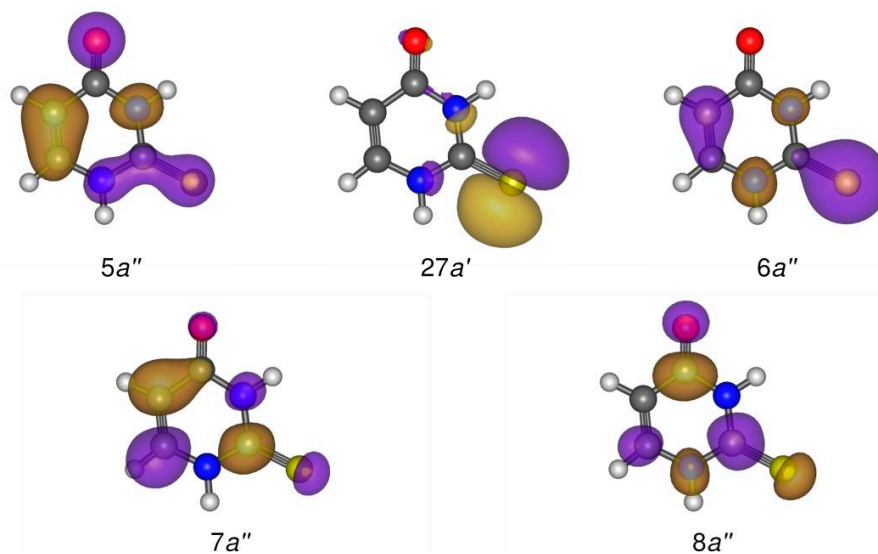
The structure and the atom numbering of 2-thiouracil is shown in Suppl. Fig. 6. The most relevant molecular orbitals involved in the valence excitations are depicted in Suppl. Fig. 7 for the Franck-Condon geometry. The singlet states S_1 and S_2 have $n\pi^*$ and $\pi\pi^*$ character, respectively. At planar geometries, they originate from $27a' \rightarrow 7a''$ and $6a'' \rightarrow 7a''$ transitions. The triplet states T_1 and T_2 originate mainly from the same transitions of S_2 and S_1 , apart from the spin-flipping, and therefore they have $\pi\pi^*$ and $n\pi^*$ character, respectively. T_3 has a $\pi\pi^*$ character and is mostly contributed by the transitions $5a'' \rightarrow 7a''$ and, to a lesser extent, $6a'' \rightarrow 8a''$.

Table S2 reports the main structural parameters of the optimized geometries. The planar equilibrium structures are indicated by an asterisk ($S_{0,\min}^*$, $S_{1,\min}^*$, etc.); the non-planar geometry optimization of the states T_2 and T_3 did not converge to a stationary point. At all minima, except for $T_{1,\min}^*$, the C–S bond is elongated by $\approx 0.1 \text{ \AA}$ as compared to $S_{0,\min}$. A larger elongation of about 0.25 \AA is found in the state S_2 . In the ground state the difference between the planar and non-planar minima $S_{0,\min}^*$ and $S_{0,\min}$ is negligible. In contrast, the states S_1 , S_2 and T_1 have non-planar minima which are depicted in Suppl. Fig. 8 and involve an out-of-plane distortion of the C–S bond, with pyramidalization angles in the range $\approx 35^\circ$ – 50° . The stabilization energy, associated with this out-of-plane distortion, is 0.30 eV, 0.48 eV and 0.17 eV for S_1 , S_2 and T_1 , respectively.

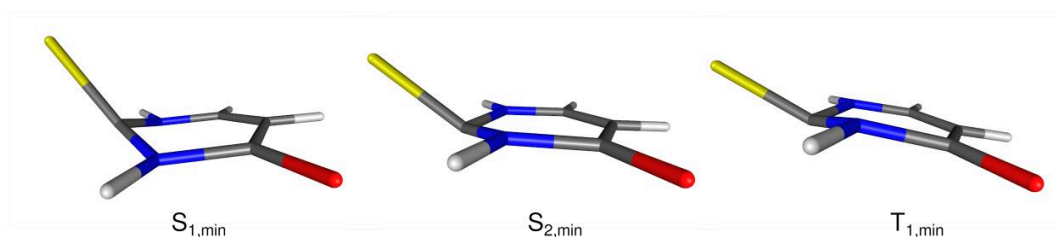
The comparison between Supplementary Table 2 and Table 2 of Ref. ² shows that the present optimized gas phase geometries agree very well with those obtained using the multi-state CASPT2 method. The main notable difference is a somewhat higher value of the pyramidalization angle p_{10324} , around the N atom bridging the C=S and C=O groups. Supplementary Table 3 reports instead the non-planar and nearly planar minima obtained in Ref. ³ for 2-thiouracil in the presence of water solvent charges, which also agree nicely with the structures found in this work. This suggests that the same sets of geometries can be in principle visited by the wave packet both in the gas phase and in solution.



Supplementary Figure 6. Structure and atom numbering of 2-thiouracil. The carbons are gray, the nitrogens are blue, the hydrogens are white, the oxygen is red and the sulphur is yellow.



Supplementary Figure 7. Most relevant orbitals involved in the valence excitations of 2-thiouracil, evaluated at the $S_{0,\min}^*$ geometry.



Supplementary Figure 8. Optimized structures of the non-planar minima of the excited states of 2-thiouracil.

	planar geometries					
	$S_{0,\min}^*$	$S_{1,\min}^*$	$S_{2,\min}^*$	$T_{1,\min}^*$	$T_{2,\min}^*$	$T_{3,\min}^*$
energy [eV]	0.00	3.78	4.44	3.17	3.65	3.76
r_{12}	1.37	1.39	1.32	1.36	1.40	1.41
r_{23}	1.37	1.40	1.35	1.39	1.41	1.37
r_{34}	1.41	1.40	1.47	1.41	1.39	1.41
r_{45}	1.47	1.47	1.42	1.44	1.47	1.44
r_{56}	1.35	1.36	1.41	1.47	1.36	1.41
r_{61}	1.38	1.37	1.39	1.36	1.37	1.39
r_{27}	1.65	1.74	1.76	1.67	1.73	1.70
r_{48}	1.21	1.22	1.22	1.22	1.22	1.23
α_{127}	122.8	122.1	120.5	121.7	122.2	121.3
α_{348}	120.4	120.3	116.0	120.2	120.3	119.7

	non-planar geometries			
	$S_{0,\min}$	$S_{1,\min}$	$S_{2,\min}$	$T_{1,\min}$
energy [eV]	0.00	3.48	3.96	3.00
r_{12}	1.37	1.40	1.37	1.40
r_{23}	1.37	1.40	1.38	1.41
r_{34}	1.41	1.40	1.41	1.40
r_{45}	1.47	1.47	1.47	1.47
r_{56}	1.35	1.35	1.35	1.36
r_{61}	1.38	1.38	1.38	1.37
r_{27}	1.65	1.77	1.90	1.77
r_{48}	1.21	1.21	1.21	1.21
α_{127}	122.8	116.8	110.6	113.6
α_{348}	120.4	121.0	120.9	121.2
ρ_{7213}	-1.5	34.0	48.8	42.5
ρ_{8435}	-0.6	-3.2	0.8	2.1
ρ_{10324}	8.0	19.8	-10.8	-22.1
ρ_{12651}	1.5	-2.5	0.5	0.7

Supplementary Table 2. Geometrical parameters of the planar and non-planar equilibrium structures of the lowest electronic states of 2-thiouracil, optimized at the (EOM-)CCSD/6-311++G** level. The largest structural changes with respect to $S_{0,\min}$ are highlighted in boldface. The bond distances r_{ij} are given in Å, the valence angles α_{ijk} and the pyramidalization angles ρ_{ijkl} are in degrees. ρ_{ijkl} is defined as the angle between the vector of the $i-j$ bond and the kl plane. The dimension for the bond lengths is Å, for angles it is degrees.

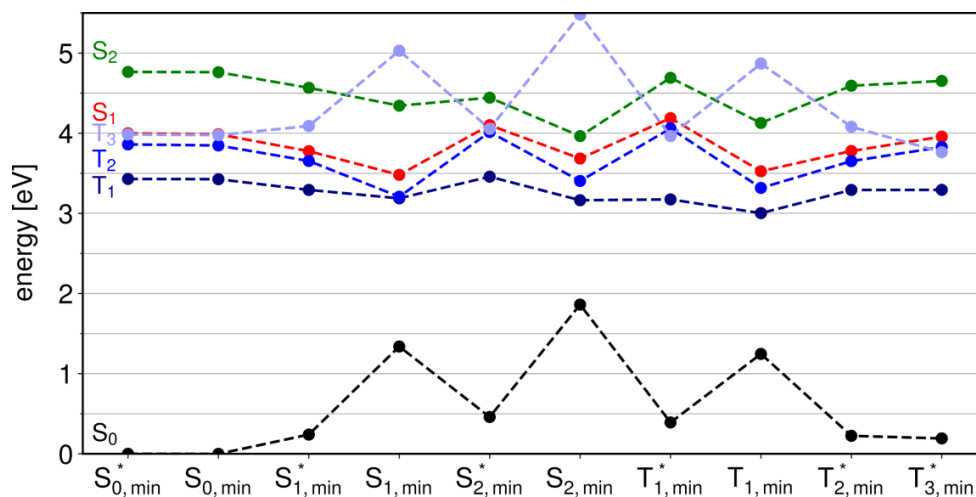
	(nearly) planar geometries				
	$S_{0,\min}^*$	${}^1n\pi^*_{\min}$	${}^1\pi\pi^*_{\min}$	${}^3\pi\pi^*_{\min}$	${}^3n\pi^*_{\min}$
r_{12}	1.36	1.34	1.33	1.35	1.32
r_{23}	1.37	1.37	1.34	1.39	1.35
r_{34}	1.38	1.44	1.46	1.41	1.45
r_{45}	1.43	1.40	1.39	1.41	1.39
r_{56}	1.36	1.41	1.41	1.44	1.41
r_{61}	1.36	1.37	1.41	1.35	1.40

r_{27}	1.65	1.74	1.73	1.69	1.74
r_{48}	1.25	1.25	1.27	1.25	1.25
α_{127}	123.9	122.3	120.8	123.1	121.2
α_{348}	120.5	116.2	115.9	117.2	115.9
ρ_{7213}	0.0	-1.2	-0.2	0.1	-1.6
ρ_{8435}	0.3	1.2	-0.2	1.3	1.1
ρ_{10324}	-9.0	-19.1	-11.2	-10.7	-11.2
ρ_{12651}	-0.3	-6.6	-7.8	-4.1	-3.5
	non-planar geometries				
	$S_{0,\min}$	${}^1n\pi^{*'}_{\min}$	${}^1\pi\pi^{*'}_{\min}$	${}^3\pi\pi^{*'}_{\min}$	${}^3n\pi^{*'}_{\min}$
r_{12}	1.36	1.39	1.37	1.39	1.39
r_{23}	1.37	1.41	1.39	1.41	1.41
r_{34}	1.38	1.38	1.38	1.37	1.37
r_{45}	1.43	1.44	1.44	1.44	1.45
r_{56}	1.36	1.37	1.37	1.38	1.37
r_{61}	1.36	1.35	1.36	1.34	1.36
r_{27}	1.65	1.79	1.86	1.77	1.78
r_{48}	1.25	1.25	1.24	1.25	1.25
α_{127}	123.9	118.4	112.6	115.8	111.2
α_{348}	120.5	119.7	120.9	120.6	120.9
ρ_{7213}	-0.0	32.2	45.6	37.5	41.5
ρ_{8435}	0.3	-1.5	0.3	0.4	0.0
ρ_{10324}	-9.0	9.5	4.2	6.7	6.5
ρ_{12651}	-0.3	-0.1	0.6	0.2	-0.4

Supplementary Table 3. Geometrical parameters of the nearly planar and non-planar equilibrium structures of the lowest electronic states of 2-thiouracil, reported by Teles-Ferreira et al.⁵. The largest structural changes with respect to $S_{0,\min}$ are highlighted in boldface. The bond distances r_{ij} are given in Å, the valence angles α_{ijk} and the pyramidalization angles ρ_{ijkl} are in degrees. ρ_{ijkl} is defined as the angle between the vector of the i - j bond and the kl plane. The dimension for the bond lengths is Å, for angles it is degrees.

The EOM-CCSD electronic energies at the planar and non-planar minima of the different electronic states are reported in Supplementary Table 4 and plotted in Suppl. Fig. 9. The excitation energies at the ground state equilibrium ($S_{0,\min}$) are larger by ≈ 0.4 eV compared to

those obtained by multi-reference calculations, although the spacing between the levels is similar. Indeed, the $S_2 \leftarrow S_0$ vertical excitation energy agrees quite well with the experimental gas phase UV absorption spectrum of thiouracil⁴. As shown in Suppl. Fig. 9, the potential energy surfaces of the states S_1 and T_2 , both of $n\pi^*$ character, are nearly parallel.



Supplementary Figure 9. EOM-CCSD/6-311++G** electronic energies of the lowest singlet and triplet states of 2-thiouracil, calculated at the planar and non-planar minima of the different states.

	State					
	S_0	S_1	S_2	T_1	T_2	T_3
	-	$^1(27a' \rightarrow 7a'')$	$^1(6a'' \rightarrow 7a'')$	$^3(6a'' \rightarrow 7a'')$	$^3(27a' \rightarrow 7a'')$	$^3(5a'' \rightarrow 7a'')$ $^3(6a'' \rightarrow 8a'')$
$S_{0,min}^*$	0.00	4.00	4.77	3.43	3.86	3.98
$S_{0,min}$	0.00	3.99	4.76	3.43	3.85	3.98
$S_{1,min}^*$	0.24	3.78	4.57	3.29	3.65	4.09
$S_{1,min}$	1.34	3.48	4.34	3.19	3.21	5.03
$S_{2,min}^*$	0.46	4.10	4.44	3.46	4.02	4.05
$S_{2,min}$	1.86	3.68	3.96	3.16	3.40	5.48
$T_{1,min}^*$	0.39	4.19	4.69	3.17	4.06	3.97
$T_{1,min}$	1.25	3.53	4.13	3.00	3.32	4.87

$T_{2,\min}^*$	0.22	3.78	4.59	3.29	3.65	4.08
$T_{3,\min}^*$	0.19	3.96	4.65	3.29	3.82	3.76

Supplementary Table 4. EOM-CCSD/6-311++G** electronic energies (in eV) of the lowest singlet and triplet states of 2-thiouracil, calculated at the planar and non-planar minima of the different states. For each state the dominant orbital transitions are reported. Energies are given in eV.

Supplementary Discussion 5: Calculated state - and geometry - dependent pump -probe XPS spectra

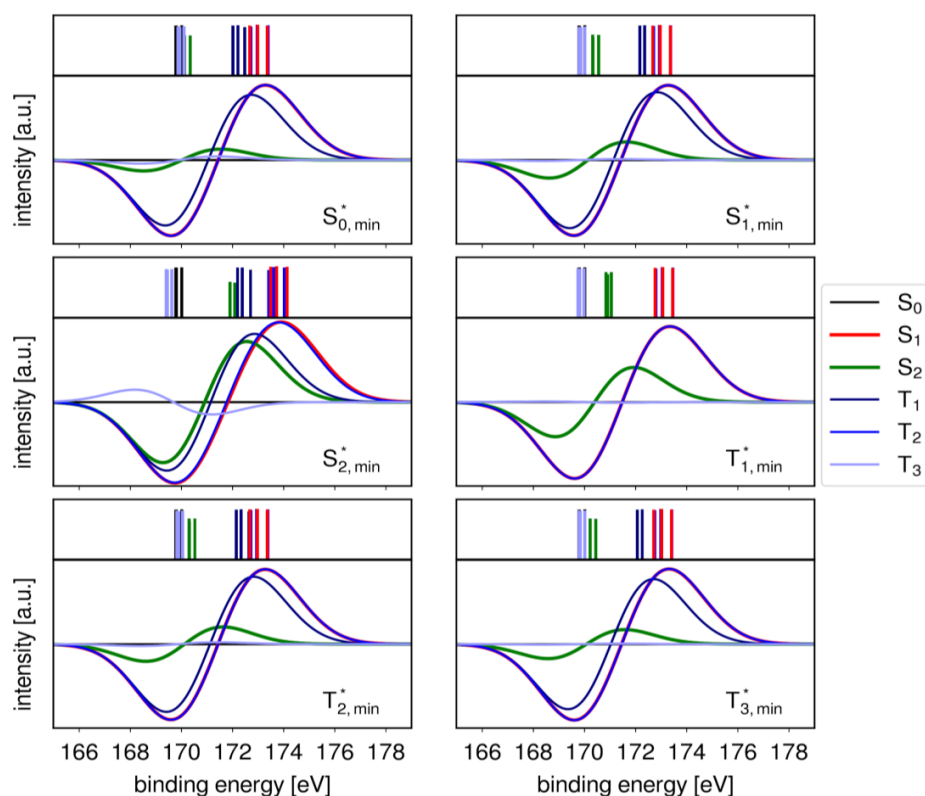
Photoelectron spectra are calculated at different geometries considering an ionisation process starting from the states S_1 , S_2 , T_1 , T_2 and T_3 . The reference “pump-off” spectrum, with ionisation starting from S_0 , is calculated only at the ground state minimum. For each geometry x the spectrum $\sigma_n^x(E)$ from the state n is given as a sum of contributions associated with the three $2p$ orbitals,

$$\sigma_n^x(E) = C \sum_{i=1}^3 A_{in}^x g(E - E_{in}^x),$$

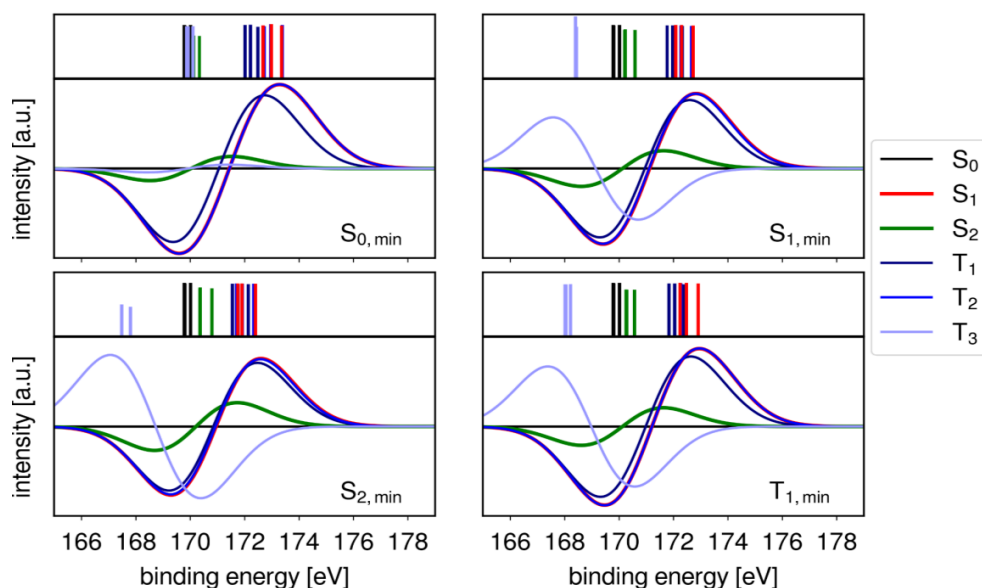
where C is a constant, E_{in}^x is the ionization potential from the $2p_i$ orbital for the state n at the geometry x , evaluated by the EOM-IP-CCSD approach, and A_{in}^x is the ionization probability, approximated as the geometric average between the norms of the left and right Dyson orbitals⁵. The function $g(\cdot)$ is used to broaden the stick transitions in order to allow the comparison with experiment; the calculated profiles are obtained by applying a Gaussian broadening with a standard deviation of 1.5 eV. Since in the EOM-IP-CCSD procedure the valence excited states are described by unrestricted wavefunctions, the two binding energies for the α and β electrons differ by 0.0-0.1 eV and have been averaged in the calculation of E_{in}^x . The (geometry-dependent) pump-probe signal $S_n^x(E)$, associated with population on a given state, is obtained as the difference

$$S_n^x(E) = \sigma_n^x(E) - \sigma_{S_0}^{S_0, min}(E).$$

The calculated pump-probe spectra are shown in Supplementary Figures 10 and 11 for the planar and non-planar geometries, respectively. Note the general trend for the binding energies $T_3 < S_2 < T_1 < S_1 \approx T_2$.



Supplementary Figure 10. Binding energies of the $2p$ electrons (top panels) and pump-probe spectra (bottom panels) evaluated for different electronic states and different planar stationary geometries. The ionization intensities are estimated using Dyson orbital norms.



Supplementary Figure 11. Binding energies of the $2p$ electrons (top panels) and pump-probe spectra (bottom panels) evaluated for different electronic states and different fully optimized geometries. The ionization intensities are estimated using Dyson orbital norms.

Supplementary Discussion 6: Potential model fits

We extend the discussion of Figure 4b of the main text. Although the linear trend is already visible in Figure 4b, the relation between the local charge and binding energy (or excited state chemical shift) becomes even more obvious, when taking geometrical effects into account. In this, we closely follow the potential model as introduced by Gelius⁶.

We fit two different versions of the potential model. Model A is a simple linear relation between the binding energy E_{bind} and local charge at the probed atom (sulphur) Q_S :

$$E_{\text{bind}} = k \cdot Q_S + l,$$

with k and l as fit constants.

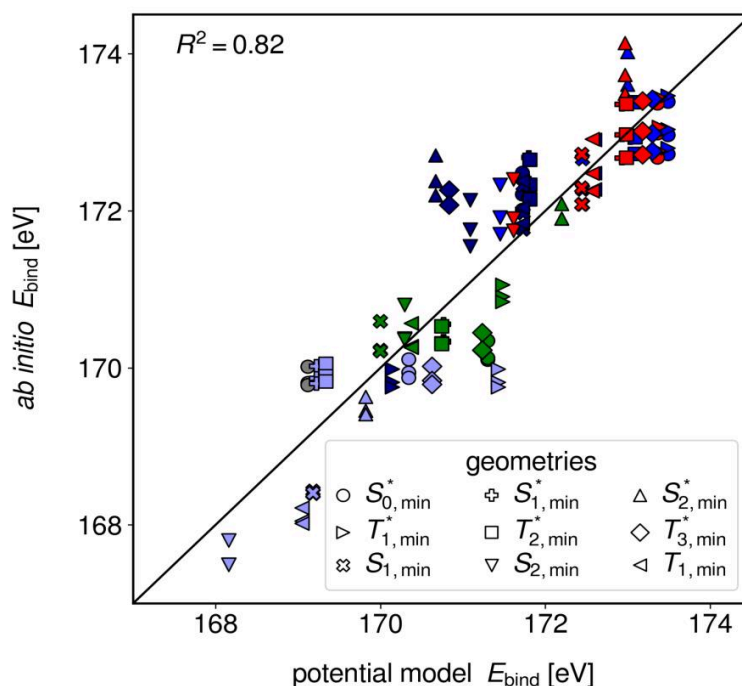
We use the calculated Löwdin charges to perform a fit and deduce k and l from the dataset in Figure 4b. The values from this fit are plotted against the model potential binding energy on the x-axis and the ab initio binding energy on the y-axis in Supplementary Figure 12. This model leads to an R^2 of 0.82.

A better fit can be obtained when taking the charge and geometry of the environment of the sulphur atom into account:

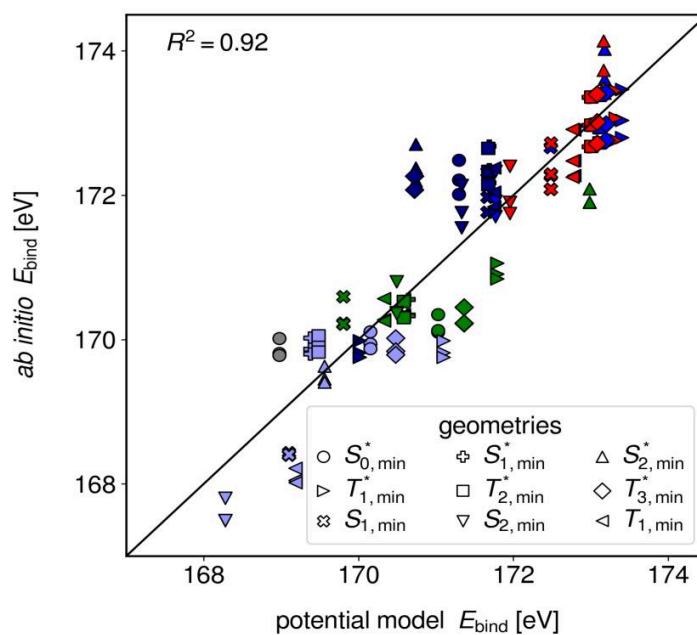
$$E_{\text{bind}} = k \cdot Q_S + \sum_{A \neq S} Q_A / R_{AS} + l,$$

where the Q_S are the charges at all other atoms at their respective distances to the probed sulphur atom R_{AS} . The result of the fit is shown in Supplementary Figure 13. It makes the fit even better, increasing the R^2 from 0.82 in the simple linear potential model to 0.92 in the more sophisticated potential model.

The remaining discrepancies between the potential model and the ab initio binding energies are due to final state effects including electronic relaxation. These effects have been discussed in the static literature (see for example Ref. ⁷).



Supplementary Figure 12. Binding energy from the ab initio calculations vs binding energy from the simple potential model for the dataset in Figure 4b.



Supplementary Figure 13. Same as Supplementary Figure 12 but using a geometrically corrected potential model.

Supplementary Discussion 7: Exceptions in the clustering according to electronic state

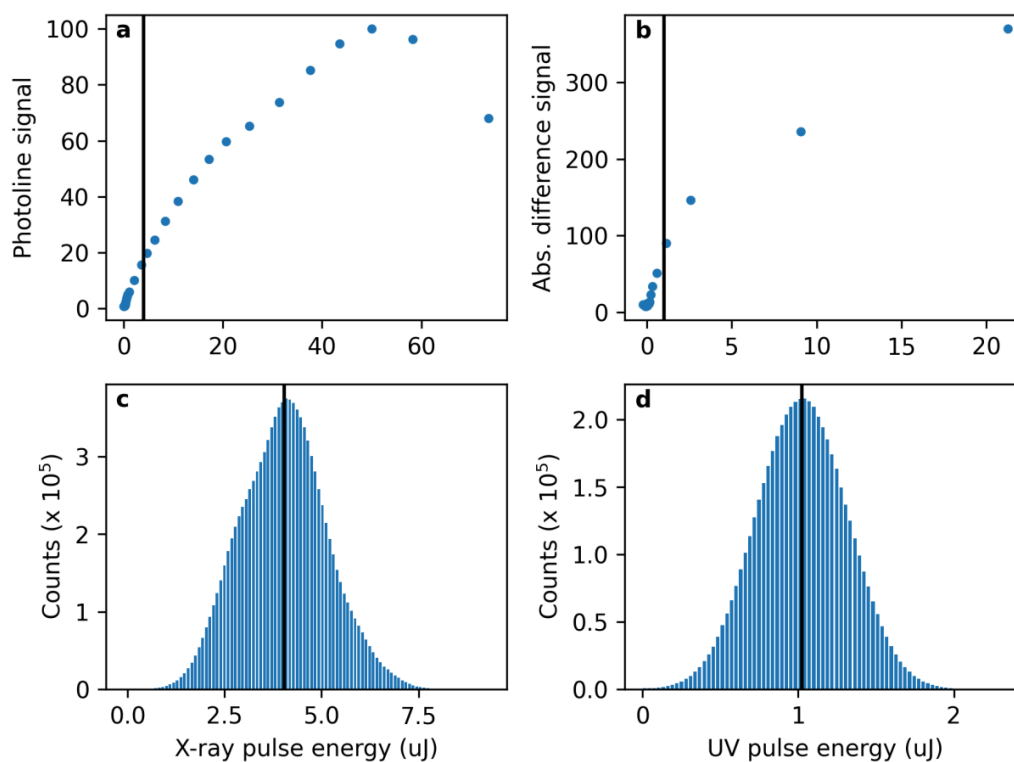
The data of Suppl. Table 2 allows us to explain the exceptions in the clustering according to electronic states reported in Figure 4(b) of the main text. For example, the dots for the T_1 state at the planar T_1 minimum ($T_{1,\min}^*$) are quite separated from the rest of the T_1 cluster. A probable reason is that this geometry is quite similar to the Frank-Condon (FC) point, except for a slight elongation of the C=C bond. In particular, in contrast to the other excited state minima, the C-S bond distance is relatively short. Therefore, it is easier for the electron hole created by UV excitation on the S atom to redistribute partially on the neighbouring atoms. Then, the $2p$ binding energy decreases.

The opposite is true for the dots of the S_2 state at the planar S_2 minimum ($S_{2,\min}^*$). Indeed, among the planar geometries, this is the one with the largest C-S bond distance, so that the hole is more likely to localize on the S atom.

Note that, although these points shift away from their clusters, the shift always correlates with the electron binding energy: the higher the partial charge on the S atom, the higher the ionization potential.

Supplementary Discussion 8: Pulse energy scans

Power-dependent scans were performed for x-ray only probing (Suppl. Fig. 14) to assure that the x-ray induced photoelectron signal is not saturated. The resulting x-ray pulse energy distribution used in the experiment is shown in Suppl. Fig. 14c. Similarly, UV-power scans were performed (Suppl. Fig. 14) to avoid UV induced saturation effects. Here, the absolute of the total difference intensity is plotted as a function of UV pulse energy. The resulting pulse energy histogram with energies in the linear excitation regime is given in Suppl. Fig. 14d.



Supplementary Figure 14 . Pulse energy scans for UV pump and x-ray probe pulse. a: X-ray-only S 2*p* photoelectron signal as a function of x-ray pulse energy. b: Integrated absolute difference signal at S 2*p* photoline as a function of UV pulse energy. c and d: X-ray and UV pulse energy distribution for the experimental data shown in the paper. The vertical black lines mark the centre of gravity of the distributions. They are also inserted in a & b for comparison to the pulse energy scans.

Supplementary Discussion 9: Data handling

Data handling procedure. The data presented covers about 8 million FEL shots. All electron time-of-flight traces have been normalised on FEL pulse energy prior to further processing. As shot-to-shot FEL photon energies are not delivered by FLASH, long term drifts and trends over the FEL pulse train have been tracked with the sulphur 2*p* photoline itself and corrected via self-referencing the photoline using the following procedure.

In order to determine the photoline position in the time-of-flight spectra better, a number of 200 consecutive pulse trains (20s of data, 50 pulses per train) were averaged pulse-wise. The resulting 50 spectra were fitted with a Gaussian function within a 200 ns window around the expected photoline position. However, only every second shot can be used to evaluate the influence of the FEL on the spectrum as the other half was additionally influenced by the UV pump. The trend over pulse train of the remaining 25 values is fitted with a second order polynomial. The resulting curve is used to shift the original 10,000 raw spectra. To track not only the trends over the pulse trains but also long-term shifts, the overall mean of the photoline position of the first of those processed data chunks is set as a global reference. The raw spectra for all data chunks are shifted towards this reference utilizing the (for each chunk determined) pulse train trend of the average spectra.

After that, shot-to-shot difference spectra were calculated and the resulting spectra were binned by delay. The delays were corrected by means of the bunch arrival monitor (BAM) which measures the arrival of the electron bunches and thus gives information on the arrival time jitter of the x-ray pulses^{8,9}. The delay binning was chosen in such a way that all bins have similar statistics (~73,000 shot pairs per bin). In combination with the delay correction via BAM, this allows a finer binning for delays close to time-zero than experimentally set.

Influence of the data handling on the experimental spectra . Both the spectral fluctuations of the x-ray pulse and the pump-probe delay fluctuations are potentially smearing out spectral-temporal signatures of the molecule. These fluctuations are resulting from the fact that the free-electron-laser is starting its lasing process from noise, part of the temporal jitter is due to other stabilization issues. Several papers have been devoted to investigate the issues of delay jitter (in Suppl. Refs. ^{8,9}) and we systematically investigated the effect of spectral and timing jitter on time-resolved photoelectron spectra in Suppl. Ref. ¹⁰.

The delay time jitter in our data is about 300 fs. While the photon energy jitter primarily changes the position and the width of the photoline, this delay jitter may also change the shape of the observed photoline. Applying a correction to the delays by tracing the arrival time of the x-ray pulses already eliminates a significant part of the random fluctuations in the time-dependent difference spectra. This has been demonstrated before in Suppl. Refs. ^{8,9}. For the difference spectra here, it makes the spectral oscillations in the region between 100 and 101 eV become visible (see Figure 4b in Suppl. Ref ¹⁰).

The most obvious 'missing' spectral feature is the sulphur photoelectron line spin-orbit splitting of 1.2 eV, that cannot be identified in our data. Since we do not have a single-shot spectral tool available, we used self-referencing for spectral correction. Based on a combination of simulations and data, we found that shot-to-shot correction by self-referencing of the photoline can correct the jitter and drifts in the static case. For pump-probe difference spectra, however, the correction of unpumped shots can only be achieved by well-adapted averaging of the data and utilising correlations in the pulse train of the FEL. Nonetheless, this allows to correct long-term drifts of the FEL photon energy. Thus, our method does not influence the shot-to-shot statistics, but narrows the long-term averaged statistics and improves it by a factor of 2-3.

Supplementary References

1. Kruit, P. & Read, F. H. Magnetic field paralleliser for 2π electron-spectrometer and electron-image magnifier. *J. Phys. E.* **16**, 313–324 (1983).
2. Mai, S., Marquetand, P. & González, L. A Static Picture of the Relaxation and Intersystem Crossing Mechanisms of Photoexcited 2-Thiouracil. *J. Phys. Chem. A* **119**, 9524–9533 (2015).
3. Teles-Ferreira, D. C. *et al.* A Unified Experimental/Theoretical Description of the Ultrafast Photophysics of Single and Double Thionated Uracils. *Chem. - A Eur. J.* **26**, 336–343 (2020).
4. Khvorostov, A., Lapinski, L., Rostkowska, H. & Nowak, M. J. UV-induced generation of rare tautomers of 2-thiouracils: A matrix isolation study. *J. Phys. Chem. A* **109**, 7700–7707 (2005).
5. Vidal, M. L., Krylov, A. I. & Coriani, S. Dyson orbitals within the fc-CVS-EOM-CCSD framework: Theory and application to X-ray photoelectron spectroscopy of ground and excited states. *Phys. Chem. Chem. Phys.* **22**, 2693–2703 (2020).
6. Gelius, U. Binding Energies and Chemical Shifts in ESCA. *Phys. Scr.* **9**, 133–147 (1974).
7. Mårtensson, N. & Nilsson, A. On the origin of core-level binding energy shifts. *J. Electr. Spectr. Rel. Phen.* **75**, 209–223 (1995).
8. Schulz, S. *et al.* Femtosecond all-optical synchronization of an X-ray free-electron laser. *Nat. Commun.* **6**, 5938 (2015).
9. Savelyev, E. *et al.* Jitter-correction for IR/UV-XUV pump-probe experiments at the FLASH free-electron laser. *New J. Phys.* **19**, 43009 (2017).
10. Mayer, D., Lever, F. & Gühr, M. Data analysis procedures for time-resolved x-ray photoelectron spectroscopy at a SASE free-electron-laser. *J. Phys. B At. Mol. Opt. Phys.* (2021) doi:10.1088/1361-6455/ac3c91.

Acknowledgements

First, I want to thank Markus Gühr for giving me the opportunity to do my doctoral thesis in his group and to do interesting research not only in our lab in Potsdam but also large facilities as FLASH and SOLEIL. I also want to thank him for having a ready ear to discuss data or problems even during stressful times and for providing the guidance through our first beamtimes at FLASH.

I also want to thank all current and former members of the group Experimental Quantum Physics in Potsdam for successful beamtimes and great discussion (physics and non-physics related) during our lunch and coffee breaks. In particular, I want to thank Jan Metje for putting all his efforts into designing and preparing the URSA-PQ apparatus during his time in Potsdam. Thanks also to Fabiano Lever who programmed the software that runs URSA-PQ and the base code for the analysis of the FLASH data. Further, I want to thank Jan Metje, Fabiano Lever, Matthew Robinson and Mario Niebuhr for great, successful beamtimes at FLASH and Fabiano Lever, Marta Murillo-Sanchez, Constantin Walz and Lisa Mehner for the beamtimes at SOLEIL.

I would like to thank Matthew Robinson for also proof-reading the thesis and keeping an eye especially on my language.

I also would like to thank Ingo Fischer who gave me the opportunity to join his group on two beamtimes at SOLEIL which turned out to be a great preparation for our own experiments there.

Last, I want to thank my family and friends.

Declaration of Authorship

I hereby declare that the thesis was written independently and without assistance except where otherwise indicated. Third parties other than the referenced sources and aids were not used. This thesis was not previously presented to another examination board or audit authority and has not been published.

Dennis Mayer

Potsdam, 08.08.2022